Title: Examining the effects of ultrasonic impact treatment as a severe plastic deformation process on the fatigue behaviour of 2024-T3 and T150-T651 aluminium alloys
Martin Castillo
: Morales
Institution: Sheffield

Acknowledgements

This work was done with thanks to many people and institutions. I gratefully knowledge the financial support of CONACyT. I also would like to thank the support of Applied Ultrasonic Inc., Airbus UK, Sheffield University, and Sheffield Hallam University – Materials and Engineering Research Institute, the last one because of the facilities provided to carry out SEM pictures and GDOES.

I am very grateful to Prof. Mike W. Brown, my supervisor in Sheffield University, who guided me through this research spending his appreciable time giving me advice, revising theoretical and physical procedures and analysis, and his marvellous patience and comprehension at the moment he read the first draft of this work.

I would like to thank Dr. Chris A. Rodopoulos who supervised me and supported me with his friendship, advice and facilities from Hallam University in order to attain research that was as good as possible, as well as the information of XRD data obtained by him. I would like to thank to all the technical staff that help to realize the technical side of this research, thanks to Mr John Goodlife for his aid to operate the hydraulic machines, to Mr Richard Kay for his electronic devices assistance to obtain experimental results, to Mr Karl Rotchell for his workshop support, to Mr Michael Jackson for his help and contribution of material and to all the staff of mechanical engineering department for their friendship and help. Thanks to Mr Aidy Ali and Pilli Srinivas for sharing knowledge, friendship and technical contribution to my project.

I am very grateful to the sacrifice of my family, my mother, my father, my brothers, and my grand parents that support me and encourage me all the time. Thanks to Tania, my girl friend, for her company, love, support and encourage throughout this work.

The time I spend in Sheffield I met many friends, Mexicans, Spanish, Chinese, English, French, Iranians, Brazilians, Italians, Malaysians etc. to whom I appreciate their friendship and their knowledge they share with me. Thanks to God to let me know all these marvellous people that gave me encourage to go on.

Preface

This thesis is based on research carried out in the Department of Mechanical Engineering at the University of Sheffield.

The content of this thesis is original and the research has been done by the author except for XRD results obtained from Dr. Chris A. Rodopoulos, and where specific references are made to other work. No part of this thesis has been submitted to any other University.

Abstract

Aluminium alloys are widely used in aerospace vehicles which are under cyclic loads through their operation. The loads may cause detrimental changes in material structure being more prone to crack initiation, starting a potential process of failure for the structure. In this research the effects of fatigue damage are assessed for two aluminium alloys, 2024-T3 and 7150-T561, after using a surface engineering method which uses the plastic deformation on the surface, like many others, to extend (or reduce) the fatigue life of materials.

Ultrasonic Impact Treatment (UIT) is the method used in this research which has been used successfully in welding zones for many materials such as steels, titanium alloys, aluminium alloys and bronze, getting fatigue life improvement. Evaluation in aluminium alloys is conducted here in order to know how fatigue life can be affected. UIT is evaluated by varying three impact process parameters at two ultrasonic frequencies, 27 kHz and 36 kHz. The parameters varied in the first part of this research are amplitude under load, impact frequency and feed rate. Four conditions of UIT treatment were investigated, by using various combinations of the parameters before mentioned. Finally, introducing a fourth parameter of pressure on the pins which was used just for Al 7150-T651 alloy, a further three UIT conditions were investigated.

Changes in microstructure, micro hardness and roughness in material were observed or measured, as well as different magnitudes of residual stresses left by the different UIT parameters used. The surface treated modified the high cycle fatigue life of the material reducing it. The presence of porosity near the surface was observed for the condition which introduced highest compressive residual stress and the highest micro-hardness, but at the same time the roughest. These changes were observed in both aluminium alloys, and a reduction in fatigue endurance. For further experiments on fatigue samples, milling 0.05 mm (50 μm) from all surfaces of the material after UIT treatment apparently eliminated porosity and defects leaving positive benefits of mechanical property changes. This skimming of the surface increased the fatigue life compared with the bare material.

Crack propagation experiments showed retardation for both of the UIT treatments examined. Retardation caused by residual stress and material properties changes enhances fatigue life, observed in the endurance test after skimming.

Two mathematical methods were developed in order to get the most realistic profile of residual stresses through the depth named MMH and MMX which were applied to the data obtained from hole drilling and XRD respectively. These two analyses were developed to include the influence of residual stress gradients and relaxation respectively.

Contents

Index of tables

Index of figures

Page Number

Notations

Symbols

$\overline{A}$, $\overline{B}$	Calibration constants
$\overline{a}$, $\overline{b}$	Dimensionless coefficients
a	Crack length
â	Average crack length
B	Specimen thickness
D	Diameter among the strain gauges circle of the rosette
D_0	Drill tip diameter
da/dN	Crack growth rate
E	Young's modulus
K_c	Fracture Toughness
L	Gauge Length
N	Number of cycles
P	Load
R	Stress Ratio $\sigma_{min}/\sigma_{max}$
Ra	Roughness
V	Voltage
W	Width of the specimen
z	Hole depth
β	Angle measured clockwise from gauge 1 to direction of σ_{max}
ΔK	Stress intensity factor range
ΔK_{th}	Stress Intensity Factor Range Threshold
ε	Strain
σ_{ys}	0.2% offset yield strength
υ	Poisson's ratio

Abbreviations

CLA	Centre Line Average
EDM	Electric Discharge Machining

EDS	Energy Dispersive Spectroscopy
EPD	Electric Potential Difference
GDOES	Glow Discharge Optical Emission Spectrometer
HCF	High Cycle Fatigue
HV	Vickers hardness
LCF	Low Cycle Fatigue
M(T)	Middle Tension Specimen
MMH	Method used to get residual stress balance through the depth using hole drilling data
MMX	Method used to get residual stress balance through the depth using XRD data
PSB	Persistent Slips Bands
SEM	Scanning Electro Microscope
UIT	Ultrasonic Impact Treatment
XRD	X-Ray Diffraction

CHAPTER I

INTRODUCTION AND OBJECTIVES

Most structures undergoing vibrations in service are prone to fatigue failure. Throughout history the study of the effects of beneficial mechanical methods on the materials has been carried out according to the necessity of extending the fatigue life of components, which also has been increasing up to now and will go on. With the invention of the airplane fatigue was taken into account deeply and the introduction of non-metallic materials spread the field of fatigue studies.

Fatigue life of materials depends mainly on its mechanical properties, surface finish, surrounding environment and applied load. Once a crack appears in the material, the propagation of the crack depends also upon the microstructure. By creating residual stress on the surface, crack initiation can be prevented and crack growth rate can be retarded [1].

Airplanes structures are under constant fatigue loading during their operation. Most of the junctions in aircraft structures, like skins to spars or ribs, are riveted and these points are stress concentrators which may lead to fatigue damage initiation in the structure and a limited life. In these areas the use of a method that can retard fatigue crack initiation and propagation would give more security and reliability to the aircraft structures. This method would be of great relevance not only in the aerospace industry, but also in automotive, transport and industries with moving machinery.

Many techniques have been developed successfully in order to generate high compressive residual stress together with changes in other properties such as grain size, micro-hardness, roughness, superficial defects, etc.[1,2], improving fatigue life in materials used in different vehicles, machines, structures, etc. Such techniques include two large groups, mechanical treatment (as shot peening, surface rolling, auto-frettage, laser peening, etc.[2]) and thermal treatment (as carburizing, nitriding, flame hardening, induction hardening, etc.[1]). The goal of these methods is to produce grain refinement, residual stress, or hardening in a material's surface to increase potentially corrosion resistance, wear and prevent early crack growth.

On the other hand when a material is welded, tensile residual stresses are induced to the joint, reducing its fatigue life. There are several techniques that can be used to eliminate tensile residual stresses left by welding, thus improving fatigue life. Most of these techniques are applied only to small pieces and/or before the assembly of various parts of a structure [3-7]. Consequently Ultrasonic Impact Treatment (UIT) was developed to fill the gap left by the techniques already in use [8].

Ultrasonic Impact Treatment (UIT) method was developed in Russia in the early 1970s [8] and its design concept showed various advantages over other techniques. Manipulation and the facility to carry the equipment manually were unique and provided the facility to treat parts of structures impossible to achieve by other methods, and moreover physical risk was reduced compared to other methods where the noise and vibrations, projectiles and lasers may pose health risks due to a prolonged use.

The UIT method was developed in order to reduce welding residual stress and deformation in submarines of Russia's Navy, introducing compressive residual stresses. Initially it was successfully applied in locations prone to fatigue fracture for steels used to build submarines. This enhanced some properties such as corrosion fatigue strength and fatigue resistance at low temperature [9]. After such success, UIT was implemented in Titanium alloys, Bronze and Aluminium alloys providing important benefits by reducing costs, time and physical risk to the operator [8, 10 & 11]. Nevertheless, the effects of UIT process in materials previously welded are unknown.

The UIT method use three free indenters with a shape of needle allocated in three different guide line holes set in a linear arrangement. They are used as the elements that impact the surface of the material. Indenters move along their axes at a frequency given by the excitation of a modulation pulse of the carrier resonant frequency of the ultrasonic oscillation system.

Aluminium alloys are generally used in aircrafts, where the extension of time operation is a priority. The two aluminium alloys most widely used in aircrafts structures are Al 2024-T3 and Al 7150-T651.

OBJECTIVES

Previous studies of UIT on welded zones of structures show that tensile residual stresses are eliminated from critical areas due to the process, but the improvement in fatigue resistance is largely due to compressive residual stresses left in those areas. Its use in materials without prior welding is uncertain because no studies have been done before, and this is where this research will be focused on.

The aim of this research is to evaluate the effects caused by different UIT conditions in Al 2024-T3 and Al 7150-T651, and to compare these effects between both materials. In addition the influence on mechanical properties, crack growth rate and the fatigue life will be evaluated.

Many parameters of the UIT technique can be changed in order to obtain different UIT conditions under different carrier frequency. Initially two carrier frequencies were chosen from previous work on aluminium alloys (27 kHz and 36 kHz). Three UIT parameters were varied: the feed rate, the amplitude under load and the impact frequency. Therefore five different UIT conditions called UIT-1-36, UIT-1-27, UIT-2-36, UIT-3-36 and UIT-4-36 conditions were obtained. Finally the pressure force was varied and from this two more UIT conditions were achieved namely UIT-5-36 and UIT-6-36.

The primary objective of this research is the examination of the effects of **U**ltrasonic **I**mpact **T**reatment as a severe plastic deformation process on the fatigue behaviour in both materials without prior welding. There is no data in the literature about any material treated with UIT without prior welding.

Secondly with the use of different UIT conditions in both materials, changes of residual stresses, hardness, microstructure, fatigue and crack propagation will be examined. The sensitivity of these properties to the UIT method will be investigated, together with possible strategies to get improvement of material behaviour and extension of their fatigue life.

CHAPTER II

FATIGUE

FATIGUE FAILURE

The repeated changing of loads (Cycles) in a material generates changes in its properties due to the repeated changes of stress or strain even below the tensile strength of the material; this is called Fatigue [1, 12]. All the machines and some structures like bridges and buildings are under fatigue loading that through time causes damage and then failure or fracture of the material. Sometimes or most of the time fatigue is interacting with other processes depending the environment where the element is operating. Creep and fatigue, cyclic loading at high temperature (Steam Turbines and Gas turbines), fretting fatigue due to small motions between fitted parts combined with cyclic loadings to produce surface damage, corrosion fatigue due to the combination of corrosion and fatigue loading (Structural members of offshore oil well platforms), are some of the combined effects to be considered in a design.

Fatigue life is divided in two zones depending of the number of cycles to fracture, low cycle fatigue (LCF) and high cycle fatigue (HCF). According to [13] if the number of cycles is large, more than one million then it is termed high-cycle fatigue. If the number of cycles is less than one million it is termed low-cycle fatigue. But [14] it is insufficient just define HCF as life above one million cycles for every material, because HCF starts when the stress applied is sufficiently low that yielding effects do not dominate the behaviour. On this basis, the rank where HCF typically starts is from 10^2 to 10^4 cycles for most metals, where the plastic strain is 50% of the applied strain range.

Initially fatigue is considered as a constant cyclic loading condition, figure 2.1a, with constant amplitude, constant maximum and minimum stress or load. Actually all the structures subject to cyclic loads do not experience such fatigue with constant amplitude but variable amplitude, figure 2.1b. This condition makes changes in the range of crack growth rate and many effects are presented that influence it, such as premature closure of the crack faces, even under fully tensile far-field cyclic loads, shielding of the crack tip, etc.

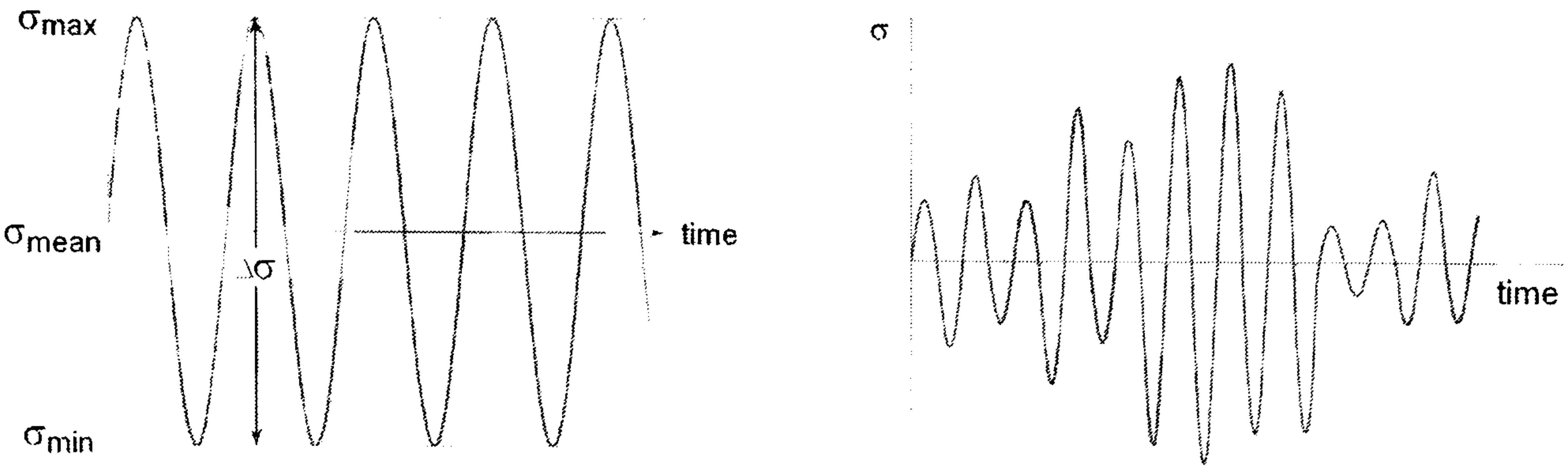

a) b)

Figure 2.1 Constant and variable amplitude load, the former is idealised, and the latter is the physical load case that is presented in true life.

CRACK INITIATION

Metal atoms are ordered in a special arrangement called a crystal. There are different crystal arrangements such as PC (Primitive cubic), BCC (Body-centered Cubic), FCC (Face-Centered Cubic) and HCP (Hexagonal close-packed). Each crystal has its own mechanical response, ordering direction and directional property. Crystal orientation will delineate a grain and each grain will have a special slip direction with respect to the load direction applied.

Fatigue starts with the slip or glide of crystal planes within a grain. (This is not just a fatigue property but a monotonic property as well.) Fatigue slip bands form intrusions and extrusions on the surface of metal due to the cyclic load and they can be seen as lines on the surface and act as a stress concentrators or notches. Removing intrusions and extrusions on the surface by electro polishing and then applying cyclic load for a period some slips bands appear again in the same place. These marks are called

Persistent Slips Bands (PSB) first published by Forsyth & Ryder in their research in Copper [1,15].

Actually slip bands are the fatigue crack embryo and tend to grow in a plane of maximum shear stress range. After that there is a coalescence of many of these incipient fatigue cracks and they tend to grow in a plane of maximum tensile stress range, called stage I and stage II respectively fig 2.2. The length of the crack in stage I is of the order of some grains. Most of fatigue cracks grow through the grains, called trans-granular, but some times they grow along grain boundaries and are called inter-granular[1, 16]. The fact that materials fail at a specific number of cycles means that a permanent change in properties occurs on every cycle [13,14].

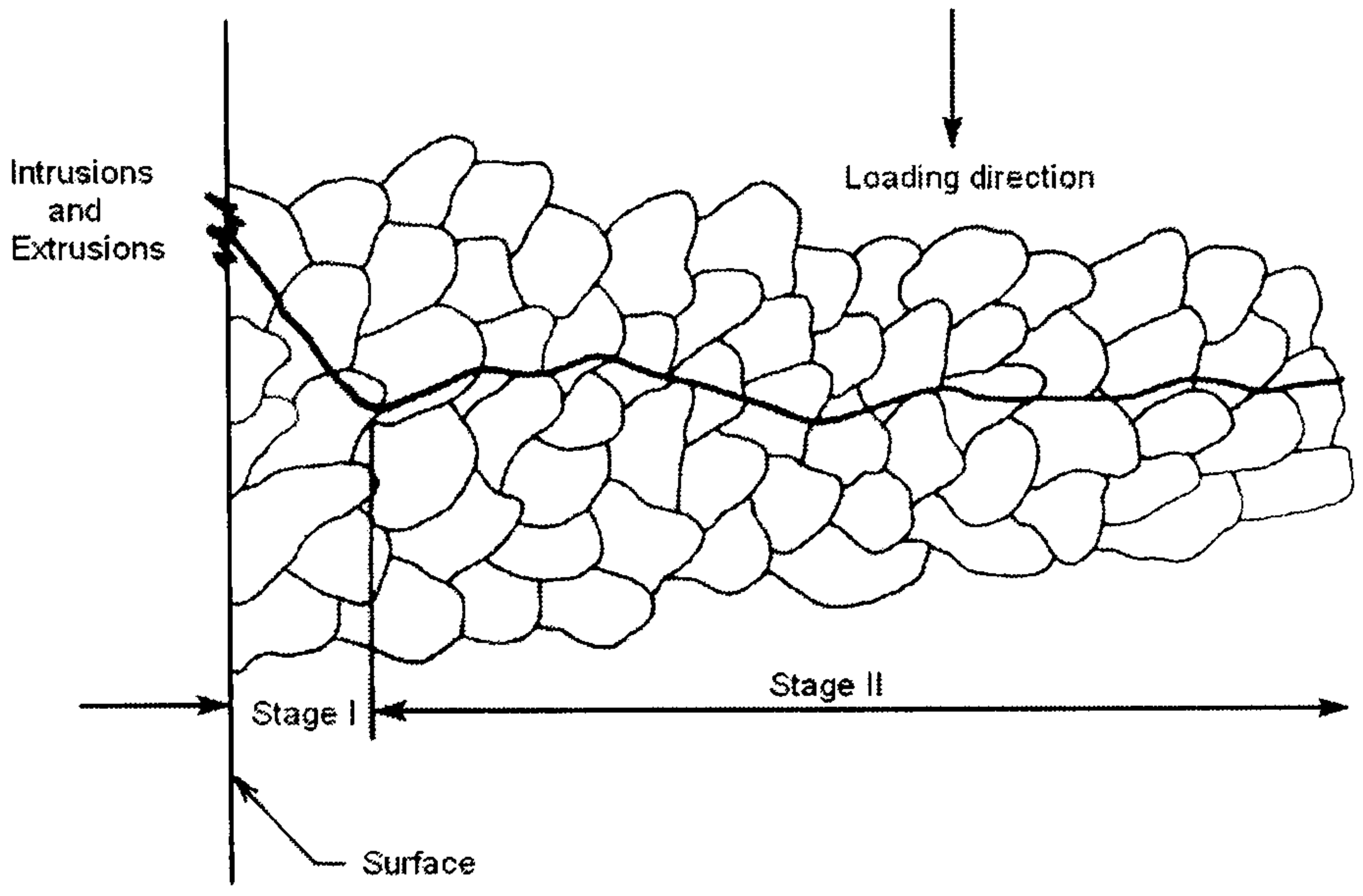

Figure 2.2 Crack growth stages, from initiation of intrusions and extrusions, through shear growth (stage I) to the crack propagation through the grains (stage II).

FATIGUE LIMIT

Data obtained from fatigue tests are useful in order to know how Stress Amplitude affects the fatigue life of the material. The best way to do it is plotting Stress Amplitude Versus Number of cycles to fracture, in ordinate and abscissa axes respectively called S-N curve. Because the number of cycles to fracture change drastically compared with Stress Amplitude is necessary to plot Number of cycles in a logarithmic scale.

When a material is under stress amplitude control and it enters in the high cycle fatigue zone (More than 1 million cycles), then it could be close to the fatigue limit or endurance limit σ_e. Initially the fatigue limit was defined as "The limit of crack initiation under cyclic stress". This could be true for some metals. Actually in some metals, small cracks can appear and start to grow. But some times after small cracks appear they do not coalescence or grow at all, called "non-propagating cracks", and material can be under the same stress amplitude for more than 10 million cycles with the same crack length and no further propagation. This may also apply for materials that do not present any crack on the surface, but inside only.

In ferrous metals specimens tested close to the fatigue limit, it has been observed that the maximum non-propagating crack length is always larger than one grain size. Testing specimens within 2-3% higher load than fatigue limit, maximum size crack exceeds the condition of non-propagation and all specimens were fractured. Testing specimens within 2-3% lower load than fatigue limit, not one crack initiation was found. So it is clear that the conditions for a fatigue limit based in non-propagating cracks are satisfied in a narrow band of stress amplitude conditions [17].

In an S-N curve it can be possible to observe a line with a specific negative slope, from high stress amplitude and low cycles (Point A) to lower stress amplitude and high cycles (Point B) as it can see in fig. 2.3. This line interrupted its path at a specific stress amplitude value (σ_e) where no failure for lower loads are observed and fatigue life increases much more exhibiting a plateau in the stress-life plot typically more than 10^6 cycles. This point is called "knee point"; in some materials the knee point is observed as in steels, meanwhile most of them continue with the fatigue line as before with no clear knee point, up to this stress value it said that material will not fail, as aluminium alloys, copper and brass. If crack initiation were correlated to the fatigue limit rather than a non-propagating threshold, a knee point would not be clear for steels, like the curves for aluminium alloys, copper and brass. In these cases a fatigue limit is considered to occur when the number of cycles reaches 10^7 or 10^8 and material has not fractured.

A proper definition for fatigue limit is given as "Cyclic stress amplitude below which initiated or pre-existing cracks do not propagate to final fracture" [18].

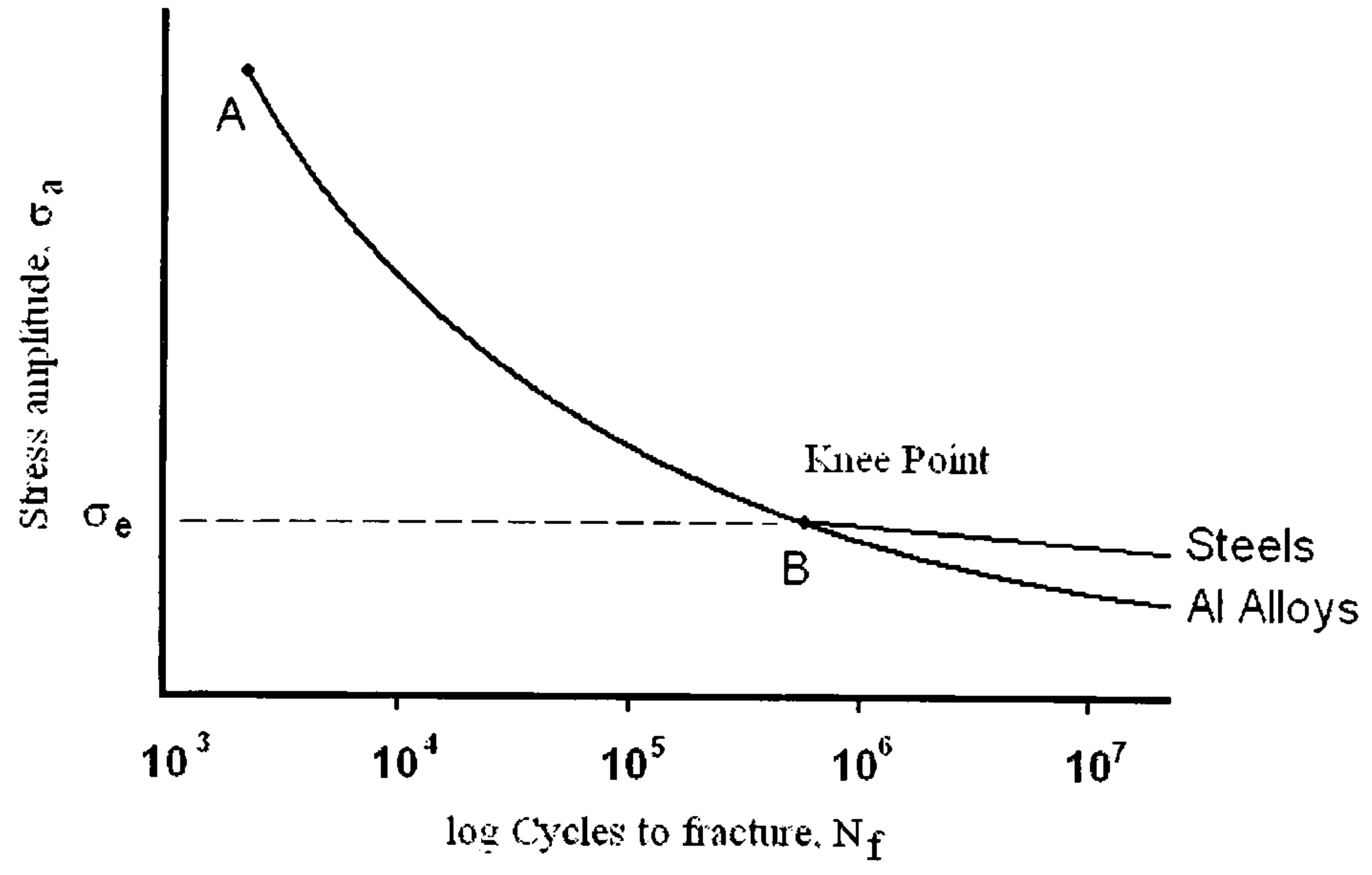

Figure 2.3 S-N Curve showing the "knee point" (B) as a fatigue limit for Steels, and for Aluminium alloys.

CRACK GROWTH

Many structures are under cyclic movement, specially those made by humans, some of them are huge and other small, employing different materials and performing different tasks. Metals are the most widely used materials in structures and machines where some behave in a brittle and others in a ductile manner. Pieces may have small defects from manufacture or they may initiate cracks during the service life. Many methods to identify a small defect or small crack have been developed through the years; some methods are basic such as inspection by naked eyes, and others use technology as x rays, ultrasonic waves, etc.

A crack can be detectable by special methods, emphasis must be placed on its possible growth by fatigue. The dominant flaw will propagate with every cycle to a critical dimension in a substantial amount dictated by fracture toughness, limit load, allowable strain or allowable compliance change [1], leading to brittle or ductile fracture once it is sufficiently large. Such a process is called fatigue crack growth, characterised and well known by the relationship of crack length (a) and number of cycles (N). The relationship is represented by ($\Delta a/\Delta N$), under constant stress range, where the crack is increasing by Δa with the number of cycles Δn as it can seen in fig. 2.4. A curve is obtained from a specific load condition, which means, if two pieces with the same geometry, material and environment conditions but with different loads magnitude are tested, they will give two different curves (different crack growth rate) from a detectable crack length (a_d) to fracture crack length (a_c), as shown in fig. 2.4.

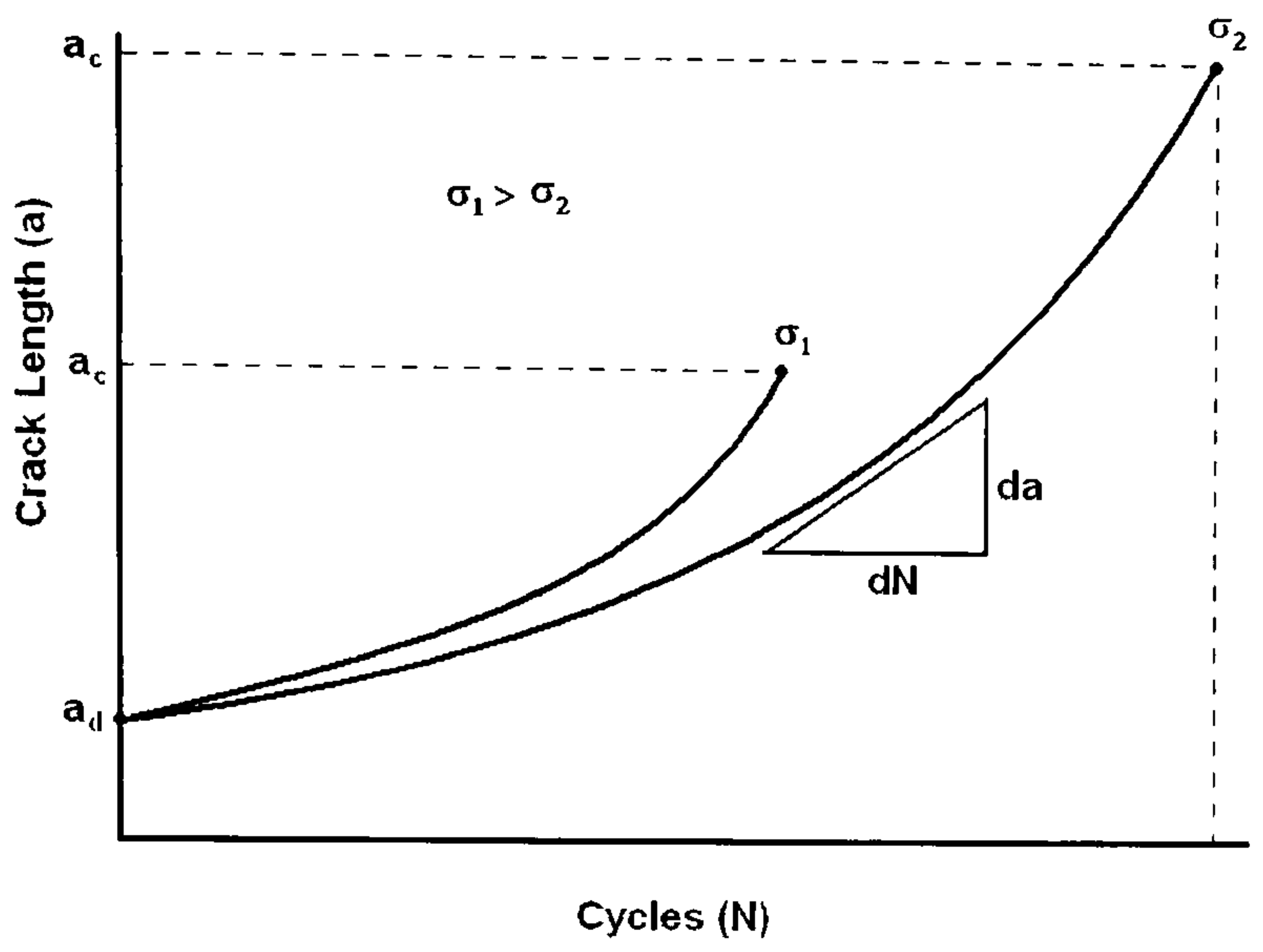

Figure 2.4 Crack growths from a detectable crack length a_d to a fracture crack length a_c under constant amplitude.

Fatigue crack growth rate is influenced by the combination of applied stresses, crack length and geometry of the structure, as well as the mechanisms introduced due to different combinations of mean stress, test frequency and environment [1].

It is observed that some discrepancies arise in crack growth rate for short cracks compared to long cracks, and due to this crack growth is divided in two regimes; short crack growth and long crack growth.

LONG CRACK GROWTH

As it was seen above crack growth rate depends of the stress amplitude. Once the crack has been identified the next question is to know how long will take to reach the fracture point. To predict the time left for the crack to growth in a stable manner under specific conditions of load and environment the use of Fracture Mechanics (FM) is required.

Crack growth rate can be represented by the ratio $\Delta a/\Delta N$, slope of the segment between two points, or for small intervals, by the derivative da/dN that is the slope of the curve at a point on the "a" Vs "N" curve. As crack growth rate depends of stress amplitude, stress intensity factor range should be used.

$$\Delta K = K_{max} - K_{min}$$

Because there are many ways to get ΔK, the stress ratio (R) is used. It should be pointed out that ΔK and R will affect crack growth rate as well as mean stress.

$$R = \sigma_{min} / \sigma_{max}$$

For a given material tested under fatigue with stress amplitude constant, ΔK versus da/dN data are plotted in a logarithmic scale for both axes, and fitted to a curve fig. 2.5. It is observed that there are three different regions with characteristic slopes along the graph; the dashed lines mark the three different stages of fatigue crack growth. Some people divided crack growth rate in more than three stages in order to get more accurate results in the prediction of fatigue life [19]. Ritchie divided in three the fatigue crack growth regimes [20], and he realized that there exist intrinsic mechanisms (that can promote the crack growth) and extrinsic mechanisms (working as a shield for the crack tip) [21].

In stage I it is seen that the smallest crack growth rate is close to zero. This point has coordinates da/dN, ΔK and its values are the smallest in the plot. The value for ΔK is called stress intensity factor range threshold ΔK_{th}. Below this point cracks either remain dormant or grow at undetectable rates. From this point a higher growth rate is seen that follows a vertical trend up to a point where crack growth rate curve starts to change its slope and enter to a new steady crack growth rate region. This stage was identified by Forsyth [22] for short cracks, and he states that "when a crack and the plastic zone at the crack tip are within a few grains diameter, crack growth occurs predominantly by simple shear along the slip system. This mechanism leads to a zigzag crack path". Studies in Ti6246 alloy show that Crack Growth rate in stage I can be affected by environment conditions [23]. As well as these effects, ΔK_{th} is affected sometimes by the thickness of the specimen, increasing when specimen thickness is reduced [24]. Basically this stage is influenced by microstructure, mean stress and environment [21].

Stage II is a deformation controlled process [25], because crack tip length increases with loading and a resharpening of the crack tip is carried out with unloading on every cycle. This mechanism is seen in mode I, but in mode II and III is not seen unless the crack path deviates. This mechanism is intrinsic and promotes the crack growth.

The crack growth fracture surface in mode I initially is smooth, and it will remain smooth if the mode I persists [26]. Forsyth who was the first in recognize the first two stages in crack growth stated "in stage II crack growth takes place in a direction normal to the applied stress" [27]. The crack directional stability is given by stresses parallel to the crack called T-Stress [28] and depending if they are compressive (negative) or under tension (positive) the crack can be directionally stable or unstable respectively, although some times in positive T-Stress a directionally stable crack has been seen [29]. A formula relating crack growth increment with stress intensity factor range knows as Paris law [30,31] represents the logarithmic line obtained in stage II. The relationship given by Paris is;

$$\frac{da}{dN} = C(\Delta K)^{m} \qquad \text{where} \qquad \Delta K = Y\,\Delta\sigma\,\sqrt{\pi a}$$

Where C and m are constants, m represents the slope; "Y" is a geometry factor depending on the loading and cracking body configuration. Measurements of $\Delta a/\Delta N$ through the depth can be done physically on steels directly from the fracture surface with the aid of beach marks (in steels) produced by a cyclic overload [32], or striations (in Aluminium) [1, 33]. The linear behaviour (on a logarithmic scale) is shown in fig. 2.5, representing the stage II crack growing up to a point where the path starts to change. Up to this point stage II is dominated by Paris law equation, where the last stage, III, begins to form.

There are some mechanisms that can contribute to the crack growth rate and others that can retard it. These mechanisms are intrinsic, which act ahead of the crack tip as cleavage fracture, micro-void coalescence and the repetitive blunting and resharpening of the crack tip, and extrinsic, which act behind the crack tip to shield it with the creation of inelastic zone around the crack wake, or to introduce physical contact by grain bridging and fibre bridging. The crack growth depends of the competition between the presence of these two types of mechanism. Stage II is mainly influenced by the combination of environment, mean stress and frequency, and little by microstructure and thickness [35, 21, 34].

Stage III is the last part of the graph, and in fig. 2.5 it is seen how crack growth rate increases to become unstable and finish when the value of $K_{max} = K_c$ is reached and fast fracture break the sample.

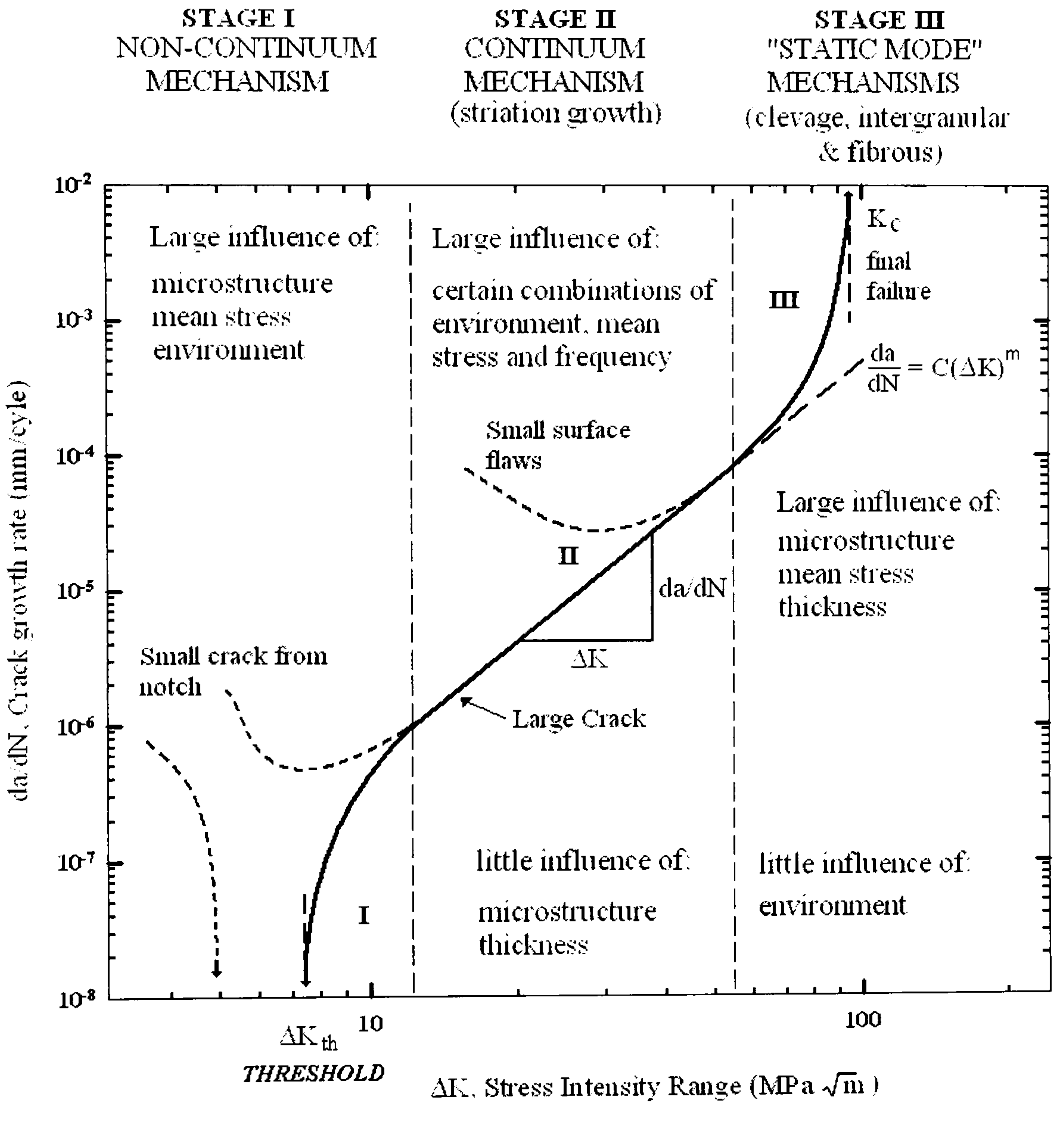

Figure 2.5 Fatigue crack growth versus ΔK graph. Plot showing a sketch of the stages of primary growth rate mechanism in a crack growth rate commonly seen from metallic materials, listing the principal influences in every stage to the fatigue crack growth rate [20] and the trend that small cracks follow depending on the specimen (notched or smooth) [36].

SHORT CRACK GROWTH

In some studies it was found that slip bands and grain boundaries are the most common points for fatigue crack initiation and this is due to the crystallographic misorientation between the grains involved [37, 38]. Although intrusions and extrusions on the surface formed by slip bands due to fatigue could be the crack initiation process, comparison between copper fatigue tests done in air and in vacuum indicates that the environment does not affect the topography and the slip behaviour [39]. So the environment does not influence short cracks in the same way as persistent slip bands (PSB), as more than one grain depth is fractured or divided during fatigue.

Physical sizes of short cracks depend on the point of view of each person. Small fatigue crack can be considered up to a length of few grains, or up to a few millimetres [14, 40]. Fatigue cracks could initially start on the surface and because of that the environment and the condition of the surface are important factors influencing fatigue behaviour. In steels small fatigue cracks are present at the beginning of the fatigue process and the quantity of them increases with the number of cycles showing a linear relationship between crack density and the maximum crack length [41, 42]. Results from Carbon steel St37 show the evolution of micro cracks during the fatigue life and it was observed that at around 20% of fatigue life micro cracks start to nucleate, at 40% of fatigue life the longest crack can reach a length of 30 μm and the density of micro cracks is as high as 86/mm^2. After that the increment in number and length is rapidly increased. At 60% of fatigue life can be seen that the longest crack can reach a length of 100 μm and the density is as high as 298/mm^2 [42].

Small fatigue crack growth has been studied apart from the long crack growth due to the differences in growth rate; because of this effect Linear Elastic Fracture Mechanics (LEFM) is not used for small cracks and Elastic Plastic Fracture Mechanics (EPFM) is employed. The small crack effect is so called because when comparing the small crack growth rate with the estimated long crack growth at the same nominal value of ΔK, the former is faster than the latter, fig. 2.5, [36] with the crack closure transient being one of the major causes [43]. This effect has been seen in low strength mild steel, aluminium and titanium alloys and nickel base super alloys under cyclic tension compression, whereas in other materials this effect is not seen such as high strength steel [1, 44-47]. On the other hand in some aluminium alloys under block spectrum loading the small crack effect is not seen [44, 48, 49]. In materials with the effects of small crack, a reduction of growth rate is seen when the crack tip reaches the grain boundary considering just the surface (2D) [50]. But one must keep in mind that the crack grows through the bulk and is growing in 3D in smooth components. considering as well the crack nucleation [42].

According to [1] a crack shorter than 0.3 mm (in a nickel base super alloy) can be considered as small crack because up to that length the results in life prediction using LEFM may not give conservative values (even if small-scale yielding conditions prevail). Actually reference [51] suggests different definitions where the length can vary and growth is dependent on grain size, interparticle spacing (for composites), size of near tip plasticity, the effect of the dependence on environmental stress corrosion fatigue, and the effects of crack dimensions.

RESIDUAL STRESS RELAXATION

RESIDUAL STRESSES

Since metals become available in the human life, they have been of great aid in our lives. Starting as a tool used to hunt, to defend or to conquer, the army who had the strongest swords was the more powerful in battle. In those days to get a stronger material was necessary to treat an existing one and in order to accomplish this they hit the material at a specific temperature (forge); this is one of the process used to improve some characteristics of metals.

Nowadays the field where metals are employed is huge and it extend from a small tool used in the kitchen to a big vehicle where hundreds of human lives are carried and which is exposed to cyclic loads. In the same manner many methods are used to manipulate some characteristics of metals (temper, shot peening, etc.), as well as methods used to create pieces that at the same time change some characteristics of metals (Fold, Weld, etc.).

A new internal state of stress or change into another internal state of stress in the material is generated for all these methods, called residual stress (or self stress). These residual stresses can be tensile, which is not good, or compressive, which is beneficial, and depending on the zone where they exist, even these residual stresses can create fracture to the material without any aid of external force applied. An example is a beam of high tensile strength steel, 12 m. long, skew cut at both ends and then laid on the floor for 24 hours, which suddenly fractured along the mid section [52]. It was supposed that the fracture was due to residual stresses that remain because of rolling and flame cutting.

Compressive residual stresses are introduced by permanently stretching a thin surface layer by yielding it in tension, so the material in the bulk tries to recover its original state by elastic deformation forcing the surface layer to compress [14]. In order to prevent fatigue or extend fatigue life a reduction in tensile stress or mean stress that occurs during fatigue can be made by creating compressive residual stress on the surface [53]. Hard materials are more sensitive to residual stresses than soft materials; it means that more improvement on fatigue life can be obtained in hard materials than in soft materials [54].

Nowadays there are many methods or treatments to produce residual stresses, which are accompanied by physical or metallurgical changes of the metal, and its magnitude depends on a) the hardness and brittleness of the metal, b) the metallurgical changes which take place, and c) the stability of the internal stresses developed [55].

The ways to produce residual stresses fall in two categories, mechanical treatments and thermal treatments. Basically mechanical methods rely on strain gradient to produce local tensile yielding; some examples are shot peening, surface rolling, laser peening, autofrettage, etc. Thermal treatments not only produce compressive residual stresses but tensile residual stresses as well. Welding and severe grinding are two examples which increase the temperature of the material and leave tensile residual stresses. On the other hand, treatments like carburizing, nitriding and flame hardening leave compressive residual stress [1, 16].

Internal stresses are divided by three different types [55]: the first, an external action (mechanical, chemical or thermal) that creates a plastic distortion in part of the body and produce non-uniform stresses through the material; second; the heterogeneities between the microscopic components of the material (as differences in elastic modulus, coefficient of expansion, etc.) that interact between crystalline grains can increase the internal stress [56, 57]; and third, increment in microstresses in a polycrystalline materials because of the non-isotropic behaviour of the crystalline grains themselves in the course of heating, straining or chemical change. The last two are called microstresses and the first are called macrostresses.

Processes like shot peening and carburizing leave residual stresses at the surface improving the performance in high cycle fatigue of the material. However as at the surface there are compressive residual stresses, inside the material (subsurface) tensile residual stresses are developed and subsurface cracks could appear [12, 14].

RESIDUAL STRESS MEASUREMENTS

Residual stress magnitude is important for engineers and it is necessary to measure it, but for stresses it is usually not possible to measure them directly. Stress in a body is accompanied by strain which can be measured physically, as can be seen when a metallic bar is under tensile stress and it deforms in longitudinal and transverse directions because of the load. Strain measurements are going to be the indirect way to evaluate stresses, and there are many methods to measure them. With the aid of elasticity, which relates stress and strain, it is possible to know the variation of stress.

As residual stress is completely internal to a body it is necessary to look for methods which can give an approximation of the internal distribution of stresses. There are many methods to try to measure the internal stress distribution through the depth, but until recently there were not any non-destructive methods at all, most techniques are destructive. The one exception is the Neutron beam diffraction method, where Neutron beam are able to penetrate the surface. All other methods up to now require the elimination of a layer of specific depth to know what would be the stress at that depth.

Even the X-ray method [58], which is the one which neither requires any measurement of the material previous to the induction of residual stress nor removal of a layer to know the residual stress on the surface, is incapable to get strain through the depth without the removal of a layer of material. There are others methods such as the slitting method, which assume that residual stress along the slit is uniform, and the contour method [59].

RESIDUAL STRESS RELAXATION UNDER MONOTONIC LOADING

The stress relaxation in a material is observed under constant strain which at the same time permits stress to be relieved, since applied stress is proportional to the applied stress; this situation is known as viscoelasticity. For small loads the behaviour is linear and the behaviour is represented physically by series arrangement of a spring and a dashpot (which includes viscosity) knowing as Maxwell model. On the other hand creep represents the non linearity of viscoelasticity and is represented physically by parallel arrangement of spring and dashpot knowing as Kelvin-Voigt model, fig. 2.6.

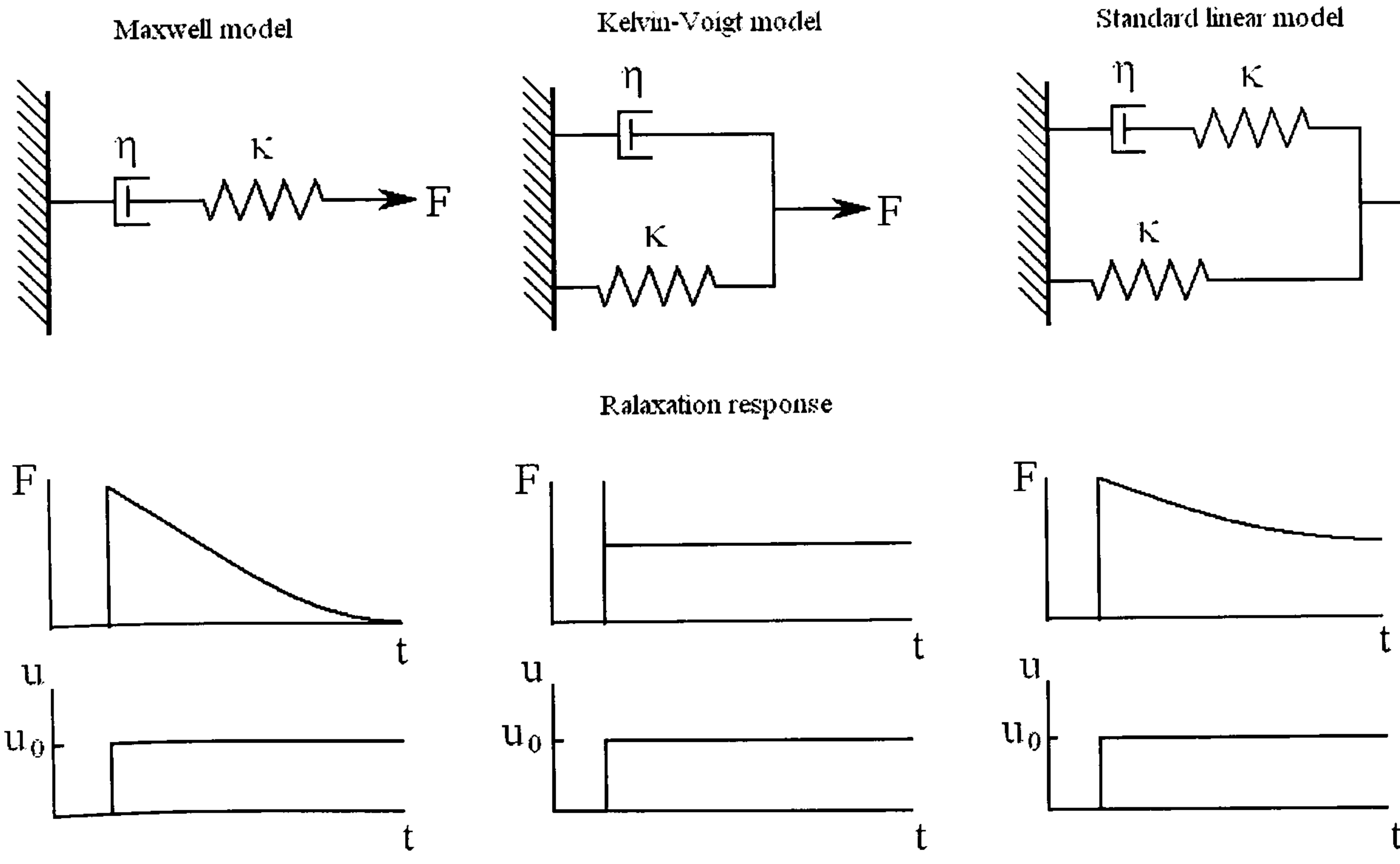

Figure 2.6 Schematic representation of relaxation response from different models, for an applied displacement u_0.

Metals and ceramics at high stresses do not exhibit the linear behaviour and can not be modelled by Maxwell model, so a combination of Maxwell and Kelvin-Voigt models can represent their behaviour, such as the Standard linear solid model. Standard linear solid model is represented by parallel arrangement of a spring and a series arrangement of spring and dashpot [1, 14].

In test on annealed aluminium monotonically loaded [60] it was observed that the higher the load the more relaxation occurs, so the stress relaxation behaviour depends on initial load. On the other hand, there was no effect on stress relaxation due to work hardening.

RESIDUAL STRESS RELAXATION UNDER CYCLIC LOADING

Residual stress in metals subject to a cyclic load experiences a relaxation. This means a steady reduction of the compressive and tensile residual stress magnitude through the number of cycles.

Residual stresses under cyclic loading in aluminium alloy AA6110 (Al-Mg-Si-Cu) [61] aged at different conditions and subsequently rolled, in polycrystalline nickel super alloy "Udimet 720Li" [62] shot peened and subjected to a cyclic fatigue at different high temperatures, and steel AISI 4140 (German grade 42 CrMo4) [63] shot peened, were measured on the surface before and after tests at some specific numbers of cycles and showed a quasi static relaxation in the first cycle of about 50% irrespective of the testing temperature. An explanation of this reduction is given by Zhuang et al. [64] and Schulze and Macherauch [63] using the Bauschinger effect. After the first cycle no significant residual stress relaxation was observed and the small cyclic relaxation behaviour is linear as a function of the logarithm of the number of cycles where the slope of this straight line is linearly dependent of the fictitious initial stress amplitude at the surface and the temperature tested.

In steels with different shot peening surface treatment and under cyclic fatigue load [65], residual stress relaxation varied through the depth with the number of cycles and with the applied tension, even under the fatigue limit, of the shot peening conditions. Only in one shot peening condition examined residual stress relaxation was null on the surface, but meanwhile underneath a relaxation occurred. It was observed that the greater the applied tension, the greater the relaxation stress.

High temperature affects residual stress relaxation and acting together with mechanical residual stress relaxation is called thermomechanical residual stress relaxation. When a fatigue test at high temperature has been started, an initial amount of thermal residual stress relaxation has occurred before cycling, and it depends on the temperature how much residual stress relaxation is purely thermal. After the first cycle up to 1000 cycles thermal residual stresses relaxation is negligible and residual stress relaxation is controlled by mechanical stress relaxation, after that residual stress relaxation is controlled by both thermal and mechanical stress mechanisms [66].

Stress relaxation is mainly affected by [64]:

a) Initial amount of residual stress and degree of cold working.
b) Cyclic stress amplitude, load ratio, number of cycles
c) Material cyclic stress-strain response, degree of cyclic work hardening/softening

SURFACE ENGINEERING TREATMENT

SURFACE TREATMENT

As mentioned before, residual stresses are obtained by different techniques and the one that definitely will be the most useful is the one than can be managed most easily, cheaply and giving good results. The most common methods used up to now are the mechanical ones specially those which can not be used on pieces already installed in structures, machines or vehicles. There are many methods suggested for use until now but the most common are shot peening, laser peening and ultrasonic shot peening (another method, not common, which is based on ultrasonic peening excitation has already been tested successfully in titanium, and is called the rotating pin ultrasonic peening (RPUP) technique [67]), which already have a good performance record and have been used in the automotive and aerospace industries. All the methods mentioned before generate from the surface through the depth a compressive residual stress, surface nano-crystallization and enhanced surface hardening.

SHOT PEENING

The shot peening process is carried out in a cabinet in order to collect the shot and reuse it, as well as to retain dust. The piece to be peened is introduced mechanically into the shot stream. The shot has spherical shape and is made of different materials and sizes ranging from 0.18 to 2.4 mm in diameter.

The classification of the shots are as follows: high carbon steel (SAEJ827), low carbon steel (SAEJ2175), cast iron, cut wire (SAEJ441), case hardened balls (AMS 241/5), atomised steel powders, glass beads (SAEJ1173), and ceramic beads (SAEJ1830). The impact velocity ranges from 20 to 150 m/s. There are three different types of machine to carry out the shot peening process, pneumatic, centrifugal and vapour slurry machines.

As the surface is impacted by the sphere a dimple is created as a result of plastic deformation fig. 2.7, after the ball strikes the surface and rebounds the deformed region tries to expand but the surrounded material restrains its expansion, creating compressive residual stress [68]. The residual stress magnitude depends of the dynamic force on the shots, the exposure time, relative hardness between the shots and the tested material, and the size of the shots [69].

For every material there is a specific shot peening condition in order to get the best improvement in material properties, too much time in shot peening could cause detrimental results in fatigue [68, 70].

Shot peening improves fatigue life of aluminium alloys 7050 [71], 7075-T7351 [72], 2024-T351 [73], 6061-T652 [69], and aluminium zinc alloy [74] by prolonging crack arrest and reducing crack growth with a lower R ratio. As the surface finish after shot peening treatment in high strength aluminium alloys is not as smooth as desired, the roughness is a problem to the fatigue life of the material, but the residual stress distribution should be enough to counteract its effects. If shot peening parameters are controlled such disadvantages can be overcome to give improvement of fatigue life at high values of stress ratio, improvement in crack arrest at low values of stress ratio. Otherwise without any control in the parameters, shot peening (SP) may not generate any improvement and even can cause damage [75].

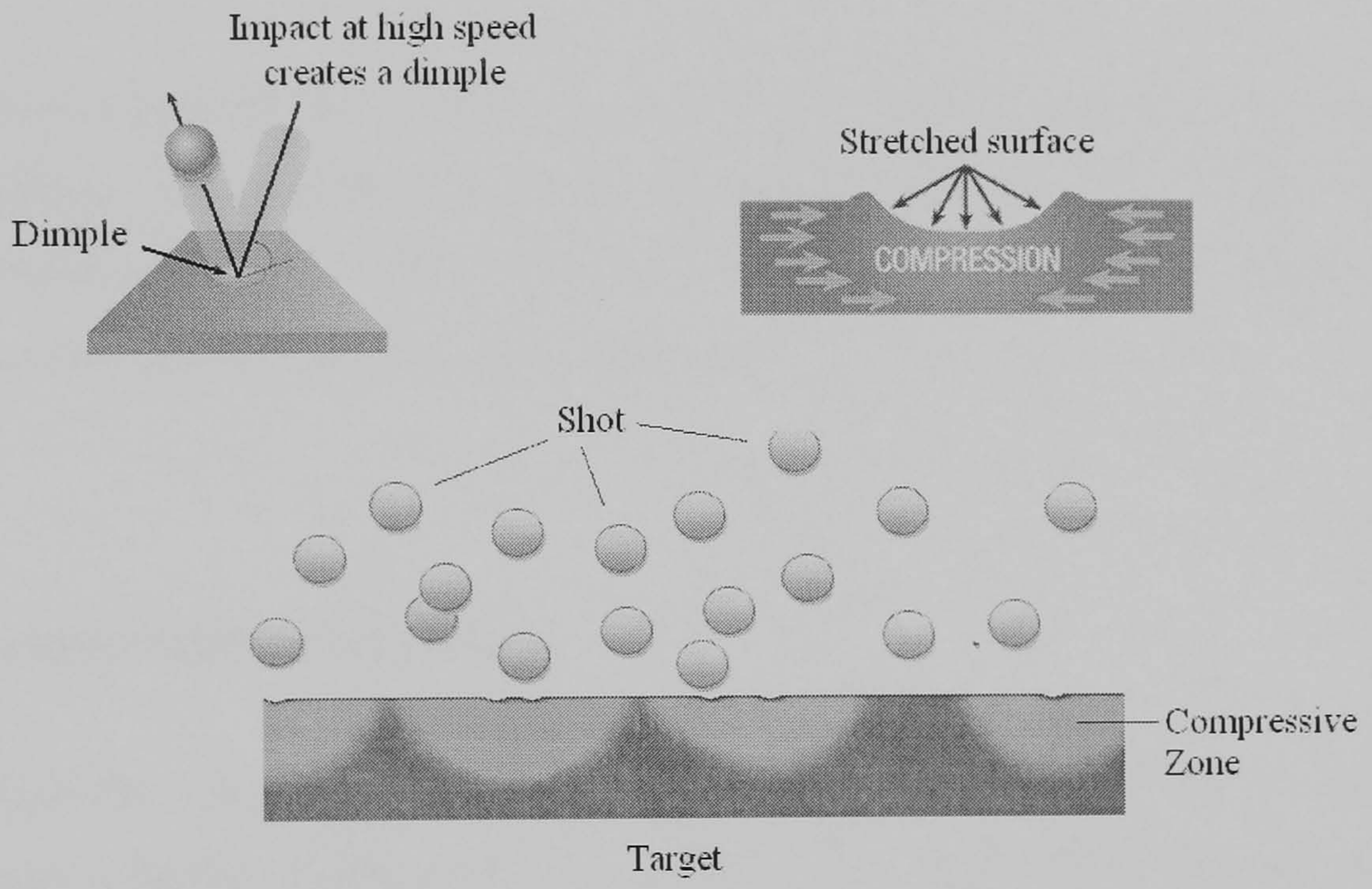

Figure 2.7 Diagram of shot peening, how it impinges on the surface of the materials leaving a compressive residual stress after the impact of a metallic sphere as well as a dimple increasing roughness [76].

Shot peening in steels such as 316L stainless steel [77], Hadfield steel [78], 080M40 medium carbon steel [74], 304 stainless steel [79], 1Cr18Ni9Ti stainless steel [80] generated a layer of nanocrystallization on the surface as well as severe plastic deformation improving fatigue life. This was seen to be due to production of martensite and the amount of phase transformation (martensite) depends of the SP treatment time. Every material has an specific treatment time to get the maximum amount of phase transformation, and after that time a small decrease is followed [79, 80]. The martensitic layer provides a significantly harder material than the base steel at the surface.

A comparison of SP between aluminium alloys and steels shows that SP promotes the subsurface crack initiation in aluminium alloy meanwhile in steels there was not any such effect. On the other hand, after being shot peened and partially fatigued and then peened again, in steels a fatigue life improvement after re-peening was observed whilst in aluminium no fatigue life improvement was seen [74].

Fatigue life improvements in Fe-2Cu-0.5C [70] and corrosion fatigue in cold worked commercially pure Niobium and commercially pure tantalum [81], as well as fretting fatigue life of titanium alloy, Ti-6Al-4V [82] are attained by shot peening.

It was observed that when a crack is approaching a peened zone (compressive residual stress) the growth rate rapidly decreases but once the crack has already penetrated and is fully inside the compressive residual stress region, it accelerates to reach the same growth rate as the un-peened zone [74].

ULTRASONIC SHOT PEENING

Ultrasonic Shot peening (USSP) is a method that is quite similar to shot peening. This method is based on impact of the surface to be treated with spherical shots using high-frequency ultrasonic energy, creating plastic deformation on the surface and nanocrystalization, inducing compressive residual stress. Another difference from shot peening is that in Ultrasonic Shot Peening a bigger shot is used (between 0.4 mm and 3 mm), the shot is harder and perfectly spherical and the shot velocity is variable between a range of 5 and 20 m/s. The surface after ultrasonic shot peening is smoother than in shot peening because of the size of the shot and its hardness. The compressive stress level is higher in the case of ultrasonic shot peening [83]. This method does not require of cabinet and dust collector, it is manual and counts as portable equipment as shown in fig. 2.8. Actually this method is used in aerospace, automotive, power plants, etc. [84].

USSP treatment in soft steel [85] and in Iron [86-88] leaves compressive residual stress, being in the former of around 309 MPa. Creation of ultra-fine grains was carried out in Iron, 304 stainless steel, aluminium alloy 7075 and pure Fe [88, 89], the variation of the grain size from the surface through the depth is uniform [90]. The time of USSP does not change significantly the size of the grain on the top layer, but increases the depth of grain refinement shown on 316L stainless steel [91].

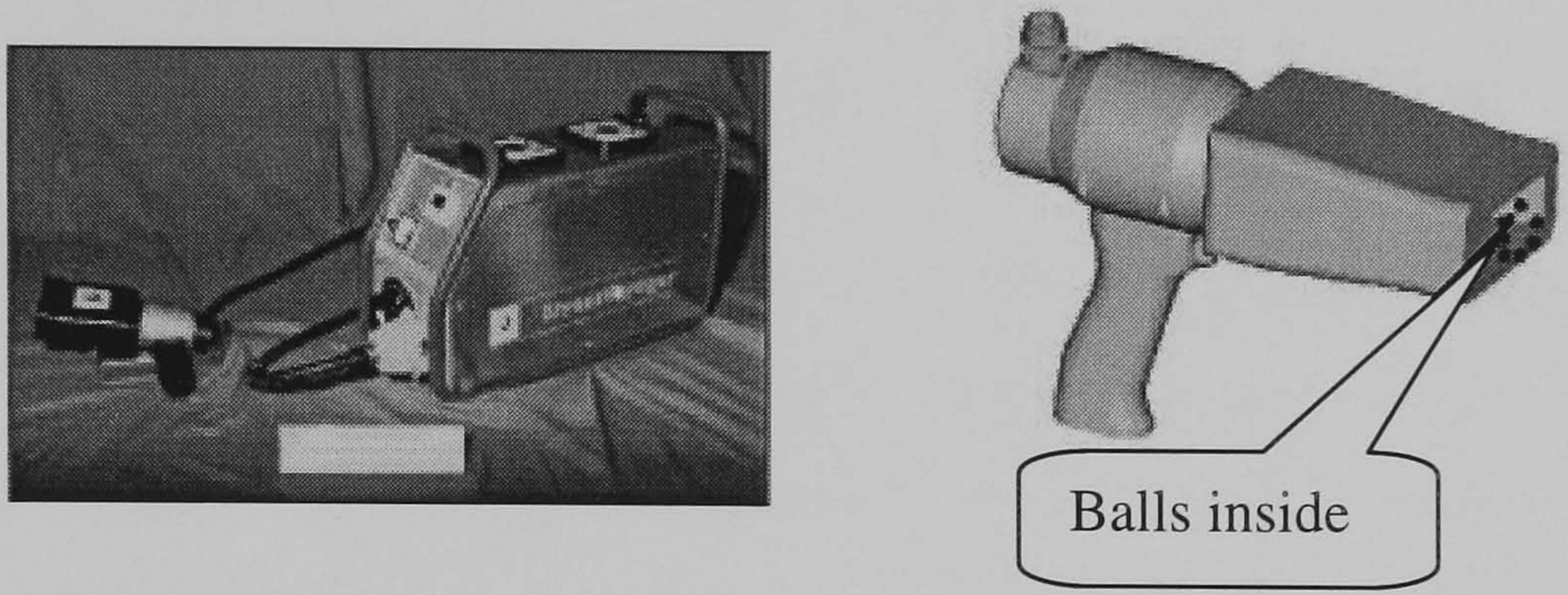

Figure 2.8 Ultrasonic shot peening Handset to be carried by one person [84].

Reduction of wear rate in materials on fretting process is another good characteristic due to USSP but this is limited by the opposite effect of roughness modification due to the peening process [92]. But in JIS SNCM439 material treated with a polished bearing ball, instead of a conventional ball, besides leaving a compressive residual stress on the surface of 1000 MPa higher than other treatments an increment of 100HV in hardness was also generated, and a smoother surface [93].

In Weld toe treatment by ultrasonic peening of 16Mn steel USSP shows an increment in fatigue strength of around 84% at $2X10^6$ cycles at constant amplitude but at variable amplitude at the same number of cycles the improvement was 80% comparing with as welded. It was observed an improvement of 3.5-27 times of fatigue life attained at constant amplitude, meanwhile the improvement at variable amplitude was 2.5-17 times at the same applied stress level [94].

LASER SHOT PEENING

Studies on Laser Shot Peening (LSP) have been carried out since the 1960s, as well as other methods it have shown that can generate greater compressive residual stress on the surface. At the same time not much changes to the finish of the surface or component shape happens because of it. Its process parameters were easier to control than shot peening [95]. Laser surface modification produces a fine-grained structure layer, low porosity and a relatively smooth surface; although it was found in 1080 steel that tribological properties of a sliding surface were improved, reducing friction [96].

This mechanical process is carried out as follows where a laser beam with a very short pulse, 15-30 ns, a wavelength of 1.06 μm, and energy per pulse of 50 J or more is used. The surface to be treated must be coated with an absorbent layer such as black paint, and a second transparent layer must be used. Distilled water is used as a transparent layer, because of this, there is a solid-fluid interaction.

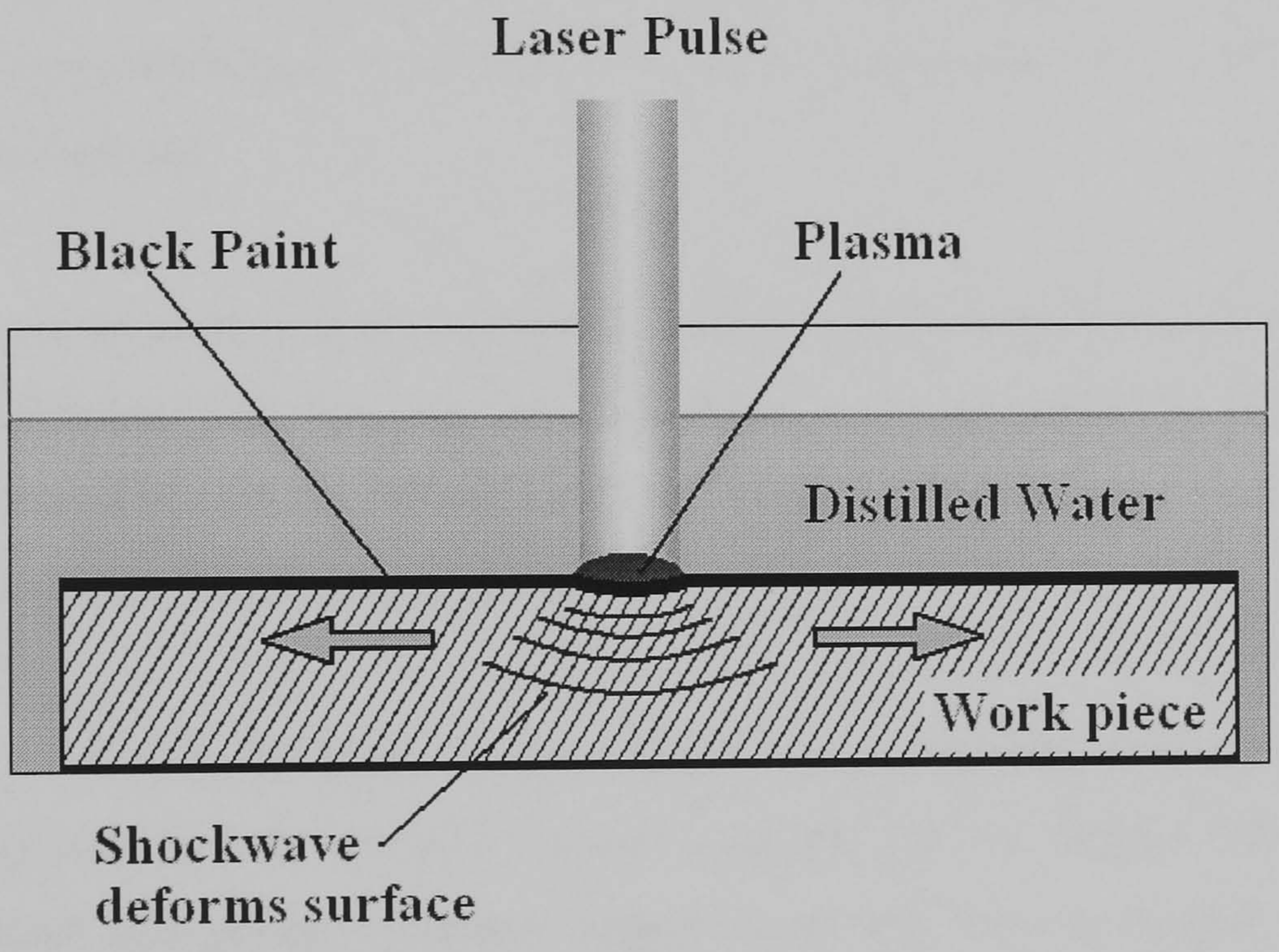

Figure 2.9 Laser shot peening process. The black coat creates plasma when a laser beam hits it driving into the metal shock waves, through the time plasma is increasing and with the aid of the water and the shock wave magnitude as well, it deforms plastically the surface.

The laser Shot Peening mechanism is as follows; The laser beam hits the surface with the black coating generating plasma because of it, as the plasma increases a shock wave is driven into the metal fig. 2.9, the strength of the impacts is given by the transparent layer. It peens the surface at repetition rate up to 0.5 Hz [97].

LSP in Aluminium alloys A356, A112Si, 6061-T6, 7075 and 2024 creates compressive residual stresses which are, bigger and deeper (1 mm) than the conventional method of shot peening [98]. In these alloys, hardening levels achieved by LSP are not more than 50% of those obtainable by shot peening (SP). On the other hand, LSP creates a uniform depression along the surface with a smoother finished surface than SP, eliminating high roughness along with potential crack initiation sites [99].

In aluminium alloy 7049-T73 the residual stress profile through the depth is influenced by several parameters, four of them considered as important are cited. One basic parameter is the influence of laser pulse (Laser energy per spot area), a second one important is the size of the laser spot, a third one is the number of layers of peening applied to a component and a fourth one is the spatial offset, or “overlap”, from one peening to another [100].

LSP can be used as a final treatment after welding as observed in a welded zone made by the Friction Stir Welding (FSW) method in aluminium alloy 7075-T7351 [101, 102], where tests showed an improvement in fatigue life eliminating tensile residual stresses, that are harmful, due to the welding.

LSP in Ti-6Al-4V titanium alloy shows the same behaviour as in aluminium alloys leaving compressive residual stresses near the surface deeper than for the shot peening method and giving a fatigue improvement and fretting fatigue improvement under ambient temperatures up to 450 °C [103, 104].

In steels such as SUS304 (Type 304) austenitic stainless steel treated with LSP and subjected to a corrosive-water environment, tests showed a prevention of stress corrosion cracking initiation. The same steel under a corrosion condition of NaCl showed a reduction of pitting corrosion, given an improvement due to large compressive residual stress and work hardening. Inhibition of the propagation of small cracks in a pre-cracked specimen, in SUS316L (Type 316L) was observed after LSP, improving fatigue strength [105, 106].

NANOCRYSTALLIZATION

It is known that the smaller the grain size the bigger the yield strength, a rule which is given by the Hall Petch relation [107, 108]. Although Hall and Petch were studying different behaviours in and around the 1950's, both of them arrived at the same conclusion, which is represented by the Hall Petch relation, and it is:

$$\sigma_y = \sigma_0 + \frac{K}{\sqrt{d}}$$

Where "K" and "σ_0" are constants and "d" is the mean grain size, "σ_0" is the flow stress of an undeformed single crystal oriented for multiple slip or approximately the yield stress of a very coarse-grained, untextured polycrystal [109]. As it can be seen in this relation yield stress is inversely proportional to the mean grain size, and this has been proved by several tests in many materials through the time.

Experiments in Fe showed that during plastic deformation, high strain with a high strain rate was enough to form dense dislocation walls and dislocation tangles within the grains creating nanocrystallization [110]. Different methods based in plastic deformation were developed to generate nanocrystallization, these methods create a layer of nanocrystals of different depths, being at the surface the smallest grain size and increasing the grain size through the depth.

A comparison between Airblast Shot Peening (ABSP) and Ultrasonic Shot Peening (USSP) in steels shows that the nanocrystallization depth is different in every method [111]. Other treatment methods used successfully are Surface Mechanical Attrition Treatment (SMAT) [112, 113] and the Equal-Channel angular rolling method (ECA) [114].

Improvement in fatigue life was observed with nanocrystallization, in Nickel-based C-2000 alloys of around 50% [115], as well as in nanocrystalline pure Ni and ultra-fine-crystalline Al-Mg alloy produced by electrodeposition [116].

Creation of nanocrystallyzation can be carried out successfully by severe plastic deformation with the aid of the most popular methods like shot peening [74, 77-80], Ultrasonic Shot Peening [88, 89] and Laser Peening [96] improving fatigue life of different metallic materials as Aluminium alloys, steel, Iron and Ti alloys. However tests on copper subjected to ECA pressing gave contradictory results [117].

Nanocrystallization improves other material properties, such as heat capacity, thermal expansion, electrical properties, magnetic properties, micro-hardness, yield strength and ultimate tensile strength, some of these improvements being considerable [118-121].

ROUGHNESS

Roughness means that the small scale irregularities of a surface [122], are present in all mechanical surfaces. The roughness of a surface in a mechanical piece or part of a machine is formed generally by mechanical processes in order to get a desired shape, for example cutting, milling, etc. Roughness parameters have been established as can be seen in figure 2.10, where a magnified profile of a surface is depicted. In figure 2.10 it can be observed that the profile has peaks and valleys, which can be measured from a specific direction over the surface and distance along it. From here the maximum roughness depth (R_t) can be defined as the sum of the height of the highest peak above the mean line (R_p) plus the lowest valley below the mean line (R_m).

Actually R_t does not provide much information for roughness, and in order to quantify surface roughness two parameters were developed, R_q (root mean square deviation or standard deviation) the RMS roughness, and R_a (average roughness or CLA centre line average or arithmetic average AA) the average CLA roughness. Both parameters were commonly used, R_q for Americans and R_a for Europeans.

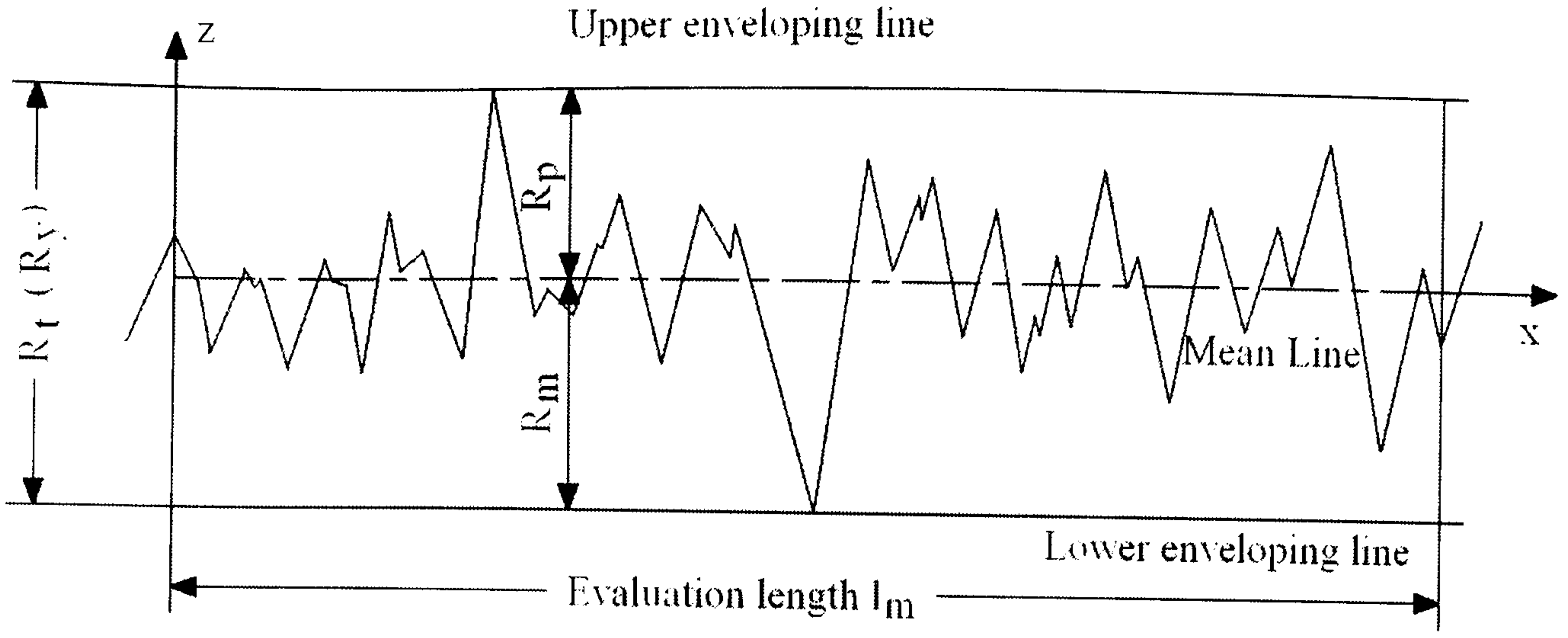

Figure 2.10 Surface profile magnification of a specific distance and direction, denoting the maximum roughness depth (R_t), the highest peak above the mean line (R_p) and the lowest valley below the main line (R_m).

R_a is defined as the total area of the material-filled profile above and the total area of voids below the mean line, both of them being equal as seen in figure 2.11 and this is given by the formula:

$$R_a = \frac{1}{L}\int_0^L |z|\,dx$$

Where "L" is the evaluation length and "z" is measure from the mean line. R_q is defined with the formula:

$$R_q = \sqrt{\frac{1}{L}\int_0^L Z^2 dx}$$

Nowadays R_q is not used so commonly; even in USA R_a is being used most widely. There is a problem with these parameters and others used in roughness among nations, because everyone has its own symbols to represent each parameter [123, 124].

Roughness in mechanical surfaces is of great importance. In fatigue it plays a role where it affects the fatigue life of components according to the roughness grade, even for surfaces with the finest polish. The fatigue life shows a fall with increase of surface roughness Ra, dramatically in the first 10% of the initial crack life given the origin of cracks due to peaks and valleys and to slip dislocations. Afterwards the incremental effects of roughness is lower up to the first major crack appearance, as experiments on AISI 310 stainless steel confirm [125].

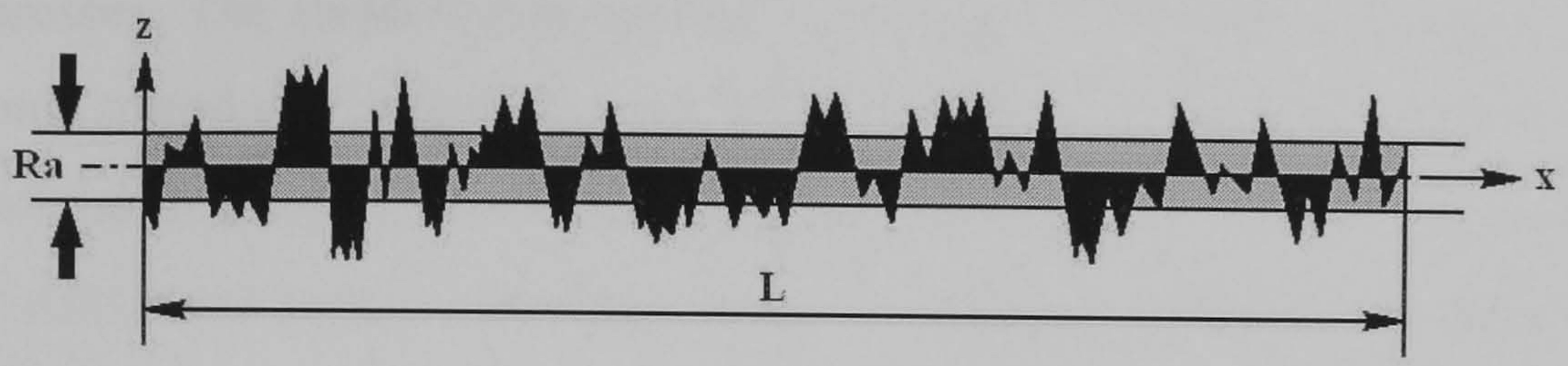

Figure 2.11 Representation of "Ra", the grey zone represents the total area of the material-filled profile above (peaks) and the total area of voids below (valleys) the mean line of a specific length and direction of a surface that gives Ra.

Test on nickel-based super alloys GH33A and steel SAE 5115 [126, 127] showed that roughness affects high cycle fatigue and low cycle fatigue. On the other hand in high strength steel (Ni-Cr-Mo steel) showed that just short fatigue life is affected by roughness, with the valleys acting as notches where fatigue cracks initiate, or the valley may be considered as flaws (studied in Ti-5Al-2.5Sn ELI alloy [128]). Meanwhile in long life regimes surface roughness does not make any effect because crack initiation takes place inside the specimen (fish eyes). The transition from surface crack initiation to internal crack initiation is affected by the roughness of the surface too [129].

Roughness in materials is present due to a material's manufacture and handling process such as scratches, pits and machining marks. Because of this surface machining plays a role in fatigue life as well as the manufacture of specimens [130], as for example in specimens of Al-7Si-Mg aluminium alloy from sand-cast formation it is possible to find hollows in the surface considered as peaks and valleys in roughness measurements [131], which are much less damaging in fatigue than sharper notches from a machined surface with the same Ra value. For another example in EN X155CrMoV12 tool steel, a surface roughness comparison between milling and Electro Discharge Machining (EDM) showing that the milling machine leaves a better surface quality than EDM, but being more prone to early fatigue fracture than the specimen machined with EDM [132].

UTRASONIC IMPACT TREATMENT

The development of the UIT method dates back to 1950 when initially an existing method used ultrasonic vibrations to deform the surface and to produce redistribution of residual stresses. The method consisted of producing continuous ultrasonic vibration at the ultrasonic transducer output end strengthened with hard materials (carbide-containing alloys, artificial diamonds, etc.) and being in contact with the surface to be treated. Ten years later a free ball was introduced between the output end of the ultrasonic transducer, although the impacts were generated in a random way with a frequency significantly lower than that of initiating ultrasonic vibration, the surface to be treated enhancing somewhat the intensity of the layer plastic deformation. The excess freedom of the ball could not provide enough consistency of effects in depth.

Ten years or more elapsed before proposal of the method that nowadays is known as Ultrasonic Impact Treatment (UIT) by E. Sh. Statnikov in the former Soviet Union. This method eliminated the idea of the free ball that impacted in a random way and replaced it with the idea of installing indenters separately with guiding holes and excitation by modulation pulses of the carrier resonance frequency of the ultrasonic oscillation system. This method uses ultrasonic frequency waves which accelerate hardened tools that, in turn impact the surface of the material. This new method gave high intensity ultrasonic impact together with ultrasonic vibration of the indenters at the same time. It was seen that this method can provide modification of the mechanical properties and condition of the surface and subsurface material at specific depth [8].

The UIT technology initially was developed for use in welded joints in the shipbuilding industry in order to reduce tensile residual stresses and deformations, to introduce compressive residual stress, to increase corrosion fatigue strength and specifically to enhance the fatigue resistance at subzero temperatures [10, 133-136].

The UIT mechanism's operation is represented in figure 2.12 and figure 2.13, the UIT device has 3 parts, an ultrasonic transducer (where ultrasound waves are created at specific frequency), a waveguide (where ultrasound waves are transferred to cyclic movement) and an indenter (which receives the excitation produced by the wave guide as an impulses and transmit them on the surface of the material to be treated), shown in figure 2.12.

The force pulses are the impacts that the indenter gives to the surface to be treated due to the ultrasound waves, resulting in plastic deformation at and under the surface to be treated. These force pulses set off forced oscillations of the indenter and in the surface to be treated, as well as the indenter rebound off the surface to be treated. Because of this some interactions [137] between indenter and the work piece surface can be experienced during the process, figure 2.13, which are described below.

- Ultrasonic periodic forced oscillations (3_{po}) in figure 2.13a of the indenter on the surface to be treated with continuous contact of indenter and treated surface (ultrasonic periodic impact). This indenter oscillation on the surface gives origin of ultrasonic periodic stress waves, figure 2.12, into the material.

- Ultrasonic non-periodic forced oscillations (3_{np}) figure 2.13b of the indenter with the indenter rebounding off the surface to be treated (ultrasonic non-periodic impact). The indenter rebound off the surface set off propagation of ultrasonic (non-periodic) stress pulses into the material.

- Single contact 3_c figure 2.13c of the indenter with its rebound off the surface to be treated causes propagation of single stress pulses into the material.

In order to know the magnitude by which UIT affects the material, an analysis of a single impact of UIT in aluminium with different indenters (ball and needle) was carried out. It was shown that micro-hardness in terms of its distribution and magnitude has a better performance with a needle than with a ball, getting a maximum hardening depth of 0.4 mm. It should be considered that the analysis is for one impact only and in the real process there is going to be more than one. It was observed that along with the impulse deformation of the impacted surface that ultrasonic impact is accompanied by ultrasonic deformation of the surface, modification of material properties and the generation of ultrasonic waves within the work piece material. This analysis showed as well that ultrasonic impact is accompanied by two effects: the activation of the relaxation of deformation caused by processing factors and external forces upon different materials, and the extension of time of the impact action on the surface of the indenter with and without rebounding.

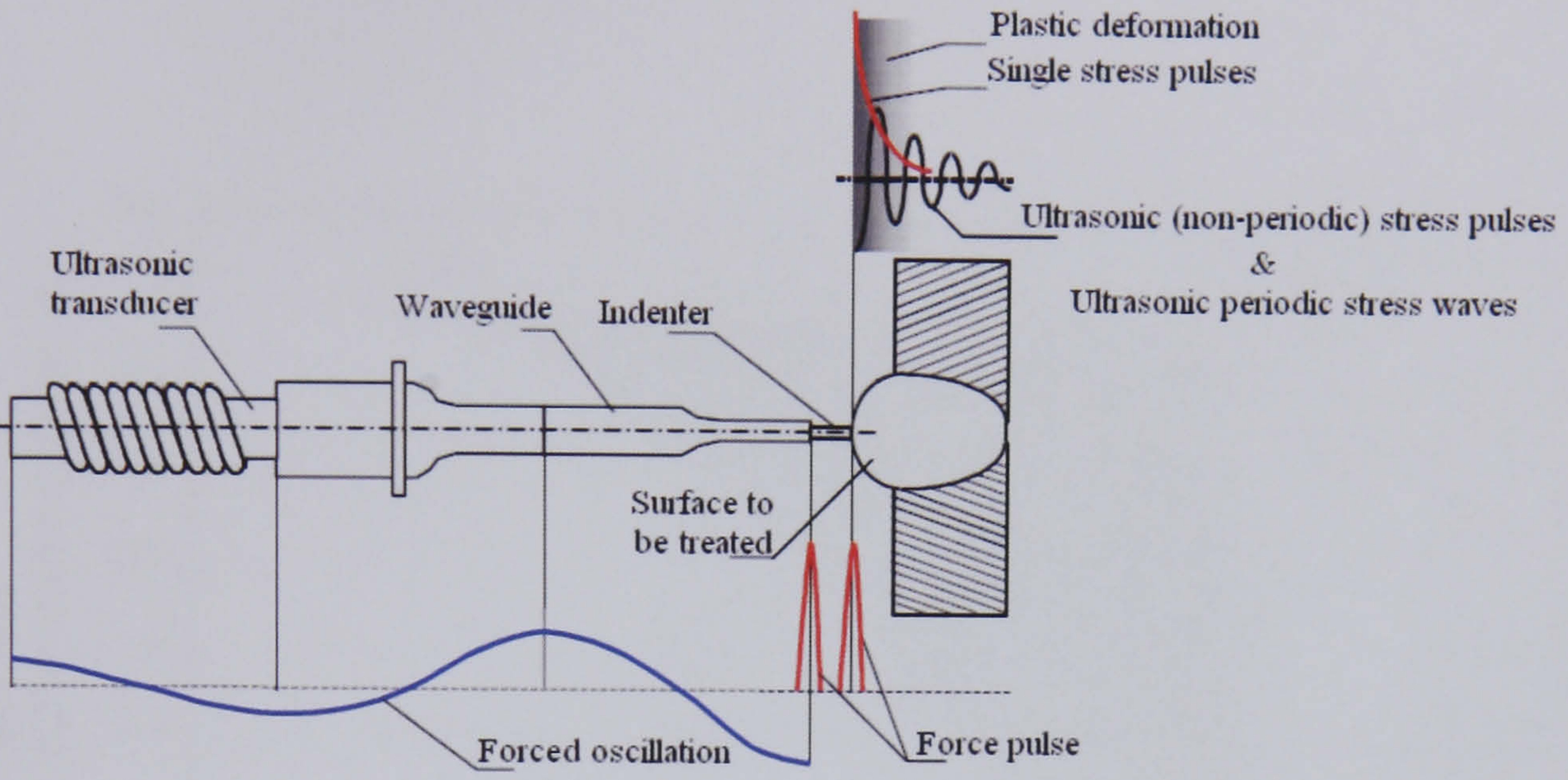

Figure 2.12 UIT components and the mechanisms transmitting force between the UIT device and the surface to be treated. Forced oscillation and the force pulse generate a deeper compressive residual stress in the material [137].

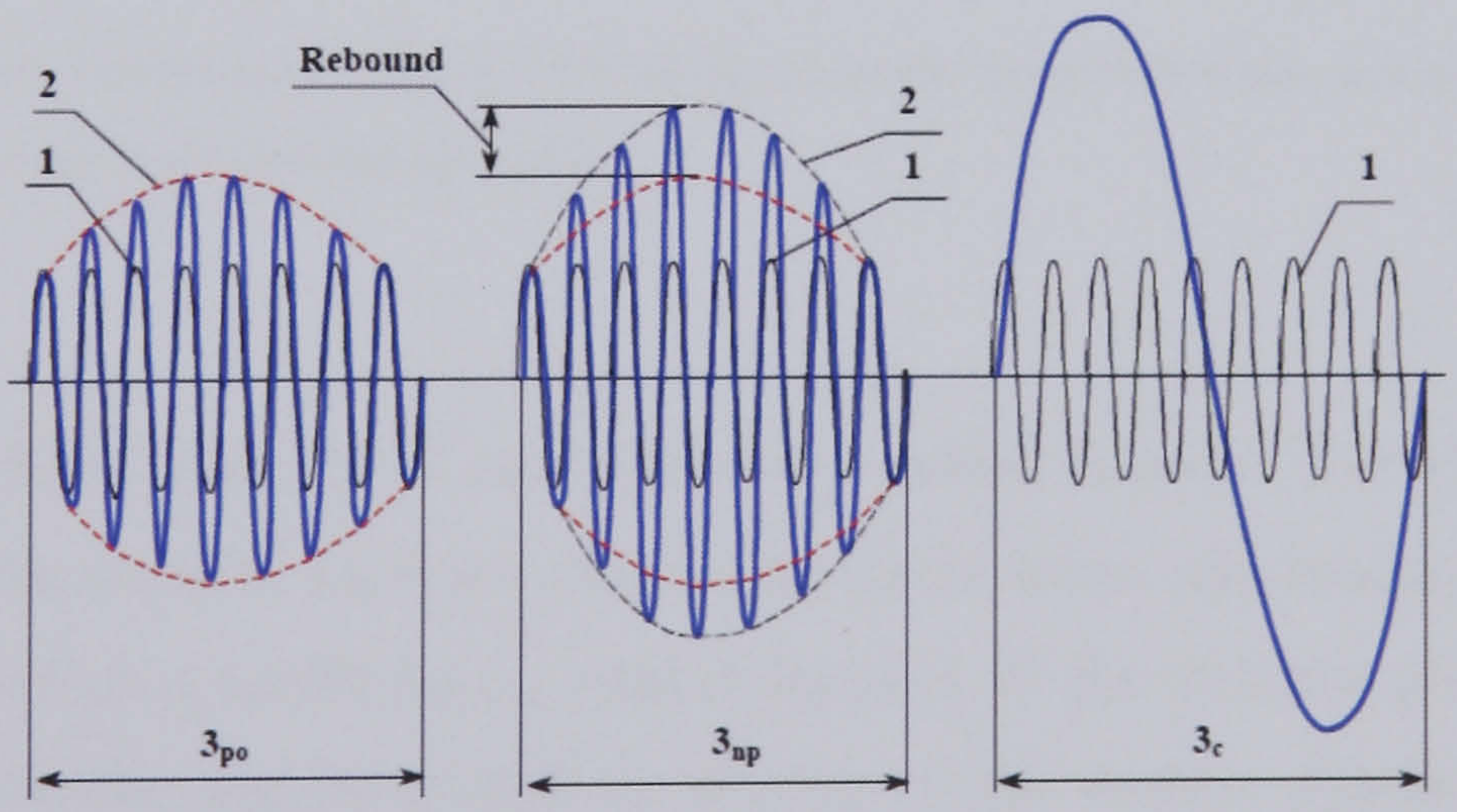

a) b) c)

Figure 2.13 Force pulses (2 in blue) and forced oscillation (1 in red) representation of the three possible interactions that could be found during the UIT process. a) Ultrasonic periodic forced oscillation, b) Ultrasonic non-periodic forced oscillation and c) Single contact [137].

The percentage of plastic deformation in a single impact of UIT method is 3.6% compared with the total amount it can be produced by an uninterrupted process, while considering impacts over the same amount of time as an uninterrupted process it can reach 78% figure 2.14 [138].

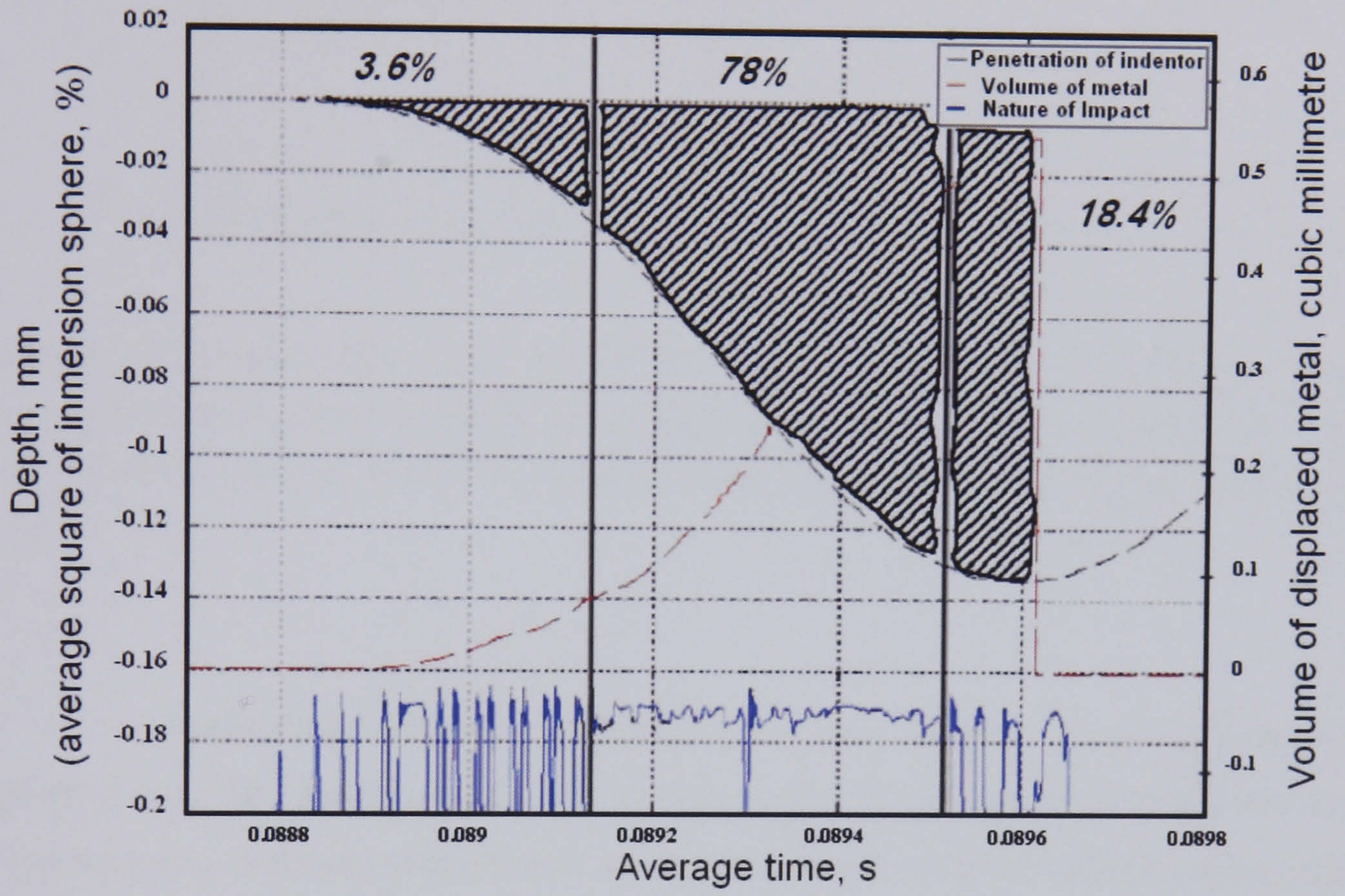

Figure 2.14 Plastic deformation Vs time. Percentage of plastic deformation due to a single impact, and due to uninterrupted process (based on [138]).

The effects observed at each depth in a welded material after UIT method in different hardness steels, titanium alloys, aluminium alloys and bronze are shown in figure 2.15, where a white layer, created because of the process, gives wear and corrosion resistance and is located on the top of the surface. Plastic deformation which is due to the combination of ultrasonic impact and the ultrasound waves transmitted into the material at the same time, is relaxed through the depth. The UIT process is accompanied by a quick local heating and a quick local cooling that together with intense local plastic deformation produce the material with new properties appearing in metallographic pictures as a white layer [8, 139].

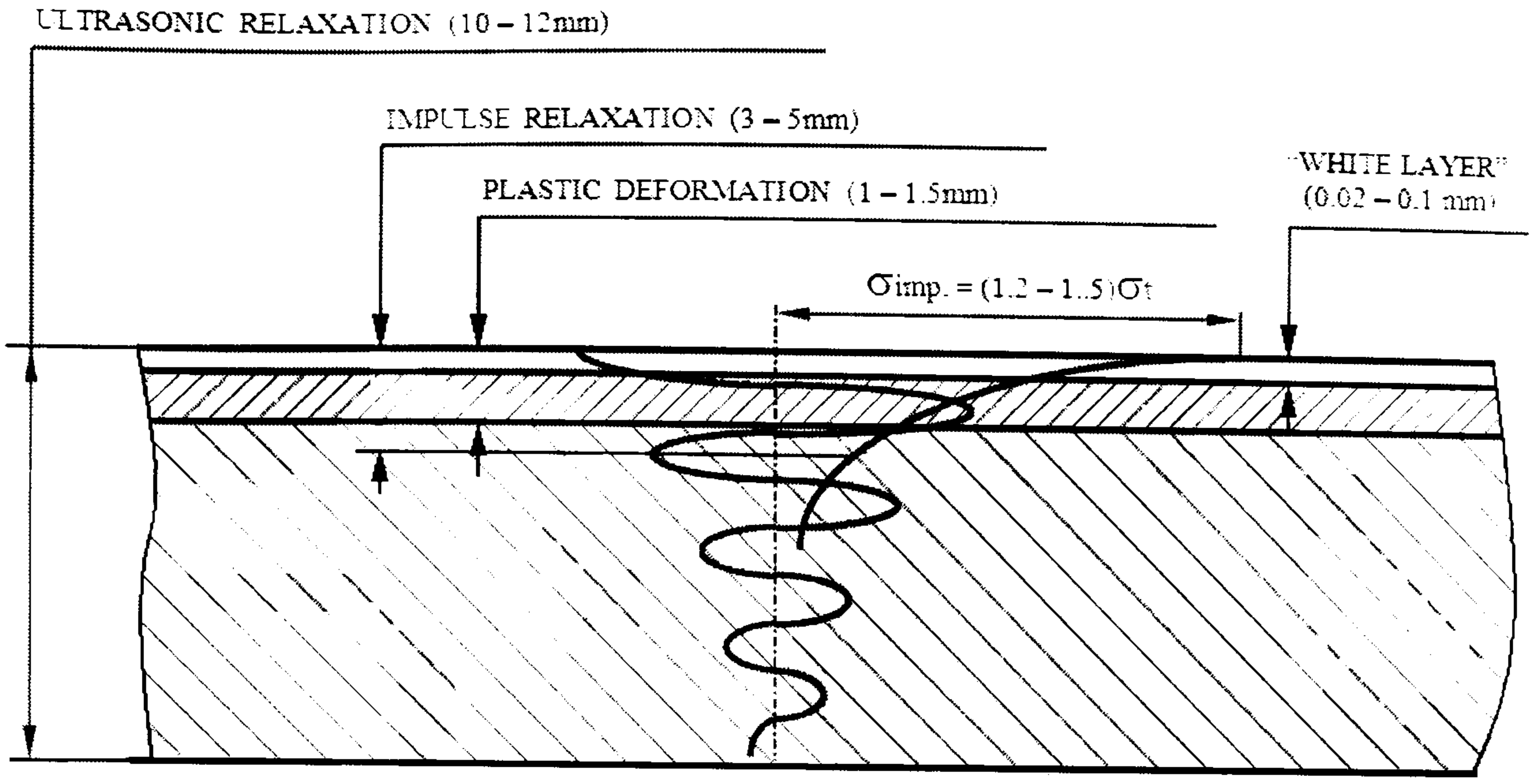

Figure 2.15 Ultrasonic Impact profile through the depth. White layer for steel is localized on the surface and on the top of the plastic deformation. Representation of the impulse relaxation and ultrasonic relaxation into the bulk for different materials as hardened steel, titanium alloys, aluminium alloys and bronze [8, 10, 11].

In comparison with other methods such as hammer peening, shot peening, needle peening [133], TIG dressing, etc., UIT is more successful at improving fatigue life in steel welded joints, reducing bbbbmicro discontinuities at the weld toe through surface erosion, plastic deformation and change in micro structure, and raising fatigue strength by up to 120 %, (in aluminium alloys the increment obtained was 80%). The enhancement in fatigue strength depends on the stress ratio R, being more at low R values, particularly at lower minimum stress (S_{min}) and lower stress range (S_r), as well as on UIT parameters [140-142]. Increments in fatigue strength can reach 46% more than as-welded [9]. Even though UIT was used successfully in high-strength steel welded structures [8] under variable loading conditions that is not viewed as practical procedure. Considerable speed reduction of fatigue crack growth and reduction of stress concentration factor in structures have been obtained successfully [143].

The UIT method has been used successfully in welded joints of different materials, namely medium strength steel [135], carbon steels of average-strength [9, 10, 133, 140, 142], high-manganese steels [10], high strength steels [144], titanium alloys [10], aluminium alloys [8, 133, 145] and bronze [8, 146] in different environments.

Because of the amount of residual stress that UIT produces, it was decided to abandon thermal treatment in a furnace, taking advantage of the fact annealing of unwanted residual stress is no longer required because it is accompanied with a UIT process too, being more efficient over the depth of the heat affected layer left than the shot peening technique that is widely used. Another advantage is its application, which can be utilised in hard to access areas, and it is the most efficient method to increase fatigue strength of welded joints at subzero temperatures [10].

Other types of apparatus that are used manually in order to get good effectiveness in peening require a pressure force against the surface to be treated of no less than 20 kgf. As the frequency used in those instruments is in the range of 50 to 100 Hz, basically the vibrations caused by the tool are transmitted to the hands of the operator, and because of that the peening tool moves in an uncertain direction, requiring to the operator to exert great effort to keep the tool aligned on the weld toe line during treatment. On the other hand, the UIT method is based on the generation and utilization of impacts from ultrasonic vibrations at a carrier frequency of 27 kHz approximately. Because of this, the pressure on the tool is not related to the effectiveness of the treatment and the pressure force required against the surface to be treated is no more than 3 kgf, making the noise and the vibration much lower than other methods. Because of this, the method is easer to use and less hazardous for the operator [133]. Some characteristics that help this method to carry out properly a neat job are [11]:

Good ergonomic design
System light and portability
Low noise
Negligible vibration transmission to operator
Compactness and easy of handling of tool
Compliance with safety standards
Compliance with environmental standards

Investigations about UIT parameters for specific joints and materials were done previously in laboratories of Northern Scientific & Technology Company (NSTC) in Severodvinsk, Russia and at the E. O. Paton Electric Welding Institute in Kiev, Ukraine, where successful results in fatigue were found for welded joints in metal structures. In the last years UIT has been developed by laboratories of Applied Ultrasonics in Birmingham, Alabama, USA in cooperation with NSTC [133, 135].

A methodical plan was followed in order to get improvement of limiting characteristics of materials according to the criteria of endurance limit, resistance to corrosion fatigue damage, corrosion under stress, corrosion exfoliation and cracking and restoration of properties of material, degraded on the basis of resistance to corrosion exfoliation and cracking [147].

A manual to apply UIT to welded zones has been completed [143], and the people who work on this technique must be trained professionally. The UIT process is applied to the fusion zone of added metal where tensile residual stresses exist due to the welding process.

UIT has been used successful in bridges reducing the costs of maintenance and repair [139, 142, 148-150].

CHAPTER III

EXPERIMENTAL PROGRAM

MATERIAL

The material used in this project was Aluminium alloy 2024-T3, commonly used in fuselage skin, wing tension members, shear webs and ribs; and Aluminium alloy 7150-T651, commonly used in upper wing skins on large commercial aircraft [151]. The material was produced by "ALCOA mill products", an industrial producer of aluminium alloy. This company supplies aluminium alloys to Airbus industry for manufacture of airplanes, among them the A380, the biggest civil airplane at this moment, as well as the Boeing Company.

Aluminium alloy 2024-T3 was received in plates of 5mm of thickness and 400 X 400 mm. Aluminium alloy 7150-T651 was obtained from Airbus industry from a panel of A380 material with a minimal thickness of 6 mm.

The chemical composition and mechanical properties of both materials are shown in tables 3.1 and 3.2 respectively. These data were taken from ALCOA and the temper is designated according to the standard designations for wrought aluminium alloys.

The values of mechanical properties could vary slightly from the company specifications to the data given in specifications as MMPDS-01 document [152], documents from NASA [153] or others sources in the web as [154, 155]. The specifications used through this research were the ones from ALCOA Company shown in table 3.1.

Table 3.1 Mechanical properties and chemical composition of Aluminium alloy 2024-T3 and 7150-T651 [151].

Chemical composition [%]											
2024											
Cr	Si	Mg	Mn	Ti	Cu	Zn	Fe	Others, each	Others total	Balance	
0.1	0.5	1.2-1.8	0.3-0.9	0.15	3.8-4.9	0.25	0.5	0.05	0.15	Aluminium	
7150											
Cr	Si	Mg	Mn	Ti	Cu	Zn	Fe	Zr	Others, each	Others total	Balance
0.04	0.12	2.0-2.7	0.1	0.06	1.9-2.5	5.9-6.9	0.15	0.08-0.15	0.05	0.15	Al

Temper	**Thickness** (mm)	**Tensile Strength** (MPa)	**Yield Strength** (MPa)	**Compressive Yield Strength** (MPa)	**Elongation %**
T3-Flat (2024)	0.203-6.32	434-441	289		10-15
T6-Flat Sheet (7150)	12.7-25.4	496	421	496	7
E	72 GPa				
Y	0.33				

Table 3.2 Principal alloying elements in standard designation for wrought aluminium alloy [156, 157].

Series	*Major alloying element*	*Series*	*Major alloying element*
1xxx	None	5xxx	Magnesium
2xxx	Copper	6xxx	Magnesium-silicon
3xxx	Manganese	7xxx	Zinc-Magnesium-Cu
4xxx	Silicon	8xxx	Miscellaneous

Aluminium alloy 2024-T3 has as a principal alloying element Cu, and 7150-T651 has Zinc and Magnesium as the principal alloying elements. The aluminium alloy plates were treated before delivering, the treatments given to them are specified with a prefix T followed by the standard designation number given by a temper system. According to the temper system the treatments are:

T3. Solution heat-treated, cold worked, and naturally aged to a substantially stable condition. Applies to products that are cold worked [14, 157].

T6. Solution heat-treated, and artificially aged.

T_51. Applies to cold finished rod or bar when stress-relieved by stretching 1 to 3% permanent set. Stretching is performed after solution heat treatment or after cooling from an elevated temperature shaping process. No straightening takes place after stretching [158].

SPECIMEN

The specimen shapes used in fatigue specially for this research were two, a dog bone shape and a centre-cracked tension specimen M(T). The former was used to create S-N curves at constant amplitude and the latter to create a graph of the crack growth rate. Small plates of around 10 cm x 10 cm were also used; the only restriction for these plates was that they should be big enough to measure the residual stress with the aid of the hole drilling technique.

Dog bone specimen

The specimen design was made according to ASTM standards. As the material supplied was in plates with 5mm thickness, one of the shapes suggested by ASTM standards is one similar to a flat bone [159]. Because of the geometry of the material supplied it was not possible to choose one with a circular cross section.

Restrictions of the dimensions according to ASTM standards are as follows. The ratio of specimen test section width to thickness should be between two and six, as the thickness is 5 mm the selected width of the test section is 10 mm, given a ratio of 2. The reduced area should preferably be between 19.4 mm^2 and 645 mm^2, as the cross section dimensions are 5 mm x 10 mm the cross section area is 50 mm^2.

The specimen design is showed in figure 3.1 with all its dimensions. As the material is rolled the specimens were cut out from the plate with the mean axis along the rolling direction. The specimen was designed for use in a hydraulic wedge grips machine, so no holes in the fastening area were necessary.

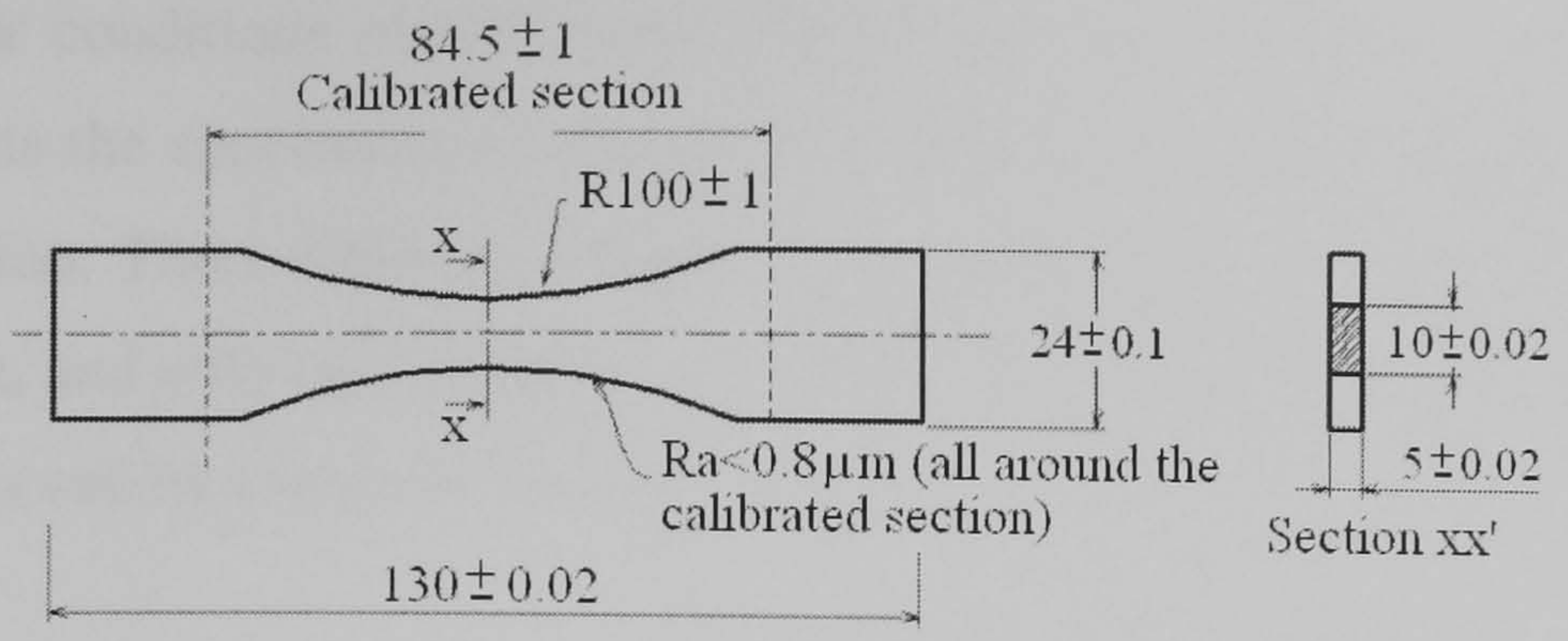

Figure 3.1 Dog bone shape specimen used to fatigue under different stress amplitude and obtain points in an S-N graph. The specimen was cut out from the plate along the rolling direction. All dimensions in mm.

UIT METHOD

The UIT method to be analysed, as was said before has parameters to be varied. In the present work three parameters were varied in two different frequencies 27 kHz and 36 kHz. The former was carried out in USA and the latter in Russia. Designations were assigned to each condition of treatment as these were used. UIT conditions used in both materials Al 2024-T3 and Al 7150-T651 are shown in table 3.3. Further conditions were used in Al 7150-T651 and their parameters can be seen in table 3.4.

Table 3.3 UIT conditions and designations used in the present work.

Designation	**UIT-1-27**	**UIT-1-36**	**UIT-2-36**	**UIT-3-36**
Carrier frequency (kHz)	27	36	36	36
Indenter, Pin Ø (mm)	6.35 x 25	5x17	5x17	5x17
Normalized impact (Impulses)	64	64	64	64
Amplitude under load (microns)	22	18	15	10
Pressure force (kg)	7	3	3	3
Impact frequency (kHz)	236	260	220	220
Feed rate mm/min	400	400	1000	1000

Table 3.4 UIT conditions used specially in Al 7150-T651 alloy.

Designation	**UIT-4-36**	**UIT-5-36**	**UIT-6-36**
Carrier frequency (kHz)	36	36	36
Indenter, Pin Ø (mm)	5 X 17	5 X 17	5 X 17
Normalized Impact (Impulses)	64	64	64
Amplitude under load (microns)	20	20	20
Pressure force (kg)	3	4	5
Impact frequency (kHz)	178	184	184
Feed rate mm/min	1000	1000	1000

The four conditions of UIT were given to the full dog bone specimen of 2024 alloy; this means the specimens were treated all around the body, including the edges in the curved section. Three different lengths in the gauge zone were treated, especially for those of 27 kHz, and only one length for the 36 kHz condition. The three different lengths in the specimens can be shown in fig. 3.2.

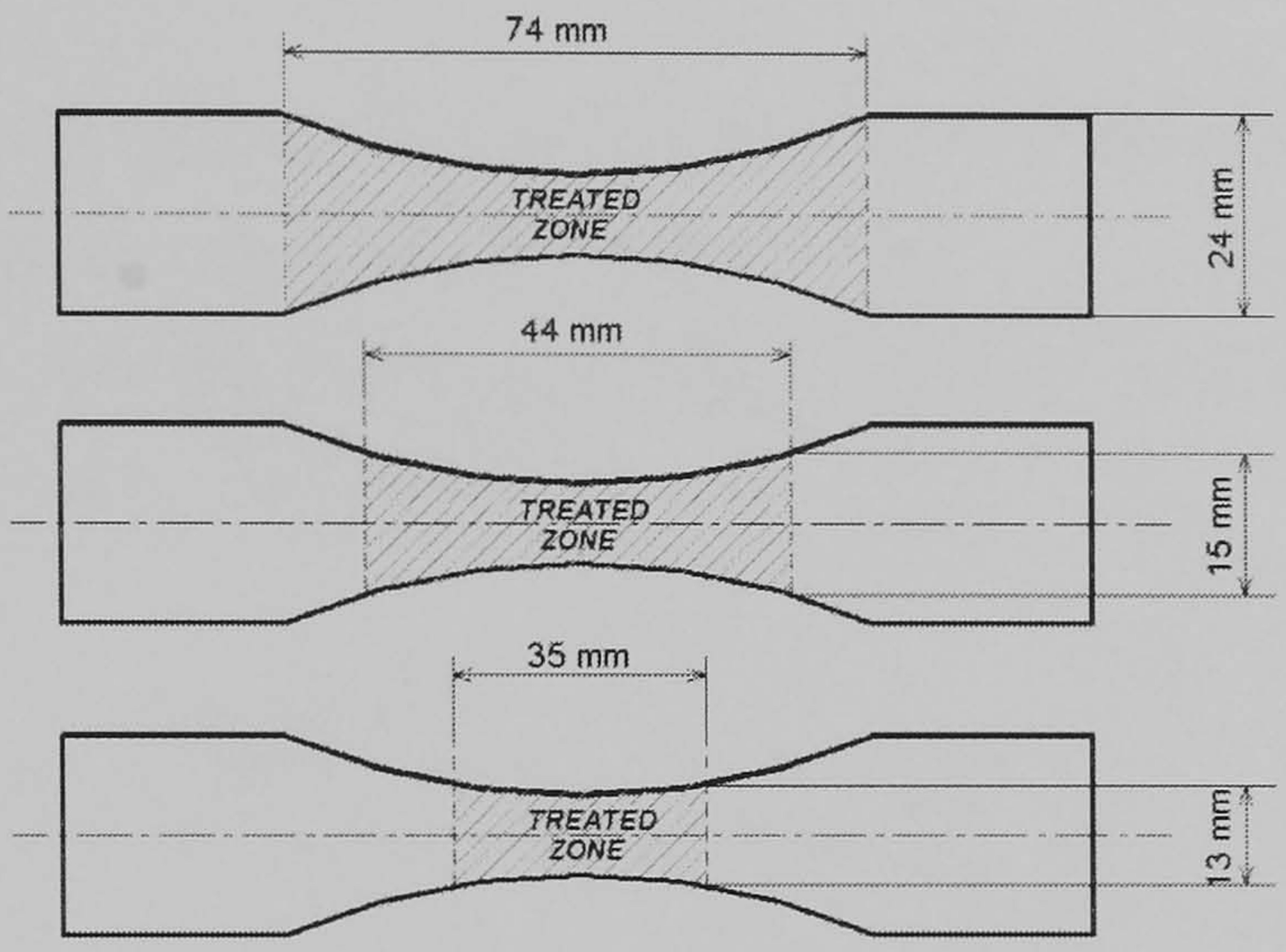

Figure 3.2 Three different lengths to be treated along the dog bone specimen including the edge. All cases were used for UIT-1-27condition, and for UIT-1-36 condition the length of 74 mm was used.

Middle-tension specimen M(T)

In order to carry out fatigue crack growth test, the M(T) specimen was chosen from the ASTM standards E 647 [160]. The design was followed as suggested by ASTM standards. Fig. 3.3 shows the M(T) design that, like the dog bone specimen, was cut out from the plate with its mean axis parallel to the rolling direction.

The size requirements for the M(T) specimen are as follows. As the thickness of the specimen can not be modified the specimen design is based on it. The upper limit recommended on thickness is given by W/8, (“W“ is the width of the specimen), so the minimum value of W is 40 mm. The value of 80 mm was taken.

The length of the gauge zone is related to the width of the specimen, the total length must be three times the width as minimum. The maximum gauge length “L” is 3 x 80mm = 240 mm.

As the test would be carried out in a hydraulic wedge grips machine, the fastening section did not require any hole, so the area to be occupied for grips must be included. ASTM standards suggest that the minimum gauge length requirement for clamped specimens is relaxed to 1.2W. The clamping area of the wedge grip in the machine is smaller than that specified by the ASTM, so the full clamping area available in the grips was employed.

The centre crack was machined with the aid of the Electric Discharge Machining (EDM) method, the notch length from the centre was 1.5 mm and its width around 0.2 mm. The maximum notch root radius suggested by ASTM is 0.25 mm so the value of 0.1 mm in the specimen is within the limit.

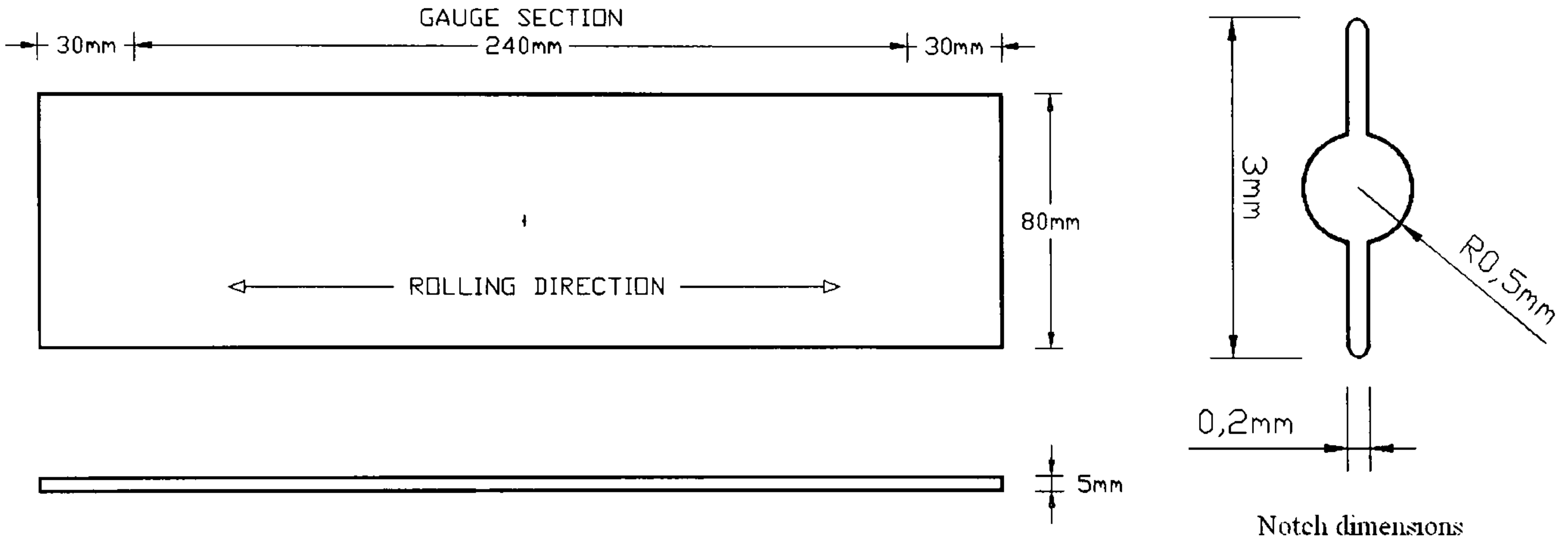

Figure 3.3 M(T) Specimen design, on the right side the notch dimensions are shown, where the notch is in the centre of the plate.

In order to compare results from bare material and treated conditions, in the specimen to test UIT conditions was set up two strips of the same treatment on each side of the middle notch in both faces, there were two specimens with UIT-1-36 and two with UIT-2-36 conditions. As the notch is central and the treatments should be at a specific distance from the notch to see the effect they have over the material, two bands of treatment were placed in each side of the notch, one at a distance of 10 mm and the other at a distance of 15 mm from the centre line of the specimen for both sides of the plate. The specimen design is shown in fig. 3.4.

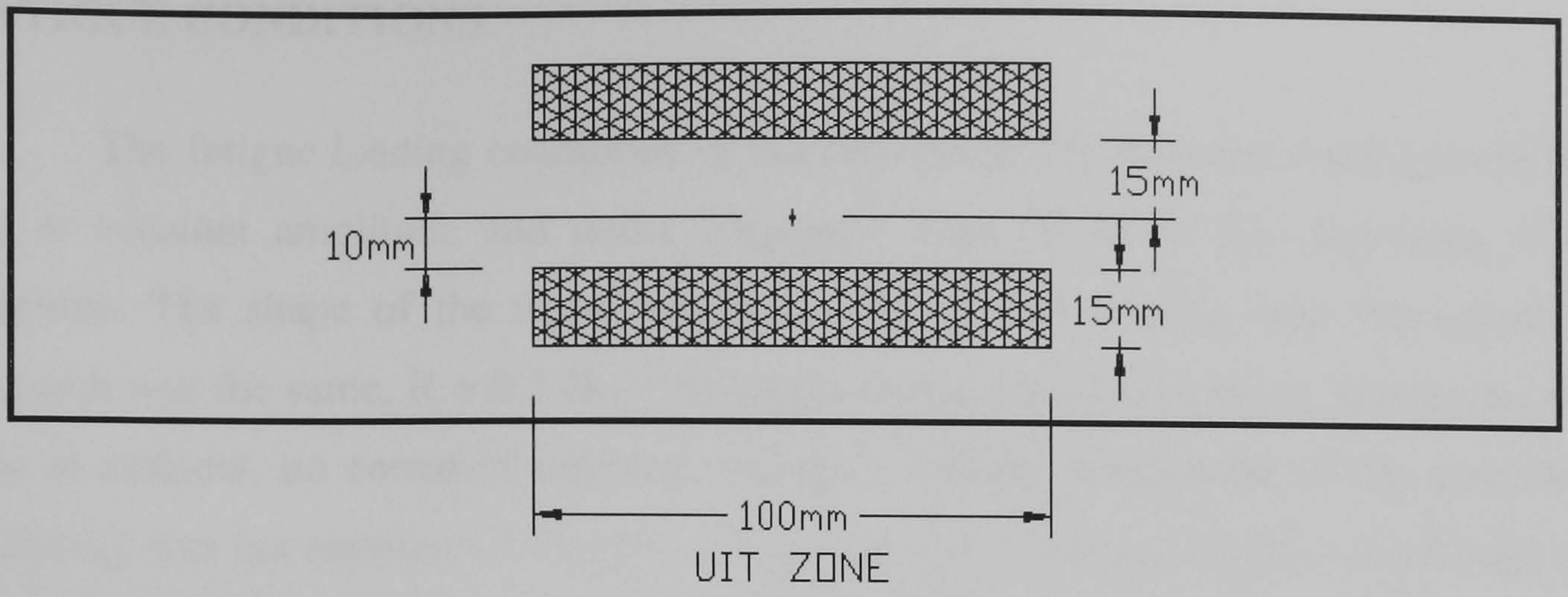

Figure 3.4 Two bands of treatment over the specimen to be tested for crack growth rate, each one at different distance from the centre with the same width band, both faces of the plate were treated.

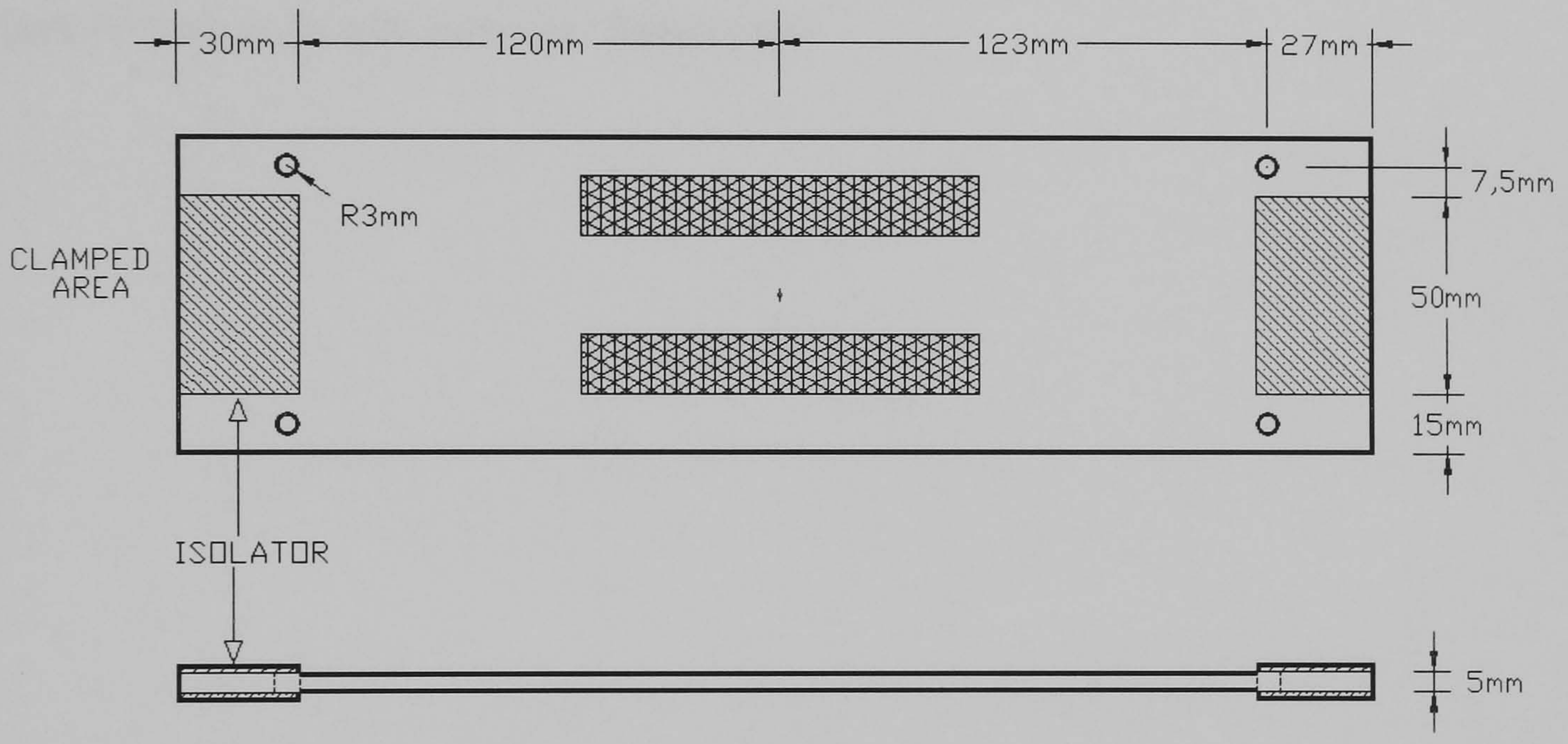

Figure 3.5 Specimen design modified to carry out EPD method, with holes placed to attach wires with electric current and Isolators to insolate the plate and the machine.

The specimen designed for crack growth was prepared in order to use Electric Potential Difference (EPD) method with direct current. As the specimen is required to be insulated because current must past through it holes were placed to attach wires with bolts to the plate which would supply the electric current. Figure 3.5 shows the specimen with the holes and the areas to be insulated. Plates of composite material were stuck on the area to be clamped in order to insulate the machine from the plate.

FATIGUE CONDITIONS

The fatigue loading conditions of the material in SN tests and crack growth tests are at constant amplitude and under frequency from 20 to 25 Hz, depending of the machine. The shape of the wave was sinusoidal. The load ratio used throughout the research was the same, $R = 0.1$ (R = minimum stress/ maximum stress). The temperature was at ambient, no corrosive material was used. Surface preparation of the material or polishing was not necessary. The flat surfaces were as received, and the curved edge was milled, to be representative of surface conditions employed in the aircraft industry. Failure was defined as final fracture.

The machines used for this research were a "Mayes DH50" and an "Instron 8510", both of them work with hydraulic wedge grips.

CHAPTER IV

TECHNIQUES TO CHARACTERISE RESULTS

HOLE DRILLING

When a hole is drilled in a surface with residual stresses, the surrounding area tends to deform because of the residual stress relaxation. The micro stresses surrounding the hole are relieved a little given each time the hole is drilled deeper incrementally until a specific depth. The micro strains are recorded by an arrangement of three gauges spaced around the hole (this special arrangement is called rosette) within a specific radius with respect to a point placed at the centre of the hole, the diameter of the strain gauge circle is denoted as D. Typical rosettes are illustrated in **Appendix A1,** where type A is the one used in this work. Readings from each gauge are taken at different depths of hole getting values of "ε" and "z" (strain and hole depth respectively); this procedure is called hole drilling. This method is frequently used to evaluate the residual stress through the depth from the surface, and in this case it is used to measure residual stress left by the mechanical treatment UIT at different conditions, and so to evaluate the effect it can have on fatigue resistance for the material.

If the stress is uniform with depth readings of ε_1, ε_2 and ε_3 are enough to calculate β (Angle measured clockwise from gauge 1 to the direction of σ_{max}). With the strain values and β it is possible to apply equations (1) to (3) to calculate the principal stresses.

$$\sigma_{max}, \sigma_{min} = \frac{\varepsilon_3 + \varepsilon_1}{4\bar{A}} \pm \frac{\sqrt{(\varepsilon_3 - \varepsilon_1)^2 + (\varepsilon_3 + \varepsilon_1 - 2\varepsilon_2)^2}}{4\bar{B}} \qquad 1$$

Here $\bar{A}$ and $\bar{B}$ are calibration constants and are calculated with the next equations:

$$\bar{A} = -\bar{a}\ (1+\nu)/(2E) \qquad 2$$

$$\bar{B} = -\bar{b}\ /(2E) \qquad 3$$

Where $\bar{a}$ and $\bar{b}$ are dimensionless coefficients that vary with hole depth and ν and E are Poisson's ratio and Young's modulus respectively. The values of $\bar{a}$ and $\bar{b}$ can be calculated by different methods such as incremental strain method, average stress method, integral method and finite elements [161, 162]. Values of $\bar{a}$ and $\bar{b}$ are tabulated in reference [163] and reproduced in a table in **Appendix A1** for three different rosettes. Each value can be obtained from normalized values using depth, and diameter of strain gauge circle data for a blind hole and a through hole.

The curve of a graph of normalized percent strains versus normalized hole depth, as shown in ASTM standards and in **Appendix A1** should yield data points close to it, otherwise the strain indicates either stress non-uniformity through the material thickness, or strain measurement errors. If there is a strain gradient which provides non-uniformity a more complex analysis is needed to adjust the $\bar{a}$ and $\bar{b}$ values to include the influence into stress gradient. This analysis has been programmed in the RESTRESS software for the uniform stress case.

To carry out the hole drilling method in this work a High Speed Milling method was used in order to mill the surface bit by bit creating a hole. In order to get the best precision in drilling, this method uses a precision milling guide model RS-200 from VISHAY products that compresses air to drill as shown in Fig. 4.1. The diameter of the drill tip (D_O) was 1.6 mm (although the diameter can be different). A strain gauge rosette type CEA-06-062UL-120 was chosen and stuck on the surface of the material (according to the procedure showed in **Appendix A2**), in order to achieve the method. The diameter of the strain gauge circle (D) for this rosette is 5.2 mm.

The method starts milling 0.05 mm depth in order to eliminate the film of the gauge. The next step is to get zero readings from each gauge before starting the drilling operation. The drilling stages of the hole depth are done in steps of each 0.1 mm, until 1.5 mm. The small plate and the equipment are shown in Fig. 4.1 where the strain gauge type used and the position of the hole can be seen. Calculation of the biaxial residual stress is performed by the RESTRESS software supplied by VISHAY Micro measurements, where data reduction is provided in accordance with ASTM E 837, as well as an approximate determination of residual stress variation with depth. The test was done at ambient temperature.

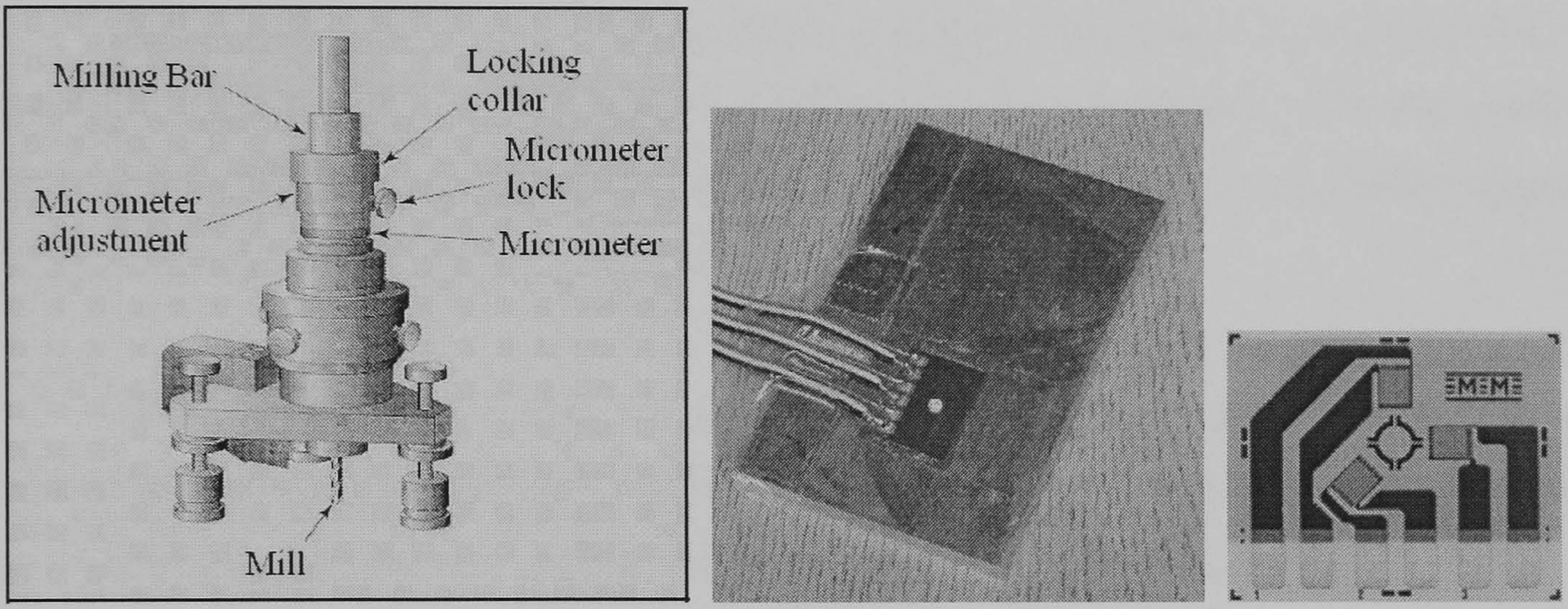

Figure 4.1 Hole drilling equipment (model RS-200) [164], plate tested and rosette gauge type (model CEA-06-062UL-120) used in the test to measure residual stresses of UIT on aluminium alloy.

MMH Method

A method developed in collaboration with Professor Brown was used in order to get results of residual stress showing the balance into the material, this method is named MMH method and is described in **Appendix A3**. Values obtained directly from hole drilling method are used in this method.

MMX Method

As XRD results were used in this work in order to get information of residual stress through the depth, a method called MMX was developed in order to consider the changes of residual stresses through the depth due to layering removal every time a reading of residual stress was required. The development of this method is shown in **Appendix A4** and its results were obtained using those obtained by XRD method.

X-RAY DIFFRACTION

Solid matter can be amorphous, where atoms are arranged in a random order, or crystalline, where atoms are arranged in a regular pattern. An element with the smallest volume with the same arrangement in three dimensions is called crystal. Lattice spacing within a crystal is constant unless something affects it.

When X-ray interact with a crystalline substance (phase) one gets a diffraction pattern, which for every material is different being like its fingerprint. This diffraction gives information about the crystal. This is a method used for many purposes as phase identification in materials, determination of unit cell parameters of new materials, to calculate the amount of crystallinity in materials, the orientation of the unit cell most common in the material, and residual stresses in materials. This method is considered as non-destructive [165].

As stress is an extrinsic property, the way to calculate it is by measuring the strain directly from the material. As the mean lattice spacing changes by the elastic strain, stress can be possible to calculate from variation of lattice spacing in the crystals. Because of Poisson´s ratio effect, if a tensile stress is applied, the lattice spacing will increase for planes perpendicular to the stress direction, and decrease for planes parallel to the stress direction. This new spacing will be the same in any similarly oriented planes, with respect to the applied stress [166]. The interaction of a monochromatic X-ray with a crystalline material, fig. 4.2, gives enough data to get the crystal lattice distance.

The lattice spacing is calculated from the diffraction angle 2θ caused by a monochromatic X-ray wavelength using Bragg´s Law, equation 4, where any change in the lattice spacing, **d**, results in corresponding shift in the diffraction angle 2θ, >120° **[165-169]**.

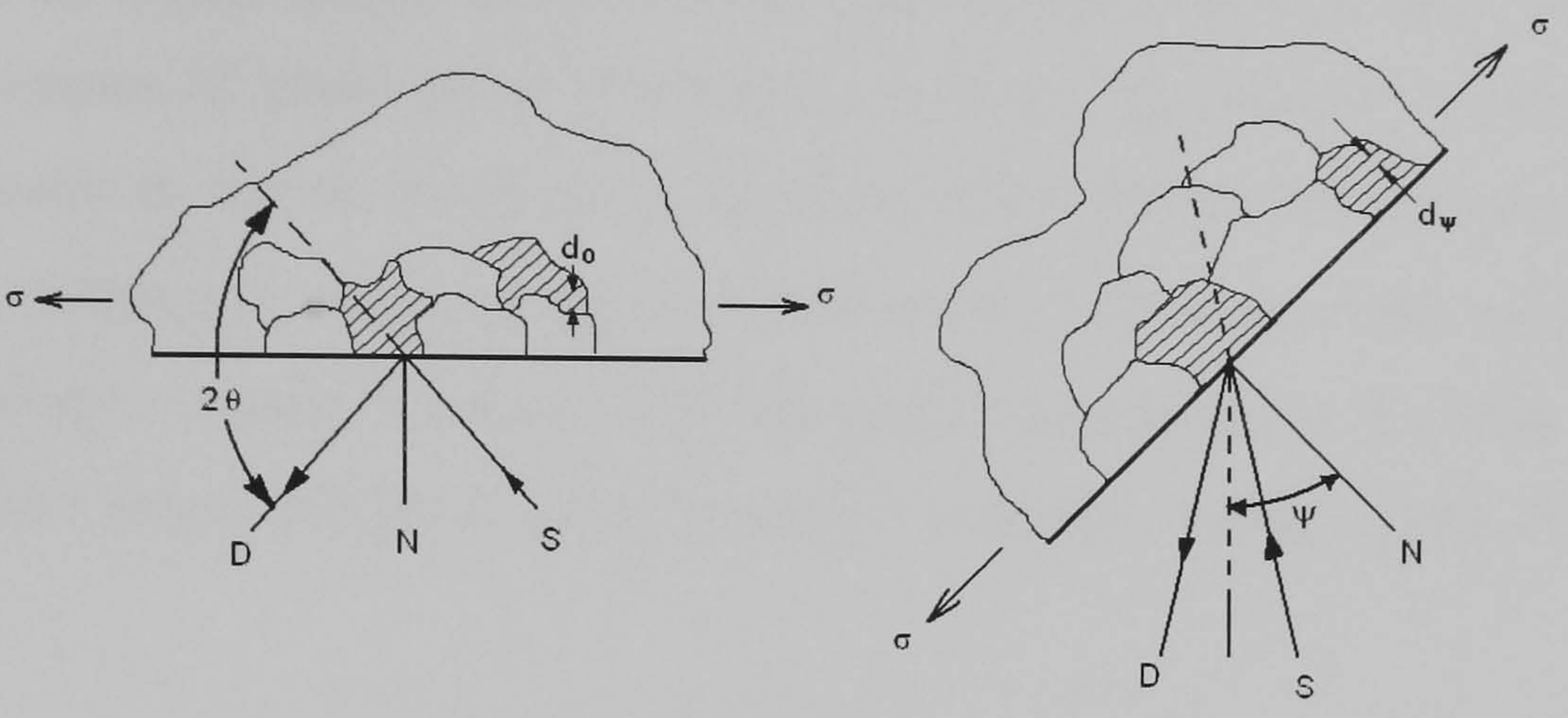

Figure 4.2. Interaction of a monochromatic X-ray with a crystalline material at 2 different angles ψ, resulted a diffracted o reflected beam at an angle 2θ **[167,168]**.

$$n\lambda = 2d \sin \theta \qquad 4$$

Where n.- Integer denoting the order of diffraction.

λ.- X-ray wavelength.

d.- Lattice spacing of crystal planes.

θ.- Diffraction angle.

Fig. 4.2 shows the surface of a sample under stress at two different orientations with respect to the X-ray beam. Where N represents the normal of the surface, ψ represents the angle between the normal of the surface and the normal to the diffracting lattice planes.

The apparatus used to carry out x-ray diffraction where the sample, detector arm and associated gearing are set up is referred to as goniometer. There are two different goniometers, one with the X-ray tube sets stationary, the sample moves by the angle θ and the detector simultaneously moves by the angle 2θ, and the other one with the sample sets stationary in the horizontal position, the X-ray tube and the detector both moves simultaneously over the angular range θ [165].

With the aid of X-ray diffraction the strain from crystal lattice is measured and then the residual stress that causes such strain is calculated, assuming a linear elastic distortion of the crystal lattice. Because of the shallow penetration of the X-ray (< 0.025 mm) the existence of plane stress is assumed. So stress distribution is represented by principal stresses σ_1 and σ_2 which act in the plane of the surface. The principal stress σ_3 and the shear stresses $\sigma_{13} = \sigma_{31}$ and $\sigma_{23} = \sigma_{32}$ acting out of the plane of the sample surface are zero. A strain component acting out of the surface perpendicular, ε_3, exist as a result of the Poisson's ratio contraction caused by the two principal stresses, figure 4.3 [166-168].

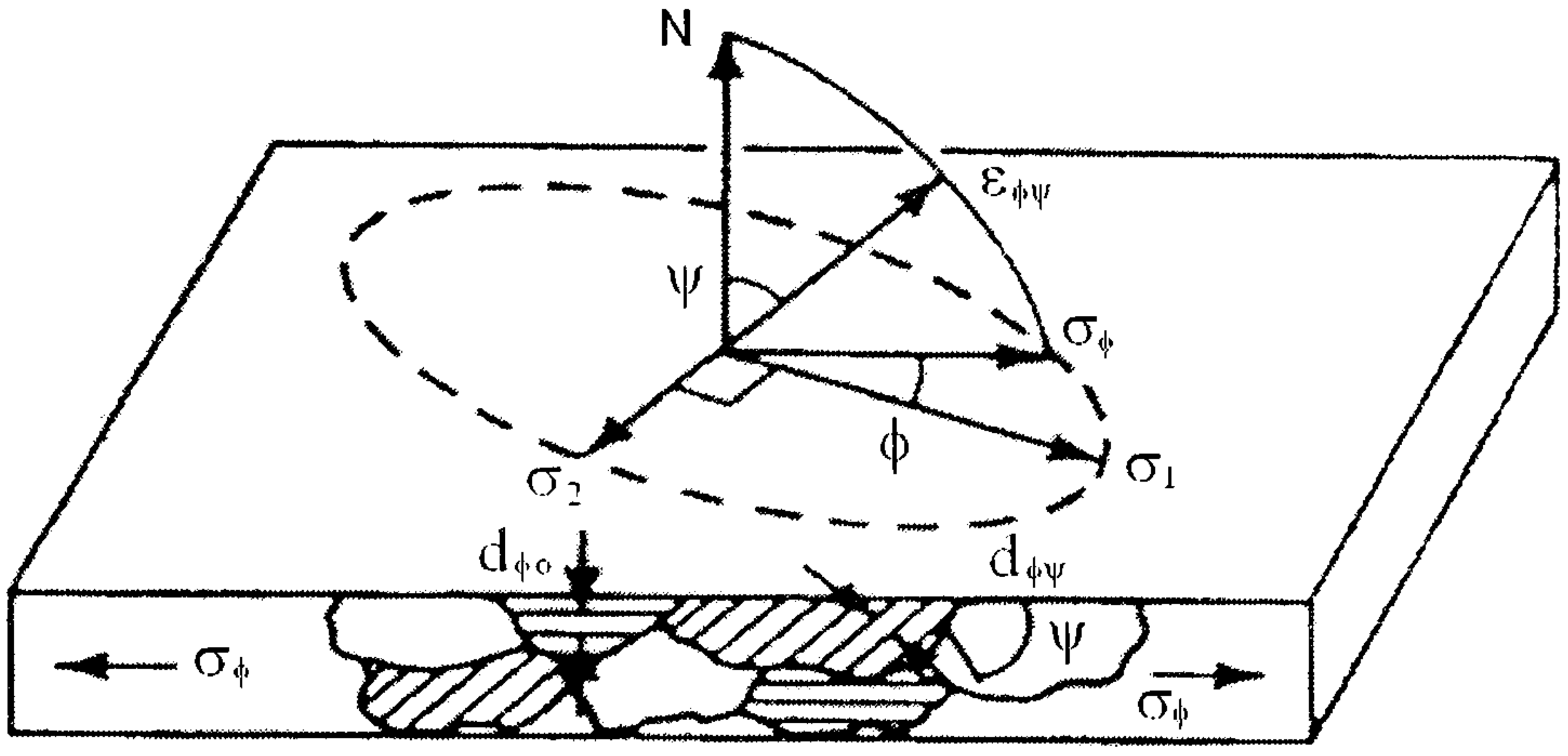

Figure 4.3. Principal stress and strain components in a plate under stress, considering the existence of plane stress [166,167].

The strain $\varepsilon_{\phi\psi}$ shown in figure 4.3, caused by stress σ_ϕ is located at an angle ϕ from the principal stress σ_1 in the sample surface, is given by:

$$\varepsilon_{\phi\psi} = \left[\frac{1+\nu}{E}\sigma_\phi \sin^2\psi\right] - \left[\left(\frac{\nu}{E}\right)(\sigma_1 + \sigma_2)\right] \qquad 5$$

This equation relates the surface stress σ_ϕ to the strain $\varepsilon_{\phi\psi}$ and the principal stresses in the surface. Considering $d_{\phi\psi}$ as the spacing measured between the lattice planes in direction defined by ϕ and ψ due to the stress, σ_ϕ, and d_0, as the stress free lattice spacing, the strain can be expressed as:

$$\varepsilon_{\phi\psi} = \frac{\Delta d}{d_0} = \frac{d_{\phi\psi} - d_0}{d_0} \qquad 6$$

Substituting equation 6 into equation 5 and solving for $d_{\phi\psi}$ yields:

$$d_{\phi\psi} = \left[\left(\frac{1+\nu}{E}\right)_{(hkl)} \sigma_\phi d_0\right] \sin^2\psi - \left(\frac{\nu}{E}\right)_{(hkl)} d_0(\sigma_1 + \sigma_2) + d_0 \qquad 7$$

Equation 7 relates lattice spacing, $d_{\phi\psi}$, and the biaxial stress, σ_ϕ, in the surface of the sample. The elastic constants $(1+\upsilon/E)_{(hkl)}$ and $(\upsilon/E)_{(hkl)}$ now are values of the crystallographic direction normal to the (hkl) lattice planes (Miller indices), where the strain is measured. It has been shown that the lattice spacing, $d_{\phi\psi}$, is a linear function of $\sin^2\psi$ **[166-168]**. A plot $\sin^2\psi$ vs **d**, made with different values obtained varying the ψ angle from 0° to 45° yields a linear dependence, where the intercept of the plot at $\sin^2\psi = 0$ equals the unstressed lattice spacing, $\mathbf{d}_0$, minus the Poissoon's ratio contraction due to the sum of the principal stresses; from equation 7 it is obtained:

$$d_{\phi 0} = d_0 - \left(\frac{\nu}{E}\right)_{(hkl)} d_0 (\sigma_1 + \sigma_2)$$

$$= d_0 \left[1 - \left(\frac{\nu}{E}\right)_{(hkl)} (\sigma_1 + \sigma_2)\right] \qquad 8$$

The slope of the linear pattern is given by:

$$\frac{\partial d_{\phi\psi}}{\partial \sin^2\psi} = \left(\frac{1+\upsilon}{E}\right)_{(hkl)} \sigma_\phi d_0 \qquad 9$$

Solving for σ_ϕ yields:

$$\sigma_\phi = \left(\frac{E}{1+\upsilon}\right)_{(hkl)} \frac{1}{d_0}\left(\frac{\partial d_{\phi\psi}}{\partial \sin^2\psi}\right) \qquad 10$$

The X-ray elastic constants can be calculated empirically, but the free stress lattice spacing, $\mathbf{d}_0$, cannot be calculated and is unknown. However, as E >> ($\sigma_1 + \sigma_2$), the value obtained from equation 8, $\mathbf{d}_{\phi 0}$, does not differ from d_0 by more than ± 0.1 %. Therefore, σ_ϕ may be approximated to this accuracy by substituting $\mathbf{d}_{\phi 0}$ for $\mathbf{d}_0$ in equation 10. The method is considered as differential technique and no stress-free reference standards are required to calculate $\mathbf{d}_0$ for the plane-stress model.

There are three most common techniques used which all of them assume plane stress at the sample surface and are based on the relationship between lattice spacing and stress. These techniques are single angle technique, two angle technique and the $\sin^2 \psi$ technique. The single angle technique is considered less sensitive than the other two but is used when a high-speed measurement is required. Two-angle technique determines the lattice spacing considering two ψ angles which are the extreme typically 0° and 45°. The $\mathrm{Sin}^2 \psi$ technique is basically the same as two-angle technique, except lattice spacing is calculated using more than two ψ angles.

Residual stress determined using X-ray diffraction is the arithmetic average of stress in a volume of material defined by the irradiated area, which may vary from square centimetres to less than a square millimetres and the depth of penetration of the X-ray beam [167,168].

MICRO-VICKERS HARDNESS

The concept of hardness is as follows, and according to Ashby, the best general definition that can be given. "Hardness is a measure of the resistance to permanent deformation or damage" [170]. Basically there are many methods to measure hardness and many authors have attempted to classify them into groups, however they can divided and explained as below [170, 171]:

1) Static indentation test: A steady load is applied to an indenter which may be a ball, diamond cone or diamond pyramid and the hardness is calculated from the area or depth of indentation produced.
2) Dynamic indentation test: A ball, cone or a number of small spheres is allowed to fall from a definite height and the hardness number is obtained from the dimensions of the indentation and the energy of the impact.
3) Scratch test: This can be subdivided into two types; (a) a comparison test in which one material is said to be harder than another if the second material is scratched by the first; (b) a scratch is made with a diamond or steel indenter traversing the surface at a steady rate and under definite load. The hardness number is expressed in terms of the width or depth of the groove formed.
4) Rebound test: The hardness is given by the height of rebound of a diamond tipped weight falling on the surface from a fixed height.
5) Pendulum recoil test: A jewel or steel ball is attached to a pendulum which is made to swing; the amplitude of the first swing or the time of oscillation of a number of swings is taken as a measure of hardness.
6) Abrasion or machinability test: Various types of mechanical test to measure the resistance to wear when subjected to a sliding or rotary motion or to various cutting operations.
7) Erosion test: In which sand or abrasive grain is caused to impinge upon the test surface under standard conditions, and loss of materials in a given time is taken as the measure of hardness. Hardness of grinding wheels is measured thus.

In order to know the hardness of the material near the surface where residual stresses lie, the micro-Vickers hardness indentation method is used because others methods would be impossible to measure hardness representative of such a depth, since the load applied was less than 1 kgf specially for soft materials. Measurements were made at room temperature through the thickness of the plate, on a transverse cross section of the material. An apparatus similar to the one shown in Fig 4.4a, is used for the test.

This method is similar to standard Vickers Hardness but with the variant that the load applied does not exceed 1 kgf. It consists in an indenter tip normal to the surface that is driven into the specimen under a known static load. This process leaves a mark with the shape of the indenter tip, generally a pyramoidal shape; the indenter is either the Vickers diamond pyramid or the Knoop elongated diamond pyramid. In this case the former was used. With the data obtained from the mean diagonal lengths "d", the hardness over the surface can be calculated.

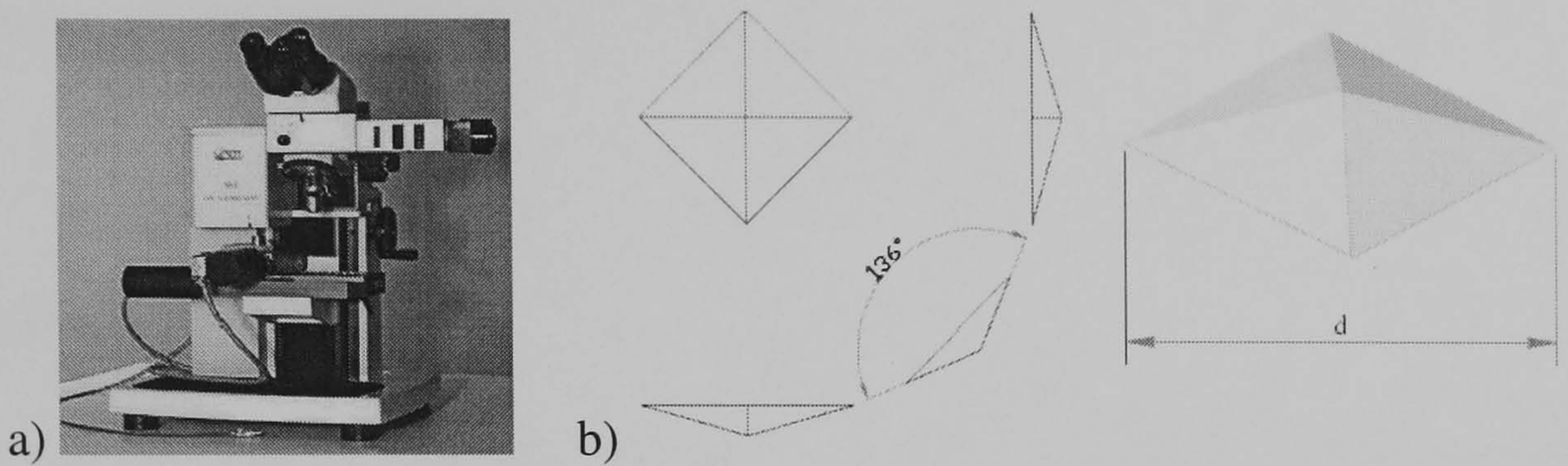

Figure 4.4 a) Apparatus used to measure micro hardness, b) Indenter shape and mean dimensions measurement "d".

In order to get the data it is necessary the use of a microscope to see and measure the size of the indentation left by the indenter. To get a good precision in the indentation measure a metallographic finish of the surface is needed, the smaller the load used, the higher the surface finish required.

The Vickers Diamond Pyramid hardness number is the applied load (kgf) divided by the surface area of the indentation (mm^2) [172]. As the shape of the indenter used is the pyramidal one the formula to get the value of the micro hardness is:

$$\mathrm{HV} = \frac{2F\,Sin\frac{136^\circ}{2}}{d^2} \qquad 11$$

$$\mathrm{HV} = 1.8544\,\frac{F}{d^2} \text{ approximately} \qquad 12$$

Where:

F = Load in kgf.

d = Arithmetic mean of the two diagonals (mm).

HV = Vickers Hardness.

The Vickers Diamond Pyramid indenter has the shape of a pyramid with a square base and an angle of 136° between sides as seen in fig. 4.4b.

REPLICATION

There are many methods to detect and follow a crack such as visual inspection, eddy-current methods, ultrasonic methods, etc [173]. Some of them are too sophisticated for this study and require a preparation of the specimen and special equipment. In order to follow and have a permanent record of the crack length at different numbers of cycles during the fatigue life, the replication method was chosen. This method does not require a special preparation of the specimen apart from polishing the surface and changes in crack length less than 10 μm can be detected with a well prepared surface [174]. This method has two technical disadvantages: 1) it only provides information from the surface of the crack growth, which may be quite different from its behaviour in the centre of the specimen, and 2) the test must be stopped every time a replica should be taken, this period of rest each time the test is halted may affect the subsequent crack growth.

As before mentioned the replication test method was chosen because it is the easiest way to set up the equipment to permanently record crack length data and the definition obtained could be 10^{-4} m on a good quality unpolished surface, the requirement needed in UIT treated specimens. Replicas were obtained during the process of fatigue testing for a few dog bone samples. The number of cycles between taking each replica would be calculated according to S-N curve to give a total of at least 15 data points before failure. Specimens, treated and untreated, would not have any additional preparation on the surfaces such as polishing, to avoid influencing the fatigue life or changing conditions compared to the S-N curves.

The replica materials used to carry out the process are:

- Acetone, 99+%
- Replication material (cellulose acetate of a thickness 35 micron, 0.0014 inch)
- Microscope slides
- Surgical blades

The procedure to achieve this method is as follows:

After a specific number of cycles halt the test and load the specimen up to 80% of the maximum load applied, in order to open a crack if already initiated. Spray the surface with acetone where the replica is required and immediately place a piece of replica film on the surface (Allowing surface tension forces to pull it down, no pressure is required on the replica film). The film should left to dry for about 2 minutes (Actually it should left up to the replica pull out from the surface completely or part of it). Replica is already taken from the surface, fig. 4.5, at that moment set up in a microscope slide in order to be examined afterwards.

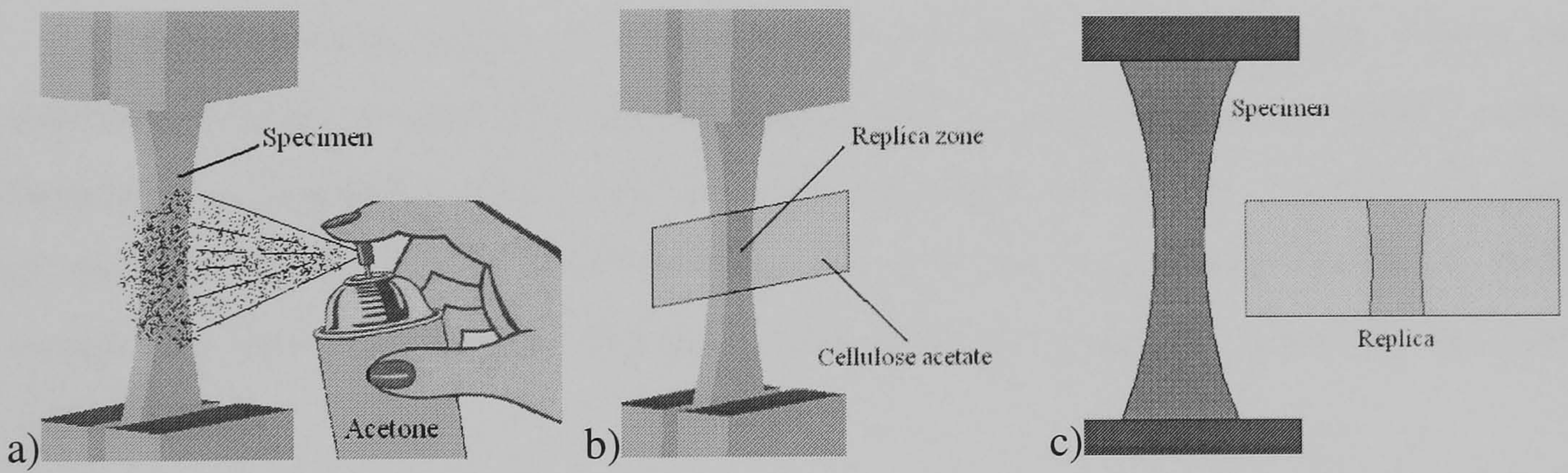

Figure 4.5 Replication procedure, a) Acetone application in the region of expected fatigue crack initiation, b) Cellulose acetate placed over the zone where the acetone was sprayed without any pressure on it and c) Cellulose acetate removed from the specimen with the replica of its surface.

DETERMINATION OF CRACK GROWTH RATE

The method is based in a precracked notched specimen under fatigue where information from measurements of the crack will be obtained. The measurements can be visual or by the aid of any other means. Crack growth rate is expressed as a function of stress intensity factor range which is calculated from expressions based on linear elastic stress analysis. For replica work, the secant method below was used, as the amount of data was small.

In order to carry out crack growth rate measurements in Aluminium alloy considering that the material is supplied in plates of 5 mm thickness, the specimen design and the procedure to follow were based on ASTM Standard E 647 [160]. As fatigue crack growth rate is expressed as a function of the crack tip stress intensity factor range, da/dN versus ΔK, the stable crack extension under fatigue can be differentiated from one material to another.

The concept of similitude is assumed here, which says that cracks from different sizes will increase by the same amount of distance per cycle under the same nominal value of ΔK. The parameters to be considered here are the environmental condition which can have an effect on the results especially in small crack growth, and the residual stresses which in this case are of some importance because of the treatment used in this work.

Specifications about the notch were mentioned in **chapter III**. There exist different methods to realize it, such as electrical-discharge machining (EDM), milling, broaching or sawcutting; every method is recommended for specific material. The length of the notch in this kind of specimen does not have any restriction according to ASTM except the need to exceed threshold, and will be given by practical machining considerations.

The design of the specimen was given in **chapter III** where its dimensions were determined, but apart from its dimensions before starting the test more specifications are required in order to get valid results. The requirements to get valid data in M(T) specimens for linear elastic behaviour are:

$$(W-2a) \geq 1.25\, P_{max}/(B\sigma_{YS}) \qquad 13$$

where:

(W-2a) = specimen's uncracked ligament

B = Specimen thickness

σ_{YS} = 0.2 % offset yield strength determined at the same temperature as used when measuring the fatigue crack growth rate data.

One other requirement is the difference between crack lengths from one face to the other; it means the crack length on one side must be within 0.25B value of difference with the other side face of the same crack, otherwise data is considered invalid.

ASTM standards suggest recording measurements intervals according to the next formula which is special for M(T) specimen:

$$\Delta a \leq 0.03 \text{ W for } 2a/W < 0.6 \qquad 14$$

$$\Delta a \leq 0.02 \text{ W for } 2a/W > 0.6 \qquad 15$$

The way to calculate ΔK for the M(T) specimen under load range ΔP is with the use of the next expression:

$$\Delta K = \frac{\Delta P}{B}\sqrt{\frac{\pi\alpha}{2W}\sec\frac{\pi\alpha}{2}} \qquad 16$$

Where: $\alpha = 2a/W$; expression valid for $2a/W < 0.95$. The R ratio is assumed to be positive.

The values of crack length "a" and number of cycles "N" can be obtained from different methods such as visual or non-visual (ultrasound, potential drop, eddy current, etc.). When the values are obtained they would exhibit a scatter in the plot "a" vs "N". There are many methods to fit those values to a curve, such as secant method or incremental polynomial; these methods are suitable to create curves of da/dN Vs ΔK as well.

Secant method

This method is based on the technique of point-to-point evaluation, which basically consists in the calculation of the slope of a line which connects one point with the next, taking into account just two data points of the crack growth on the "a" vs "N" curve. It is expressed as follows:

$$(da/dN)_{\bar{a}} = (a_{i+1} - a_i) / (N_{i+1} - N_i) \qquad 17$$

Since the value of da/dN represents the average range of two values of crack length ($a_{i+1} - a_i$), the crack length value to work out ΔK is from:

$$\hat{a} = \tfrac{1}{2}\,(a_{i+1} - a_i) \qquad 18$$

Incremental polynomial method

This method is used to fit values of da/dN to a second-order polynomial (parabola) to sets of (2n + 1) successive data points, where "n" can take values of 1, 2 3 and 4. The equation of the curve for the local fit is as follows:

$$\hat{a}_i = b_0 + b_1\left(\frac{N_i - C_1}{C_2}\right) + b_2\left(\frac{N_i - C_1}{C_2}\right)^2 \qquad 19$$

where:

$$-1 \le \left(\frac{N_i - C_1}{C_2}\right) \le +1 \qquad 20$$

The parameters b_0, b_1 and b_2 are the regression parameters that are determined using a least squares method (that is, minimization of sum of the squares of the deviations between observed and fitted values of crack length) over the range $a_{i-n} \le a \le a_{i+n}$. In order to obtain the values of the regression parameters the next expression was used:

$$A = \begin{bmatrix} m & \sum_{i=1}^{m} N_i & \sum_{i=1}^{m} N_i^2 \\ \sum_{i=1}^{m} N_i & \sum_{i=1}^{m} N_i^2 & \sum_{i=1}^{m} N_i^3 \\ \sum_{i=1}^{m} N_i^2 & \sum_{i=1}^{m} N_i^3 & \sum_{i=1}^{m} N_i^4 \end{bmatrix} \quad b = \begin{bmatrix} b_0 \\ b_1 \\ b_2 \end{bmatrix} \quad G = \begin{bmatrix} \sum_{i=1}^{m} a_i \\ \sum_{i=1}^{m} N_i a_i \\ \sum_{i=1}^{m} N_i^2 a_i \end{bmatrix} \qquad 21$$

Where:

m = the number of successive data points to be fit into the local curve which is equal to (2n + 1)

N = Number of cycles for every crack length in the rank of N_i to N_m.

a = crack length values within the rank of a_i to a_m.

In an arrangement of the matrix Ab = G and using matrix solutions is possible to get the values of matrix "b" with $b = A^{-1} G$.

The value of the crack length $\hat{a}_i$ is the fitted value corresponding to N_i. C_1 and C_2 are parameters to scale the input data, thus avoiding numerical difficulties in determining the regression parameters. The parameters to scale the input data are expressed as follows;

$$C_1 = \tfrac{1}{2} (N_{i-n} + N_{i+n}) \qquad 22$$

$$C_2 = \tfrac{1}{2} (N_{i+n} - N_{i-n}) \qquad 23$$

To obtain the crack growth rate at N_i is necessary to differentiate the equation of the curve (parabola) given above which finally is given as follows:

$$\left(\frac{da}{dN}\right)_{ai} = (b_1)/(C_2) + 2b_2(N_i - C_1)/C_2^2 \qquad 24$$

In order to get the value of ΔK for the crack growth rate $\left(\frac{da}{dN}\right)_{a_i}$, the value of $\hat{a}_i$ corresponding to N_i is taken and computed from equation 16.

A Fortran computer programme based on the incremental polynomial method was written and utilized for the n values of n=1, 2 and 3, that is m = 3, 5 7 successive data points. This programme was based on the principles given in ASTM standards and stress intensity factor calibrations. The programme can be seen in **Appendix A6**.

CRACK GROWTH MEASUREMENTS

The crack length measurements achieved in this work were travelling microscope, CCTV camera recording, replication, and by means of electric potential difference. There are many methods to get measurements of crack length at a specific number of cycles of a specimen under cyclic fatigue and there are some advantages and disadvantages among them. The methods used were selected because of the facilities in the department and equipment available.

Electric Potential Difference (EPD) Method

The electrical potential or potential drop technique is one of the methods used commonly in fracture research. This technique is considered one of the most accurate and efficient methods to monitor the crack growth extension in metallic materials and in non-metallic materials by firmly attaching a conducting foil or film and treating it as replicate specimen to be monitored.

This method is based in the electric potential field or voltage drop disturbance due to a discontinuity in a current-carrying body. The magnitude of the disturbance depends of the size and shape of the discontinuity [175]. It means that if a constant current (keeping it constant from an external means) passing through a crack plane is affected by the modification of the uncracked ligament (or increment of the crack length), the electric potential or voltage drop will increase. Monitoring potential difference between two points (one on each side of the crack plane) through the test the change of the potential difference between those points will indicate the increments of the crack, and the crack length value.

As all methods, this one has some disadvantages. In principle elastic and plastic deformation can affect material resistivity, as well as variation of temperature. The current must be large enough to produce measurable potential but at the same time must be checked because an excess of current can raise the temperature of the specimen which must be avoided. Accuracy of the technique can be affected by electrical contact between crack surfaces where the fracture morphology is particularly rough or because of the crack closure effect.

Within the equipment required to carry out this technique is the current supply unit (can be alternating current AC or direct current DC). This unit must provide a constant current during the total test. Both AC and DC have some limitations. DC is susceptible to thermoelectric effects, that even are present without the input current, this can be sorted out simply by subtracting the voltage measured when current off from that measured when the current on. Alternatively, all thermoelectric junctions between dissimilar materials must be kept at the same temperature. The circuit using DC is simpler than using AC. The main consideration using AC is the frequency, which if it is less than 100 Hz the field is approximately two dimensional in a plate as in DC, so current is constant through the thickness in all points. For frequencies higher than 100 Hz a non-uniform current distribution though the thickness occurs, this effect is called "skin effect" because the current tends to be carried only near the surface of the specimen.

The leads used to get readings of potential difference from the plate were made of 18-8 stainless steel and the way they were attached was by spot welding on the point where the readings of potential should be acquire with the aid of high-current. In order to get readings in voltmeters the wires made of steel were jointed to wires made of copper, because of that junction a variation in temperature would induce a thermoelectric voltage as an error in crack length. A constant-temperature junction box was used to solve that problem, for all steel to copper junctions. Stainless steel is very close to aluminium in the thermoelastic series, and so no significant errors in potential can arise at the spot-welded junctions on the specimen.

As the machine used to fatigue the material does not have electric insulation in the grips a plate of composite material was used. The current throughout the test was DC and the equipment used to perform this technique was:

- 50 amp constant DC Current supply
- 4 Voltmeters as voltage measurement equipment, with IEEE digital outputs.
- Constant-temperature junction box
- Computer (To record the data in a file to compute them later)

In ASTM standard E 647 [160] there are recommended positions of the leads for voltage measurement on the M(T) specimen and an equation to use specially for that configuration. The purpose of this work is to try to get the crack growth rate for each side of the crack because the distance of the treated zone is different for each side producing unsymmetrical crack growth, so the lead configuration proposed to attain it is shown in fig. 4.6a.

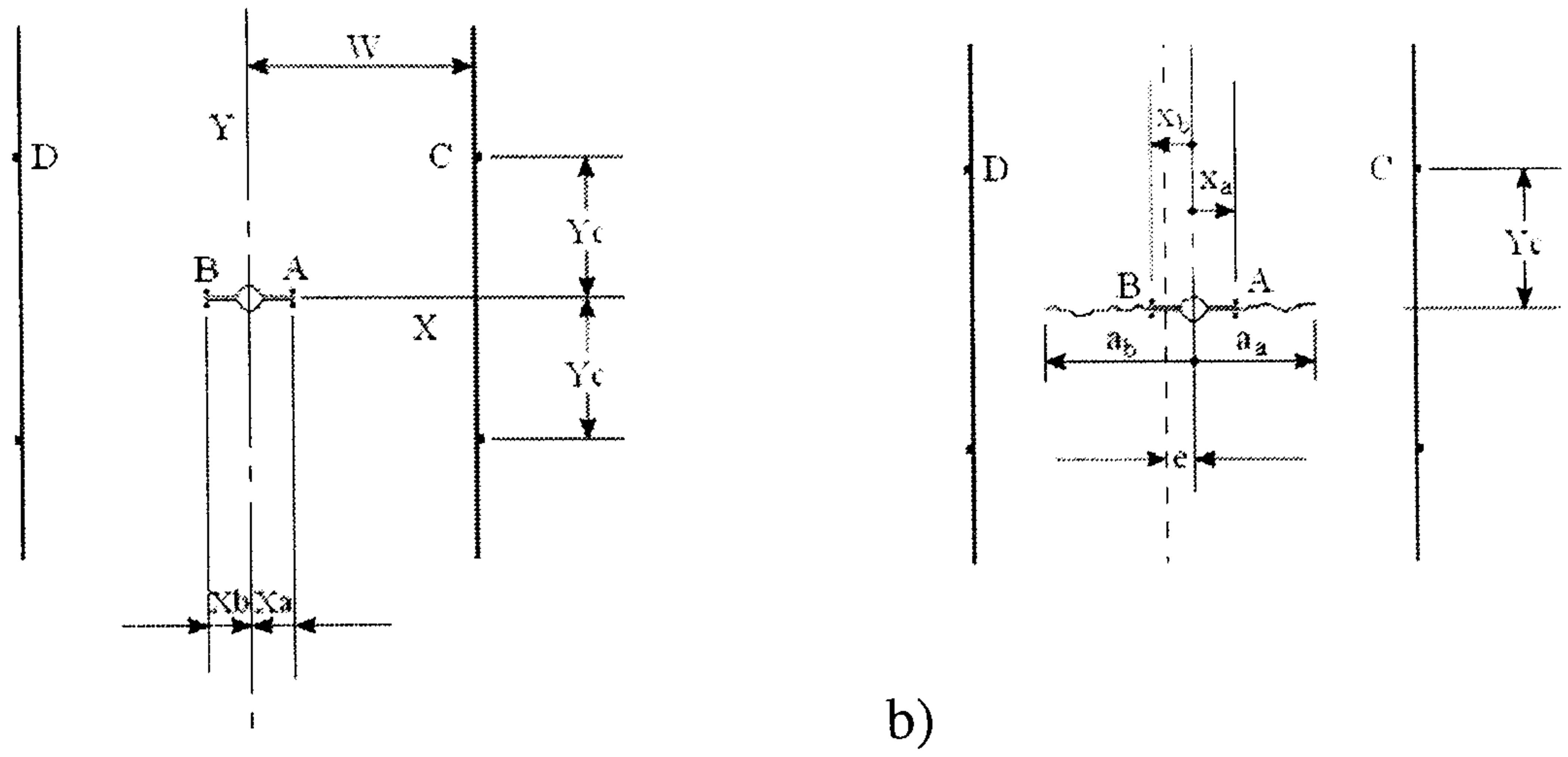

a) b)

Figure 4.6 a) Wire placement location for this work, the positions close to the crack tip on the "y" direction were as close as possible considering y = 0. b) Nomenclature used for the equations considering eccentricity.

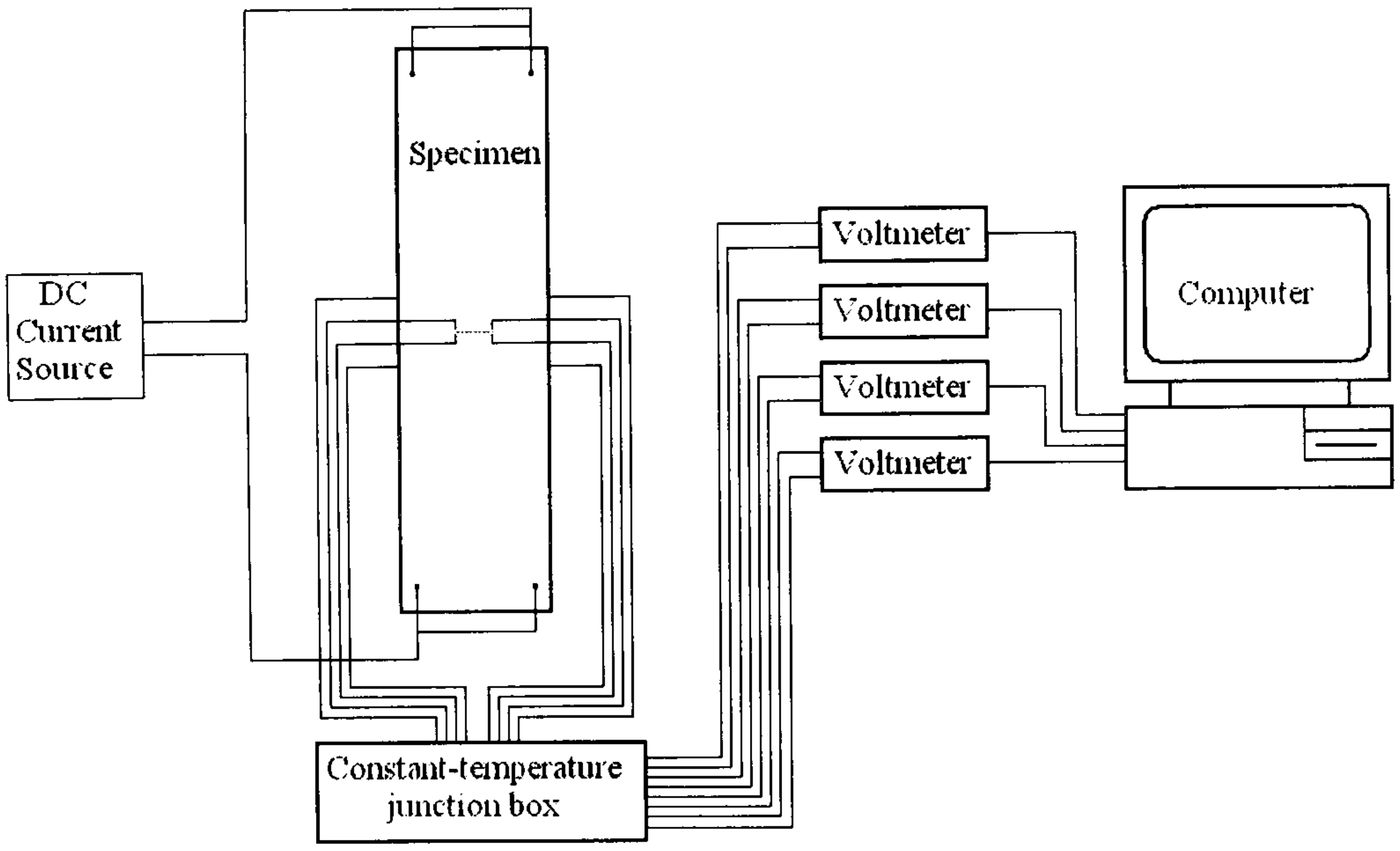

Figure 4.7 Schematic diagram of the equipment set up to perform fatigue crack growth measurement by EPD method.

The equipment used to carry out the test was set up as in fig. 4.7. The current of 20 amps was supplied by a DC current source, the leads were attached to the plate as the configuration in fig. 4.6a), the junctions between leads made of steel and wires made of copper were put into a constant-temperature junction box in order to keep a constant temperature. The voltage readings reach their destination in the four voltmeters, which send that information to the computer wherever requested to be stored for analysis later.

The equation to calculate the crack length for this specific arrangement was the Gilbey and Pearson equation that is expressed as follows:

$$\mathrm{Cos}^2\left(\frac{\pi a}{2W}\right) = \frac{Cos^2\left(\frac{\pi x}{2W}\right)Cosh^2\left(\frac{\pi y}{2W}\right)}{Cosh^2(KV)} + \frac{\left(1-Cos^2\left(\frac{\pi x}{2W}\right)\right)\left(Cosh^2\left(\frac{\pi y}{2W}\right)-1\right)}{Cosh^2(KV)-1} \qquad 25$$

As the coordinates for the leads in the plate are for the point close to the crack tip x = “constant” and y = 0 (considering this value because is close to the “x” axis), and there are two leads one each side of crack tip, and the other two points placed on the edge their coordinates are x = W and y = “constant”, the total of number of equations obtained are four. Considering eccentricity, as seen in fig. 4.6b, between the mid axis of the plate and the mid axis of the total crack the equations finally are expressed:

$$\mathrm{Cosh}\,(K_aV_a) = \frac{Cos\left(\frac{\pi(x_a+e)}{2(W+e)}\right)}{Cos\left(\frac{\pi(a_a+e)}{2(W+e)}\right)} \qquad 26$$

$$\mathrm{Cosh}\,(K_bV_b) = \frac{Cos\left(\frac{\pi(x_b-e)}{2(W-e)}\right)}{Cos\left(\frac{\pi(a_b-e)}{2(W-e)}\right)} \qquad 27$$

$$\text{Cosh}\,(K_aV_c) = \sqrt{1+\frac{Cosh^2\left(\frac{\pi y_c}{2(W+e)}\right)-1}{Cos^2\left(\frac{\pi(a_a+e)}{2(W+e)}\right)}} \qquad 28$$

$$\text{Cosh}\,(K_bV_d) = \sqrt{1+\frac{Cosh^2\left(\frac{\pi y_c}{2(W-e)}\right)-1}{Cos^2\left(\frac{\pi(a_b-e)}{2(W-e)}\right)}} \qquad 29$$

Where: W – Distance from the centre of the plate to the edge

X_a and X_b - Distance from the plate centre to the point where the lead is attached.

Y_c and Y_d - Distance from the crack plane to a certain point in "y" direction.

V_a, V_b, V_c and V_d – Volts readings from the voltmeter for each point on the plate.

K_a, K_b – Constants for each crack tip.

a_a, a_b – Crack lengths evaluated from the volts reading.

e – Eccentricity measured from the centre of the plate to the dividing line between current flows to each side of the specimen.

As it can be seen there are four equations and five unknowns. A programme was written in order to calculate the unknowns and the values of the crack tips length. The method for solution of the equations is in **Appendix A7** and the programme is in **A8**.

Clearly a fifth equation is needed. It is assumed that the "e-line" in fig 4.6b is the dividing line between current that flows round the left tip and current that flows to the right. If that line is straight, a further Gilbey and Pearson equation may be derived, to evaluate the potential gradient far from the crack (see **Appendix A7**).

CHAPTER V

EXPERIMENTAL RESULTS

Results of the experimental tests are shown in this chapter in tables and graphs. The way they were planned and achieved is covered in previous chapters. There were two materials tested, Al2024-T3 Alloy with 74 fatigue tested specimens and Al7150-T651 Alloy with 19 fatigue tested specimens. Al2024-T3 was the main material to generate results because of the amount of testing and breadth of investigation. Discussions and conclusions are in further chapters.

FATIGUE TESTS

As the objective of this work is to know the effect of UIT on the fatigue life of Al2024-T3 and Al7150-T651, fatigue test on both materials after treatment were carried out and compared with bare material in the as received state.

2024-T3

Fig. 5.1 shows the plot of number of cycles to fracture (N) versus stress amplitude of treated and bare materials, best known as the S-N curve. Here can be seen the data obtained from fatigue under the conditions given in **chapter III**. There are five different batches tested at different loads (NUIT, UIT-1-27, UIT-1-36, UIT-2-36 and UIT-3-36).

Bare material is the first to appear in the table specification of the graph. There were 8 specimens tested, and with the aid of these specimens a curve was fitted in order to have an indication where the average fatigue life is placed. The curve that fits the points was obtained from a second order equation, which at the same time was used to get the best fit curves for the rest of the fatigue data. The fatigue limit of virging material can be inferred from the graph, with a value of stress range of around 210 MPa. Strictly for aluminium alloys which do not show a clear knee in the S-N curve, the fatigue limit used in this thesis is the fatigue strength at 10^7 cycles to failure. Specimens treated with UIT-1-27 condition numbered 12 and their values are represented by a square with a cross inside in fig. 5.1. A specimen tested with this condition reached 10^7 cycles without fracture, meaning that fatigue limit for that condition might have been reached. Fatigue limit for this condition is around 130 MPa stress amplitude. All the data obtained from UIT-1-27 treated specimens gave stress ranges that were below the data obtained from bare material. Table 5.1 shows the data obtained in every single fatigue test for NUIT and for different UIT conditions.

Table 5.1 Results from fatigue test with R = 0.1 at constant amplitude loading in Al2024-T3 under different treatments conditions.

Stress Range *[MPa]*	**Max Stress** *[MPa]*	**Untreated** *[Cycles]*	**UIT-1-27** *[Cycles]*	**UIT-1-36** *[Cycles]*	**UIT-1-27 74 mm** *[Cycles]*	**UIT-1-27 44 mm** *[Cycles]*	**UIT-1-27 35 mm** *[Cycles]*	**UIT-1-36 74 mm** *[Cycles]*	**UIT-2-36** *[Cycles]*	**UIT-2-36 74 mm Milled** *[Cycles]*	**UIT-3-36** *[Cycles]*
117	130		9999872*								
135	150		3384320								
148.5	165		584448								
153	170			317264							
162	180		460784	4303104*							
171	190			208872					5014986*		
180	200		315792	228920					1268800		10000000*
184	210								1850000*		
193.5	215			130640							
198	220		178392						553280		
207	230										2439680
210.6	234	9814420							338000		
216	240	84584**		124056					721700		541437
220.5	245	6883414	147992								
225	250	154824** 403536***	87232	103604			82300***		278500		
234	260	268592	142430	68400					197660		1720718*
243	270	267888 226288***	67176	111760	118892	77712	72284 114000***	107204 131936 524039*^{a} 790990*^{a}	197600	909258* 2000000*	
252	280										237409
256.5	285			66472							
270	300	186512	47404	70616	81468	75852	59282	94324 65094 156180*^{a} 144371*^{a}	126000	233837 285878	258541
297	330	89708	44232	42234					58800		
306	340								95300		68000
369	410										27281

*Not fractured, **Erroneous data obtained due hydraulic transient, not considered in plot to fit the curve ***Replica, *^{a}Milled

The UIT-1-36 condition gave data quite similar to the UIT-1-27 condition, in comparison to the bare material. The fatigue limit for this condition is a bit higher than UIT-1-27 condition, given by a test passing $4x10^6$ cycles of fatigue life without fracture, fig. 5.1. The fatigue limit for this condition is around 140 MPa stress range and the difference in fatigue life is small with respect to UIT-1-27 condition. At higher stress ranges, behaviour is quite similar to the UIT-1-27, and even is a bit lower than UIT-1-27 condition.

The UIT-2-36 condition generated a curve that, like the last two is underneath the bare material curve, fig. 5.1. A difference of this curve from the other two last conditions is that at higher stress ranges the curve joins the bare material response. The pattern of the test showed that fatigue limit is around 170 MPa stress range, where two tests were suspended and left as run outs because of the loos of hydraulic pressure.

The UIT-3-36 condition is represented by 8 empty square points on fig. 5.1, and shows that there is no effect of this condition on the fatigue life of the material because the curve is almost in the same place as the bare material. The fatigue limit of the UIT-3-36 condition is almost the same as the bare material.

Fig. 5.2 shows three S-N curves, bare material, UIT-1-27 and UIT-1-36 in order to observe the effect of UIT on the material over different lengths of treatment in the gauge section. The two reduced lengths were selected such that the cross-section width of 10 mm was enlarged by 30% and 50% (13 mm and 15 mm) as shown in fig. 5.3. The section of 74 mm in length occupied the whole curved part. Two specific load amplitudes were used to study fatigue endurance of these specimens; the load amplitudes were chosen from the loads already employed to test bare, UIT-1-27 and UIT-1-36 conditions.

There were 2 specimens treated at UIT-1-27 condition along a 74 mm length, two more at 44 mm length and two more at 35 mm length. Almost all of them gave results for fatigue life close to the S-N curve of the UIT-1-27 condition. The best fatigue life obtained from these specimens was from the samples treated at 74 mm length for both loads as shown in fig. 5.2, numerical data are in table 5.1.

For UIT-1-36 condition there were 4 specimens, all of them were treated over a 74 mm length along the gauge section; no shorter lengths were treated due to the results previously obtained with UIT-1-27 condition. The loads used for these specimens were the same as used in UIT-1-27 conditions and in the graph, fig. 5.2, are represented by empty triangles. Data for these conditions behave similar to those in UIT-1-27, being the results close to the previous tests at 74 mm length.

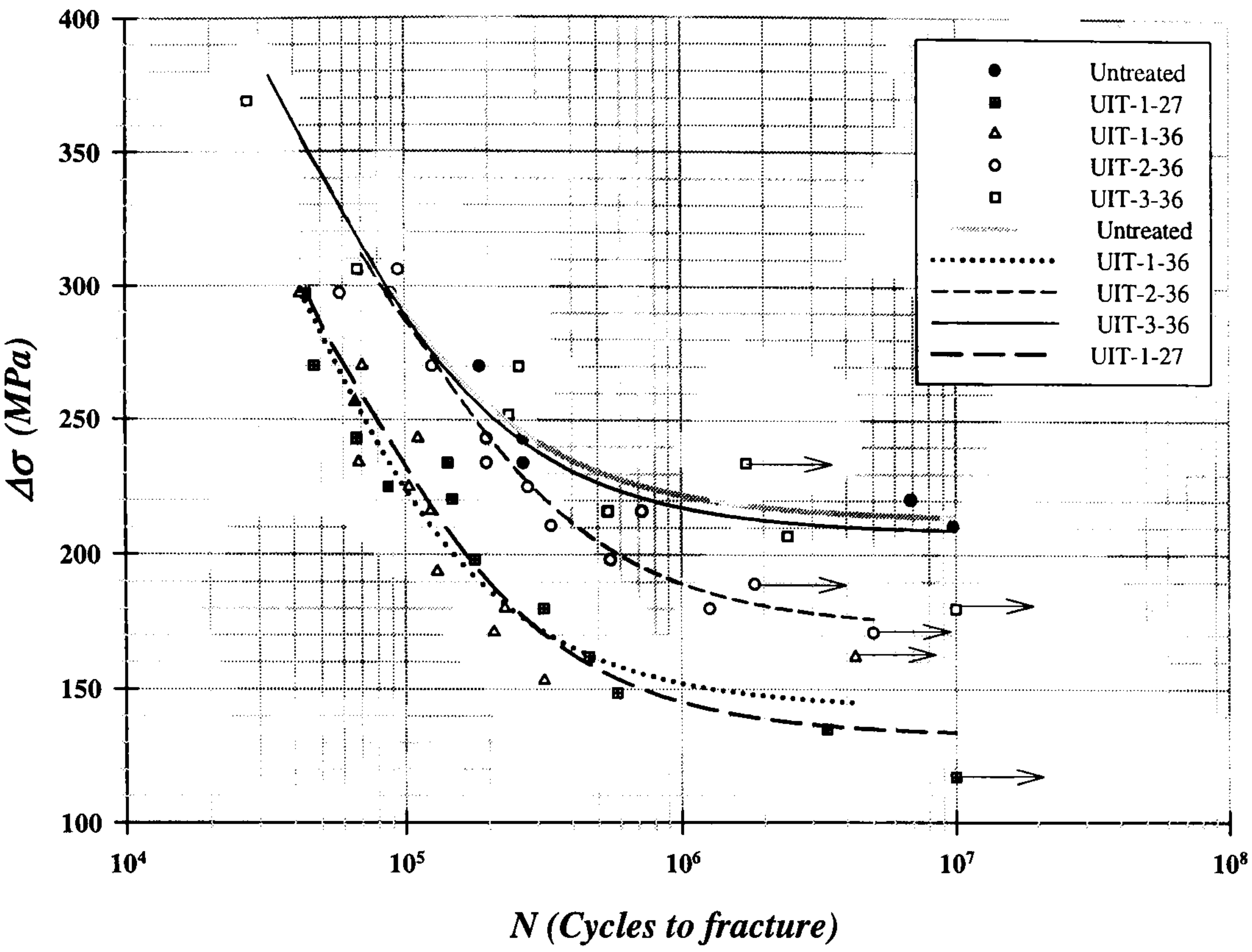

Figure 5.1 Fatigue test of five different batches represented in an S-N curve. Graph stress amplitude versus number of cycles to fracture with data from Al 2024-T3 Bare material, UIT-1-27, UIT-1-36, UIT-2-36 and UIT-3-36 conditions.

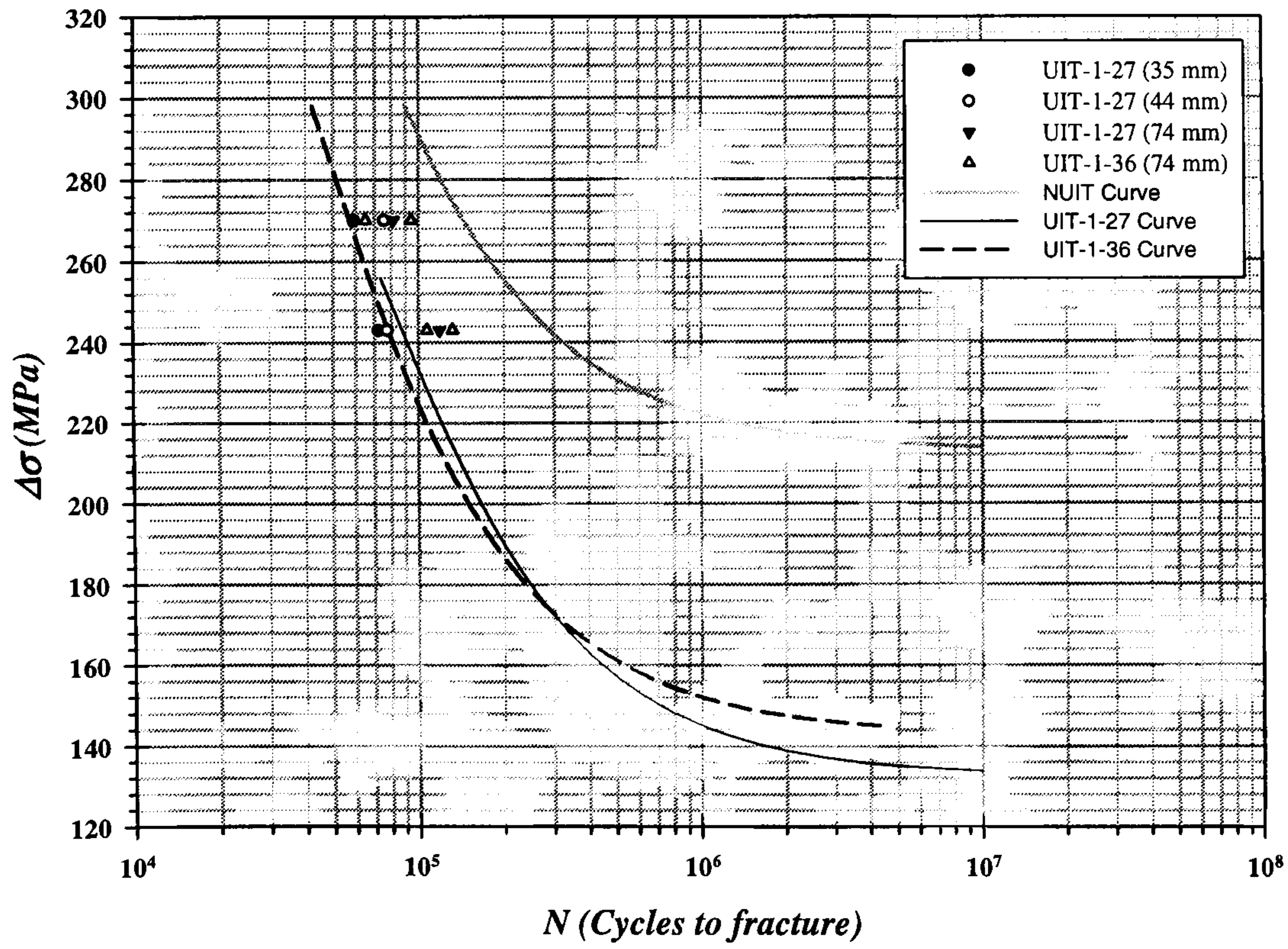

Figure 5.2 S-N curve of specimens treated at different lengths compared to Al 2024-T3 Bare material, UIT-1-27 and UIT-1-36 S-N curves in order to show the effect of treatment for a specific length of treated zone.

According to the failed zone in these specimens, fig. 5.3, the fracture did not occur in the untreated zone but in the treated zone. It means that the UIT conditions introduced affect in a bad manner the fatigue life of Aluminium alloy 2024-T3, giving a decrement in its endurance and having no improvement at all for UIT-1-27 and UIT-1-36.

Figure 5.4 shows the fatigue life of specimens after take some replications from their surfaces. The replication method was used in specimens treated at UIT-1-27 and bare in order to measure crack propagation of small cracks. As described in **chapter IV**, in the replication method it is necessary to spray acetone on the surface with an open crack, and therefore it is important to know how much the fatigue life could be affected by this substance. A load of 80% of the maximum load was applied during the replication process that sometimes lasted more than 5 minutes. This period of time with that specific load did not affect much the fatigue life, as shown by comparison with expected values from previous tests, data can be found in table 5.1 in the untreated column.

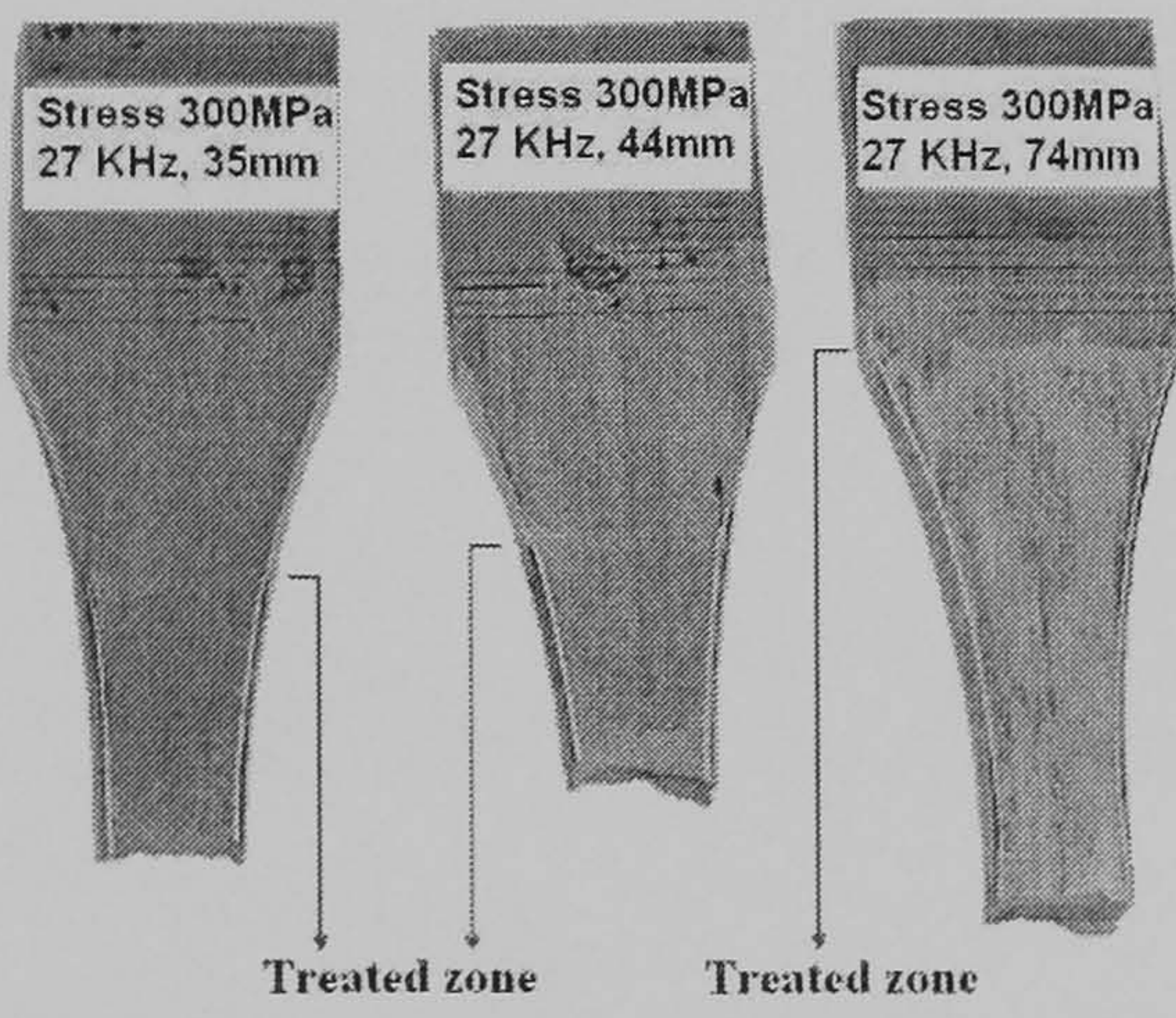

Figure 5.3 Al 2024-T3 specimens treated with UIT-1-27 over different lengths and fractured in the treated zone.

In Fig. 5.5 can be seen some data points acquired from eight fatigue tests on specimens milled 0.05 mm (50μm) on their surfaces after being treated at UIT-1-36 and UIT-2-36 conditions. For UIT-1-36 some places were difficult to mill 50 μm deep because of the severity of the treatment which left some curvature of the surface, especially on the edge where the treatment was so severe that the finish of the surface was odd. As it can be seen in figure 5.5, a bare material fatigue test curve is plotted and compared with points data obtained from milled specimens at different load ranges and

UIT conditions. Milling the surface improves fatigue life of most specimens, and more so for those of UIT-2-36 than UIT-1-36 condition in the long fatigue life zone. Load magnitudes were chosen to correspond with those in replication method and those of different treatment length. The maximum stresses used here were 300 MPa and 270 MPa. Numerical data for this graph is found in table 5.1 in the columns of UIT-1-36 (74 mm) and UIT-2-36 (74 mm) milled.

Table 5.1 shows all the data values acquired from fatigue tests of bare material and different UIT treatments, as well as those milled and used to take replicas. Two data points were taken as erroneous because of a failure of the constant hydraulic fluid pressure. The supply pressure from the ring main dropped periodically on the machine; this could generate a single overload, and cause an erroneous data for fatigue life, as observed.

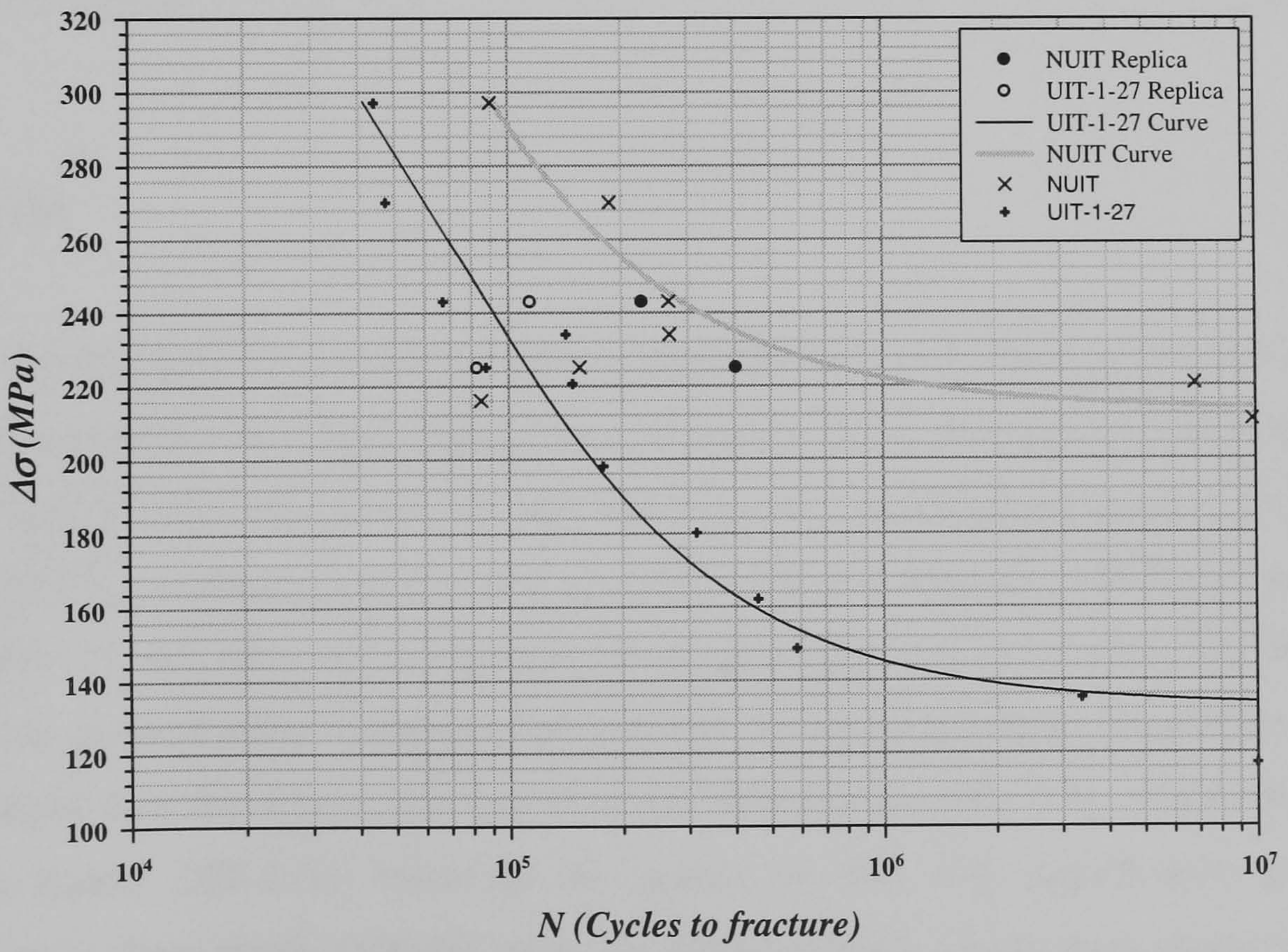

Figure 5.4 Bare Al 2024-T3 and UIT-1-27 S-N curves in a plot where some data from replication method were tested and the data was close to the curves.

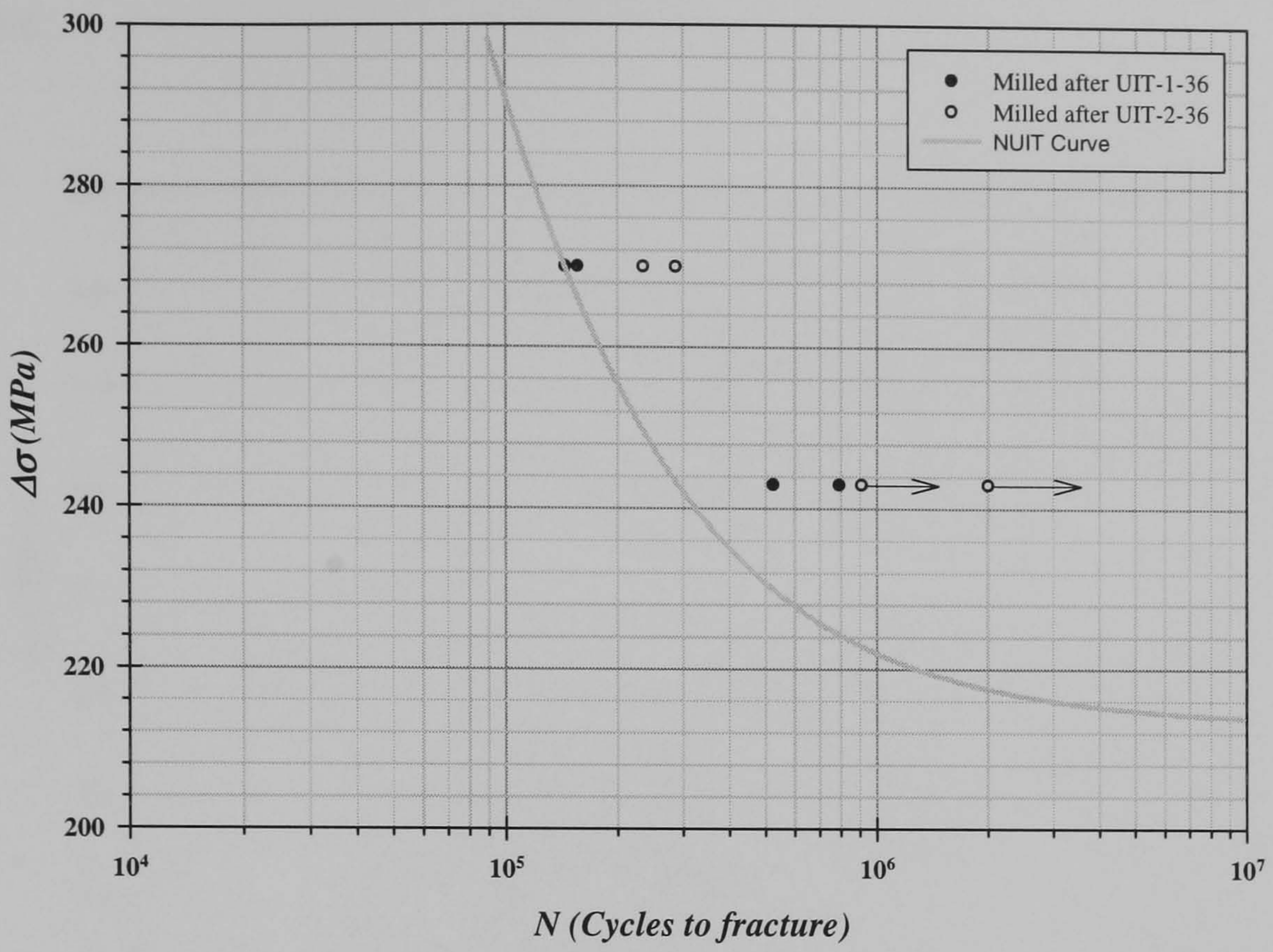

Figure 5.5 S-N curve from Al 2024-T3 Bare material and some points data from milled specimens after being treated with UIT-1-36 and UIT-2-36 conditions, showing an improvement in their fatigue life.

7150-T651

Fatigue tests for specimens made of Al7150-T651 were made as well for bare and different treatment conditions. Fig. 5.6 shows the S-N curve obtained from bare specimen fatigue tests and the data points of bare material and 5 different conditions of UIT. The effects of UIT conditions on this material were similar to those on Al2024-T3. As UIT-3 in Al2024-T3 did have not a big effect in fatigue life, it was omitted. The treatment having the greatest effect on fatigue life was UIT-4, decreasing rather more fatigue life of the material than the others, and then that was followed by UIT-1-36, UIT-6-36, UIT-5-36 and finally UIT-2-36. However the scatter of data was significantly (±80000), compared to these trends (106000 mean life improvement). Loads were chosen from the zone of longer fatigue life of the bare material in order to get more remarkable fatigue life differences among all the conditions used in this material. Two specimens of every condition under the same stress amplitude were tested in order to analyse fatigue effects.

Table 5.2 shows data values obtained from fatigue tests and used to create the plot shown in fig. 5.6.

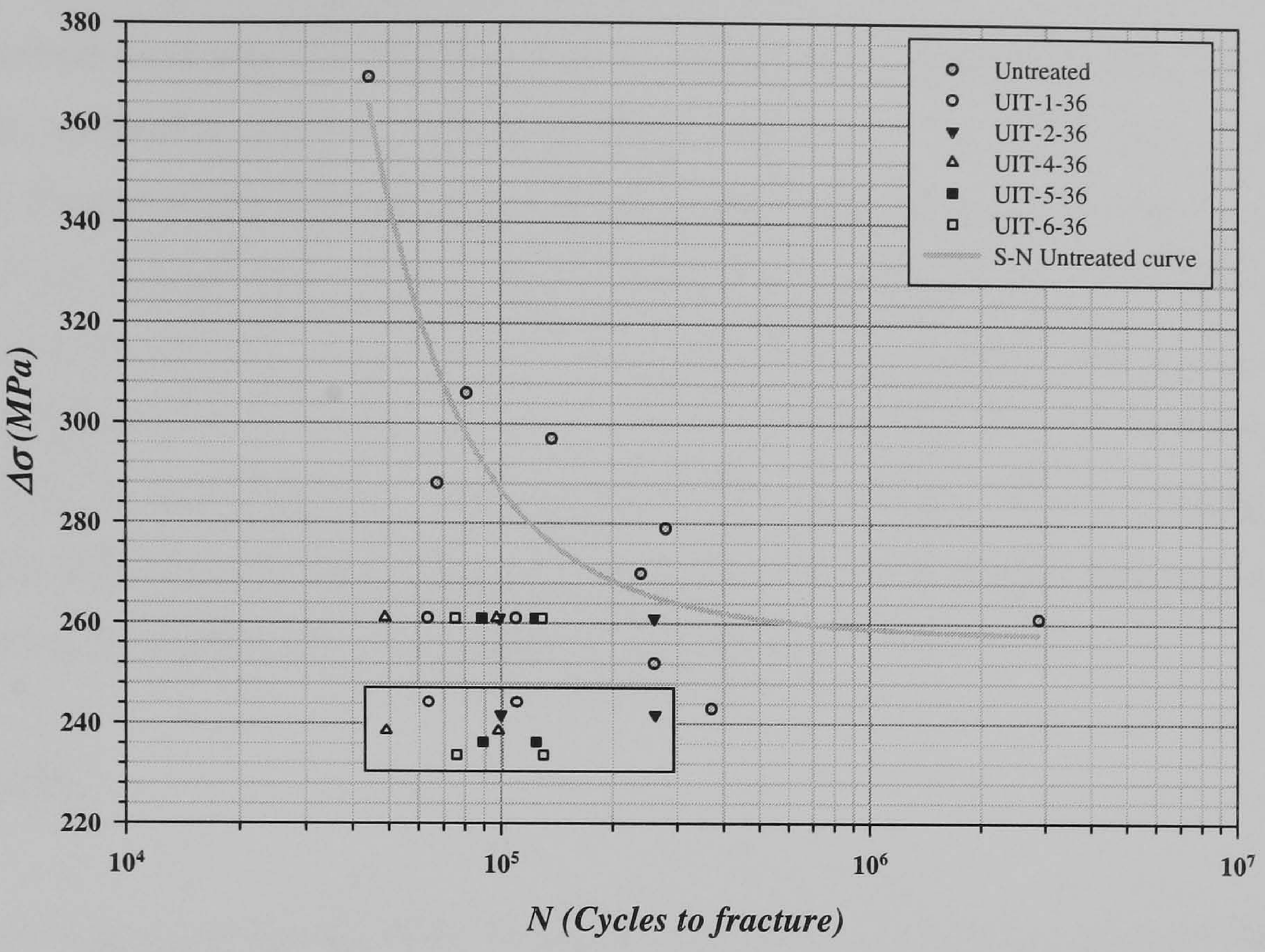

Figure 5.6 S-N curve fitted from data points obtained from specimens made of Al7150-T651 and tested at different loads. Within this plot can be seen data points from specimens previously treated at different UIT conditions and fatigued with a maximum load of 290 MPa, listed in table 5.2. A small square within the plot represents the vertical position of every symbol on the graph.

Table 5.2 Results from fatigue test with R = 0.1 at constant amplitude loading in Al7150-T651 under different treatments conditions.

Stress Range *[MPa]*	**Maximum Stress** *[MPa]*	**Untreated** *[Cycles]*	**UIT-1-36** *[MPa]*	**UIT-2-36** *[MPa]*	**UIT-4-36** *[MPa]*	**UIT-5-36** *[MPa]*	**UIT-6-36** *[MPa]*
243	270	371340					
252	280	259716					
261	290	2875709	109914 63596	259529 99141	97593 48872	123721 88887	75393 129074
270	300	239161					
279	310	279312					
288	320	67551					
297	330	137354					
306	340	81052					
369	410	44493					

RESIDUAL STRESS

Measurements of residual stresses in both materials were carried out through the depth of the sample. There were two methods used to obtain residual stress values. The main method used was hole- drilling (previously described in **chapter IV**), and raw data from this method is given in **Appendix A5**, the other was the XRD (x-ray diffraction) method. Results of the hole-drilling method and XRD are shown below for Al 2024-T3, and residual stresses were computed with different methods mentioned in **chapter IV**. Residual stress data for Al 7150-T651 were only obtained from the XRD method. Stress plotted in the following figures are $(\sigma_{max} + \sigma_{min})/2$, where σ_{max} and σ_{min} are the principal values. The X-ray diffraction measurements were provided by Dr. C. Rodopoulos of Sheffield Hallam University, data was obtained for every depth variation removing material by machining and taking readings of XRD.

Al 2024-T3

As before mentioned there were different UIT specifications used on the surface of the material, and every UIT condition developed residual stresses on the surface and through the depth. Fig. 5.7 shows results from plates treated under condition UIT-1-27 using the Re-stress programme (provided by Vishay Company) and data obtained using MMH equation described in **chapter IV**. Fig. 5.7a shows data from two tests leaving the compressive residual stresses close to the surface within the rank of 160 and 220 MPa decreasing through the depth. Results obtained from MMH equation are shown in fig. 5.7b, where it can be seen that compressive residual stress left close to the surface are in the same rank as those in fig. 5.7a. The reduction of compressive residual stresses is faster through the depth according to MMH equation than results from Re-stress programme, the equilibrium balance of the internal stresses can not be seen either in fig. 5.7b but should be after 2 mm depth where tensile residual stresses are present in the treated material. In both figures it can be seen that the UIT-1-27 condition considerably affects the internal stress of the material leaving at 0.1 mm depth, close to the surface a compressive residual stress from 160 to 220 MPa.

Fig. 5.8 shows data obtained from UIT-1-36 condition using hole-drilling together with Re-stress programme and MMH equation. Fig. 5.8a shows five tests where four of them are close each other and the fifth one shows more compressive stresses. The compressive residual stresses left by UIT-1-36 condition at 0.1 mm depth from the surface is in the rank of 40 to 320 MPa and according to fig 5.8b at 1.1 mm depth tensile residual stresses can be present. In fig 5.8b it can be seen clearly with the aid of several tests there is an area enveloped where residual stresses due to that specific UIT condition can be found. In this graph plotted with values obtained from MMH equation the transition from compressive residual stresses left by the treatment to tensile residual stresses tend to be present in the bulk due to the internal balance of stress in the material.

In fig. 5.9 data points can be seen for three tests carried out on Al2024-T3 after UIT-2-36 treatment condition. Actually hole-drilling tests of material under treatment of this condition were not as many as previous treatment conditions. In fig 5.9 it can be observed that compressive residual stresses left on the material at 0.1 mm depth are within a small rank which is from 16 to 30 MPa, and then a small reduction through the depth is observed compared to the previous conditions. The MMH formula was not used in this batch because residual stresses level was too low compared to the last one. It is pointed out that before UIT treatment material was rolled and a possible compressive residual stress could exist near the surface, so the effect due to this UIT condition should be combined with the pre-existing residual stress from rolling to give the residual stresses obtained. Hole drilling tests were carried out on both sides of a plate treated under UIT-2-36 condition and data from these were computed and results are shown in fig. 5.9.

Fig. 5.10 shows two lines from two tests performed in a plate of Al 2024-T3 after being treated under UIT-3-36 condition, leaving residual stress that in one of them is around 23 MPa compressive, meanwhile in the other is around 3 MPa tensile. Comparing these results with previous graphs the effect of this kind of treatment is not much. The values of compressive residual stress are smaller than those obtained from UIT-2-36 which were considered negligible, so these values are within that range of UIT-2-36 and can be considered negligible too by the same reason.

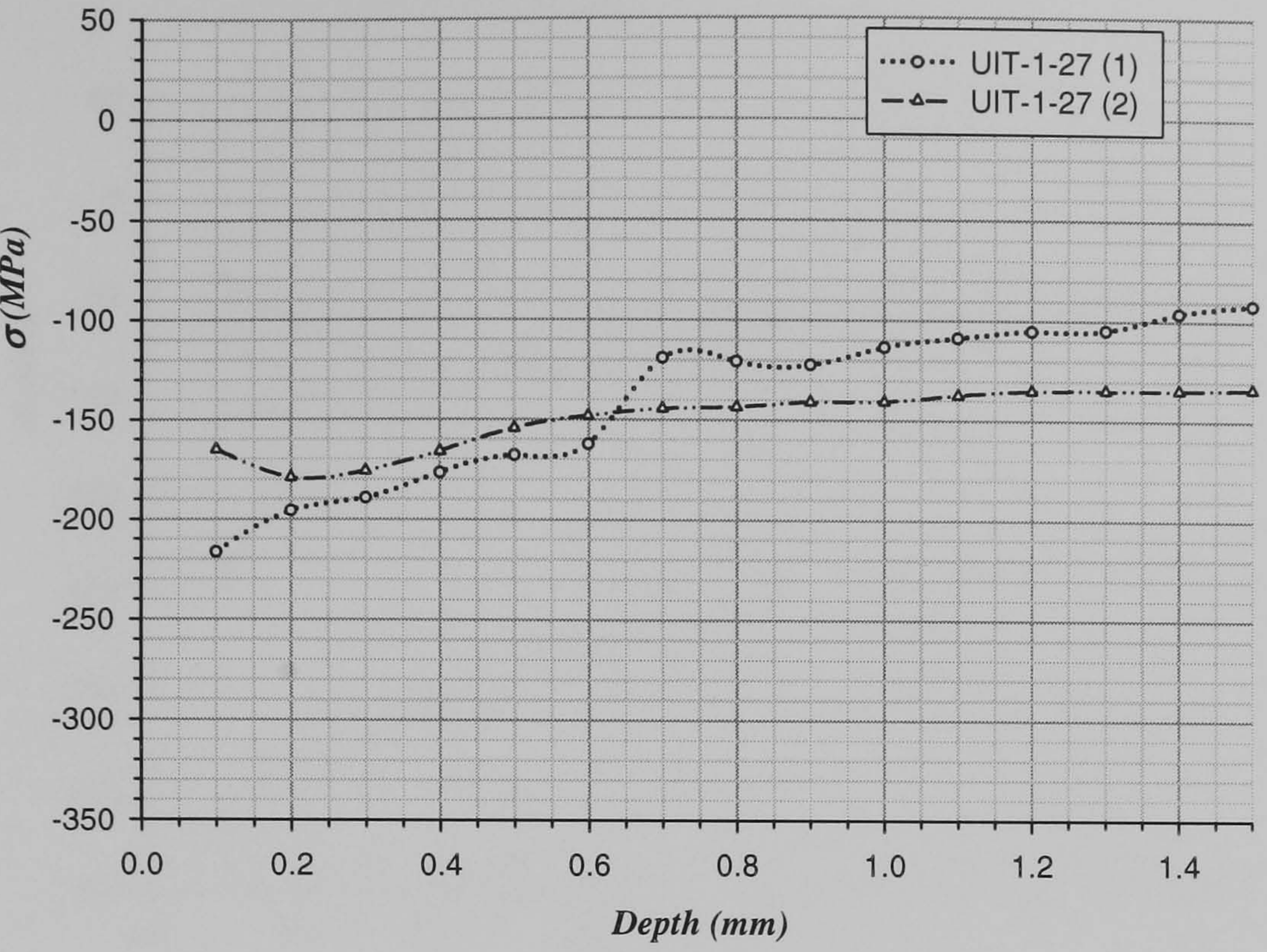

a)

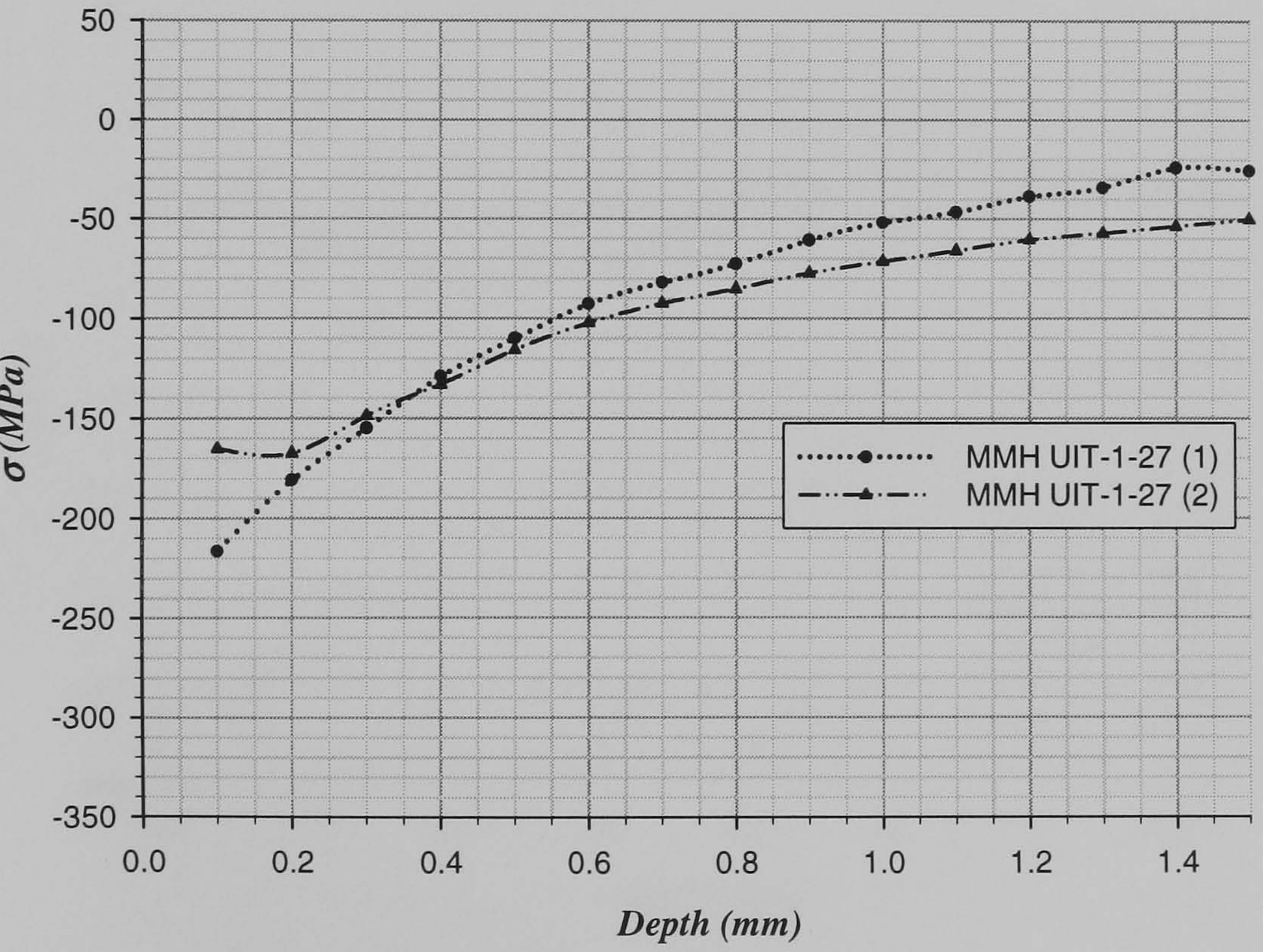

b)

Figure 5.7 a) Plot of two different tests in UIT-1-27 condition in Al 2024-T3 using Vishay programme "Re-stress. b) Plot from the two tests already shown in "7a" using MMH equation in order to get stress internal balance.

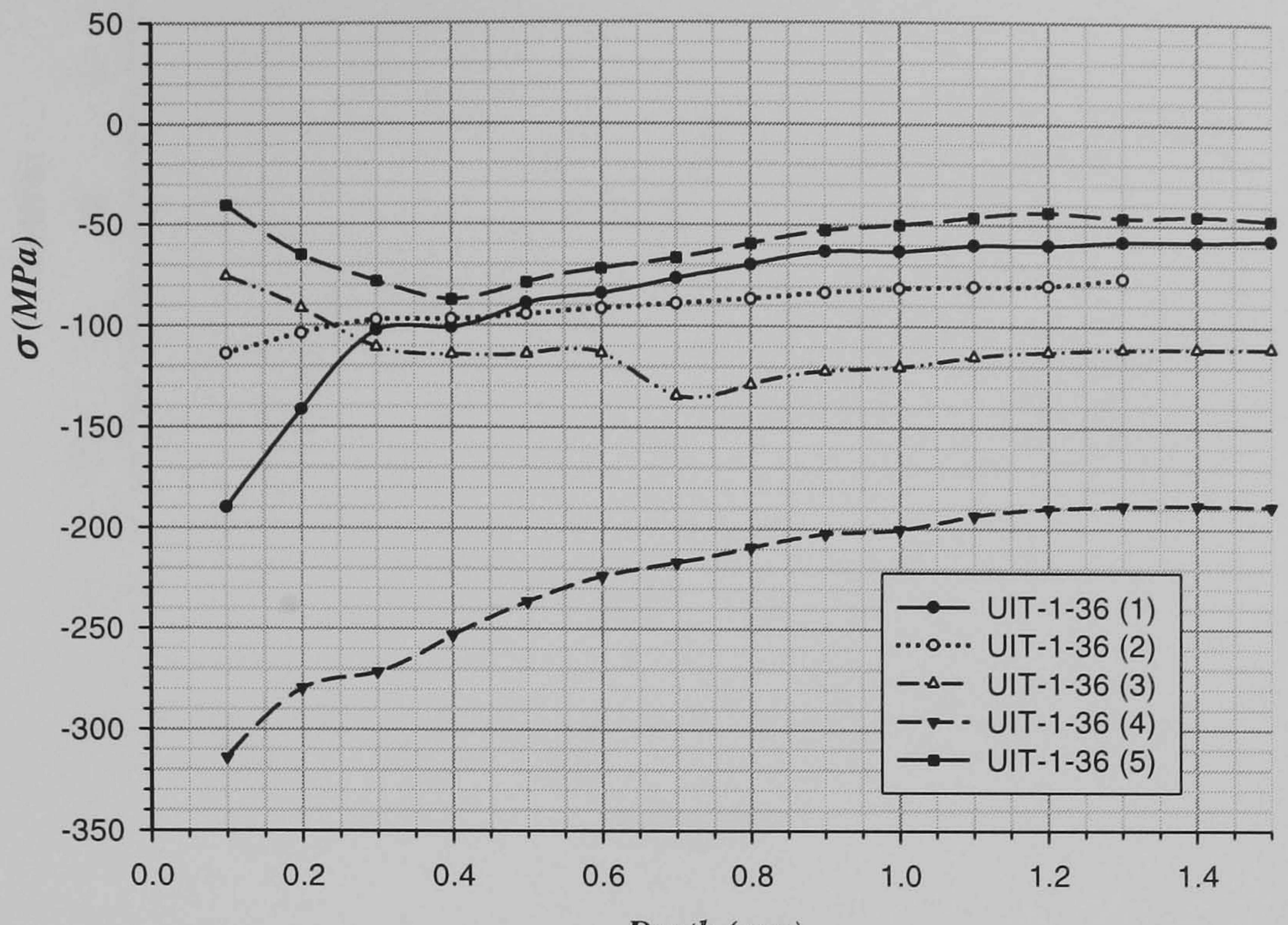

a)

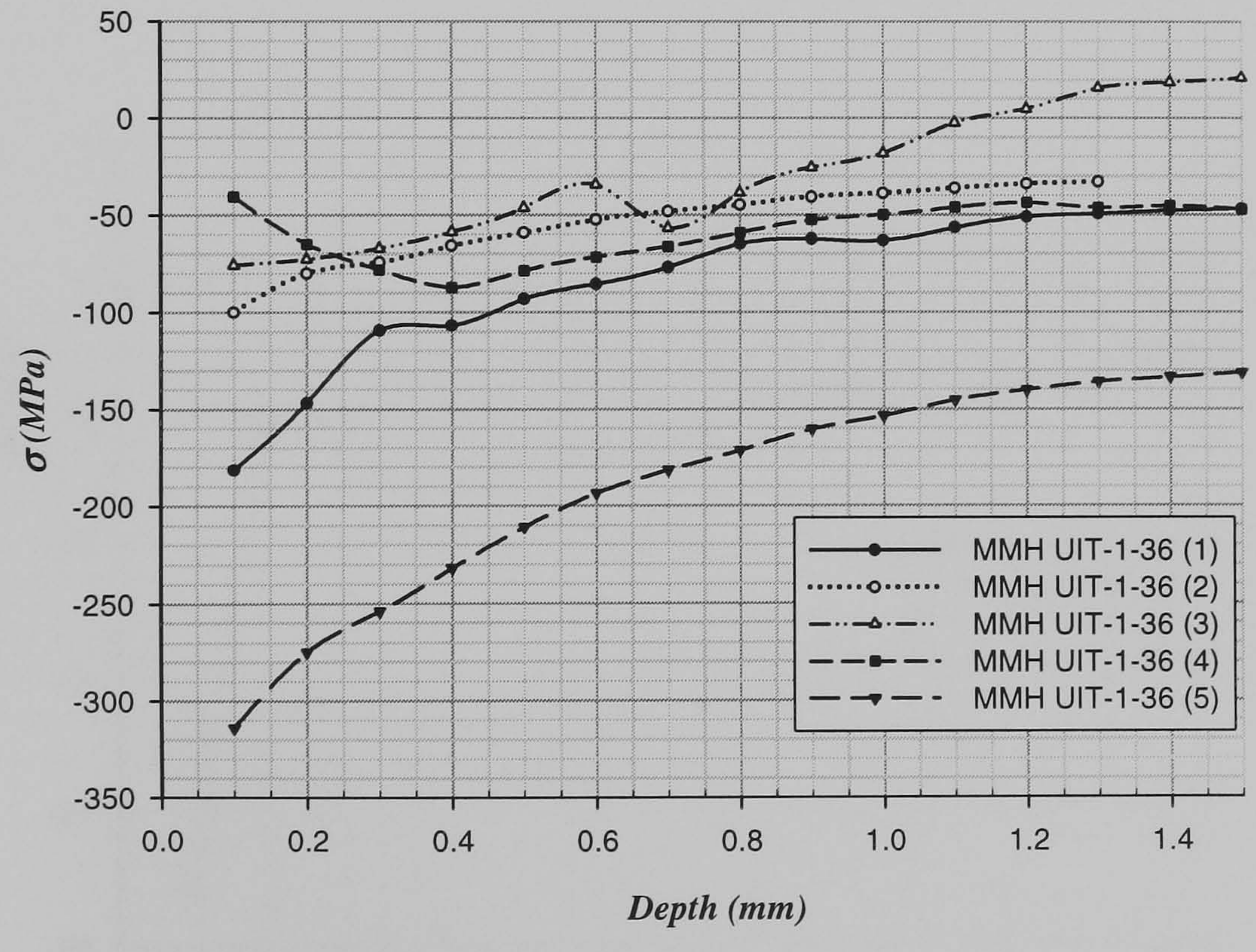

b)

Figure 5.8 a) Plot of five different tests of hole drilling obtained using Re-stress programme showing compressive residual stress left on Al 2024-T3 due to UIT-1-36 condition at 0.1 mm from the surface in the rank of 40 to 310 MPa and reducing through the depth. b) Plot showing the five tests included in fig. 5.8a analysed using MMH equation in order to get internal balance.

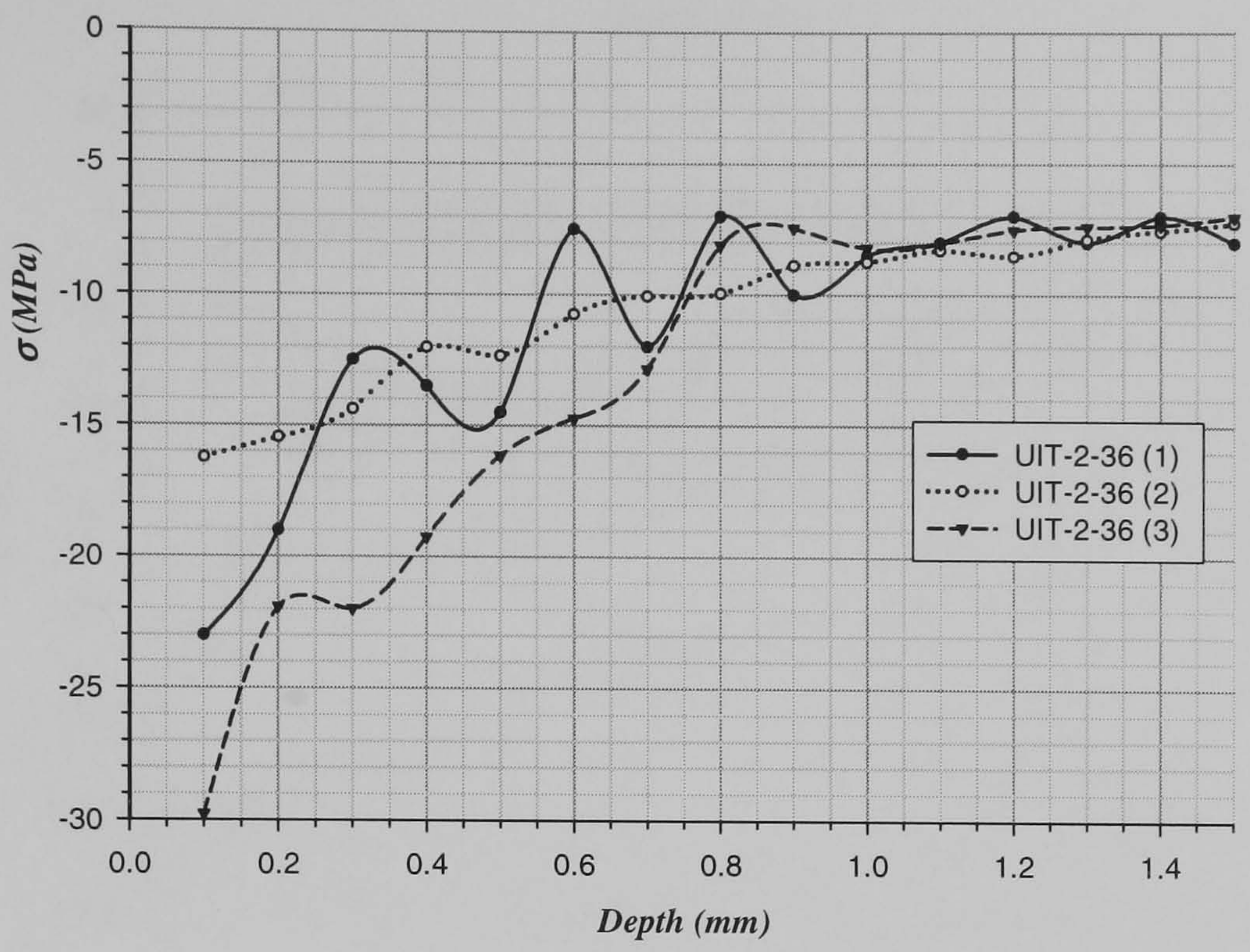

Figure 5.9 Graph of data obtained from hole drilling method of UIT-2-36 condition on Al 2024-T3. Here are shown three different tests where a rank of compressive residual stresses left closer to the surface at 0.1mm depth is within 16 to 30 MPa,

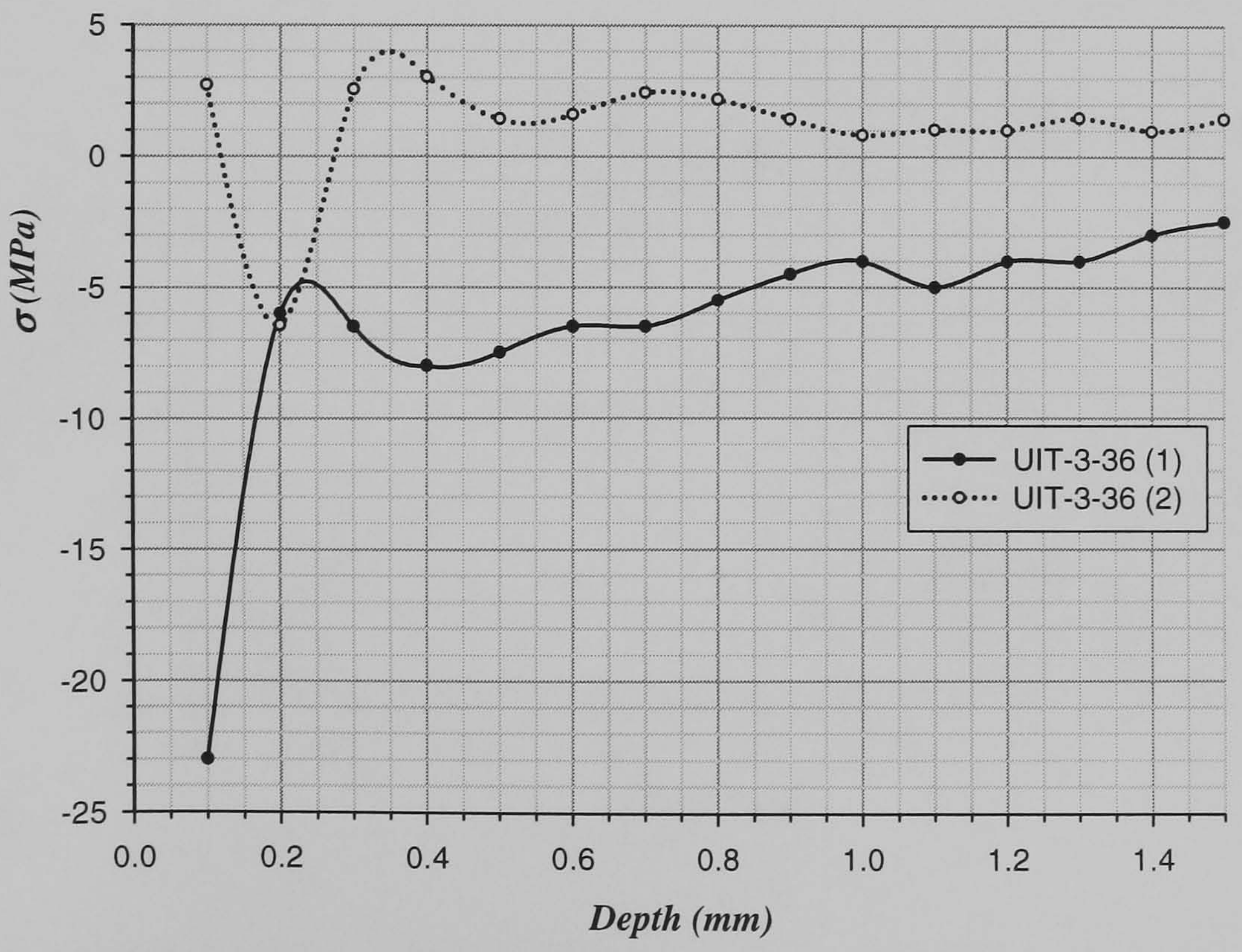

Figure 5.10 Plot of two hole drilling tests of Al 2024-T3 after UIT-3-36 condition showing a small compressive residual stress left close to the surface at 0.1 mm depth from the surface and then reduced though the depth.

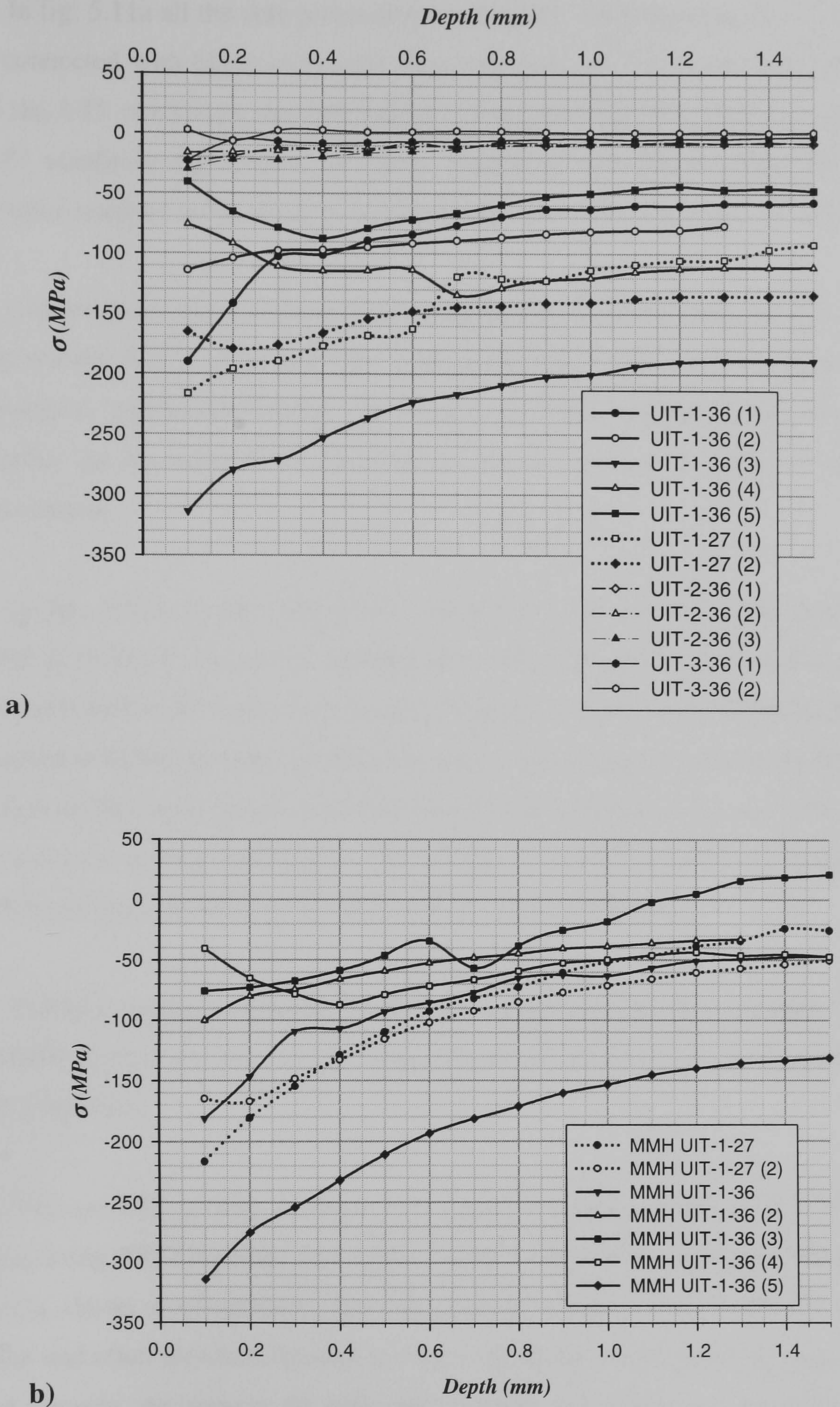

Figure 5.11 a) All UIT conditions on Al 2024-T3 plotted in this graph where can be compared among them and see the effect everyone has over the material according to Re-stress programme, b) UIT-1-27 and UIT-1-36 conditions obtained from MMH equation are plotted here, where the effect of every condition in the material through the depth is observed.

In fig. 5.11a all the data points from all the UIT conditions can be compared. Data points connected with black wide solid lines represent the UIT-1-36 condition, which is one of the UIT conditions that left higher compressive residual stresses together with UIT-1-27 condition represented by points connected with dotted lines, the maximum compressive residual stress obtained by these two conditions is around 320 MPa.

Compressive residual stress represented by black dashed lines and thin black solid line correspond to UIT-2-36 and UIT-3-36 conditions respectively. Comparing the last two conditions mentioned with the other two, it is evident that the former do not have as much effect on the material as the latter, as can be seen in the ranks of compressive residual stresses.

In fig. 5.11b all the data points from UIT-1-27 and UIT-1-36 conditions are presented as in fig. 5.11a, but as before points were considered to show the equilibrium balance presented in the bulk due to residual stresses. The graph is different showing that compressive residual stresses in the first point at 0.1 mm depth are similar to those obtained from Re-stress programme but compressive residual stress decrease faster than those from hole drilling technique. An envelope of residual stresses is generated where data points can appear due to UIT-1-27 and UIT-1-36 conditions.

Residual stresses obtained by XRD technique are shown together with results using MMX method in order to show the balance of residual stresses through the depth after UIT treatment.

Figures 5.12 a and b show two graphs obtained from UIT-1-27 treatment condition using XRD readings and MMX method which uses data obtained from XRD. Fig. 5.12a shows a comparison between residual stresses before UIT-1-27 treatment condition and after. Residual stresses in bare material are nearly zero; close to the surface residual stresses are around 10 MPa and through the depth are negligible. Residual stresses after UIT-1-27 treatment compared to those obtained from bare material exhibit bigger compressive residual stresses and the values at the surface are around 200 to 230 MPa. After UIT-1-27 condition treatment values in compressive residual stresses increase around 190 to 210 MPa generally.

Fig. 5.12b shows both data XRD and MMX from UIT-1-27 treatment condition. Here can be seen the early appearance of tensile residual stress at greater depths, around 1.3 mm, after using the MMX method. However the straightforward XRD data does not show any tensile stress, even on the plate centre line at 2.5 mm depth. Since tensile stress must exists at the centre of the plate to balance the surface compressive residual stresses after UIT-1-27 described by MMX lines are more reasonable than the XRD lines. Although the residual stresses on the surface are the same for XRD and MMX, the values of these diverge from each other through the depth. Dotted lines represent XRD data and black solid lines represent MMX values reaching a maximum tensile residual stress of around 160 MPa.

Fig. 5.13 shows, similar to fig. 5.12, data obtained from both techniques where in fig. 5.13a a comparison between bare material data and UIT-1-36 condition data can be observed. Data from material treated after UIT-1-36 condition give information of residual stress on the surface being around 150 to 170 MPa. These values are closed to those obtained by UIT-1-27 condition. Residual stresses profile obtained by XRD due to UIT-1-36 is interesting because after the surface compressive residual stresses tend to reduce, but after 0.1 mm depth start to increase up to a maximum value of 200 MPa at 0.4 mm depth and then tend to reduce again.

Fig. 5.13b shows both graphs obtained by XRD and MMX methods and can be compared in the same way as in figure 5.12b. There are two XRD tests represented by dashed lines which indicate that tensile residual stresses are just about present but insignificant after 2.25 mm depth which it is not totally credible because there is no equilibrium tension and compression. Using the MMX method which is represented by solid black lines indicates the most likely profile of residual stresses through the depth, and a much more credible one. They indicate that tensile residual stresses starts at around 1.25 mm depth getting a maximum tensile residual stress of around 125 MPa before the middle of the plate thickness, indicating an asymmetric profile of residual stresses due to the treatment of the two surfaces at different times.

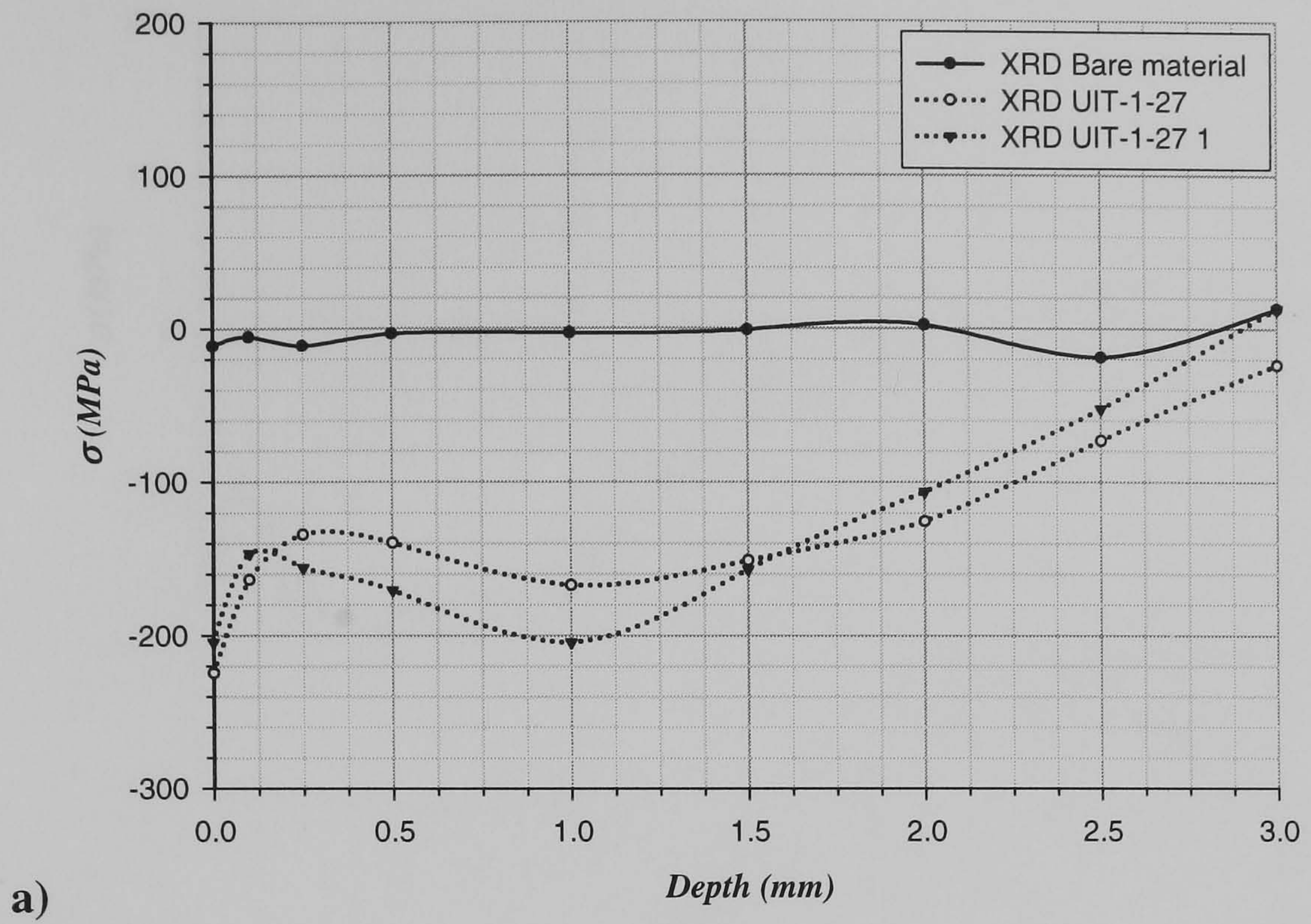

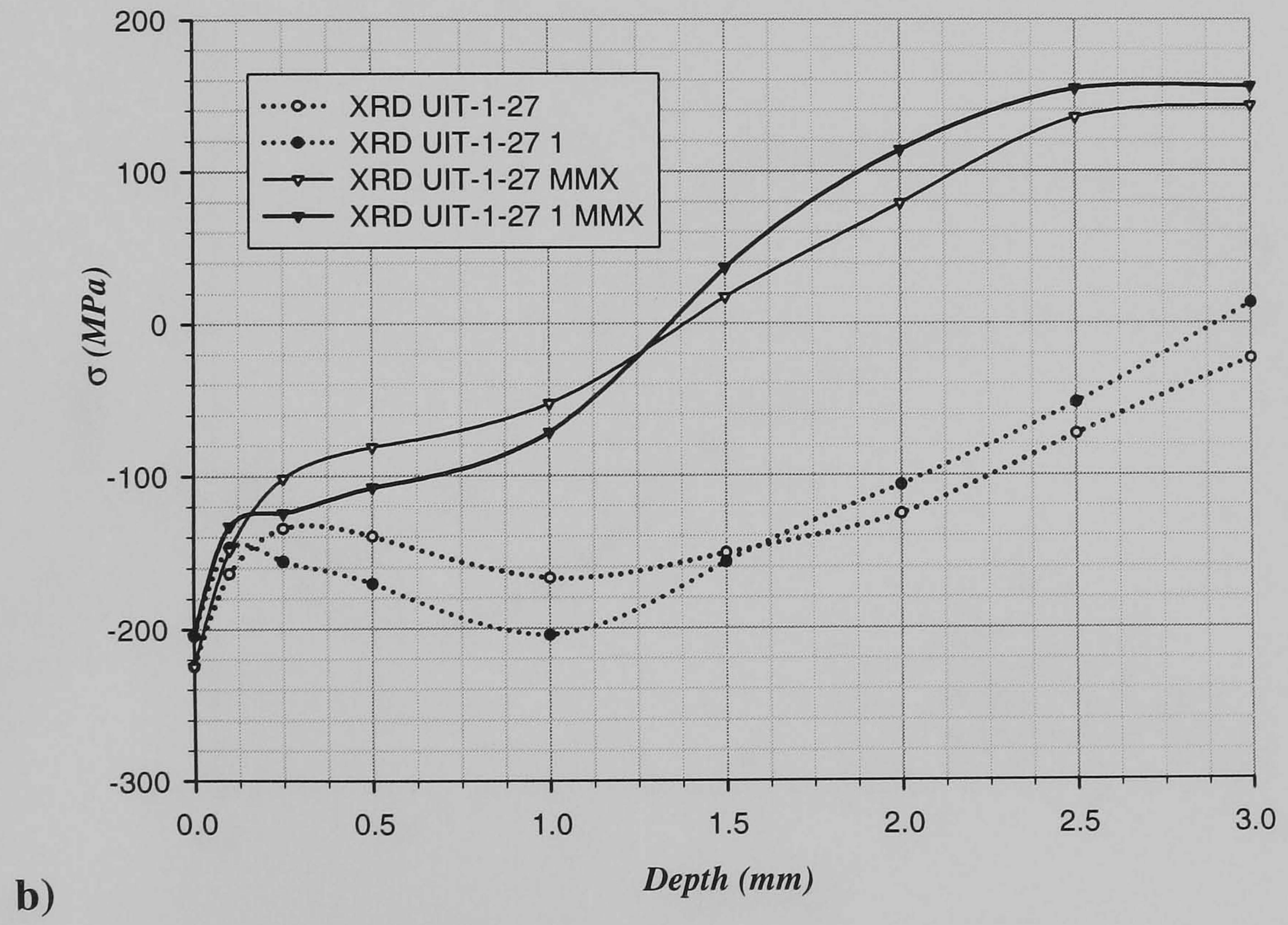

Figure 5.12 a) Residual stresses obtained by XRD (X-ray) method at different depth through the thickness for bare material and after UIT-1-27 condition on Al 2024-T3. b) Comparison between residual stresses obtained by XRD method and MMX method.

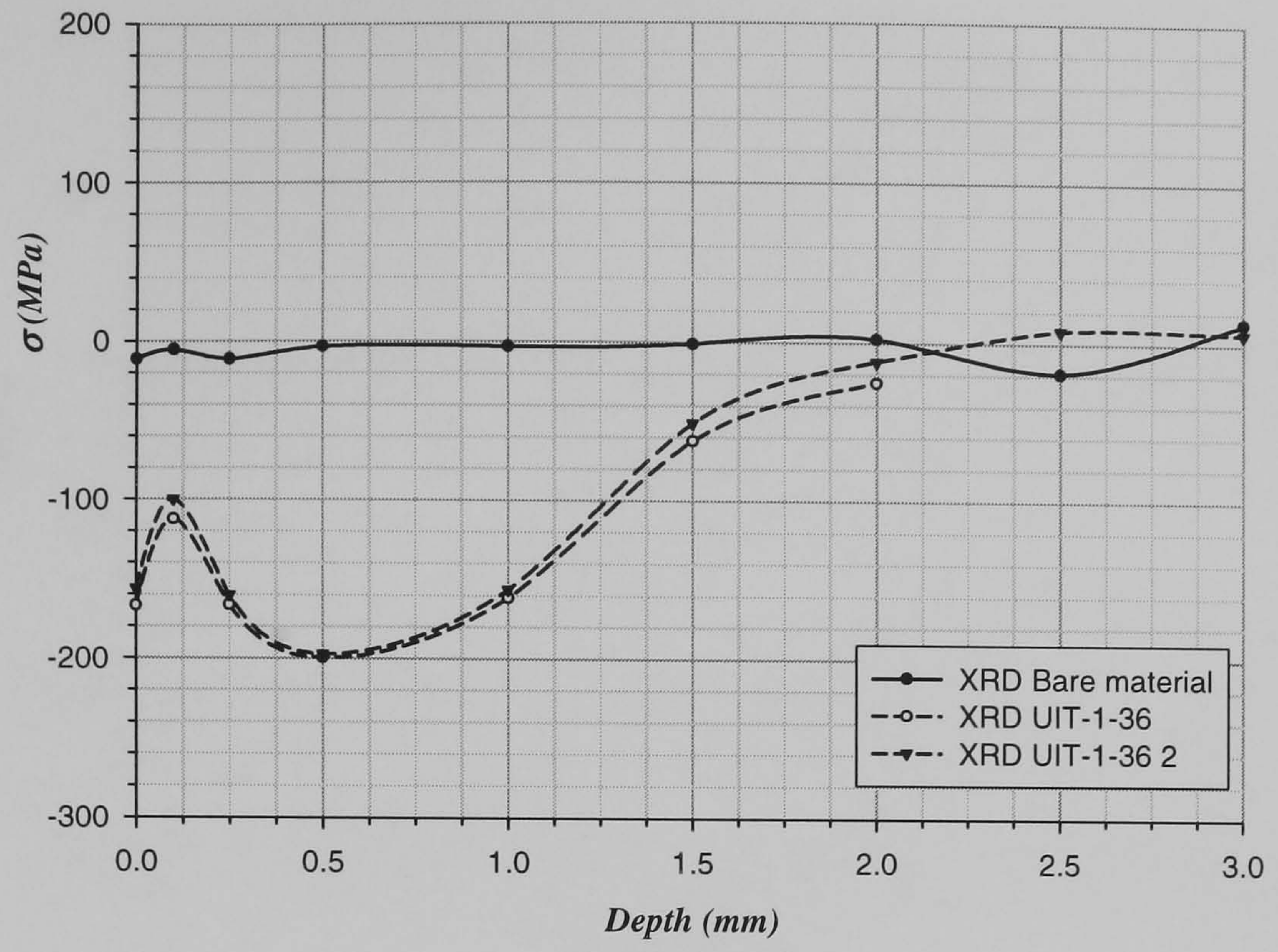

a)

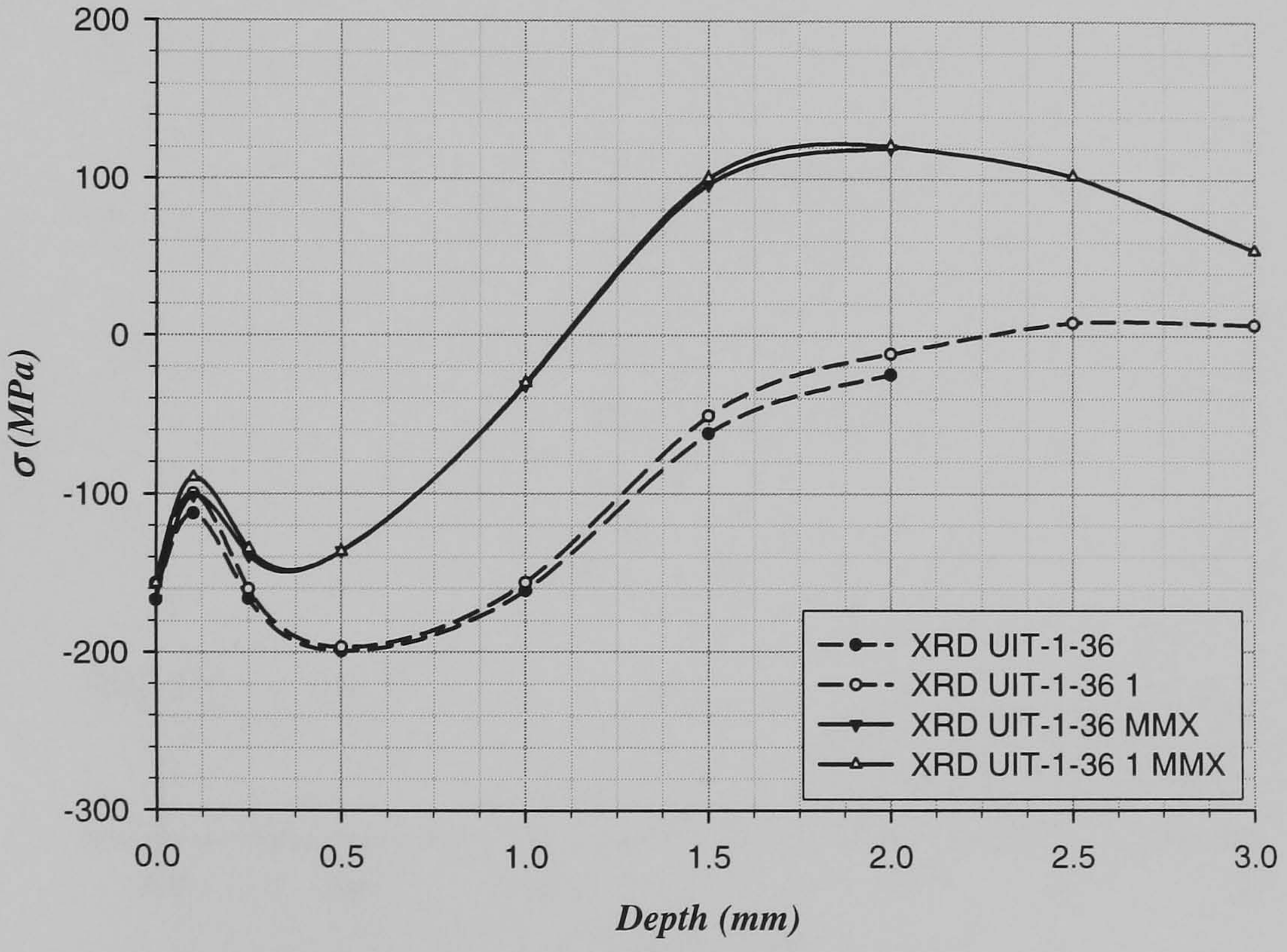

b)

Figure 5.13 a) Residual stress obtained by XRD method through the thickness before and after UIT-1-36 treatment condition. b) Data obtained from XRD technique and using MMX method after UIT-1-36 treatment condition in Al 2024-T3 aluminium alloy.

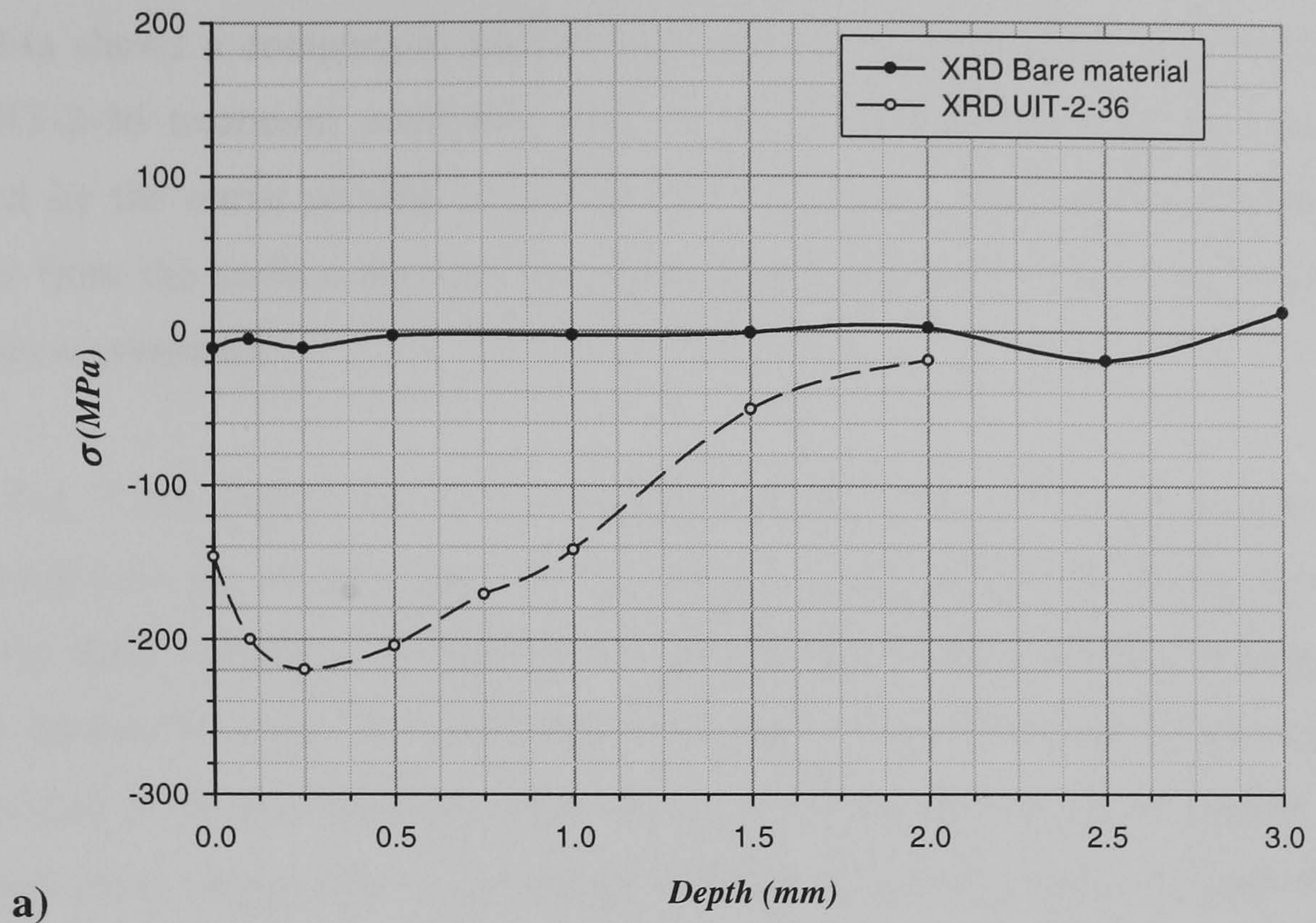

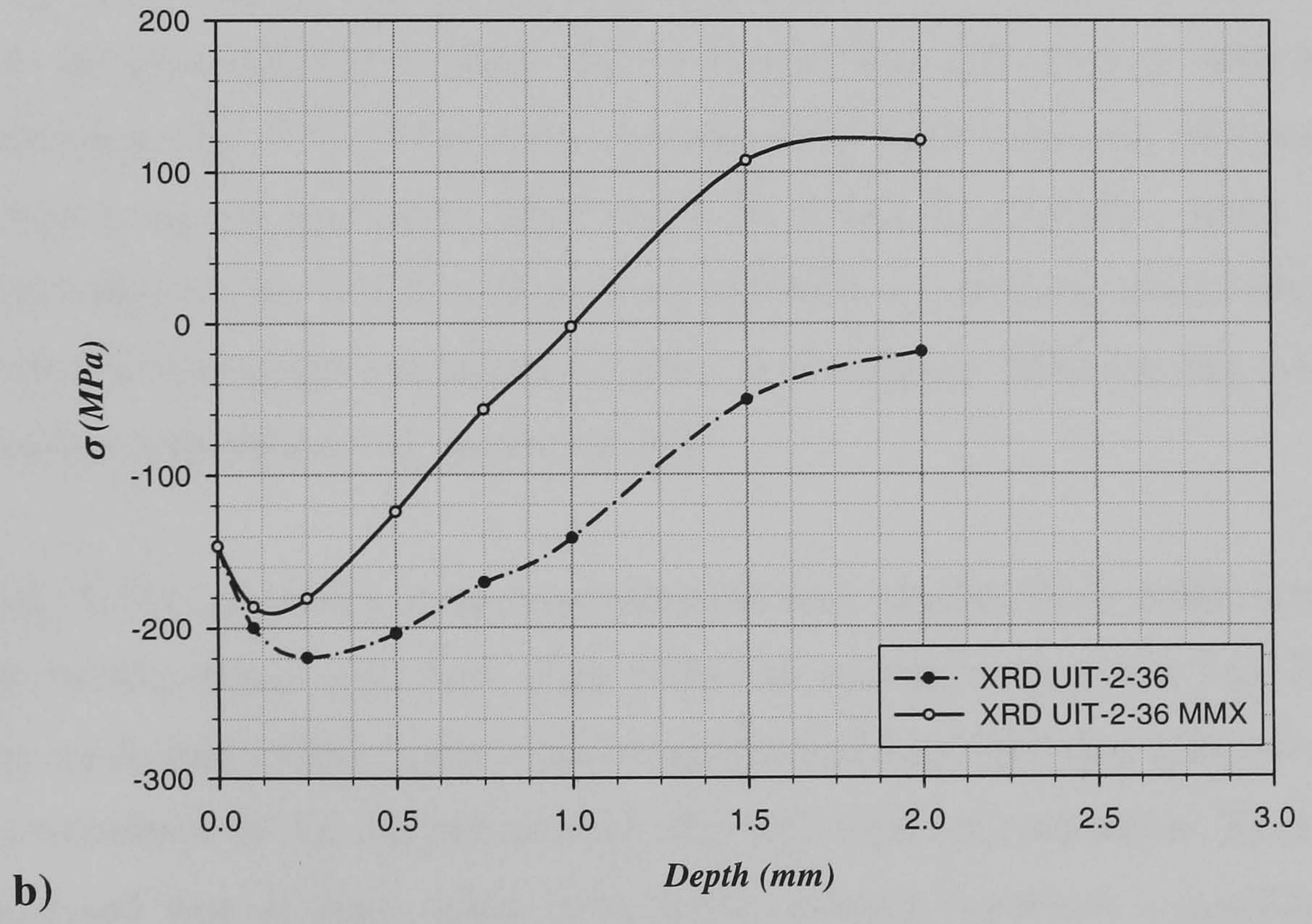

Figure 5.14 a) Plot of residual stress obtained by the aid of XRD technique from a plate after UIT-2-36 treatment condition in Al 2024-T3. b) A comparison between residual stress results obtained by XRD and MMX method from a plate after UIT-2-36 treatment condition.

Fig. 5.14 shows results from UIT-2-36 treatment conditions in Al2024-T3 alloy. Fig. 5.14a shows a comparison between data obtained from bare material and material after UIT-2-36 treatment condition with the aid of the XRD technique. The pattern followed by the curve created by the data points shows compressive residual stresses increase from the surface through the depth up to around 0.25 mm depth, after that a reduction is presented.

Fig. 5.14b shows the results of data obtained from XRD and MMX methods which both have the same pattern. In this treatment data up to 2mm depth was obtained where for XRD technique, dashed line, until that depth tensile residual stresses are not present. Meanwhile from the MMX data, solid black line, tensile residual stresses start at around 1mm depth and obtaining a maximum tensile residual stress of around 120 MPa near 2mm depth suggesting an asymmetric pattern of residual stress balance due to the treatment of the plate on both sides at different times.

Fig. 5.15 shows data points obtained from plates after UIT-3-36 treatment condition and are compared to those data obtained from bare material with the aid of XRD technique. Fig. 5.15a shows data obtained from XRD technique from two plates, one without treatment and other after UIT-3-36 treatment condition, where one may observe an influence due to UIT treatment. At 100 MPa, this is the smallest residual stress level of all UIT treatments investigated. Table 5.3 of **chapter III** shows this corresponds to the smallest amplitude of 10 microns in UIT.

Fig. 5.15b shows the comparison between data obtained from XRD, chain dotted line, and MMX, black solid line, after UIT-3-36 treatment condition. As in the last treatment conditions, in this figure it can be appreciated that XRD data does not show any tendency to balance of residual stresses left after UIT treatment conditions. The maximum depth analysed was at 2mm. Data from MMX method can show a sensible balance through the depth of residual stresses, suffering a transition between compressive to tensile residual stresses at around 1mm depth and a maximum tensile residual stress of around 60MPa at 2mm depth.

Fig. 5.16 shows all the graphs plotted together using XRD technique and MMX method. Fig. 5.16a shows the data obtained by XRD technique after all the treatment used in Al 2024-T3, the black solid line represents the condition of the material before applying UIT treatment, where just one test was carried out. The rest of the curves represent residual stress state after UIT treatment and can be seen that for every treatment condition the internal stress state is affected in different amounts. The UIT-3-36 condition had the lowest compressive residual stresses compared with the rest of the UIT treatment conditions, and UIT 1-27 shows the higher penetration of stress, corresponding to the highest amplitude of UIT at 22 microns.

UIT-1-36 and UIT-1-27 treatment conditions showed an interesting path in the residual stresses left through the depth having a specific amount of residual stress at the surface and then through the depth they were decreasing up to a specific distance and then increase again even more than the stresses acquired at the surface, as in the case of UIT-1-36 treatment condition the highest stress internally. This unusual response indicates that enhanced stress levels are obtained when removing layers of materials, due to plastic bending as residual stresses are released. Therefore the revised calculation of XRD stress is necessary to include the contribution of plate bending. Considering residual stresses left on the surface UIT-1-27 condition has more effect followed by UIT-1-36 and UIT-2-36 conditions.

Fig.5.16b shows data obtained after different UIT treatment using MMX method, and where the profile obtained of the first 0.25mm is quite similar to that using XRD technique. Here the transition between compressive residual stresses to tensile residual stresses is observed in the earlier depth. The highest compressive residual stresses were obtained by UIT-1-27 treatment on the surface or close to the surface having as well the highest tensile residual stress though the depth. The balance of residual stresses though the depth is more sensible in this graph for all the UIT conditions. Treatments UIT-1-36 and UIT-2-36 have almost the same magnitudes of residual stresses after 0.5 mm depth.

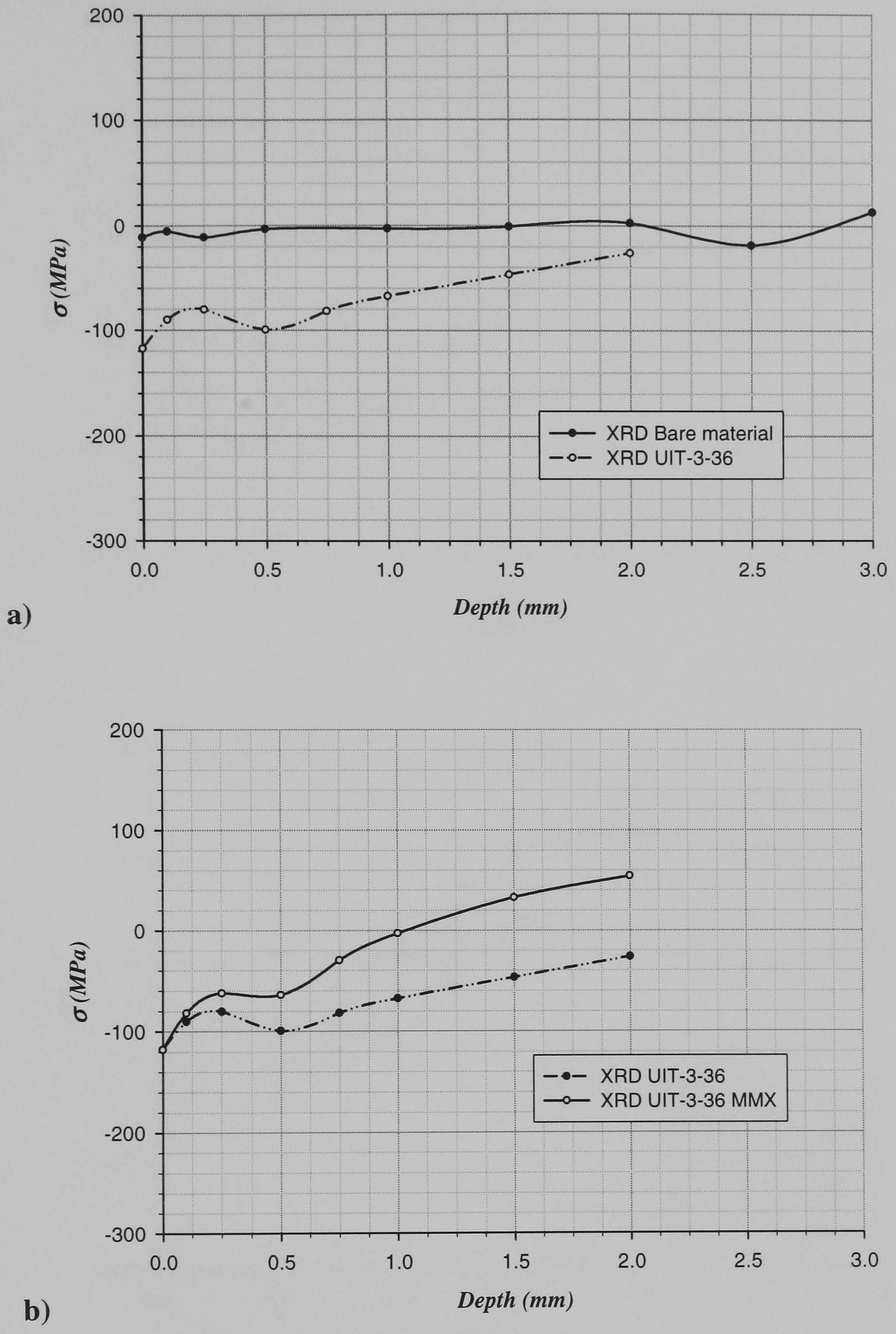

Figure 5.15 a) Data points obtained from plates before and after UIT-3-36 treatment condition on Al 2024-T3 plotted in a graph stress Vs depth with the aid of XRD technique. b) Comparison between data obtained from XRD and data obtained from MMX method after UIT-3-36 treatment condition.

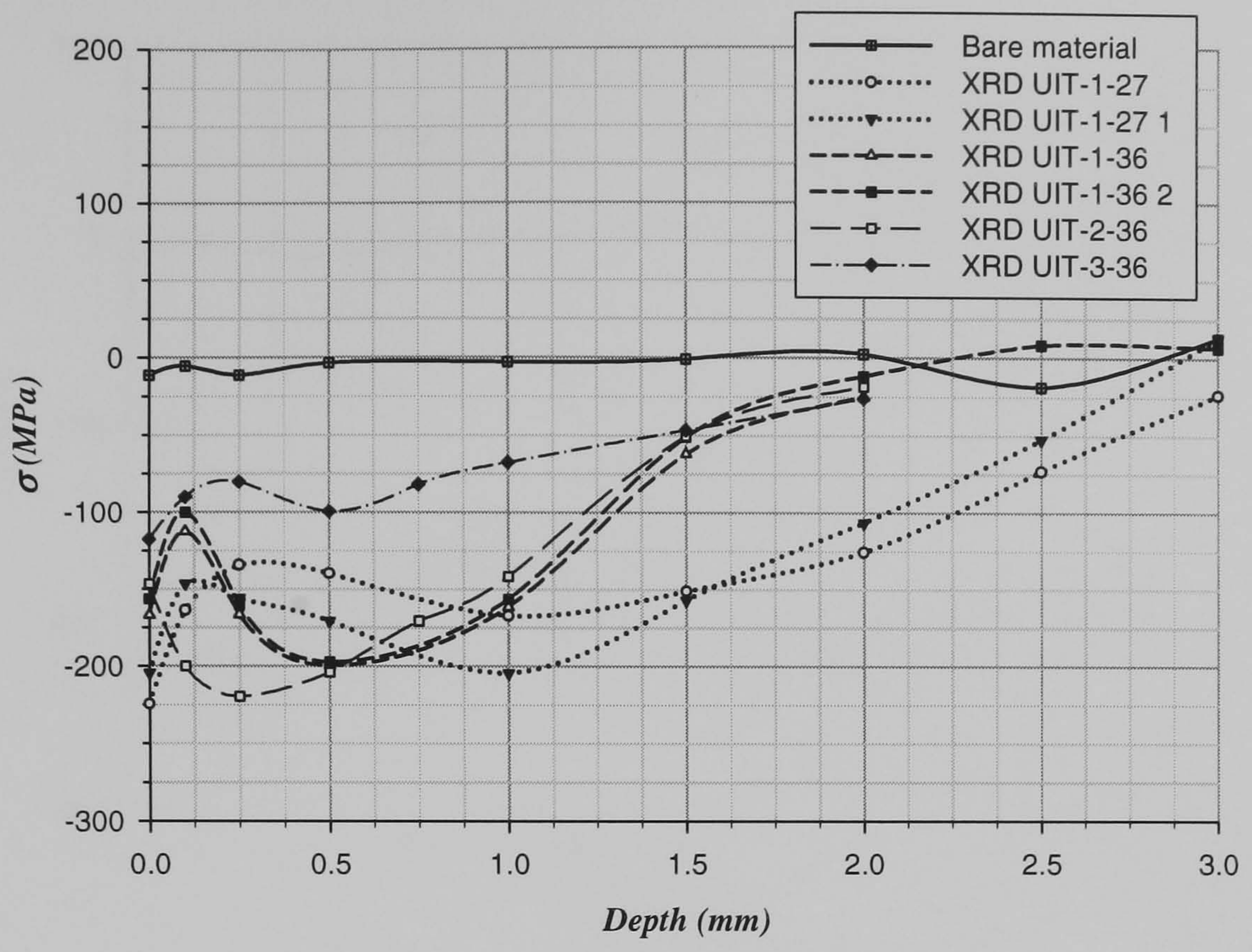

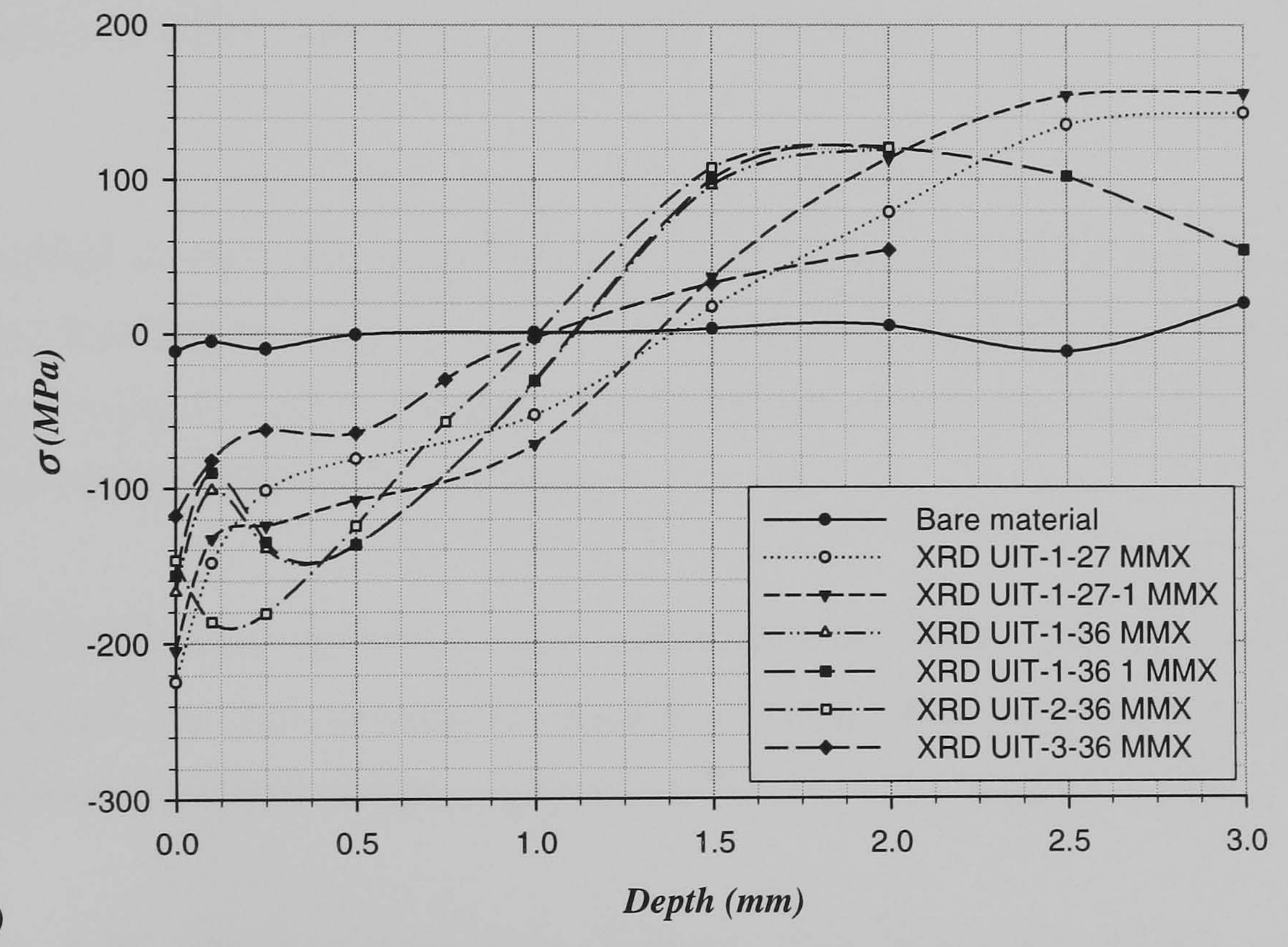

Figure 5.16 a) Plots of all UIT conditions in Al 2024-T3 obtained from XRD technique are represented here in this graph and can be compared each other. b) All UIT conditions data obtained with the aid of MMX method are plotted and can be compared each other.

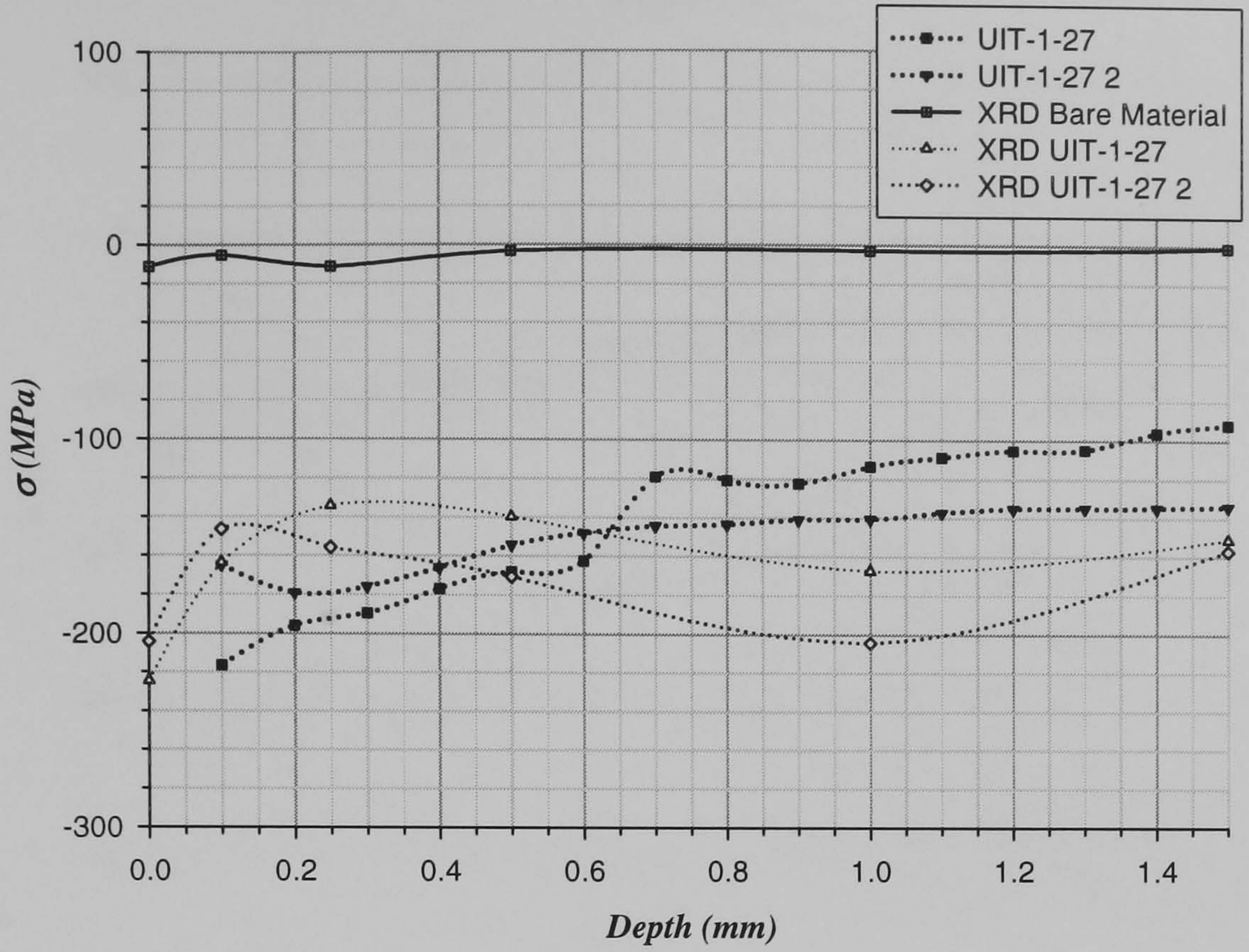

Figure 5.17 Comparison between data obtained by hole-drilling technique using Re-stress programme and XRD technique in Al 2024-T3 after being treated by UIT-1-27 condition.

Residual stresses obtained from the XRD technique were compared to those obtained by hole-drilling technique. Fig. 5.17 shows the data plotted and compared to bare material using the XRD technique and data obtained from the hole-drilling method from Al 2024-T3 after UIT-1-27 treatment.

The comparison between values obtained from XRD and the hole-drilling technique shows that are quite similar describing a rank where residual stresses for that specific treatment can be developed, this rank of values can be taken as scatter.

Fig. 5.18 shows a comparison between data from hole-drilling and XRD techniques used in Al 2024-T3. XRD data appears within the zone enveloped by the values acquired by 5 test of hole-drilling. Hole drilling data except from one test says that compressive residual stresses close to the surface, specifically at 0.1 mm depth, are between 40 and 180 MPa, where data is obtained from XRD. After 0.2 mm depth the variation between the big group of data from hole drilling and the one obtained by XRD increase. The XRD data fell within the scatter of the hole drilling technique.

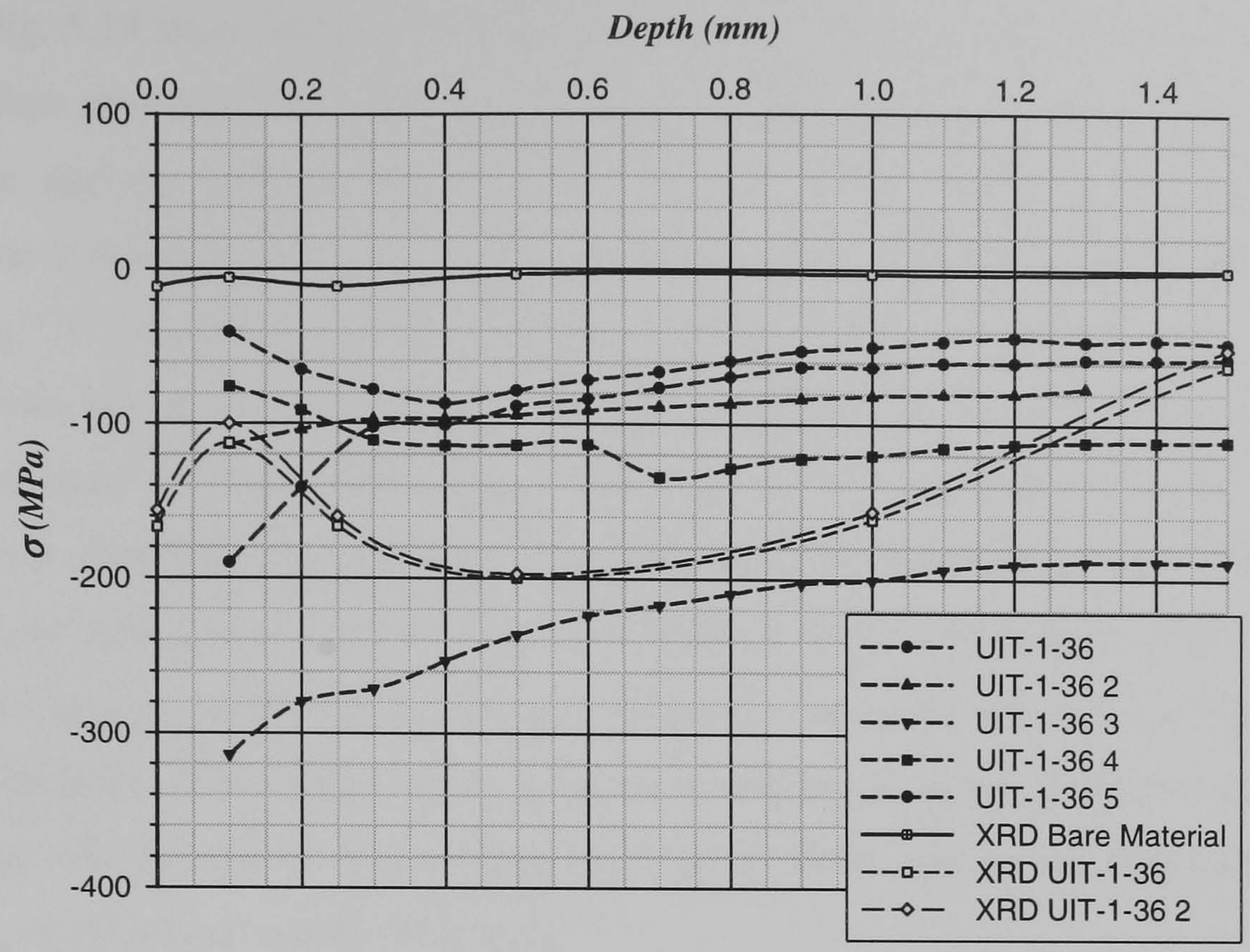

Figure 5.18. Comparison between data obtained from XRD and hole drilling from Al 2024-T3 after UIT-1-36 condition and bare material.

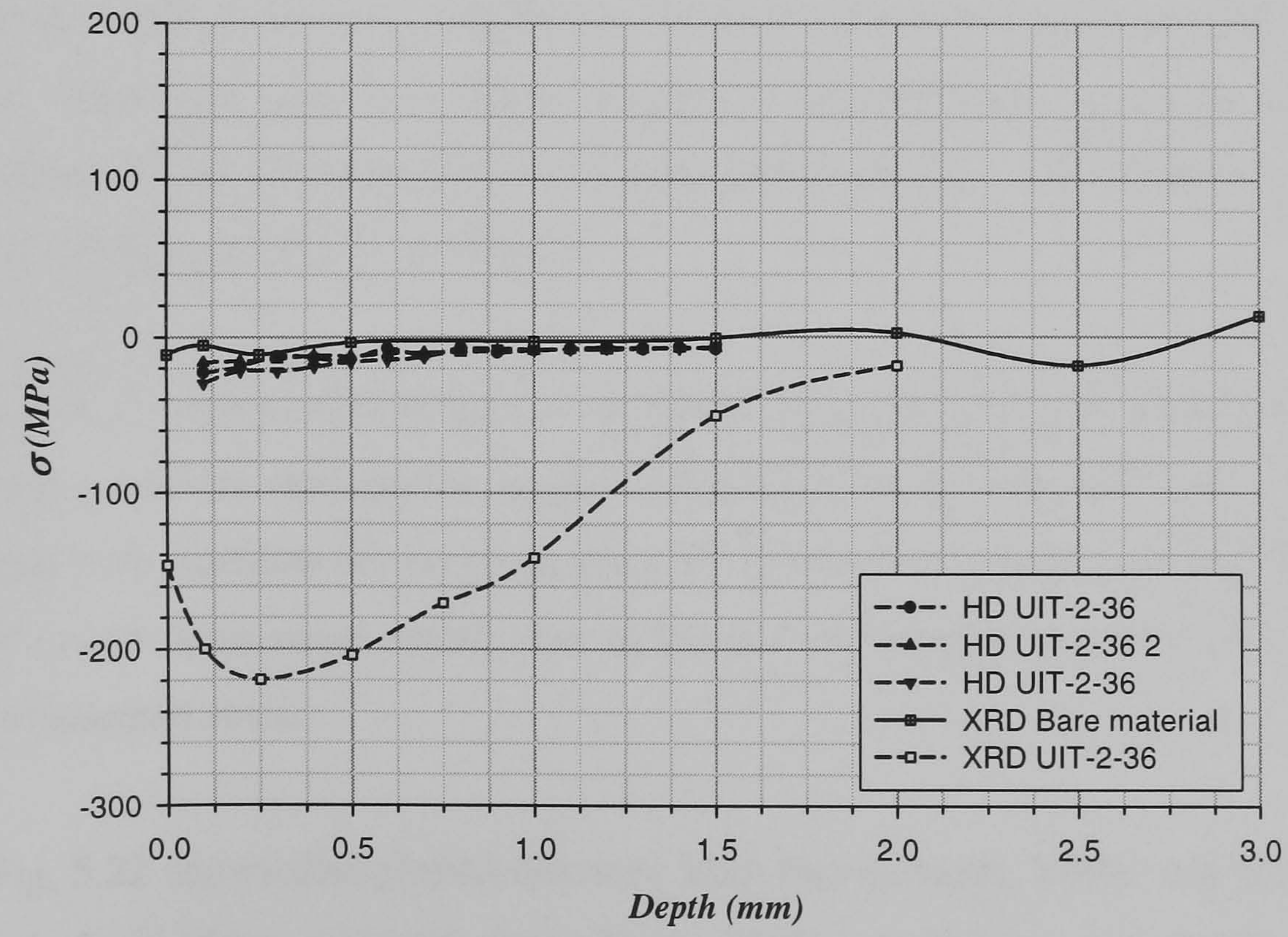

Figure 5.19 Data comparison obtained by hole drilling technique and XRD technique from Al 2024-T3 after UIT-2-36 condition.

Fig. 5.19 shows data points of residual stresses obtained from a bare material and from a plate after UIT2-36 treatment condition with the aid of two techniques, the XRD technique and the hole-drilling technique. As it can be seen from the figure a big difference in residual stress is obtained from XRD and hole-drilling technique from this particular UIT condition. The black solid line represents the pattern obtained from data points taken from bare material where negligible compressive residual stresses exist. Data points acquired from the hole-drilling technique pointed out that compressive residual stresses left after UIT-2-36 treatment condition are close to those before the treatment, but on the other hand XRD technique says that compressive residual stresses left by UIT-2-36 condition can not be negligible having a difference between values at 0.1 mm depth of around 160 MPa. From hole-drilling technique compressive residual stresses closer to the surface are the maximum and are around 10 to 40 MPa, meanwhile from XRD at that depth residual stress is around 200 MPa.

Fig. 5.20 shows as a comparison between data obtained from the hole-drilling technique and XRD in a material treated under UIT-3-36 condition. As in UIT-2-36 condition, here can be seen the same behaviour of the data obtained which results in a big difference in stress levels. In the graph it can be seen that from hole-drilling technique data indicates that almost no compressive residual stresses are obtained after UIT-3-36 condition, meanwhile data from XRD suggest the contrary that significant compressive residual stresses are left after UIT-3-36 treatment condition. The difference here at a depth of 0.1 mm is around 70 or 90 MPa.

Fig. 5.21 shows data obtained from MMH and MMX methods used in order to get residual stress balance through the depth in Al 2024-T3 alloy after UIT-1-27 condition. It is clear that both methods converge on one path followed by residual stresses through the depth, of course with some scatter, but at the end of the day both tend to indicate the balance of residual stress.

Fig. 5.22 shows data plotted obtained from two methods, MMH and MMX, which are based from data acquired from hole drilling technique and XRD technique respectively from Al 2024-T3 after being treated under UIT-1-36 condition. Both methods are within a similar range of residual stresses for the first millimetre depth, except for one test obtained from MMH method which gave more compressive results.

After 1 mm depth the two methods seem to diverge, but the MMX results tend to converge to produce the balance of residual stresses through the depth.

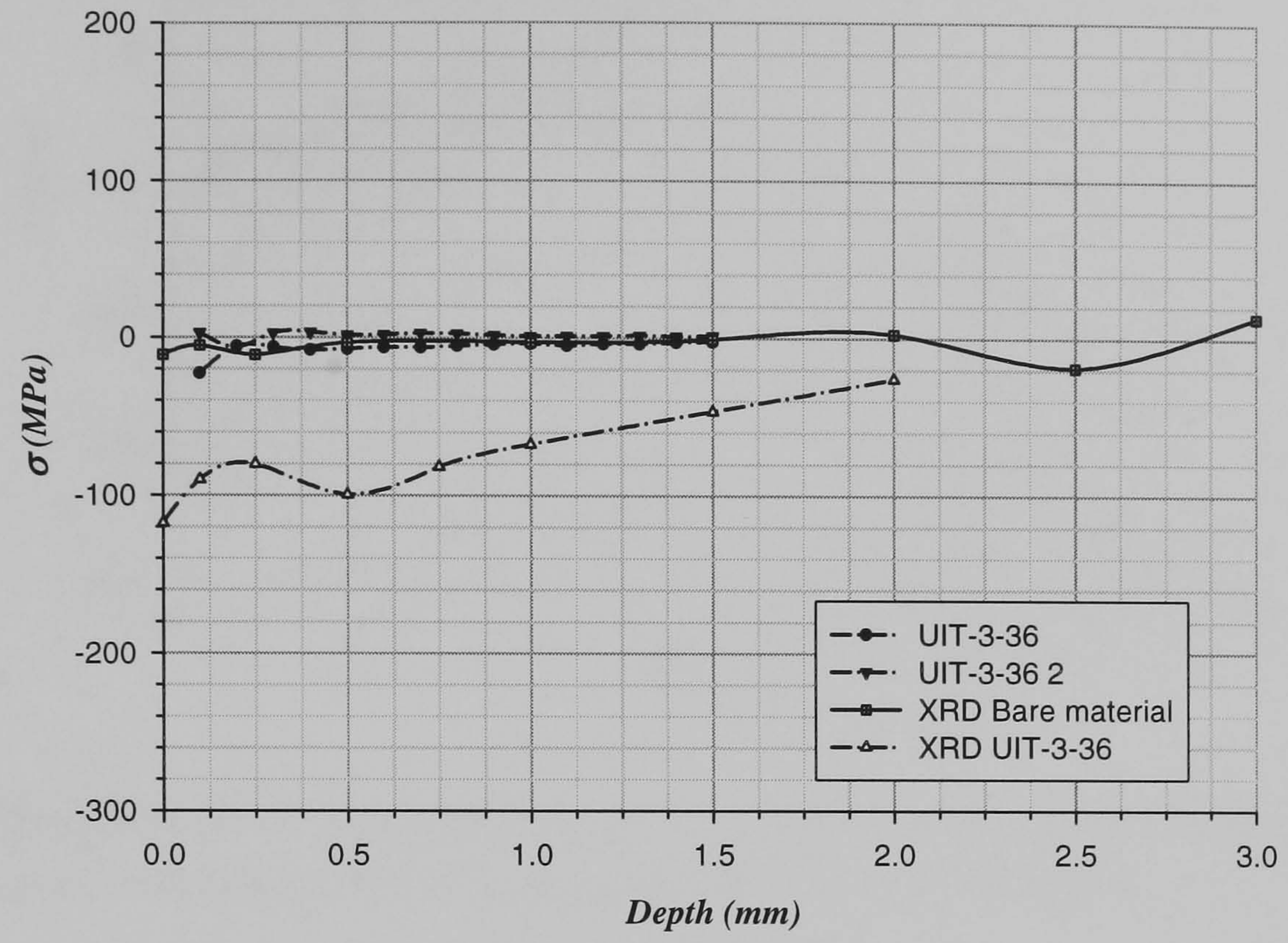

Figure 5.20 Data plotted from XRD and hole drilling techniques use to obtain residual stresses from Al 2024-T3 alloy before and after UIT-3-36 condition.

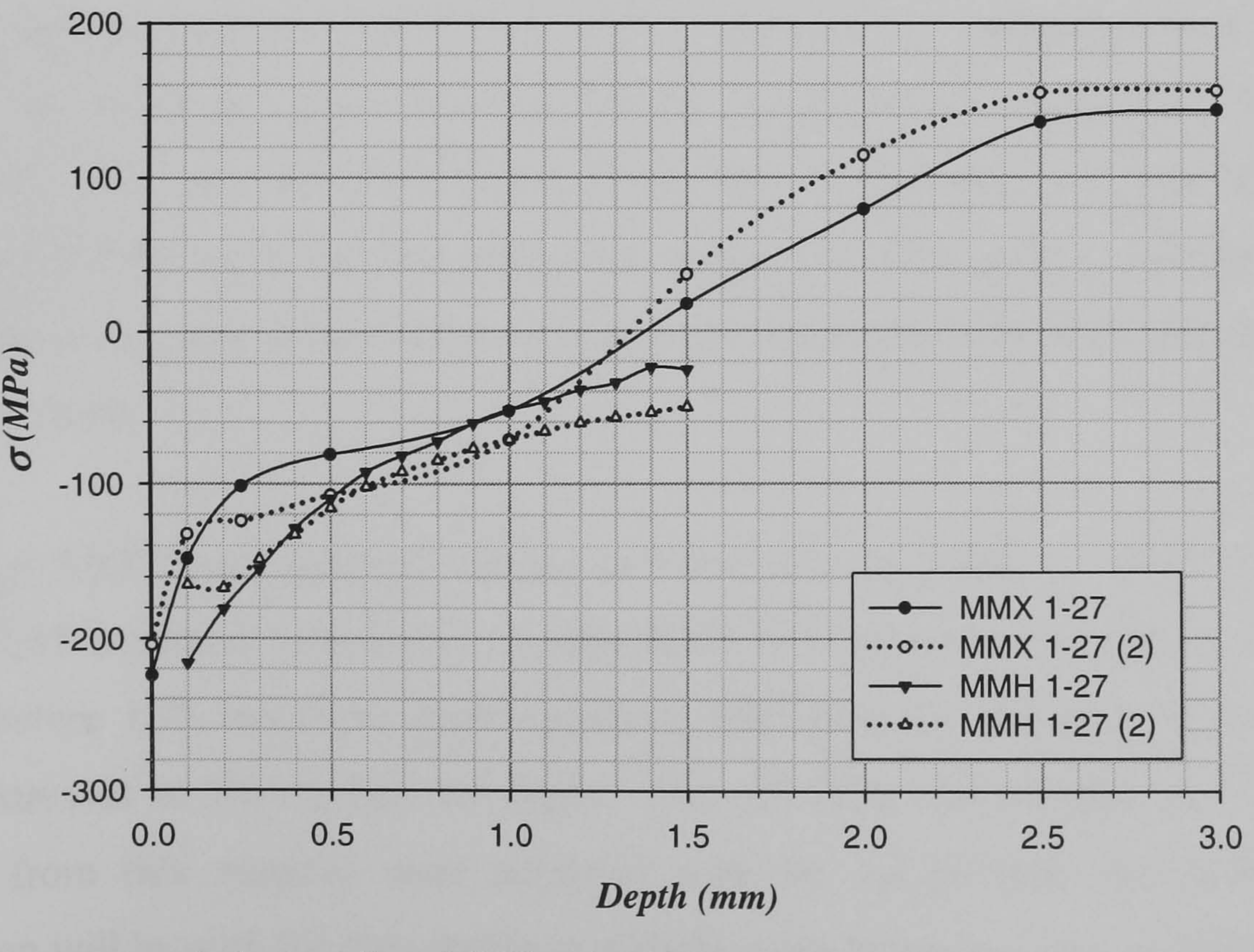

Figure 5.21 Data plotted obtained from MMH and MMX methods from Al 2024-T3 alloy after UIT-1-27 condition.

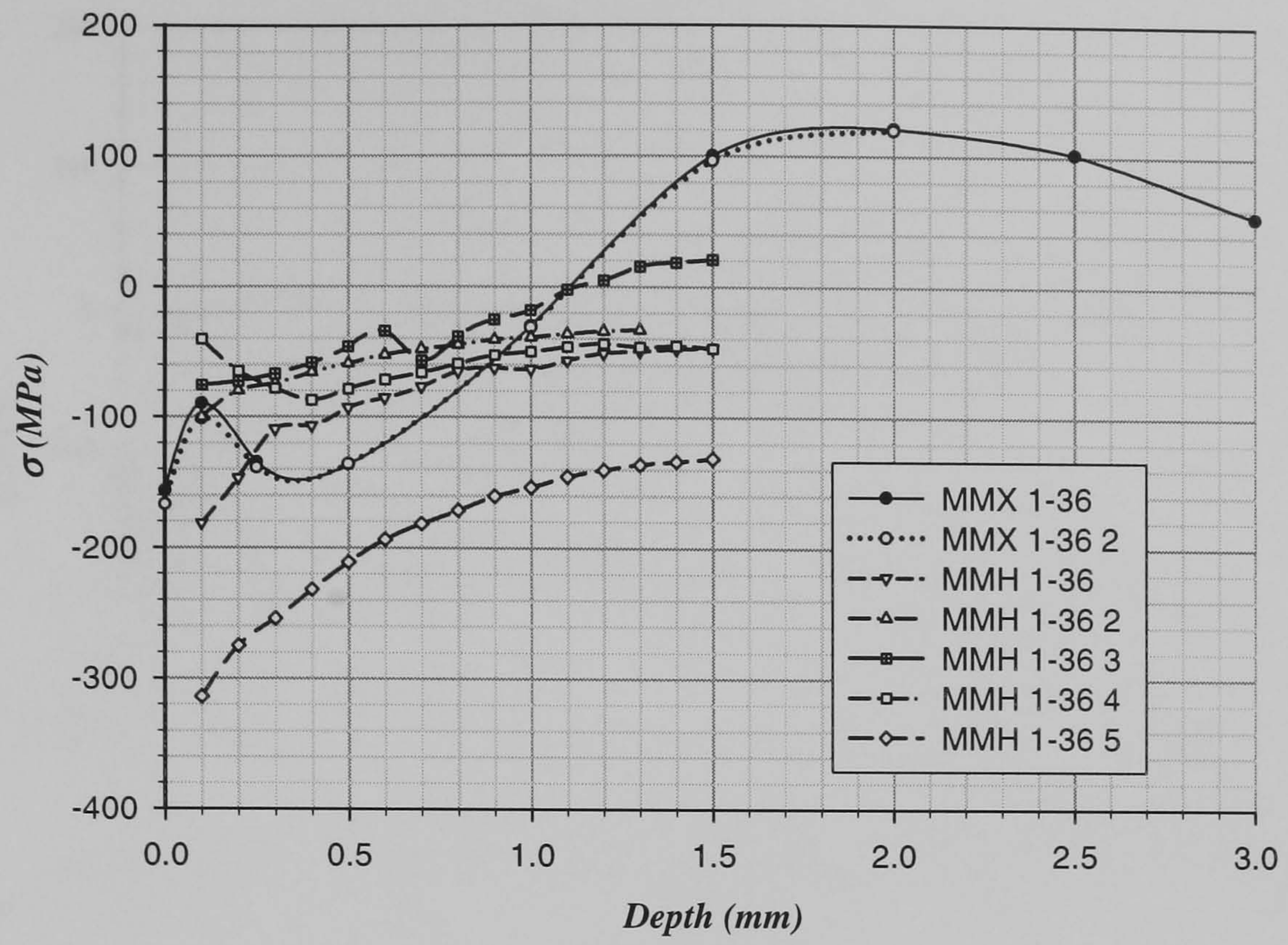

Figure 5.22 Graph of data obtained by different methods, MMH and MMX, in order to get residual stress balance through the depth in Al 2024-T3 after being treated under UIT-1-36 condition.

Al 7150-T651

In this material residual stresses left by different UIT treatments were measured only with the aid of the XRD technique. Others UIT parameters were added to the ones already used, and were called UIT-4, UIT-5 and UIT-6. As seen before those were tested in fatigue and there were just two specimens treated with each added condition. Material treated with these same conditions was used to get information about residual stresses left through its depth.

Fig. 5.23 shows residual stresses left through the depth of Al7150-T651 after different UIT treatment conditions. A solid black line represents the pattern of residual stresses before UIT treatment (bare material) indicating the presence of compressive residual stresses in the surface no higher than 20 MPa. As residual profile stresses obtained from this material were acquired with the aid of only one technique the comparison will be with the data obtained with the same technique used in Al2024-T3.

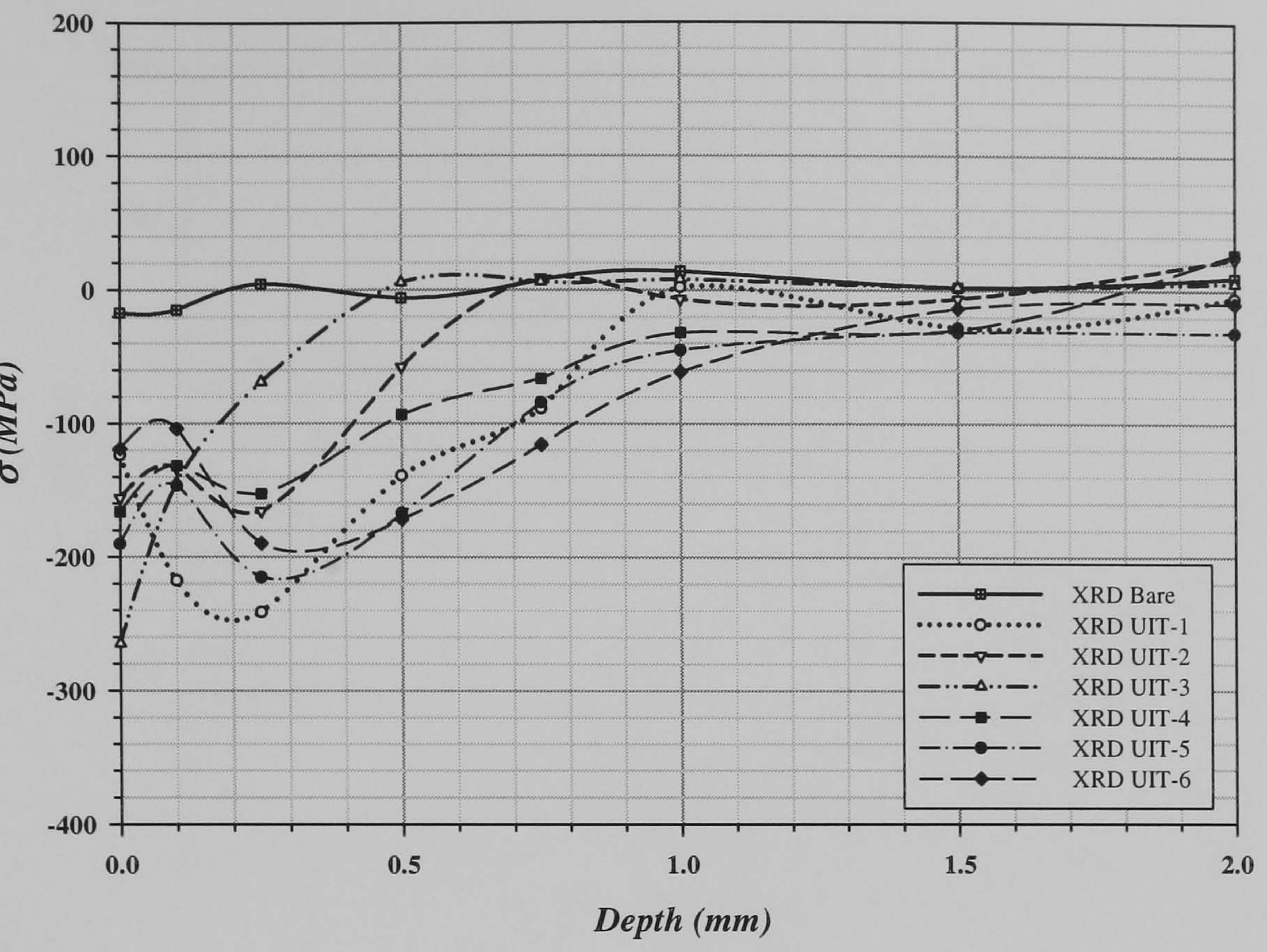

Figure 5.23 Residual stresses measured by X ray diffraction method. Residual stresses through the depth of the material Al7150-T651 at different UIT conditions and bare material.

At the surface the highest compressive residual stresses left was created by UIT-3 condition with an amount of around 265 MPa followed by UIT-5 with an amount of around 190 MPa, UIT-4 of around 165, UIT-2 of around 160, UIT-1 of around 120 and finally UIT-6 of around 118 to 120 MPa. As it is seen UIT-3 condition left a high compressive residual stress in the surface but a rapid reduction is observed through the depth faster than the rest of the UIT conditions. UIT-1 condition has almost the lowest compressive residual stress at the surface but this increase through the depth up to a maximum amount of around 240 MPa at 0.25 mm depth before starting to reduce through the depth at that point. These two types of behaviour are presented for just two UIT conditions, where one starts to reduce faster, the other starts to increase its compressive residual stresses and then reduce them at greater depth. In comparison with 2024-T3, it is observed that UIT-1 and UIT-3 gave highest and lowest surface stresses respectively, opposite to fig. 5.23.

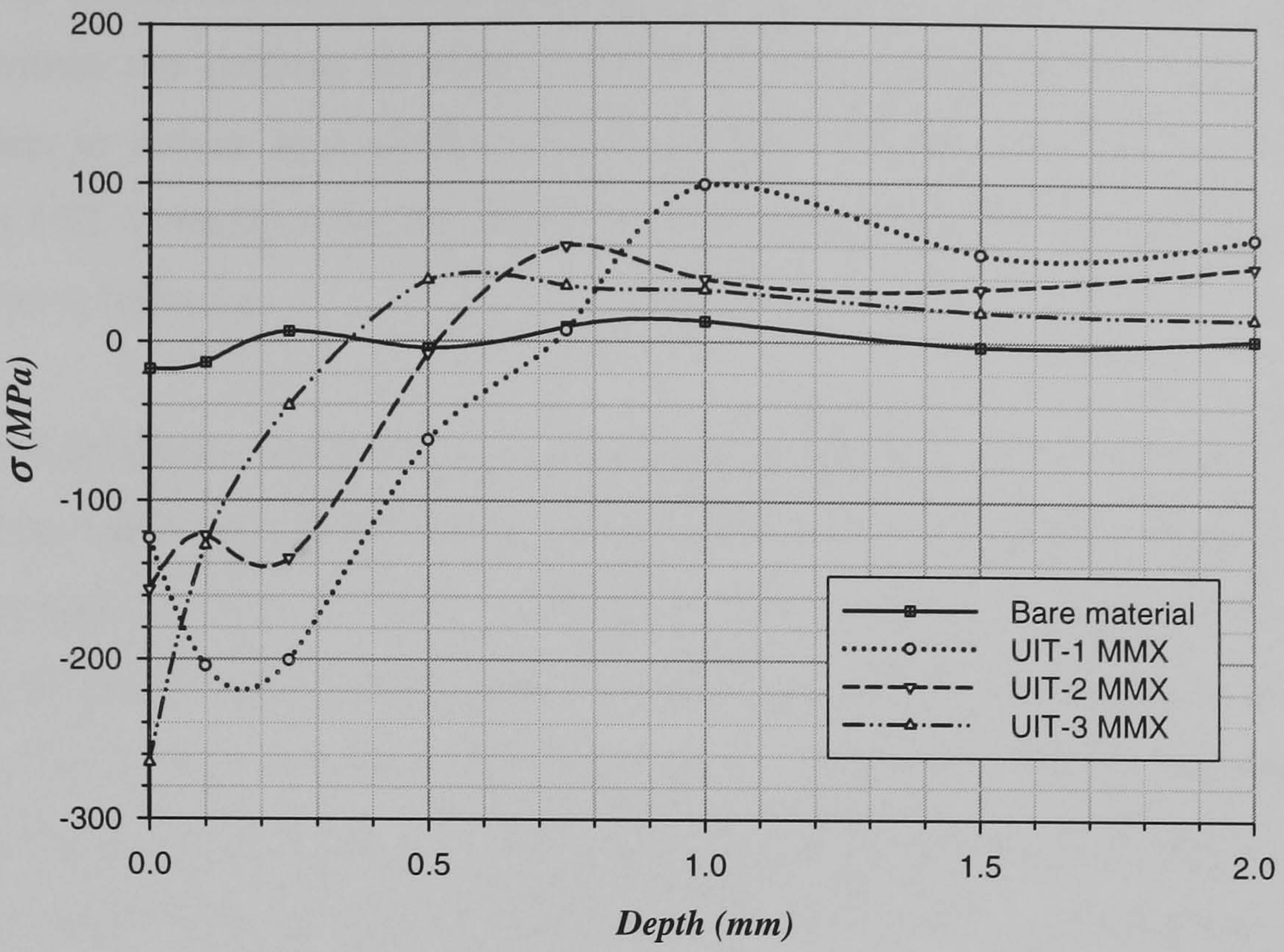

a)

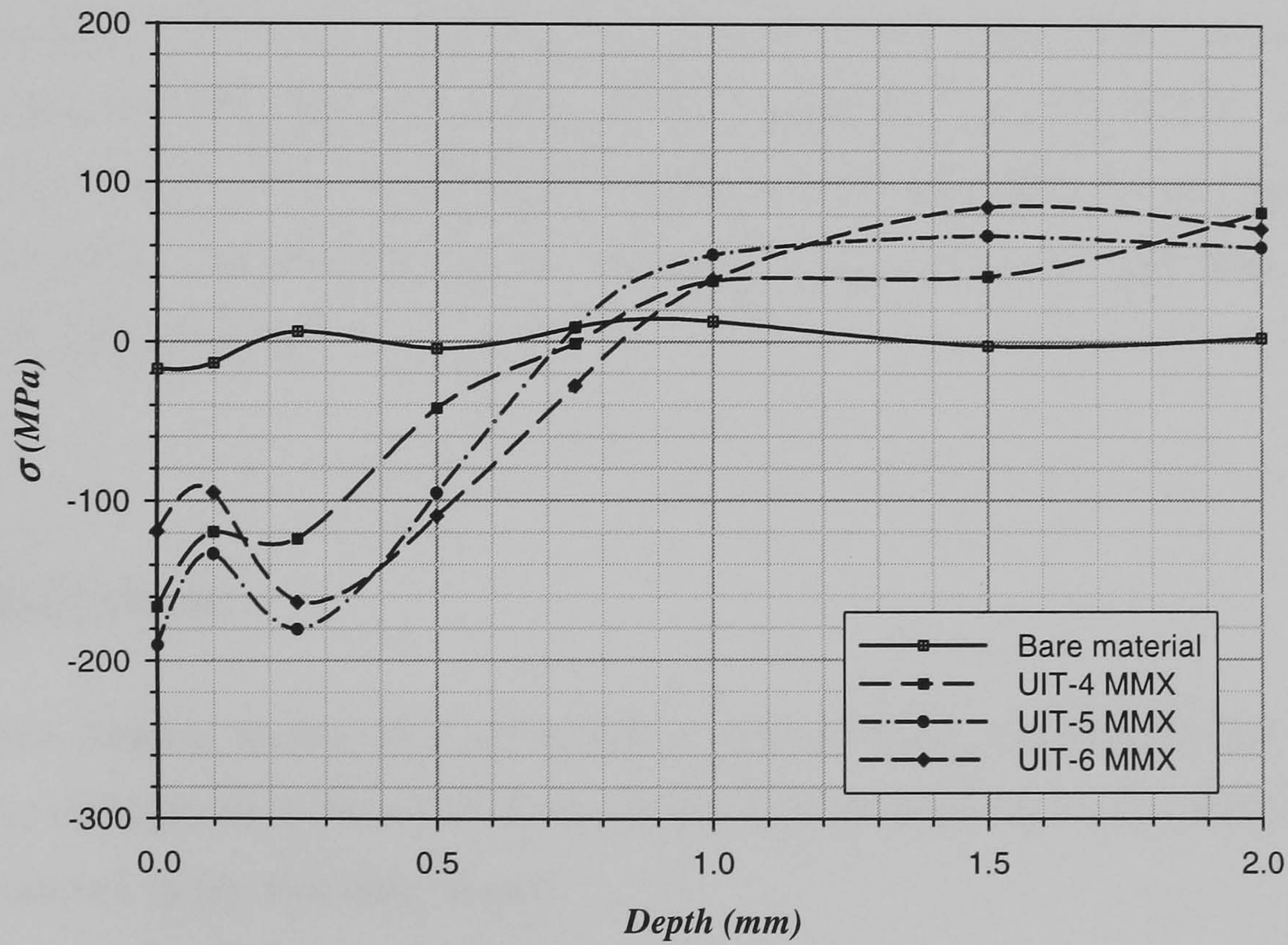

b)

Figure 5.24 Residual stresses obtained from MMX method from Al 7150-T651 alloy a) before and after UIT-1, 2 and 3 conditions and b) before and after UIT-4, 5 and 6 conditions.

The rest of the patterns represented by compressive residual stresses left by different UIT conditions follow a third general profile, and close to the surface these are bounded within the patterns for UIT-3 and UIT-1 conditions. Residual stress at the surface tends to reduce in a shallow zone and then increases, but no more than that obtained by UIT-1 condition but generally more than the obtained in the surface, after that the reduction is followed.

Fig. 5.24 shows residual stresses obtained for all the UIT conditions in Al 7150-T651 with the aid of the MMX method. Figure 5.24a shows residual stresses developed through the depth by UIT-1, 2 and 3 conditions and those which already existed before the surface treatment (bare material). Residual stresses on the surface for all cases have the same values as those obtained by XRD as shown in fig. 5.23. The profile obtained by XRD gradually diverges from those obtained by the MMX method. The MMX method is designed to satisfy axial load and bending moment equilibrium, and therefore it should provide a more credible profile than XRD concerning the balance of residual stress through the depth. This trend can be seen in fig. 5.24a, and a similar trend is seen in fig 5.24b for UIT conditions 4, 5 and 6 on Al 7150-T651 after using MMX method. The highest tensile residual stress in the interior of the specimen was obtained by UIT-1-36 condition with the aid of the MMX method with an amount of 100 MPa at 1 mm depth. However with data from XRD the tensile residual stresses were never higher than 20 MPa for all of the UIT conditions.

MICRO HARDNESS

Micro-harness testing was carried out in both materials, Al2024-T3 and Al7150-T651 alloys through the thickness of 5 mm before and after different UIT conditions. The results are shown in the following pages.

Al 2024-T3

Fig. 5.25 shows data results from Vickers test on Al 2024-T3 alloy for bare material and material after UIT-1-27, UIT-1-36, UIT-2-36 and UIT-3-36 treatment conditions. The wider black solid line represents the micro-hardness profile obtained from bare material through the depth. The closest point to the surface where the first value was obtained is at 0.1 mm depth, for bare material the micro-hardness at that point is around 113Hv. The profile that micro-hardness follows through the depth is increasing up to 0.5 mm depth and then oscillates in a constant rank between 128 and 136 Hv.

The UIT-1-27 treatment condition was the only one where micro-hardness was obtained at 0.05 mm depth until 0.6 mm depth. At 0.05 mm from the sample edge, the hardness measurement may be an underestimate. Even for 0.1 kg load, the indentation diameter becomes comparable with distance from the edge, so distortion of the edge may occur. The behaviour of micro-hardness through depth is decreasing from the closest point to the surface until 0.6 mm depth where bare material micro-hardness is attained. UIT-1-36 treatment condition produced a micro-hardness at 0.1 mm depth of around 144 Hv, bigger than that obtained from bare material. The profile decreases down to the same level as bare material at 0.5 mm depth.

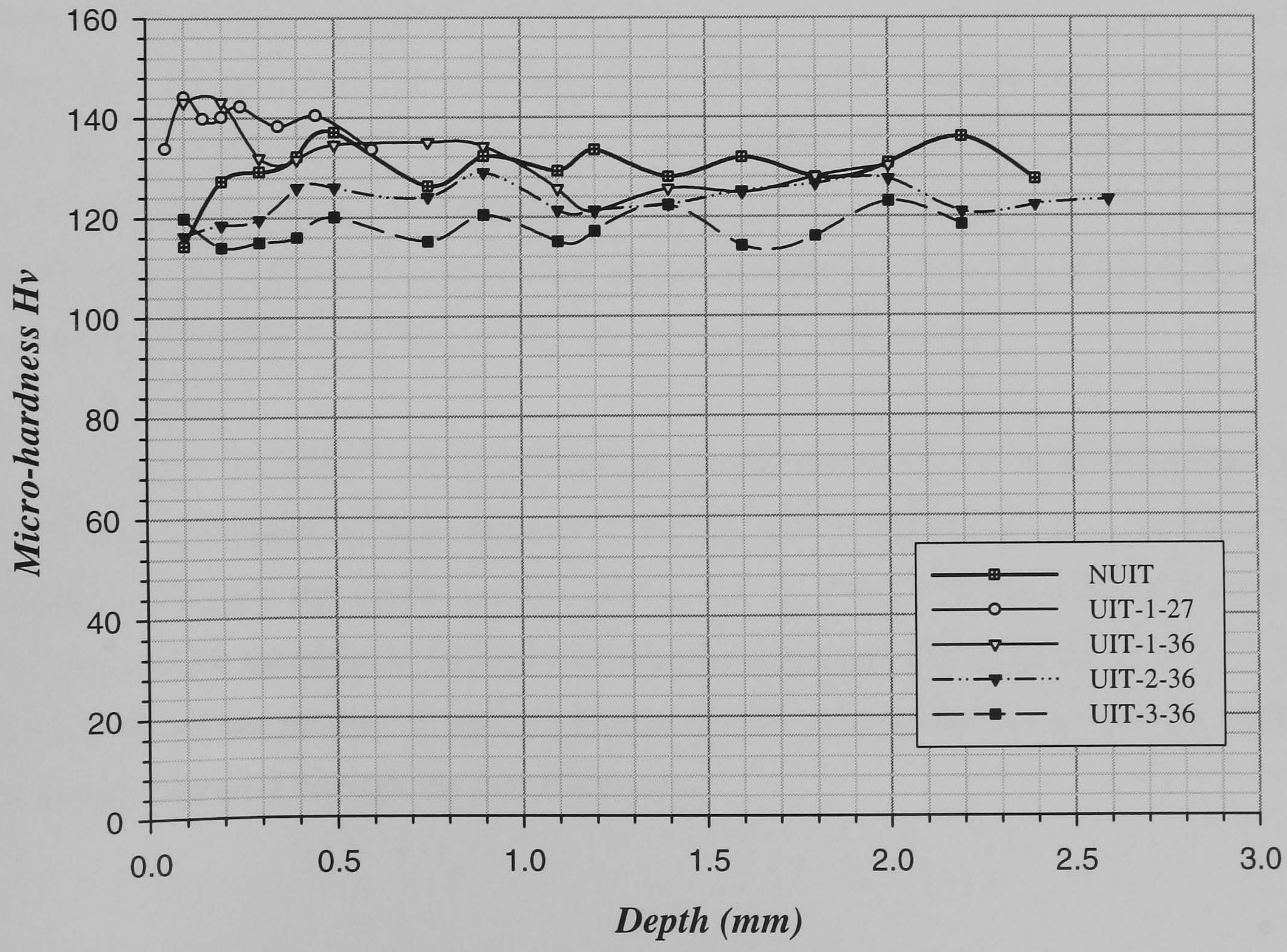

Figure 5.25 Micro-hardness Vs Depth graph from Al 2024-T3 alloy before and after UIT-1-27, UIT-1-36, UIT-2-36, and UIT-3-36 conditions.

For UIT-2-36 and UIT-3-36 treatment conditions at 0.1 mm depth has almost the same level of micro-hardness as bare material. As before mentioned the bare material profile tends to increase through the depth, but in UIT-2-36 and UIT-3-36 treatment conditions it appears different. In UIT-2-36 treatment condition hardness tends to increase but no more than bare material and then oscillate within a rank of around 120 and 128 Hv, being always below the bare material profile. In the case of UIT-3-36 the profile is always oscillating between 112 and 124 Hv.

Al 7150-T651

In Al 7150-T651 alloy the Vickers test was used to get information about micro-hardness through the depth before and after different UIT treatments conditions. Fig. 5.26 shows micro-hardness data points from material after different UIT treatments conditions compared to bare material. Fig. 5.26a shows hardness profiles through the depth of bare material and UIT-1-36, UIT-2-36 and UIT-3-36 treatment conditions applied to the material. The bare material profile is represented by a solid black line which starts at 0.05 mm depth with a hardness of around 200 Hv and then oscillates through the depth between 190 and 210 Hv. At that depth the hardness values obtained from material treated by UIT-1-36 and UIT-2-36 conditions are quite similar, being a little higher for the UIT-2-36 condition but from 0.1 mm depth hardness in UIT-1-36 is above UIT-2-36 and UIT-3-36 treatment conditions and also the profile of bare material. But such differences are small and not much more than general scatter of experimental data.

Fig. 5.26b shows the micro-hardness profile due to UIT-4-36, UIT-5-36 and UIT-6-36 and compared to that obtained from the bare material, all three produce more hardness through the depth. In this plot it can be observed that UIT-4-36 condition produces more hardness in the material than the other two UIT conditions. UIT-5-36 and UIT-6-36 did not produce as much hardness as UIT-4-36 condition but have small effects over bare material through the first millimetre.

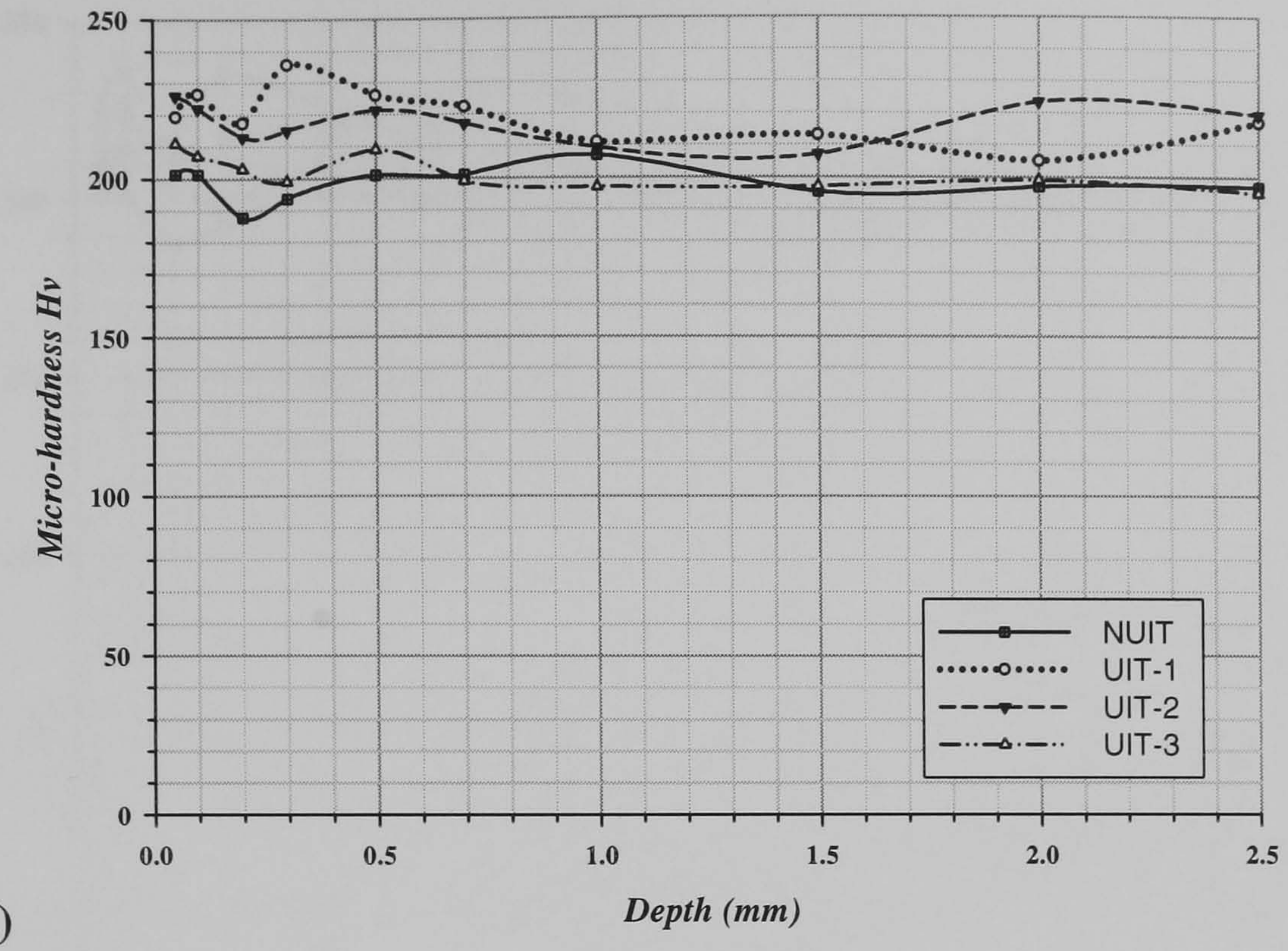

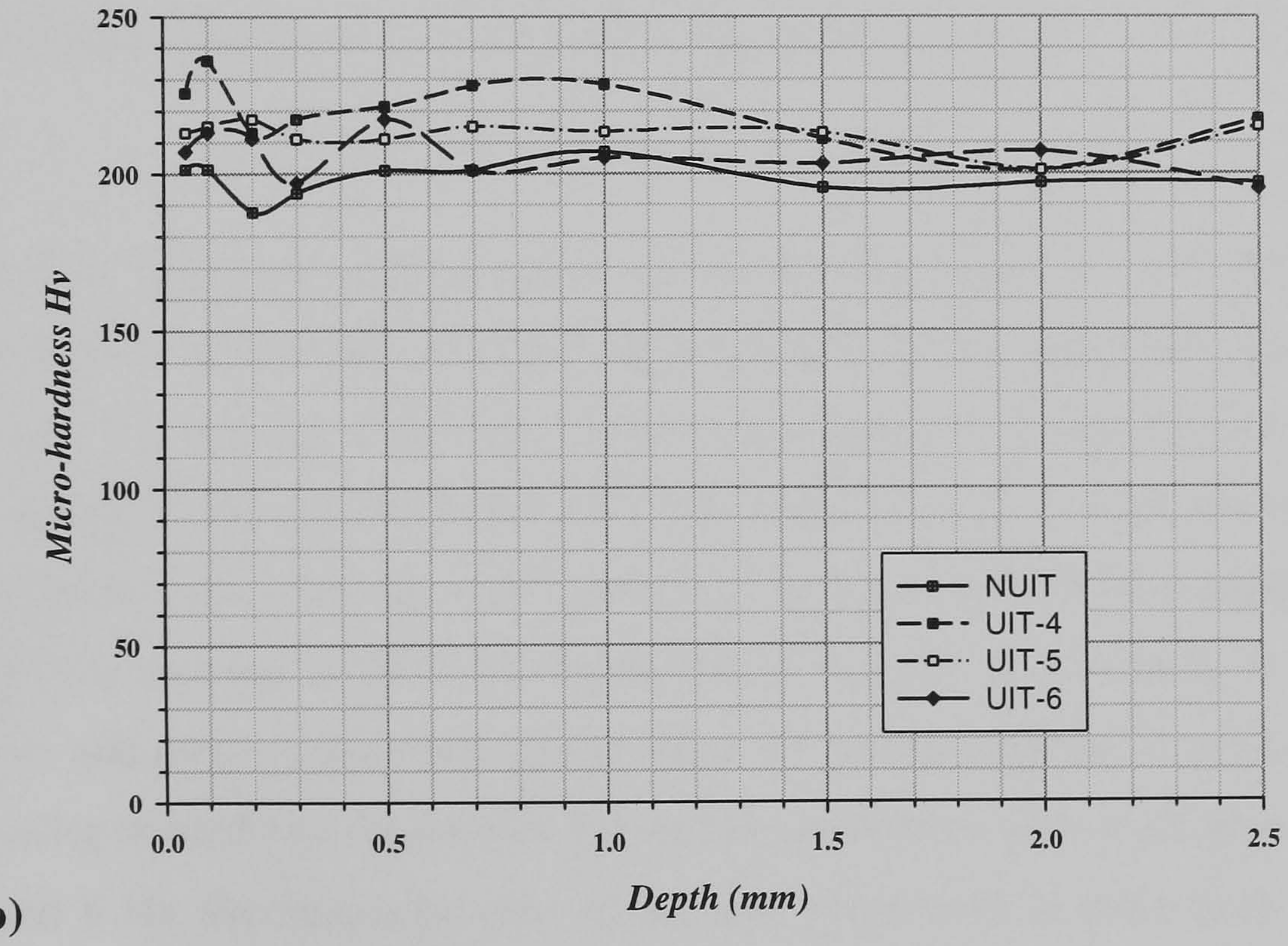

Figure 5.26 a) Micro-hardness data points from bare material and material after UIT-1-36, UIT-2-36 and UIT-3-36 treatment condition on Al 7150-T651. b) Micro-hardness data points from bare material and material treated after UIT-4-36, UIT-5-36, and UIT-6-36 treatment conditions.

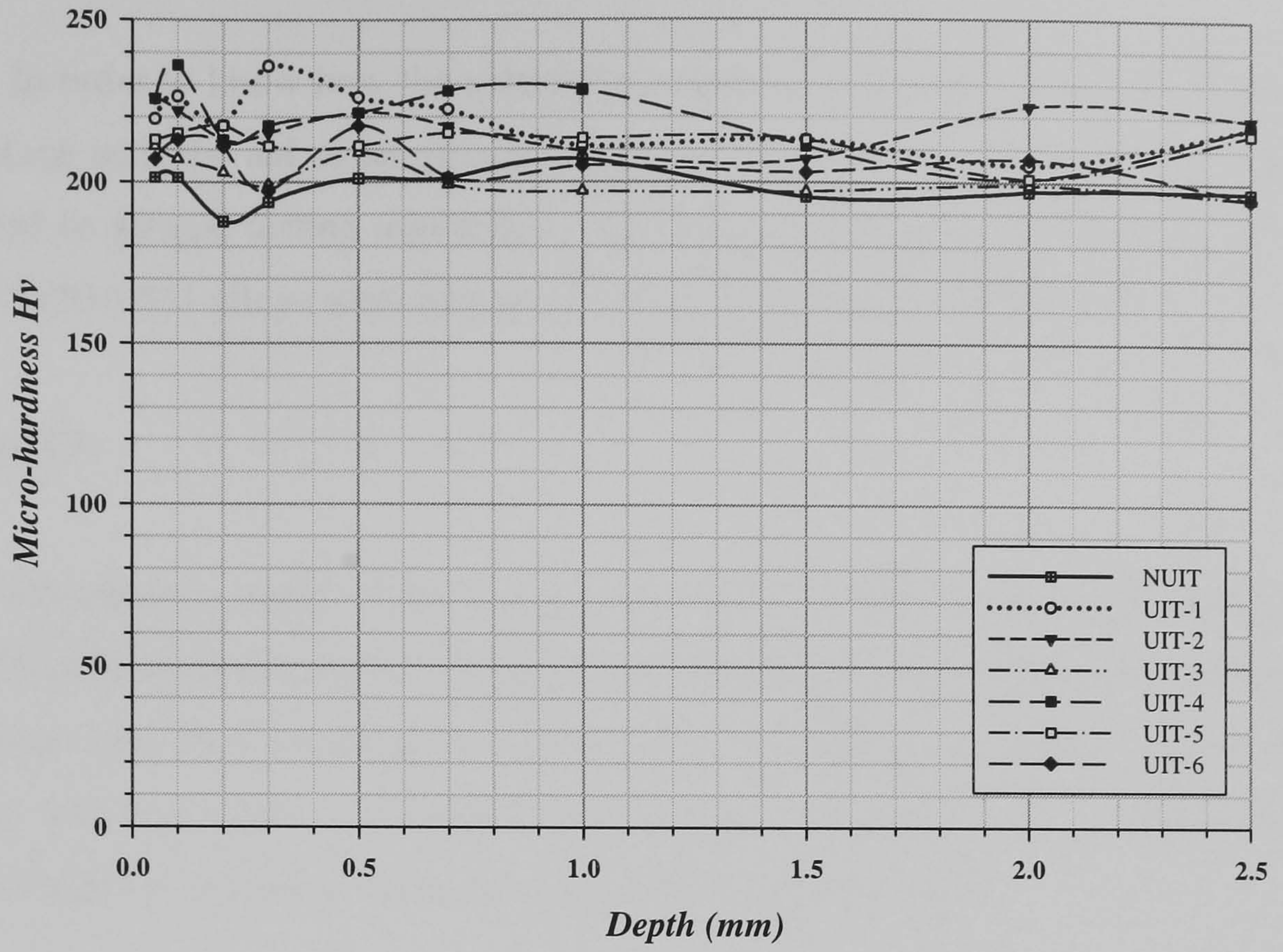

Figure 5.27 Graph of all micro-hardness profiles due to UIT-1-36, UIT-2-36, UIT-3-36, UIT-4-36, UIT-5 and UIT-6-36 treatment conditions in Al 7150-T651 and bare material

Fig. 5.27 shows all profiles due to all conditions used in Al 7150-T651 alloy as well as the profile due to bare material. In this graph can be compared clearly all the conditions and one may see which one creates more hardness through the depth. As seen separately in fig. 5.26a and fig 5.26b UIT-1-36 and UIT-4-36 conditions created more hardness in the material than the other conditions. In this graph can be compared both of them and is observed that at 0.05 mm depth both of them are quite similar to the UIT-2-36 condition, and their patterns through the depth are similar over the first 0.2 mm depth, then decreasing in hardness magnitude. The difference in these first readings is not much, being around 8 Hv the maximum one. At 0.2 mm depth both of them have almost the same hardness magnitude and after that UIT-1-36 condition creates the hardest zones before decreasing its magnitude. Basically this zone is where both conditions develop bigger hardness magnitudes than that in bare material.

CRACK INITIATION LOCATION

In order to know how the material is affected by the UIT treatments inspection on the surface with the aid of an optical microscope was achieved in specimens after being subjected to fatigue testing and failure. Specimens made of both materials Al 2024-T3 and Al 7150-T651 alloys were inspected, and the results are as follows.

Al 2024-T3

Observation under a light microscope at 50X magnification of specimens from Al 2024-T3 to localize the crack initiation gave information about how many visible cracks are present and their localization after fracture, in order to know the behaviour of the material with and without treatment on the surface. Fig. 5.28 shows the places where it is more probable to see crack initiation along the cross section area.

a) Untreated specimen.

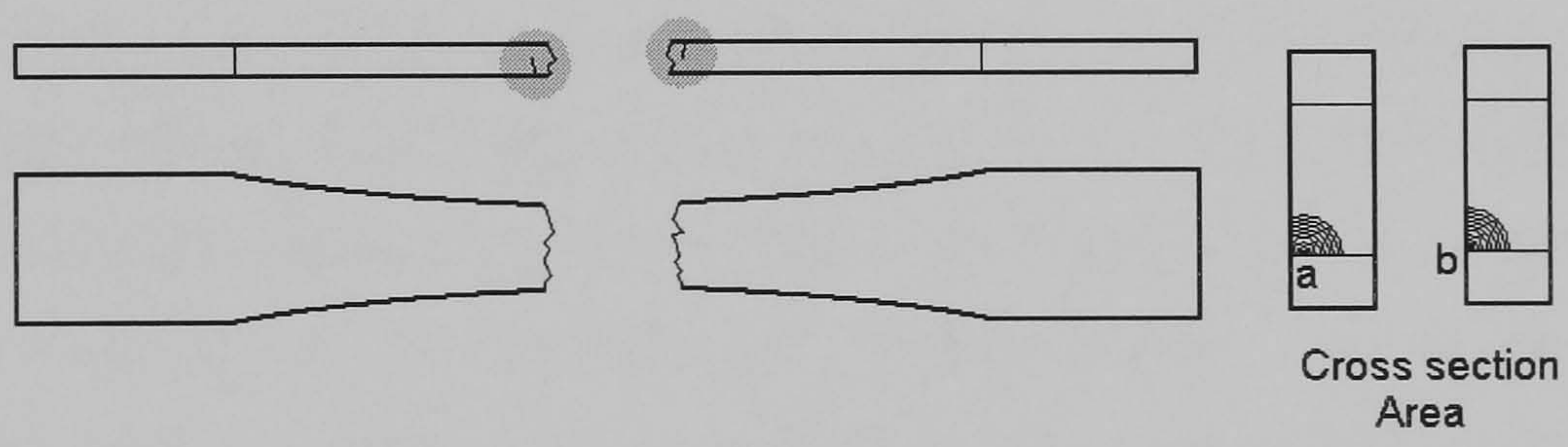

b) Treated specimen.

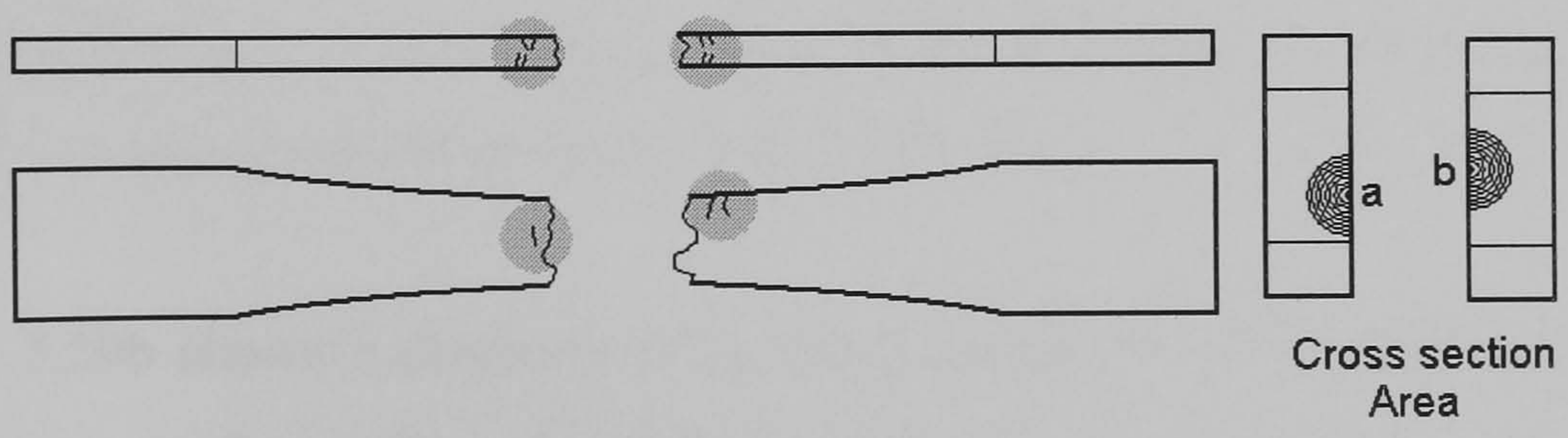

Figure 5.28 Map of cracks on the Al 2024-T3 specimens treated and untreated, showing the cross section area where the fracture occurs and the points where commonly started.

In specimens without treatment it was more common to see that the crack initiation was at the edge and near the corner as can be seen in Fig. 5.28a at the points *a* and *b*. While in specimens with treatment the initiation point was more common to be localized on the face in both cases (27 kHz and 36 kHz treatments), almost at the middle of the specimen as can be seen in Fig. 5.28b for points *a* and *b*. In specimens with treatment present, there are plenty of cracks near crack fracture in the four sides as shown in Fig. 5.28b by grey areas. The grey areas represent the zones where it was more common to see cracks. In specimens without treatment there were not many cracks, so treated specimens look susceptible to initiation of cracks because in many samples on the fracture surface more than one crack initiation site appears and mainly on the flat faces, as well as small cracks around the specimen near the fracture.

Al 7150-T651

The same procedure to examine the gauge zone after fracture was followed for specimens made of Al 7150-T651 alloy with the aid of a light microscope. Fig. 5.29 shows the places where crack initiation was more common for bare material and for material treated with different treatment conditions.

Fig. 5.29 shows the zones in the specimens where cracks initiation took place to lead to the final fracture. Fig 5.29a shows the cross section area of the fracture surface in order to see the place where in treated specimens it was most common to start the crack to fracture. As it can be seen in the figure in all specimens with only one exception crack started at the corner. In the left hand side figure the zones where small cracks after fracture where found are marked with a grey circle. Actually in this material not many cracks were found close to the fractured zone, and just in three specimens a single small crack was found and seems its initiation was in the corner.

Fig. 5.29b shows a diagram of the crack initiation in bare material. In the right hand side figure is shown the cross section area of the specimen that is seen because of the fracture surface, where it can be appreciated how the crack initiation was placed according to the specimen. It was observed that for bare material it is more likely to find a crack initiation on the face than on the edge or in the corner, as in treated material. All the specimens made of bare material analysed presented the crack initiation in that zone and not one showed small cracks close to the fracture zone.

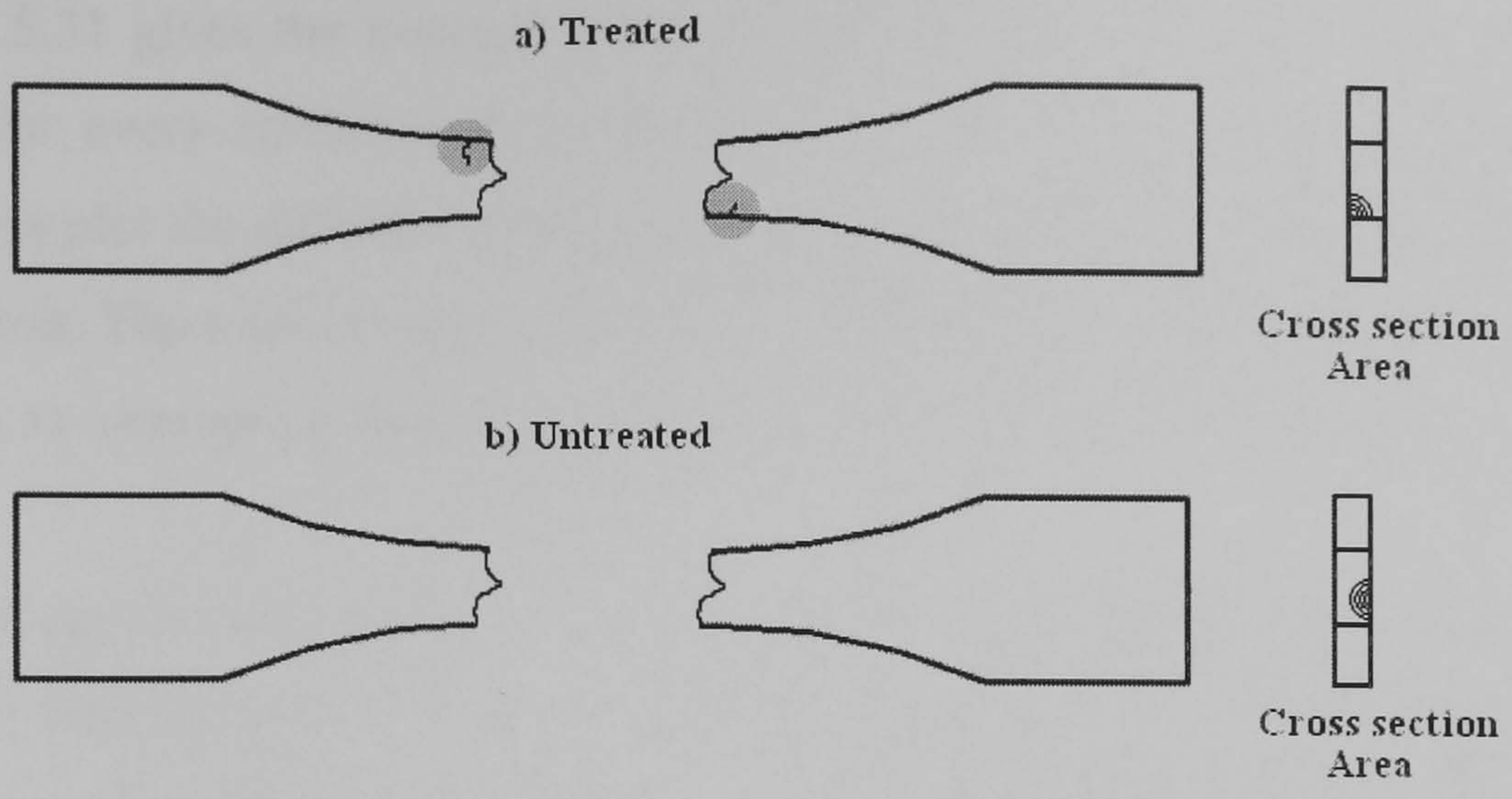

Figure 5.29 The most common zones where crack initiated to finally fail in fatigue test and small cracks observed after fatigue failure near the fracture surface for a) treated material with different UIT conditions and b) Untreated material Al 7150-T651 alloy.

ROUGHNESS FOR Al 2024-T3

Roughness is important because it can affect fatigue life of the material and it varies depending on the condition of the treatment. This test was carried out on small square plates of around 6 x 6 cm, for as received and after UIT-1-36, UIT-2-36 and UIT-3-36 treatment conditions.

Fig. 5.30 shows a graph where is represented different roughness surface of material before and after different UIT treatment. Six separated measurements were taken along the rolling direction, which is parallel to the treatment direction, and perpendicular to it, for every UIT condition. Along the “x” axis are placed the six results, grouped by treatments and direction for every plate and in “y” axis is placed the value of the roughness in µm, using Ra, the CLA (Center-Line Average) measure of roughness.

As one can see in the graph bare material has quite similar roughness along and perpendicular to the rolling direction and take values within a large rank of values which are from 0.05 to 0.28 µm in all the 12 tests. It can be appreciated that roughness due to UIT-3-36 condition especially at longitudinal direction kept in a small rank compared to those of different conditions, meanwhile the rest of the treatments including bare material show large variability.

Fig. 5.31 gives the average values of roughness considering the total number of tests done for every condition in longitudinal and transversal directions as mentioned before. In this plot the different materials are compared, treated and untreated, and plotted on the "x" axis. The total average value of six roughness tests is placed in "y" axis, so that longitudinal as transversal roughness can be compared for every condition.

As it can be seen in fig. 5.31 average roughness in both directions is nearly the same in bare material and is within the rank of 0.15 to 0.165 μm. The UIT-1-36 treatment condition increases the average roughness compared to bare material, having a bigger increment for transversal direction. UIT-2-36 condition does not have much effect in roughness in transverse direction compared to bare material but in longitudinal direction this condition improves the average roughness, diminishing it.

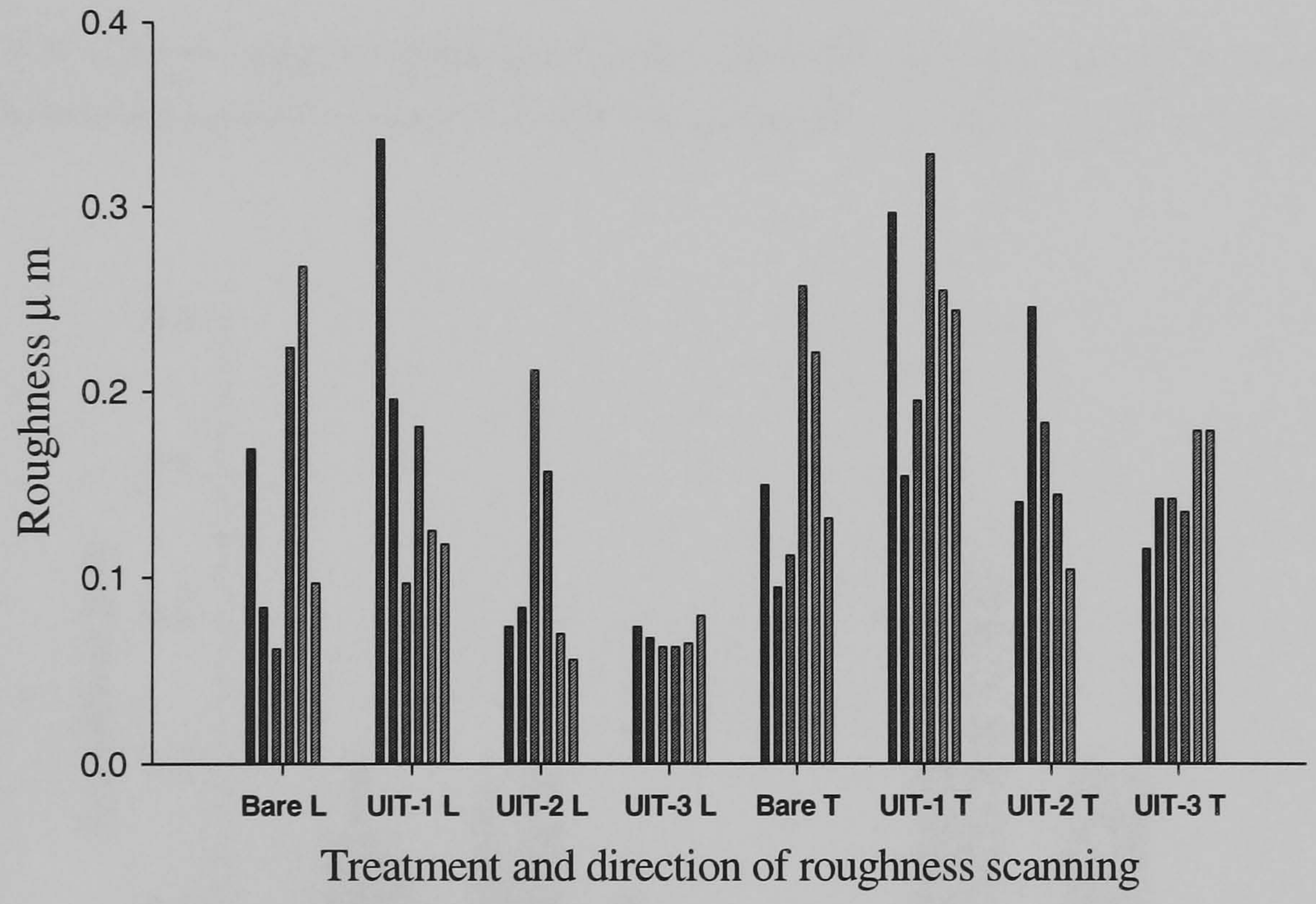

Figure 5.30 Groups of roughness measurements from small plates made of bare material and material after UIT-1-36, UIT-2-36 and UIT-3-36 conditions on Al 2024-T3. The direction of the readings of roughness are according to rolling direction which is parallel to the treatment direction and were taken along the rolling direction (L) and transversal to that (T).

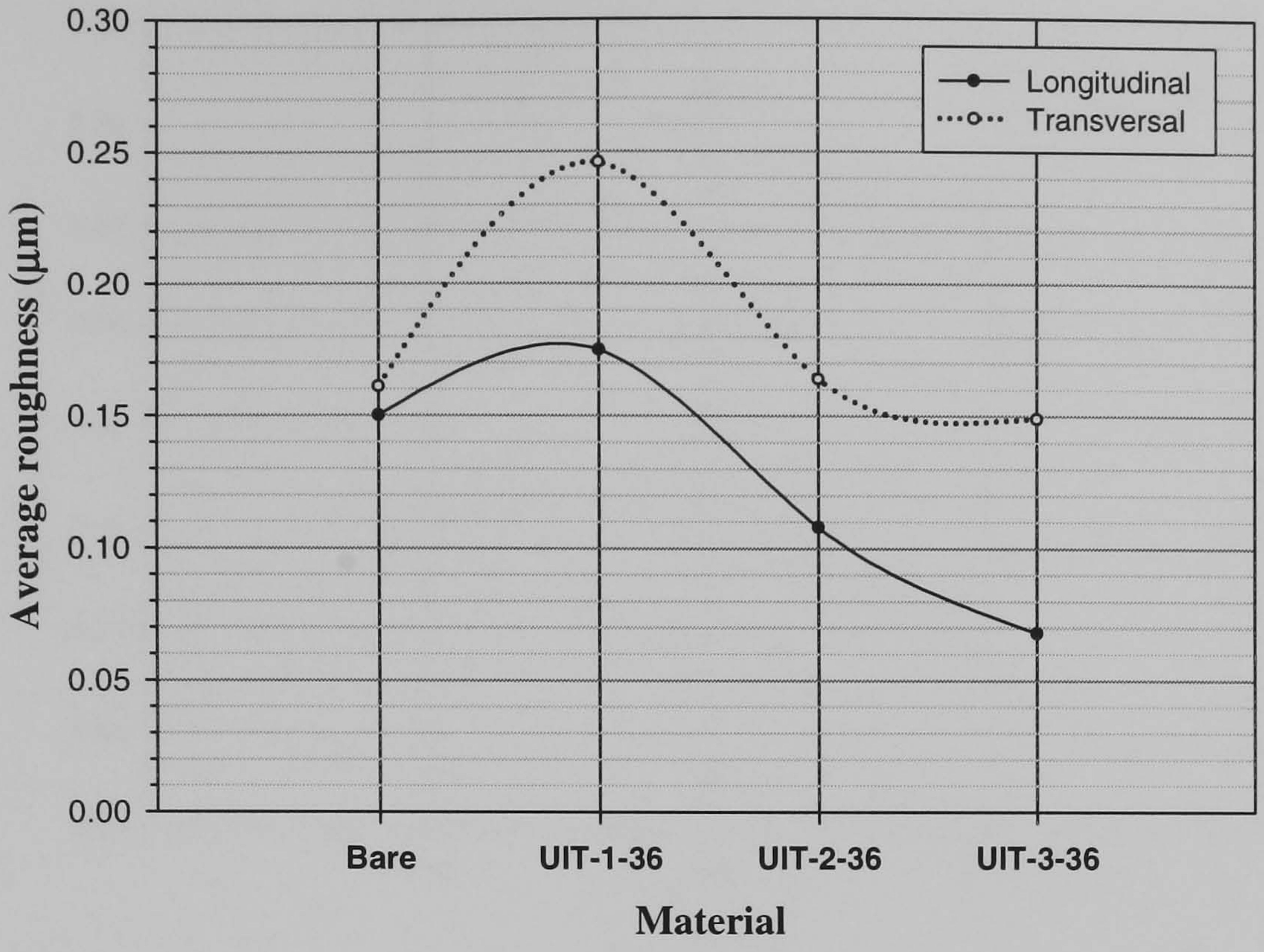

Figure 5.31 Average roughness comparison among different UIT conditions and Al 2024-T3 bare material in longitudinal and transversal direction obtained from small plates of dimensions about 6 x 6cm.

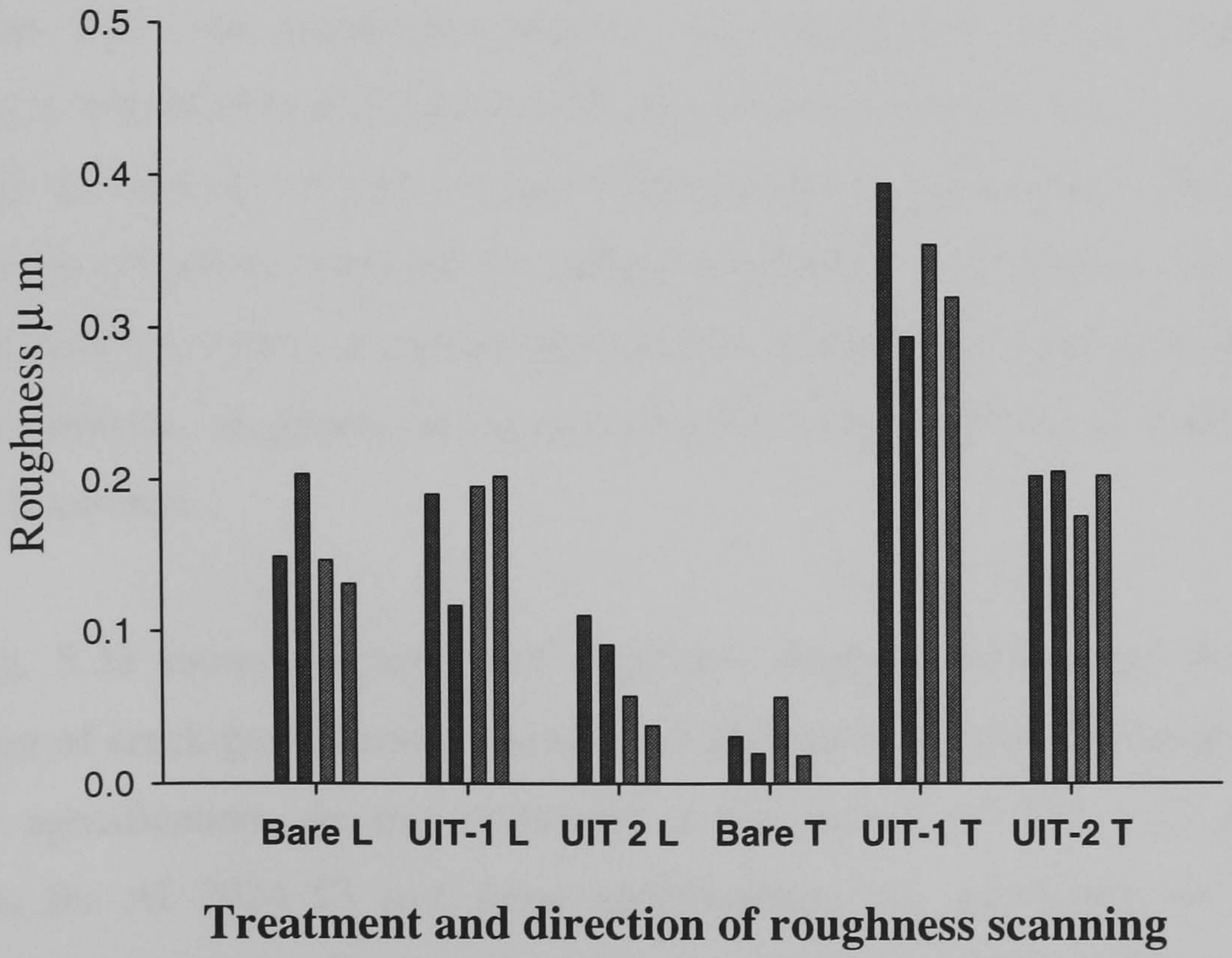

Figure 5.32 Roughness obtained from plates made of Al 2024-T3 designed to get information of crack growth ratio from places with and without treatment in both directions longitudinal and transversal.

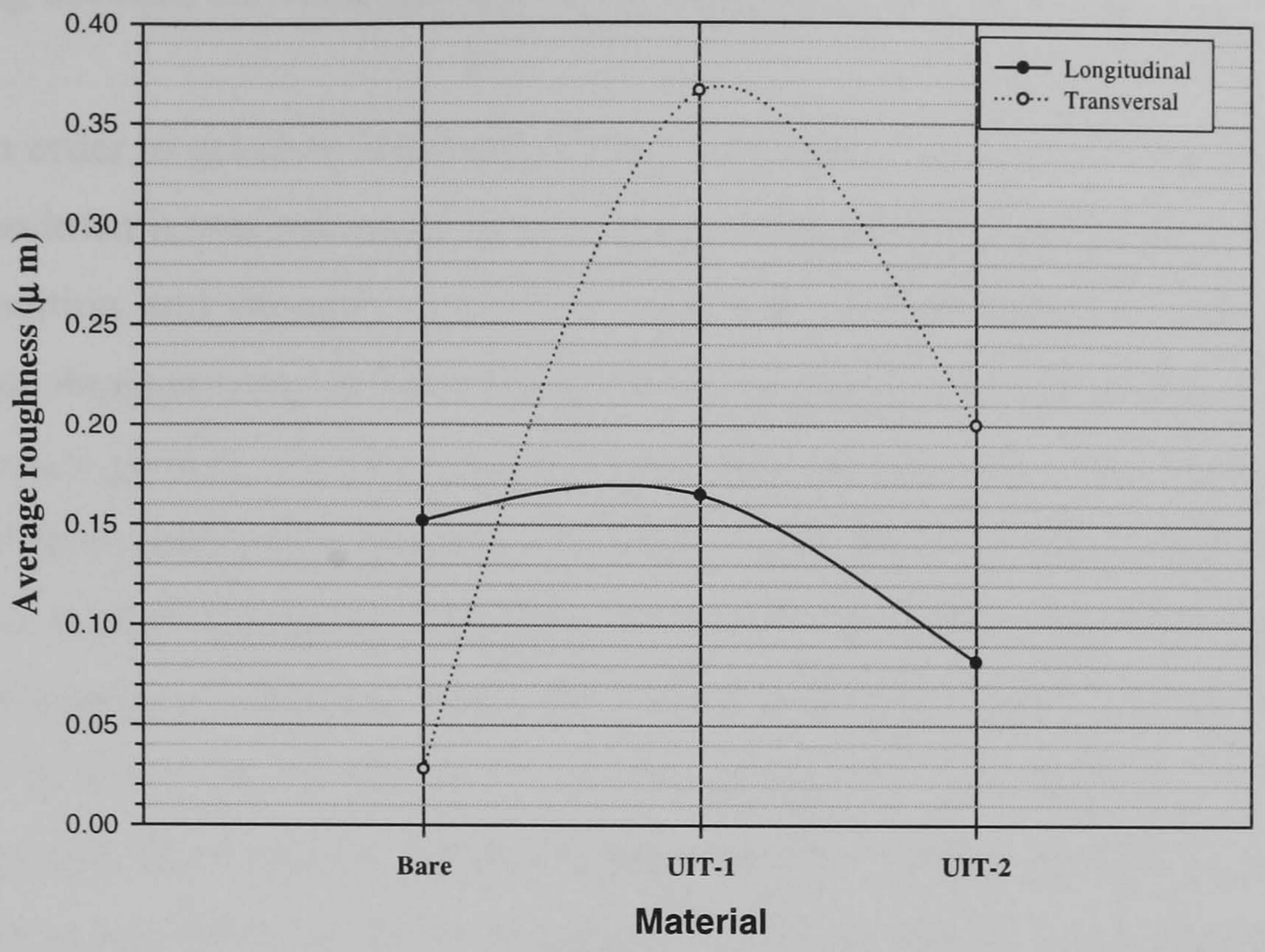

Figure 5.33 Average roughness acquired from the total amount of readings done in specimens made of Al 2024-T3 designed to get information of crack growth ratio in both directions longitudinal and transversal.

The UIT-3-36 condition improves the roughness in longitudinal direction comparing it with bare material meanwhile in transversal direction the average roughness kept within the rank of average roughness obtained from bare material. This graph shows that UIT-3-36 condition improves the surface roughness of the material especially along the rolling direction (same as treatment direction) compared to other conditions but a big difference between roughness along and perpendicular to rolling direction exists after UIT-3-36 treatment.

Fig. 5.32 shows the results of roughness obtained from plates designed to get information of crack growth ratio. There are 4 different tests where roughness is acquired for every specification. As the treatments to be studied are UIT-1-36 and UIT-2-36 conditions for Al 2024-T3 just those specifications are mentioned as well as bare material. Readings were along and across the specimen. The results show that bare material has values of roughness across the specimen within a rank of 0.02 and 0.06 μm and along the specimen this value increases and keep between the rank of 0.13 and 0.2

µm. Actually the rougher surface is left by UIT-1-36 treatment across the feed direction oscillating between the values of 0.29 up to 0.47 µm.

In order to get clear information about roughness left by UIT treatment conditions in the specimen it was necessary to get another average, but from the four tests done for each condition and direction. Fig. 5.33 shows the values obtained from the average roughness obtained from all the amount of data acquired from specimens to be tested in fatigue crack growth. Results illustrate that bare material has less roughness surface across rolling direction than along it. The UIT-1-36 treatment condition increases roughness in both directions especially across the specimen. The UIT-2-36 treatment condition improves roughness along the rolling direction compared to bare material but increases it across the rolling direction. Comparing UIT-1-36 and UIT-2-36 conditions the best results in roughness can be obtained from UIT-2-36 conditions which improve roughness in one direction, as the amplitude of UIT oscillation is reduced from 18 to 15 microns, but more significantly the feed rate is increased from 400 to 1000 mm/min.

MICRO STRUCTURE

Analysis of the material must be carried out in order to know the effects of the UIT treatment causes in the material. Micro structure has been analysed in different ways with the aid of different techniques. In order to get an image of the microstructures of the material before and after UIT treatment, the use of Scanning Electronic Microscope (SEM) was required, and together with other methods information will be collected.

Images from fracture surfaces from specimens made of Al 2024-T3

Analysis in the SEM was carried out in order to get more information about crack initiation, as well as the influence of UIT treatment on microstructure. Fig. 5.34 shows crack initiation of two different specimens loaded at different loads without UIT treatment condition.

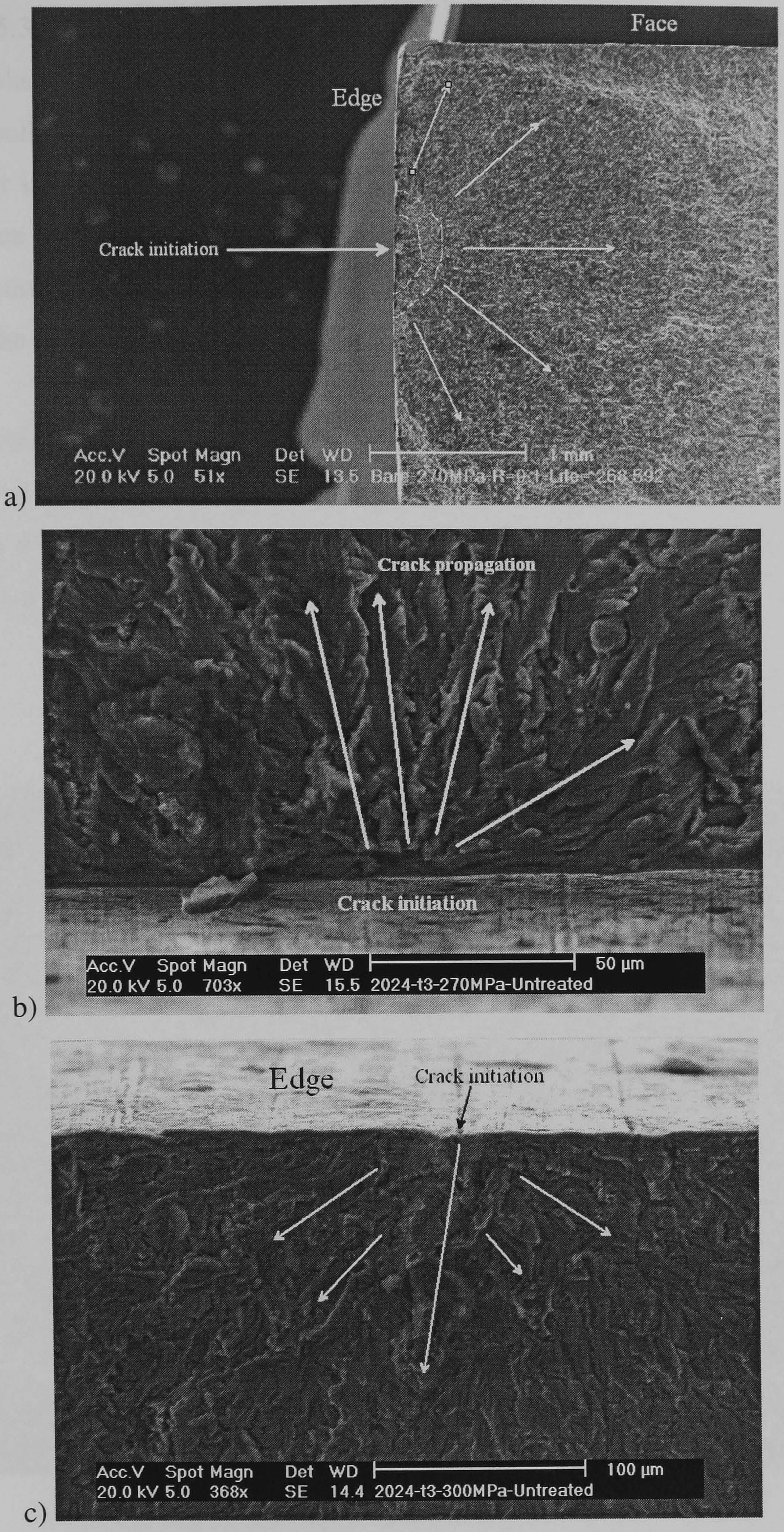

Figure 5.34 a) Magnification of the crack initiation zone from specimen of Al 2024-T3 bare material subjected to a maximum load of 270 MPa. b) Higher magnification of the crack initiation zone of the same specimen showing some river marks. c) Magnification of the crack initiation zone from different specimen loaded with a maximum load of 300 MPa.

Fig. 5.34a shows the crack initiation of a specimen subjected to a maximum load of 270 MPa placed on the edge of the specimen (left side of the photo) and its propagation through the bulk, which is radially. It can be appreciated that crack initiation could be on the surface or in the bulk close to the surface. Fig. 5.34b shows a close up of the crack initiation place from the same specimen seen in fig. 5.34a where can be seen that crack initiation occurred from the surface propagating to the bulk given by some river marks observed in the picture.

Fig. 5.34c shows the crack initiation zone from a different specimen subjected to a maximum load of 300 MPa of bare material. The same as the other specimen, the crack initiation was from the surface of the machined edge of the specimen propagating radially through the bulk; some river marks can be observed.

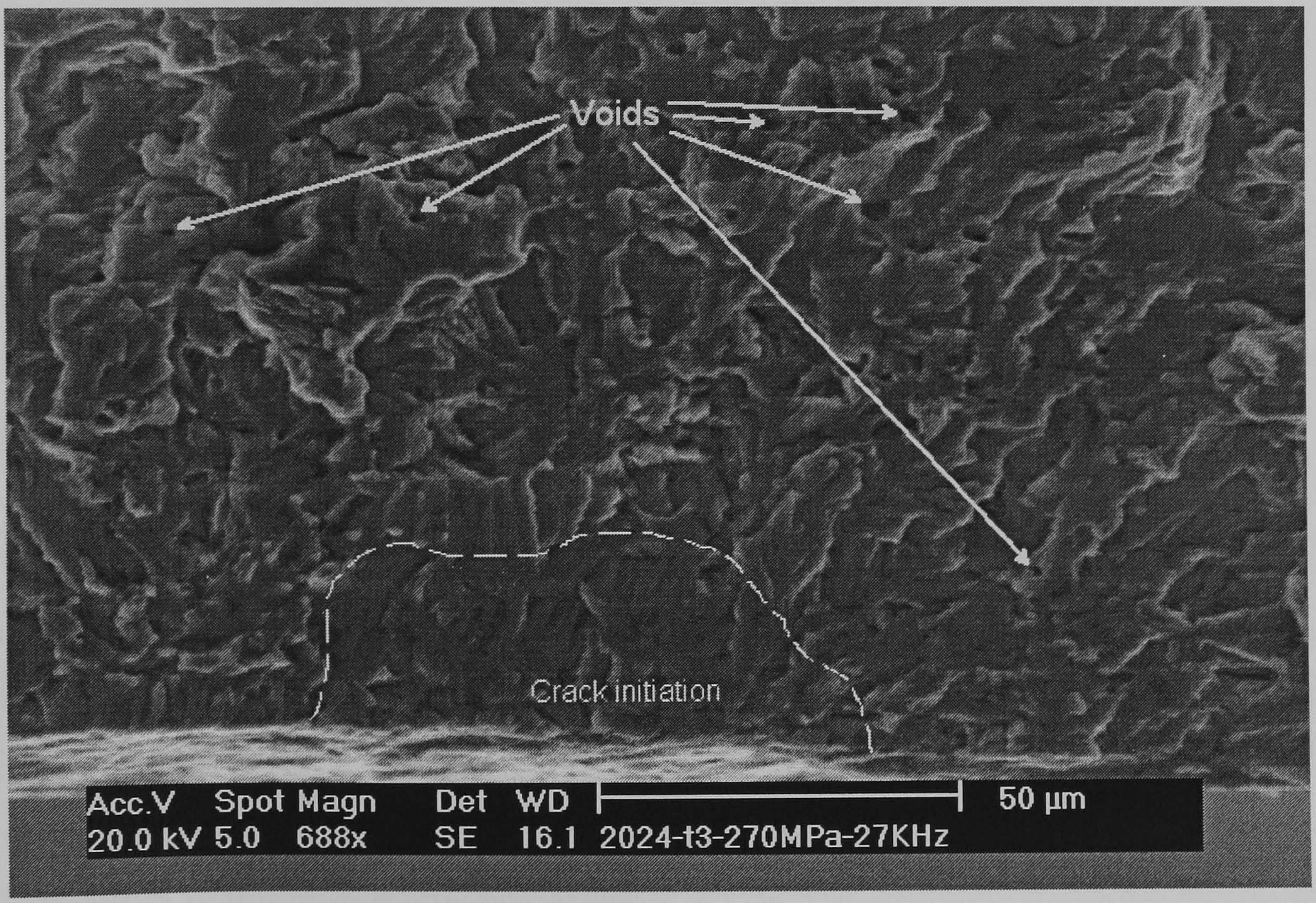

Figure 5.35 Magnification of the fracture surface of a specimen treated at UIT-1-27 treatment condition on Al 2024-T3 of the crack initiation zone and fatigued under a maximum load of 270 MPa.

In order to see the effects of UIT treatments in the material an analysis in specimens already treated before fatigue, and then fractured was achieved. Fig. 5.35 shows magnification of a surface fracture of the crack initiation site of a material treated at UIT-1-27 condition loaded under a maximum load of 270 MPa.

Here the crack nucleus is marked and its propagation through the bulk can be followed with the aid of the river marks. In this picture the presence of some voids is observed which can affect the fatigue life of the specimen by joining to the main crack and accelerating crack growth rate.

Magnifications of fracture surfaces of specimens treated with UIT-1-36 condition are shown in fig. 5.36. It can be appreciated that cracks initiate in the harder zone (fig. 5.36a) and propagate through the specimen. In fig. 5.36a the presence of a small second crack is appreciated which later would be joined to the main one which is located on the right side. The propagation of both cracks can be followed by the river marks appreciated in this figure.

In order to get a better resolution of the fracture zone and the crack initiation point a higher magnification in another specimen is given. This specimen was under fatigue with a maximum load of 170 MPa and its crack initiation place is observed in fig. 5.36b. In this picture the presence of voids can be appreciated, where in this case it is seems as if the quantity of voids is high.

Even near the surface some voids were found, as seen on the right side. Here one can see just one place where crack started and river marks of the pitted fracture path go from the bottom center to the left top corner through an area of dense voids, and from the bottom center to the right top corner. It is worth noting that the presence of voids causes a faster crack growth because those voids joining each other and/or the main crack, losing the capability to retard or stop crack growth.

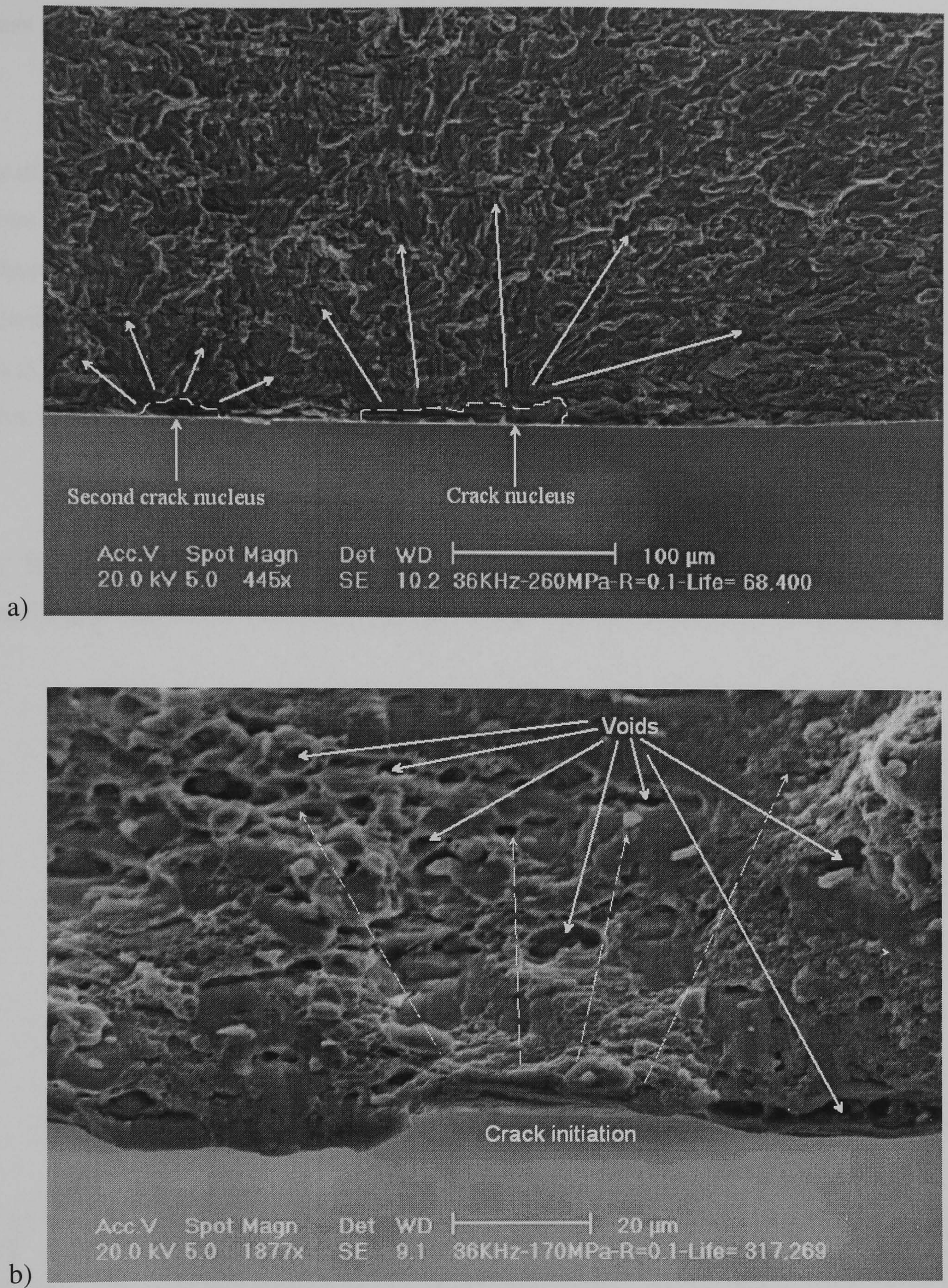

Figure 5.36 Magnifications from specimens treated with UIT-1-36 condition on Al 2024-T3 material. a) From the crack initiation showing a second crack nucleus and their propagation direction from a specimen load at a maximum load of 260 MPa. b) Higher magnification from other specimen subjected to a maximum load of 170 MPa and where it can be seen the presence of voids.

Cross sectional view of samples made of Al 2024-T3

Alteration of copper as a secondary particle phase after the UIT process is investigated with the aid of EDS (Energy Dispersive Spectroscopy) and SEM. Fig. 5.37 shows part of the surface of material already treated and the EDS spectrum from two different particles found in the bulk material apart from base material which is Aluminium. EDS spectrum shows the presence of Oxide as black spots, these particles are rich in O, Al, Mg, Si and small quantities of Mn, Fe and Cu. Actually this kind of particle is due to the Oxygen trapped during the rolling process.

The EDS spectrum from white particles shows a rich composition of Al, Cu, Mg, Mn, Si and Fe. Basically these particles are the secondary compound elements of the material and their distribution will change the mechanical properties of Aluminium alloy.

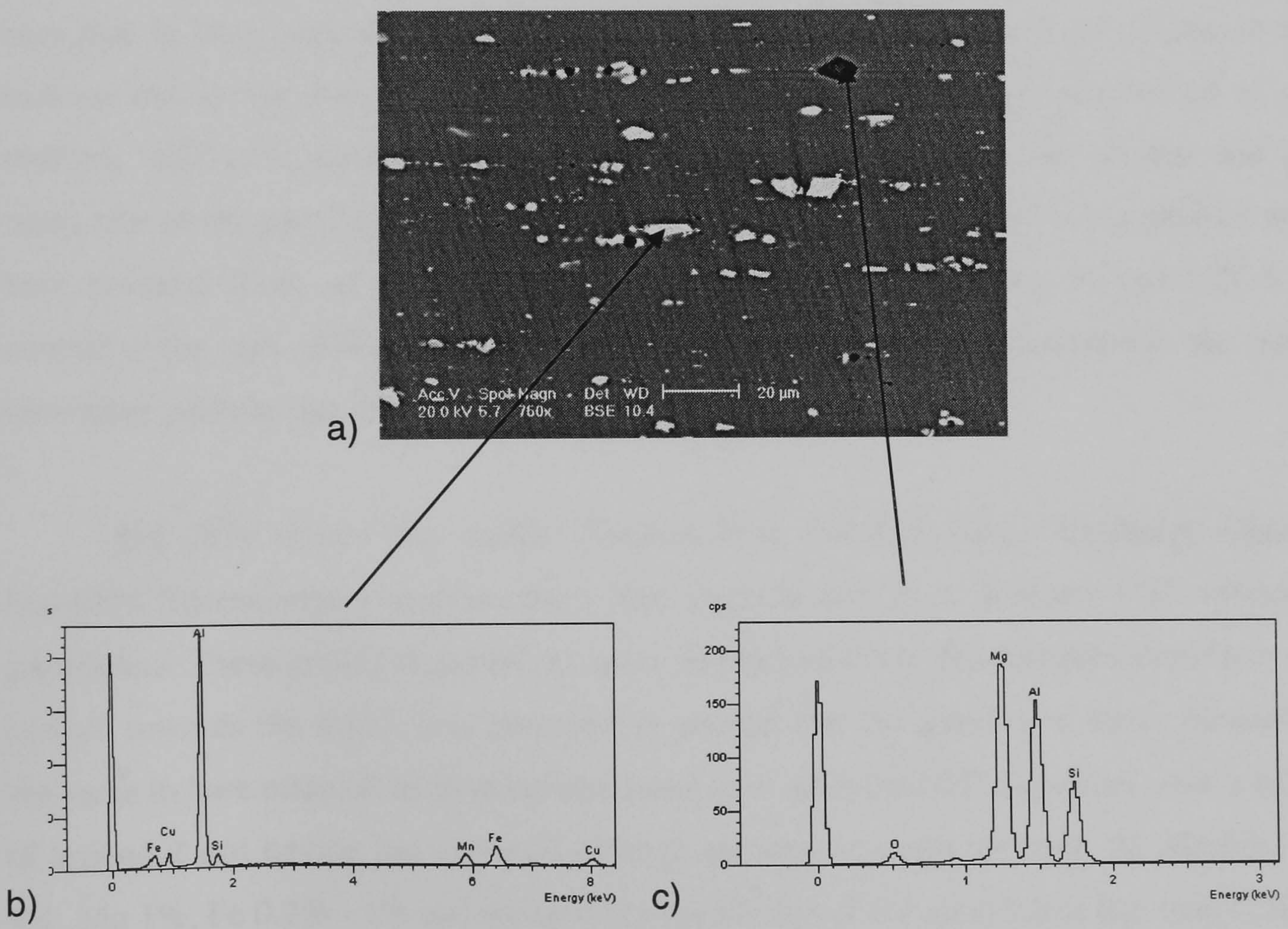

Figure 5.37 a) View of the surface of Al 2024-T3 material treated with UIT showing an oxide particle (black particle, rich O, Al, Mg, Si) and secondary particles phases (white particles rich Al, Fe, Mn, Cu, Si), b) EDS spectrum from precipitation phase and c) EDS spectrum from oxide.

Fig. 5.38 shows cross section view magnifications from plates as received and after being treated with the UIT method. In the left hand side column can be seen different cross section pictures at the same magnification having a calibration bar with a value of 200 μm. A comparison among bare material and the rest of the treated materials just for the left column shows that materials are quite similar in the distribution of the secondary particles through the depth. There is a difference that can be appreciated in this column between bare material and UIT-2-36 condition, it is clear that the size of secondary particles in UIT-2-36 condition is bigger close to the surface that in the bulk; meanwhile in bare material secondary particles there is not a big difference between secondary particles close to the surface and in the bulk.

The right hand side column of fig. 5.38 also shows figures from cross sections of the material with and without different UIT treatments. The magnification in these figures is higher than the left ones having a scale bar equal to 50 μm. A comparison among them says that in bare material secondary particle distributions are quite similar close to the surface and in the bulk, but compared to UIT-1-36 condition the distribution is not uniform. UIT-1-36 condition has less secondary particles close to the surface and the mean size of the particles is bigger than that close to the surface even in comparison with bare material these secondary particles are bigger too. For UIT-2-36 and UIT-3-36 condition the only difference observed in comparison with bare material is the mean secondary particle size that is bigger than in bare material.

Fig. 5.39 shows the results obtained from GDOES (Glow Discharge Optical Emission Spectrometer) analysis from bare material and three different UIT treatment parameters. These graphs represent the mass quantity of every element presented from the surface towards the depth. It is observed in general that the quantity of every element is the same in bare material as in material treated with different UIT conditions after a depth of around 2 μm having the expected average quantity of every element. Al 90-95%, Cu 4%, Mg 1%, Fe 0.7% - 1% and the quantity for the rest of the elements is less than 0.5%.

a)

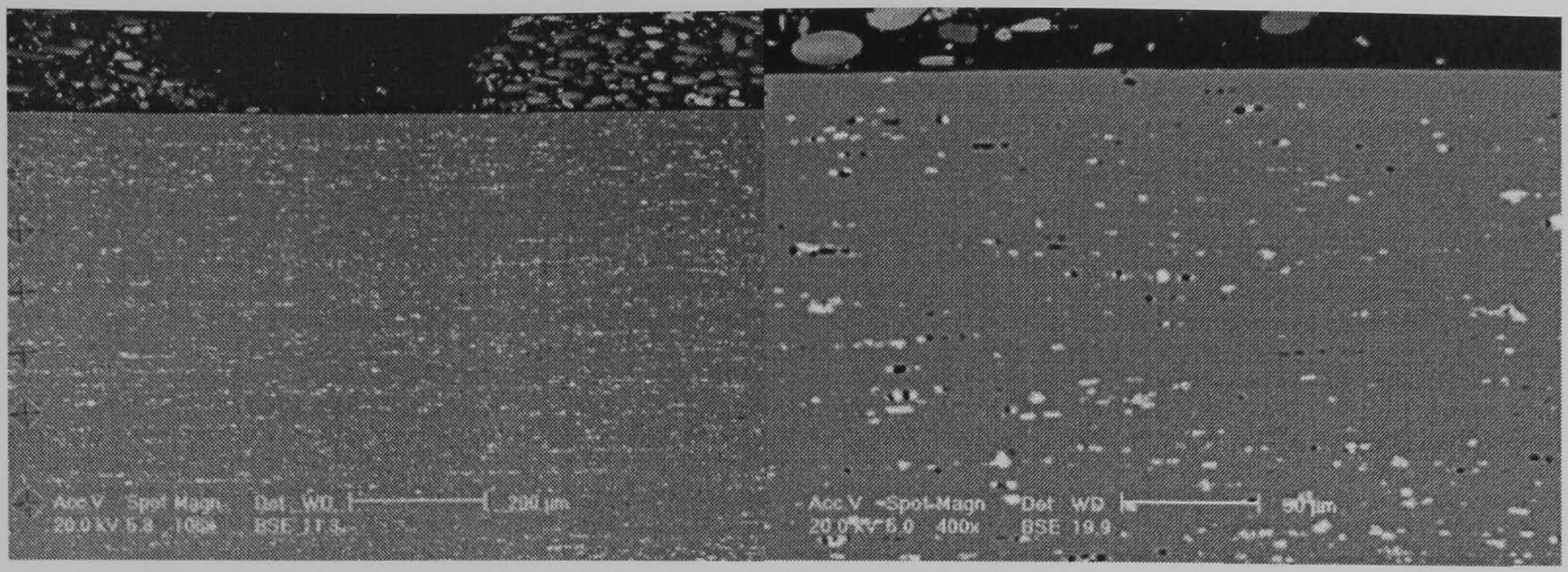

Bare material

b)

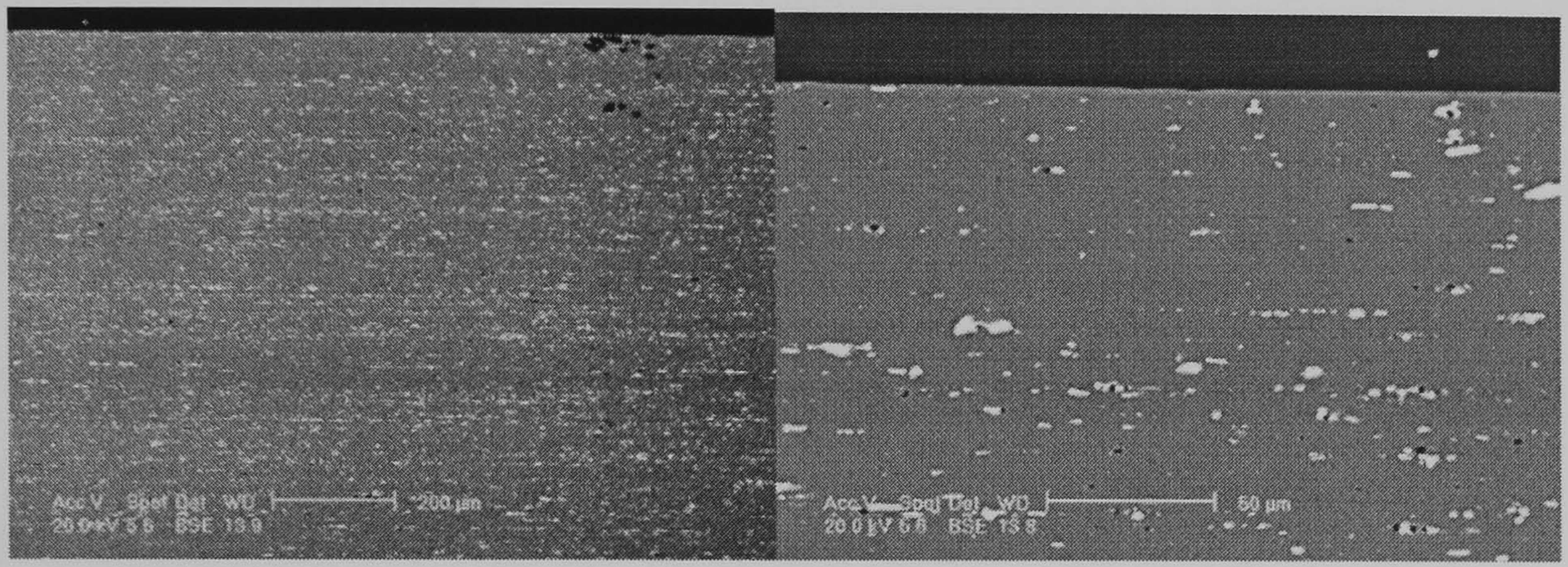

UIT-1-36

c)

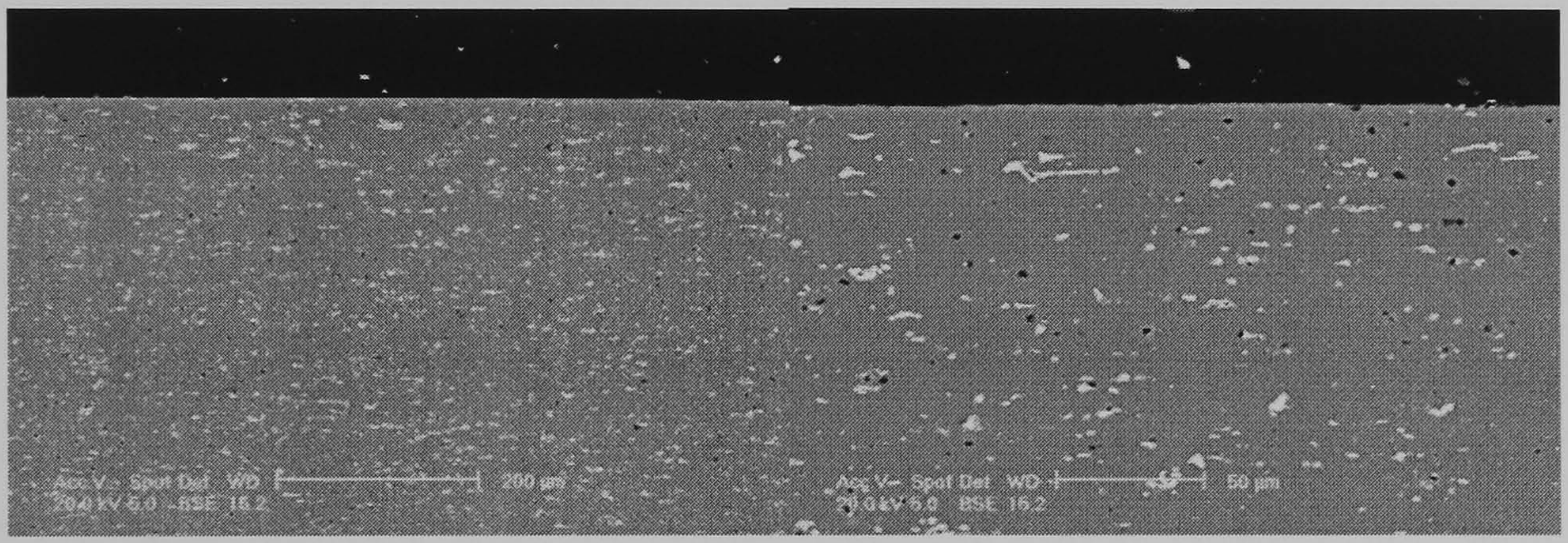

UIT-2-36

d)

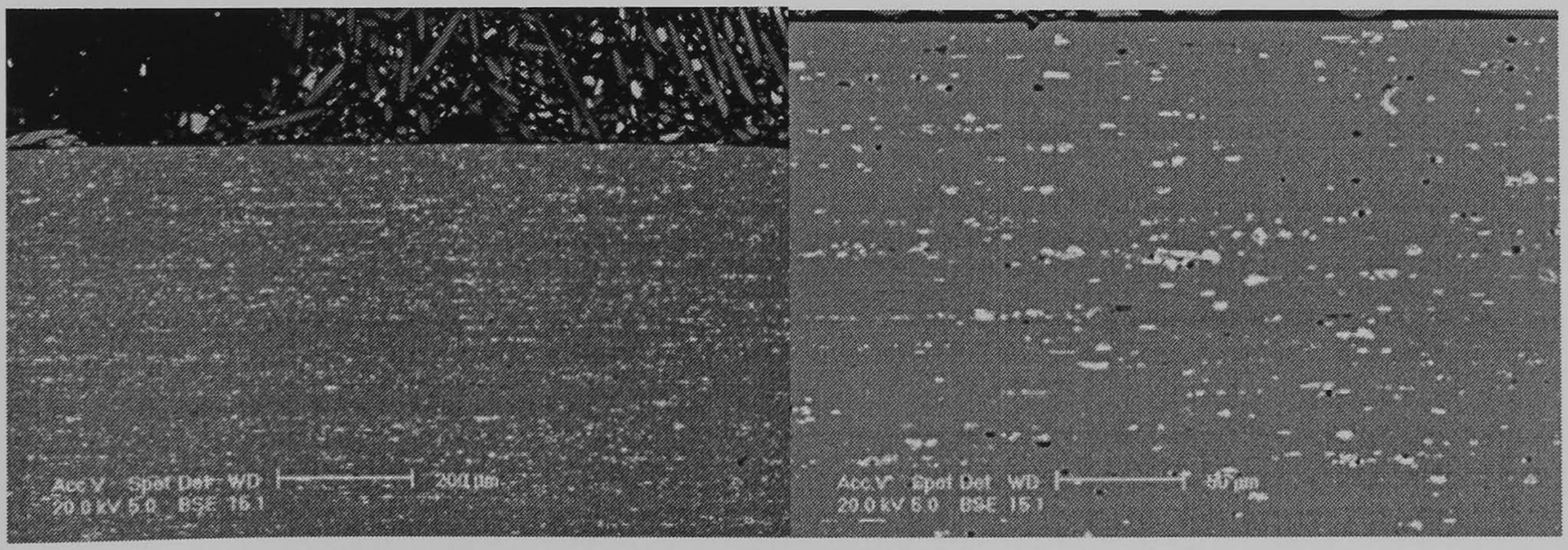

UIT-3-36

Figure 5.38 Magnification of cross section view from specimens as received and after a specific UIT treatment parameters on Al 2024-T3 where can be appreciated the distribution of secondary particle of Al alloy. Right side figures have a bar calibration equal to 200 µm, meanwhile left side figures have a bar calibration equal to 50 µm.

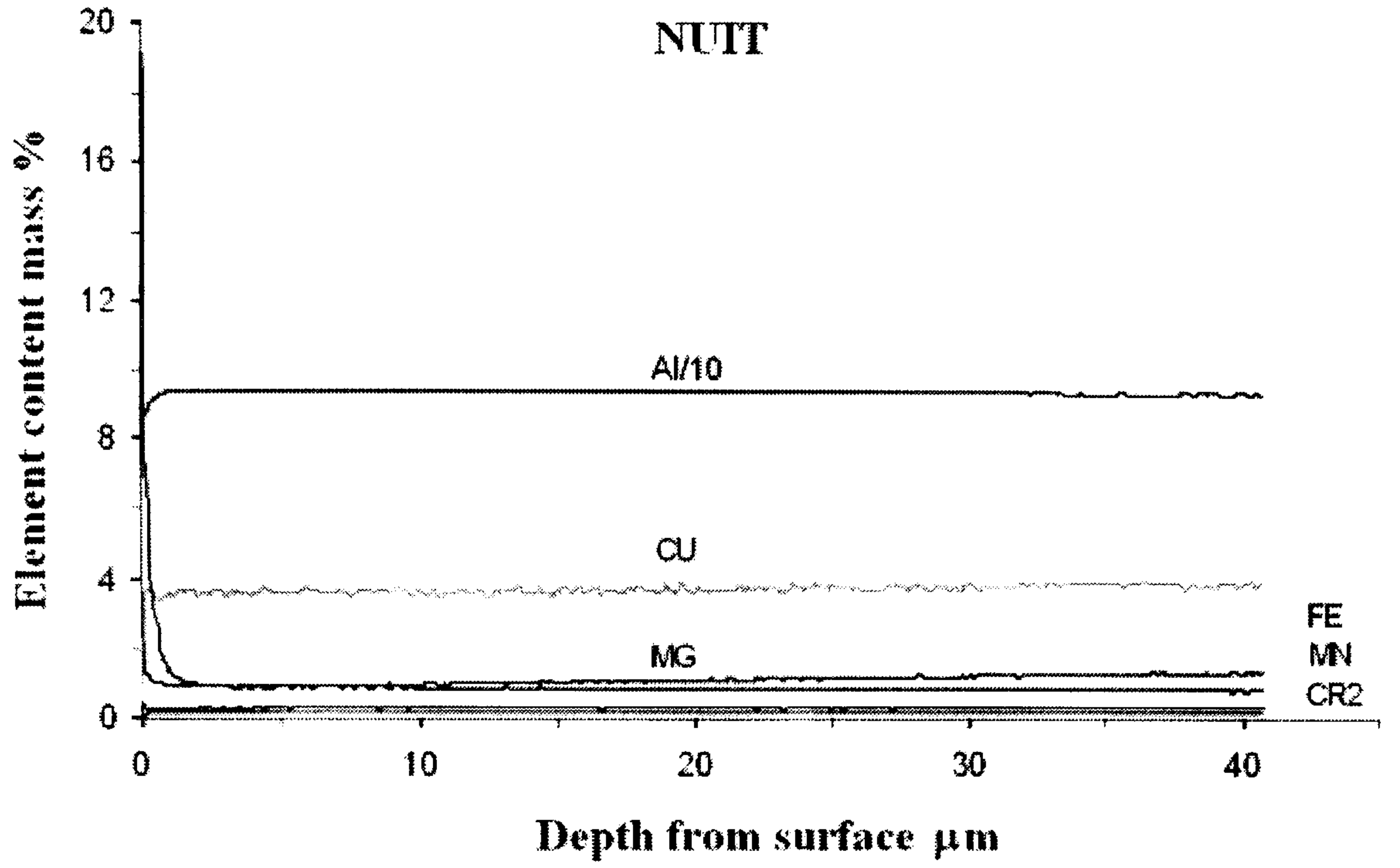

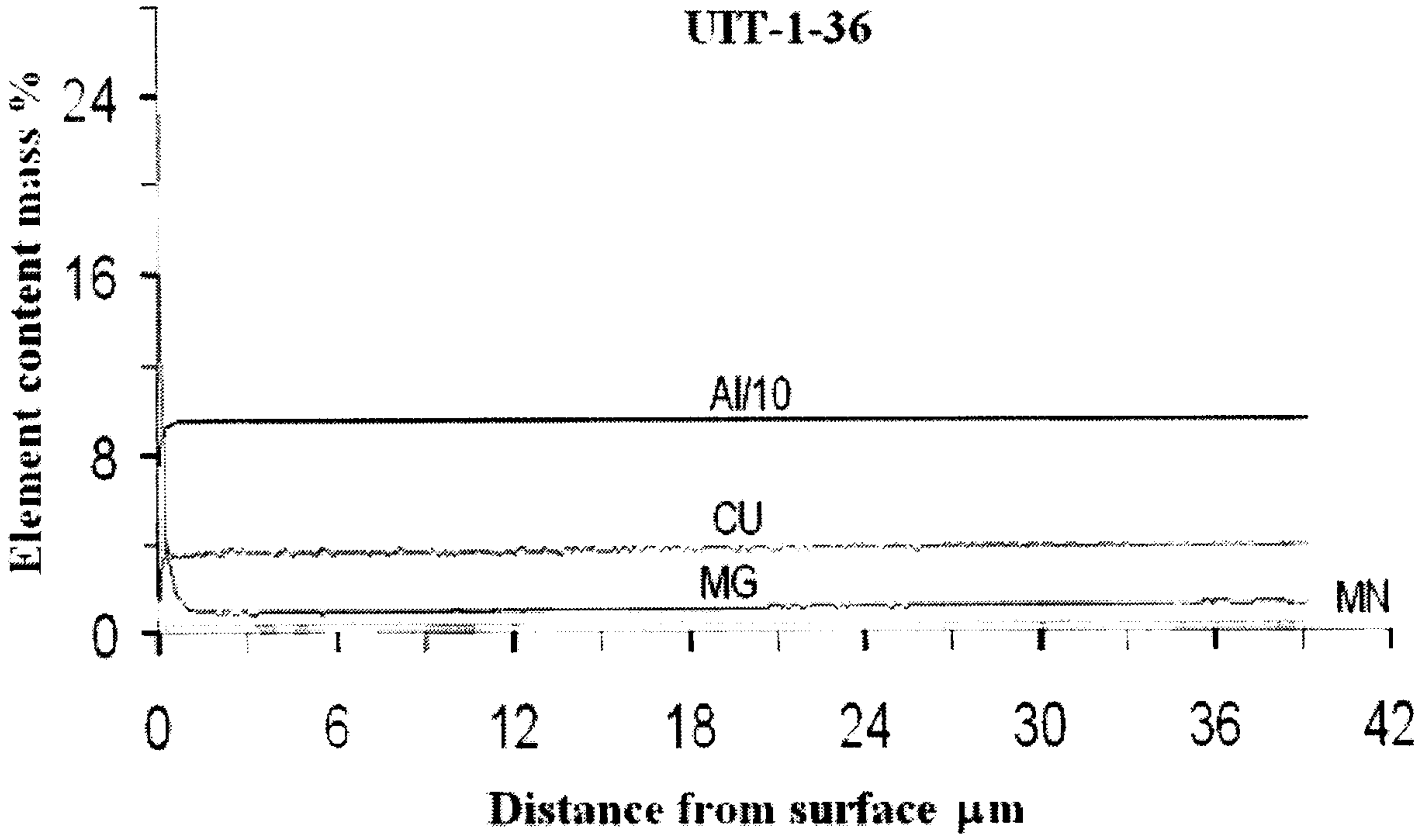

Figure 5.39 GDOES results from Al 2024-T3 bare material and UIT-1

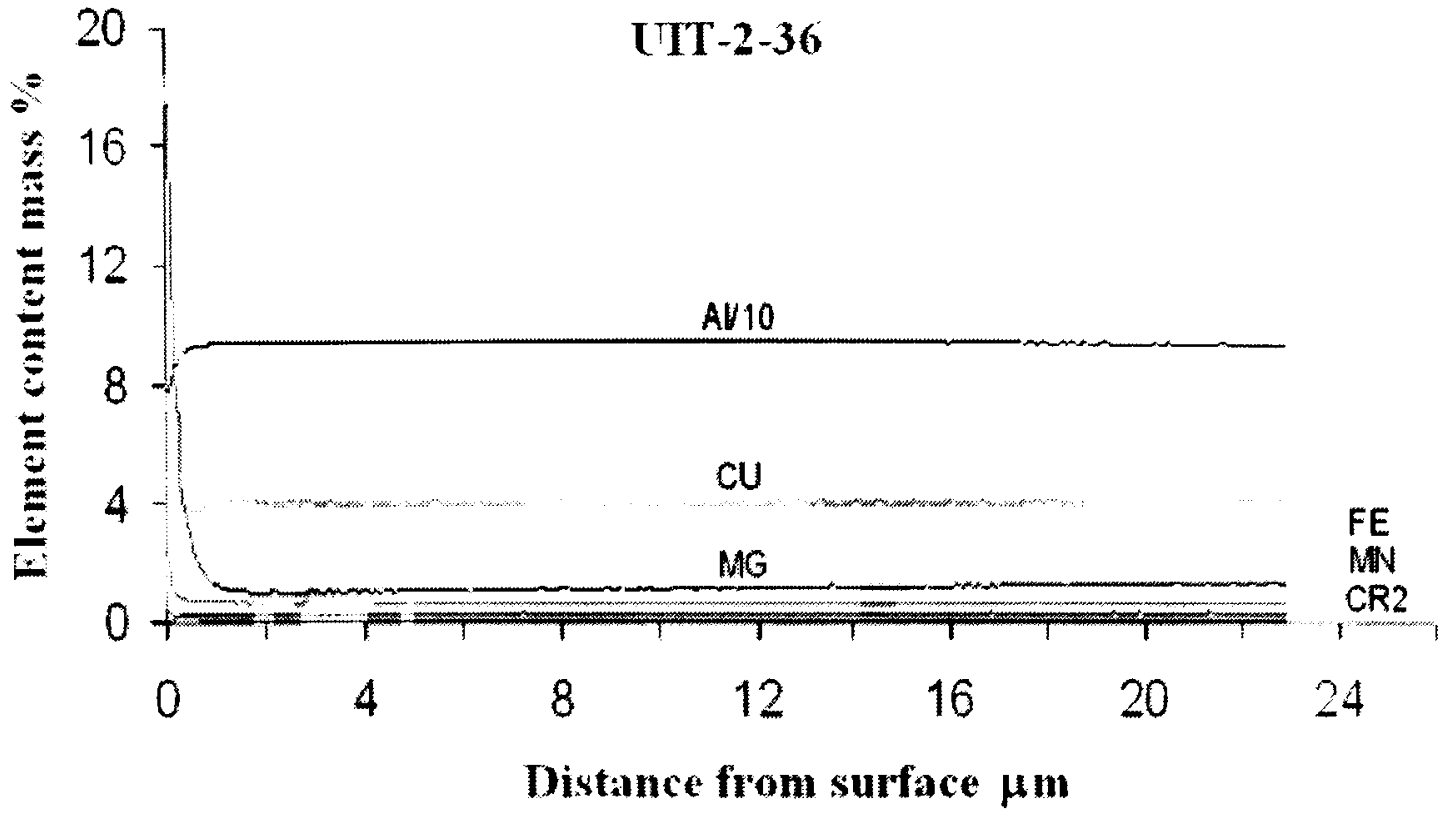

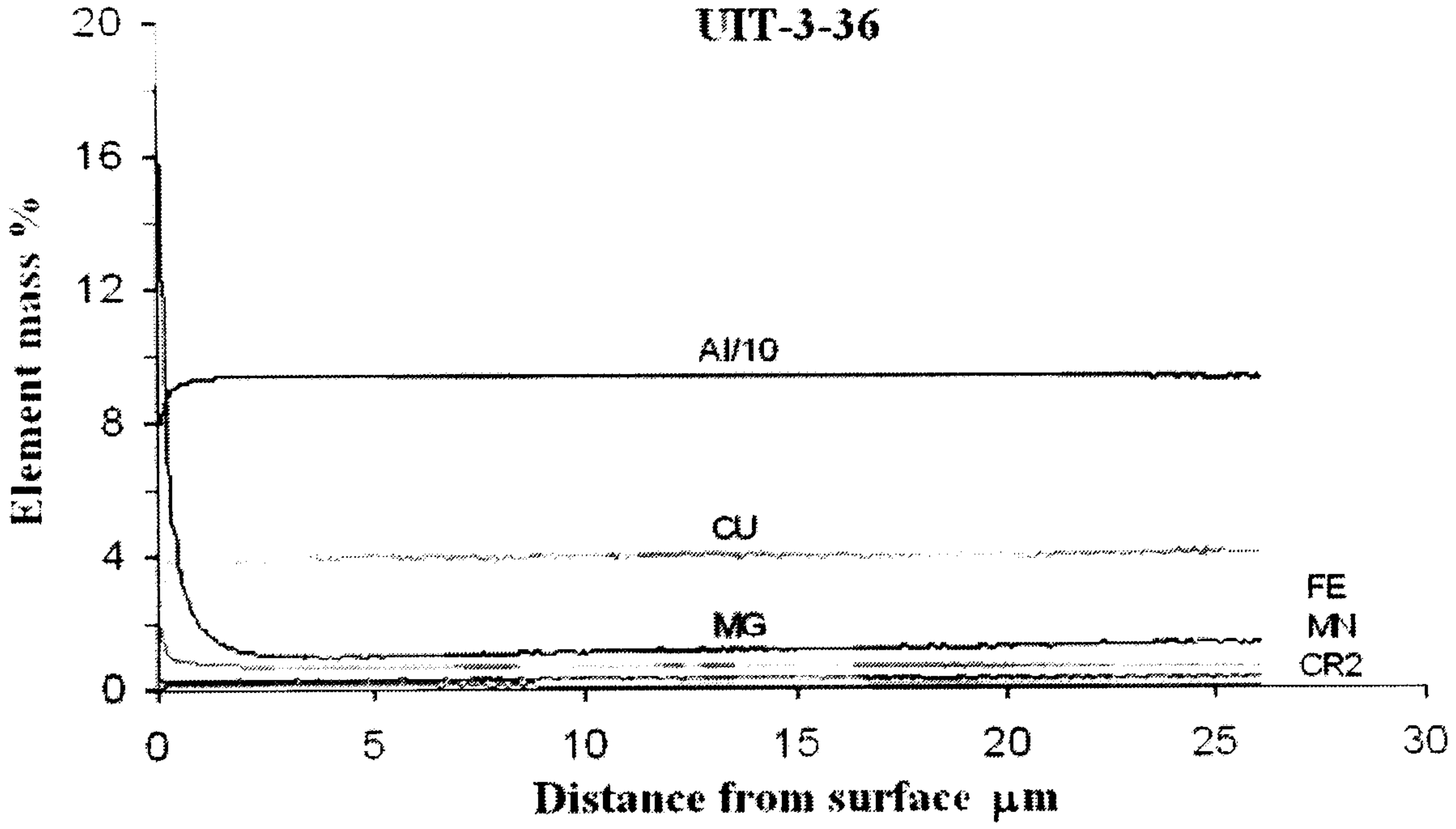

Figure 5.39 Cont. GDOES results from Al 2024-T3 bare material and after different UIT conditions treatment though the depth.

The amount of mass material for every element varied after every UIT condition throughout the first 2 µm. In Bare material can be seen that after Al (around 80%) there was a higher quantity of Mg material (around 19%) followed by Fe and Cu (around 2% each one) and the rest of the elements in minimal proportions.

On the other hand UIT-1-36 condition increased the amount of Mg on the surface from around 19% to around 24% and reduced the Cu amount from around 2% to around 0.8%, the amount of Al kept constant but Fe element quantity was reduced to less than 0.5%.

UIT-2-36 condition the amount of Fe material on the surface increased a lot to around 18%, decreasing in the first µm to around 1%. The amount of Mg on the surface was quite similar to that of Fe being around 17 % followed by Cu with around 1 % and the rest of the elements less than 0.5 %, Al percentage was around 80 %.

For the UIT-3-36 condition, as well as UIT-2-36, the amount of Fe material on the surface increased in the same proportion followed by Mg material quantity of around 16 %, then by the rest of the elements less than 0.5 %, Cu material in this case was as much as in bare material, and Al is around 80%.

Grain size Al 7150-T651

The revelation of grains in etched cross-section for Al 7150-T651 alloy material can be seen in fig. 5.40 where elongated and thin grains can be observed in bare material due to the cold-rolling preprocess the material had. Here can be seen as well the grain size for every UIT condition, there are two columns, on the left one the grain size can be observed for every material at 500x magnification and on the right hand side column the magnification is higher at 1000x.

As one can see, the columns are divided by different kind of materials. In the first row are the pictures of bare material followed by the microstructure for each condition given to the Al 7150-T651 alloy. The next row is occupied by photos from microstructure of material treated under UIT-1-36 conditions, here can be seen the reduction of the grain size on the surface at a shallow depth and some original grain boundaries still preserved as well as the grain refinement, not uniform through the depth.

Figures from the UIT-2-36 condition show that just at the surface small grain size is achieved by this condition and grains just bit smaller than those from bare are observed in the bulk. Microstructure due to UIT-3-36 treatment does not develop a refined grain size, as can be seen in fig. 5.40d. The grain size obtained due to this condition is as if the pancake shape obtained originally is lost and divided longitudinally.

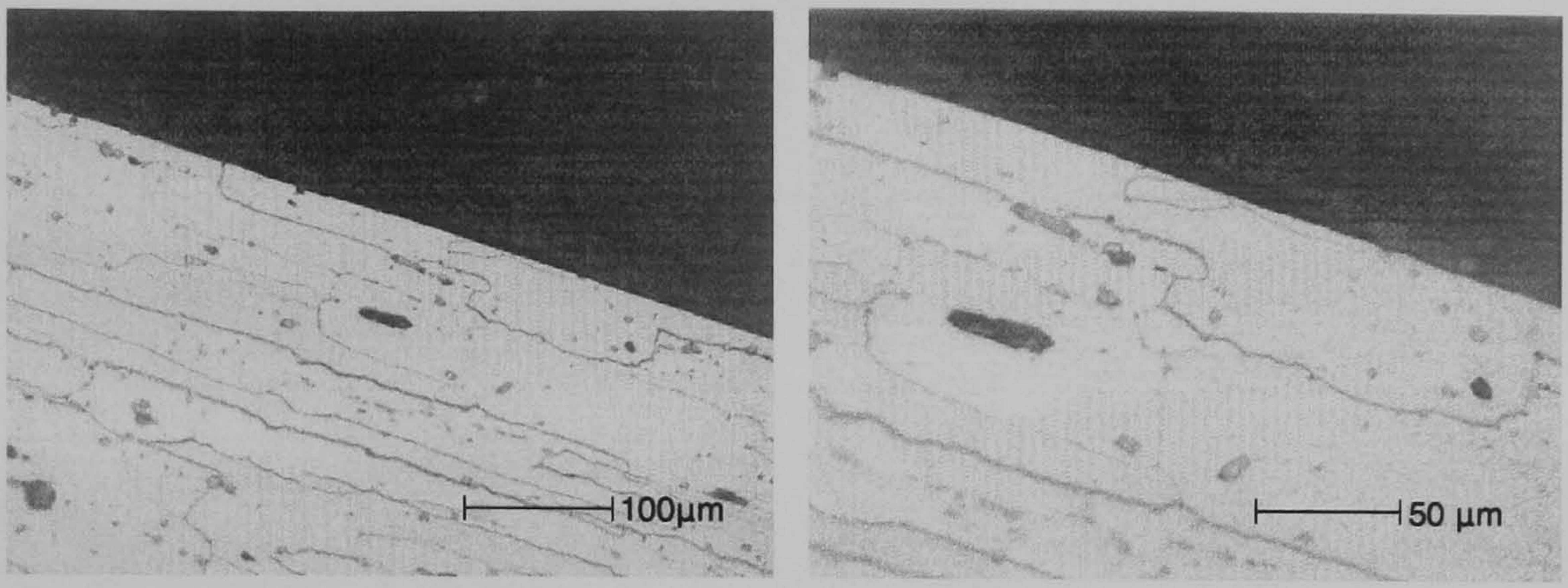

a)

Bare material

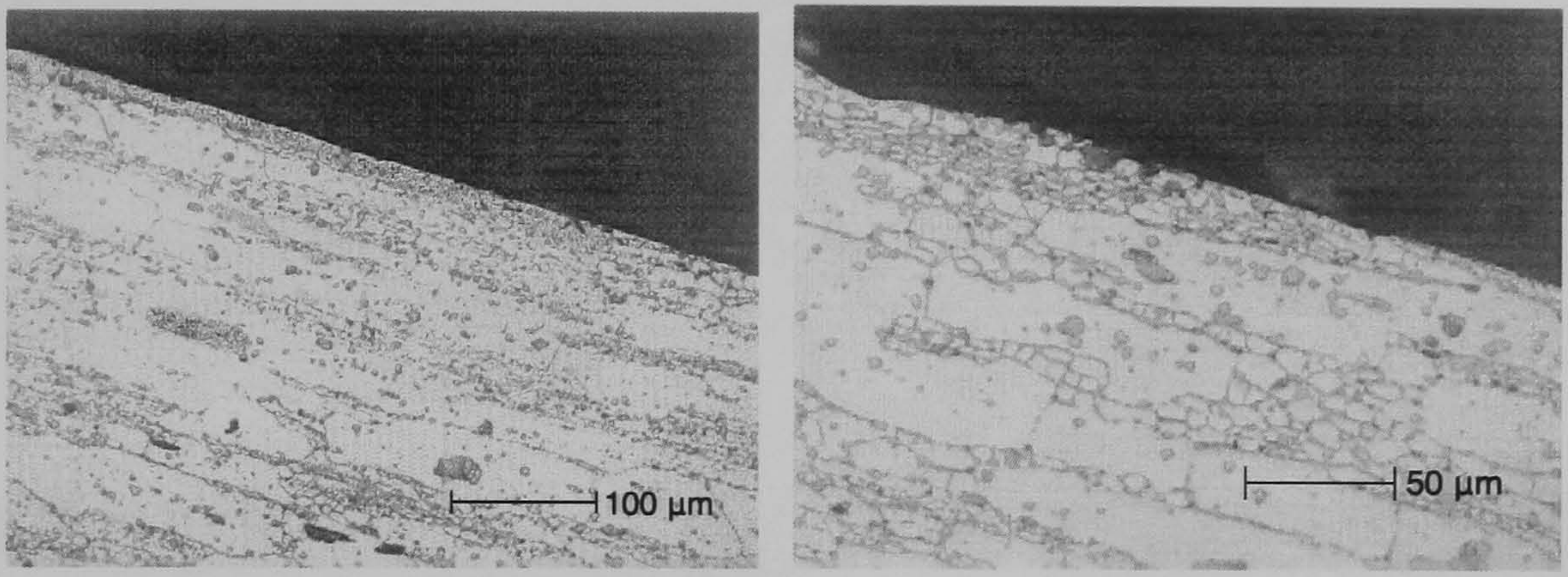

b)

UIT-1-36 Condition

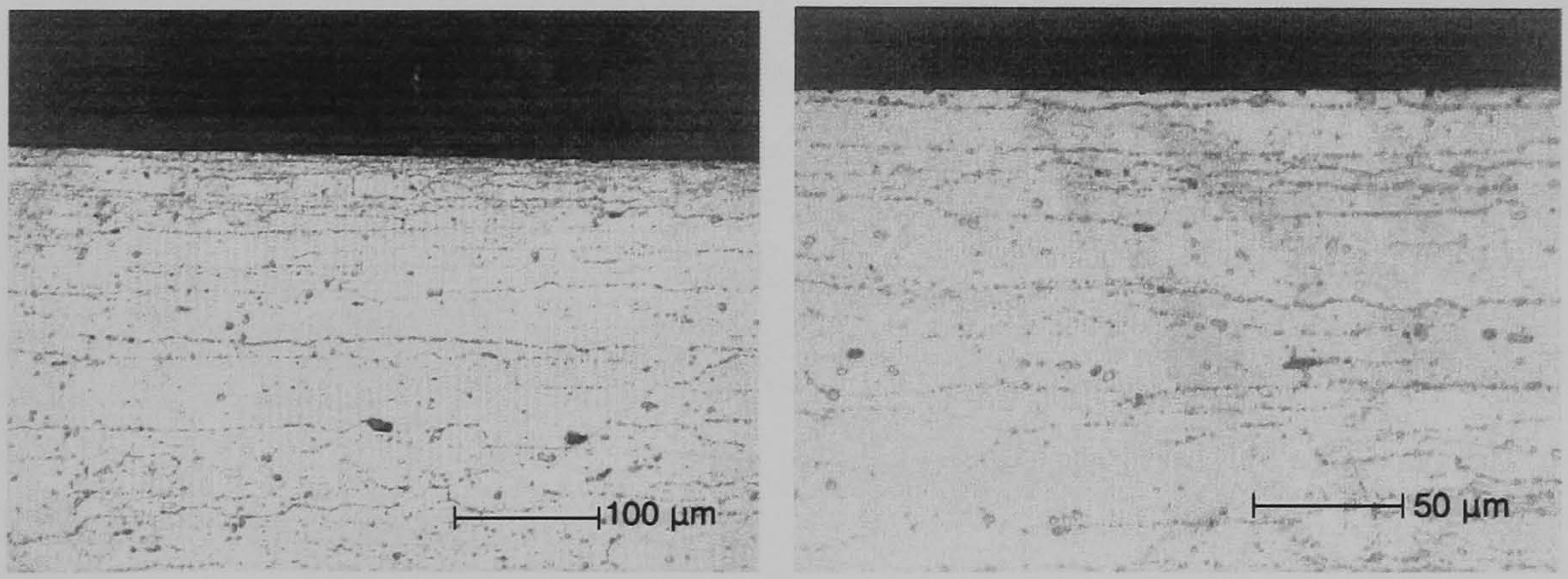

c)

UIT-2-36 Condition

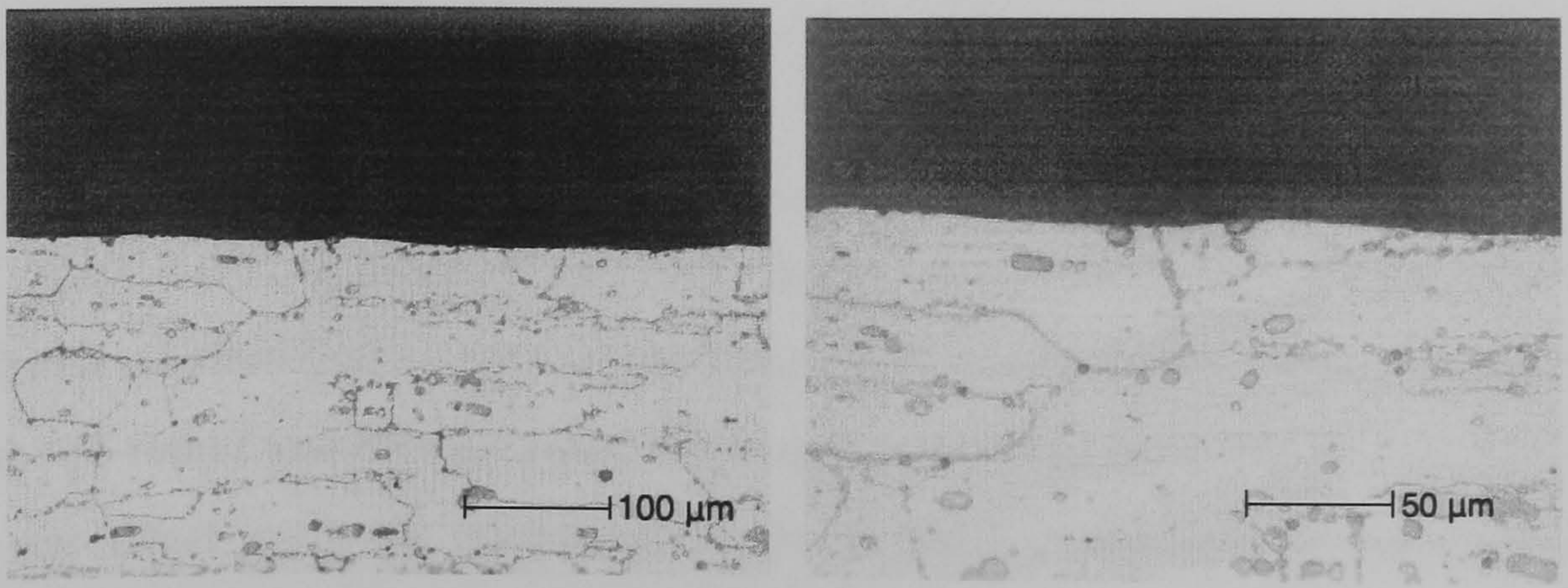

d)

UIT-3-36 Condition

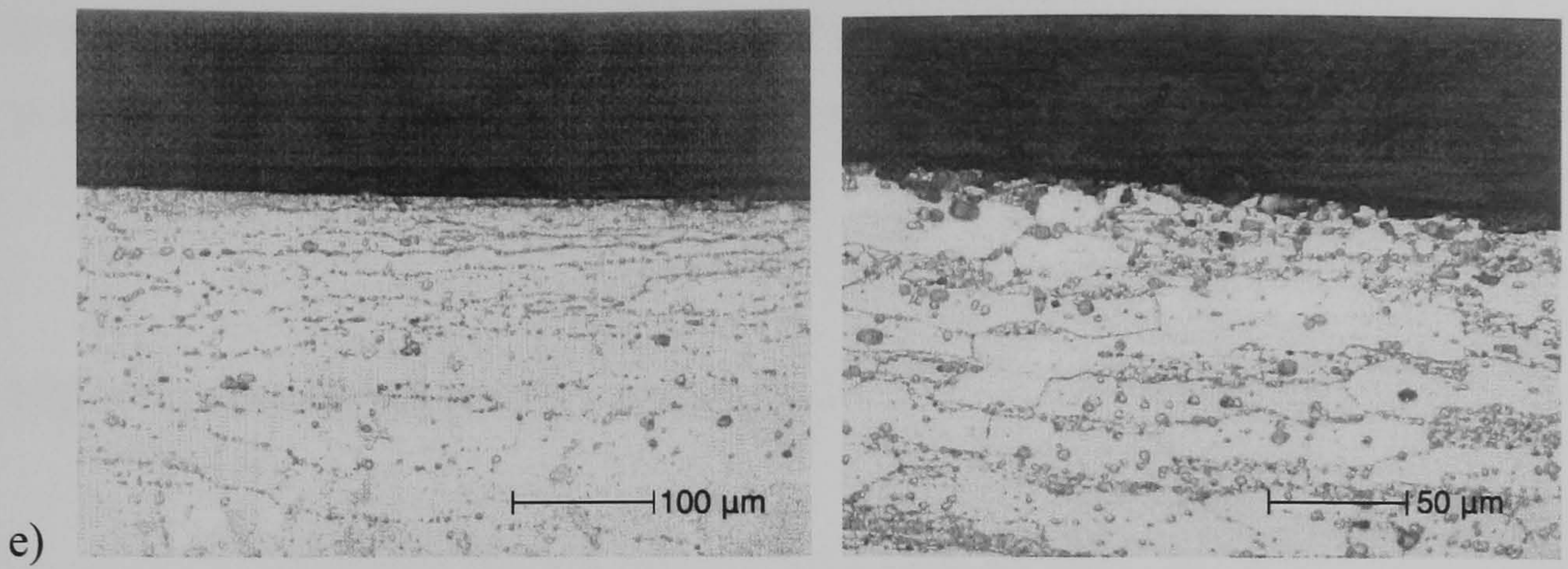

UIT-4-36 Condition

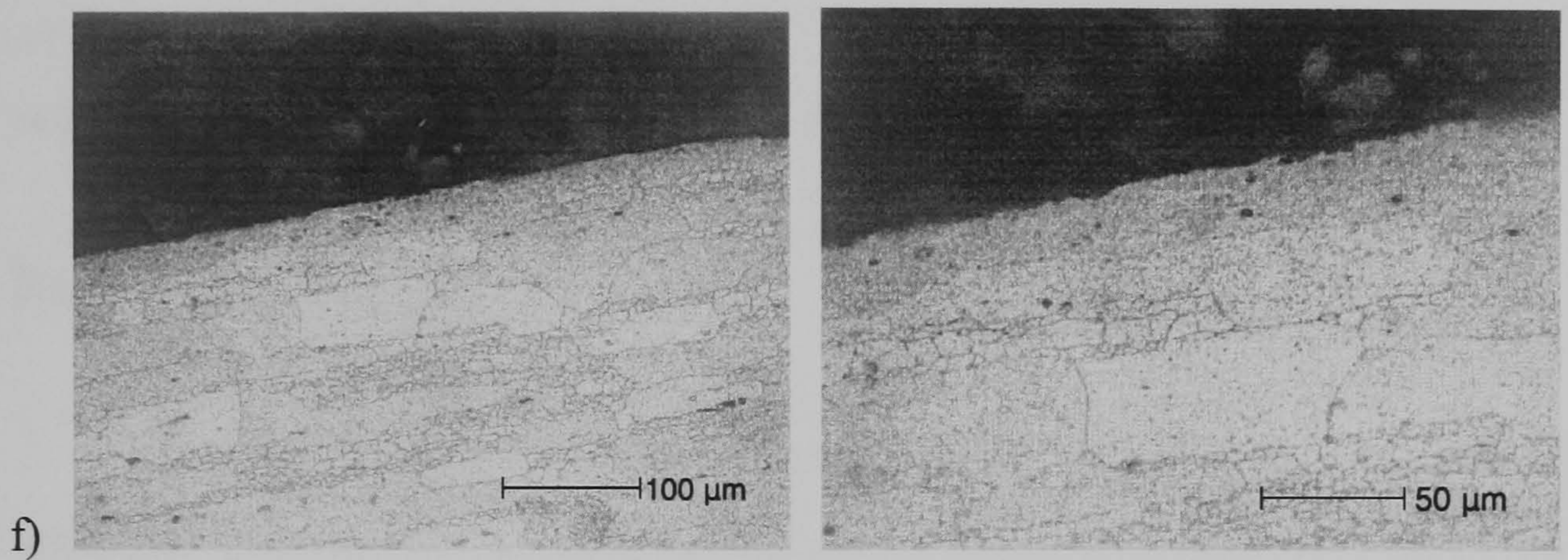

UIT-5-36 Condition

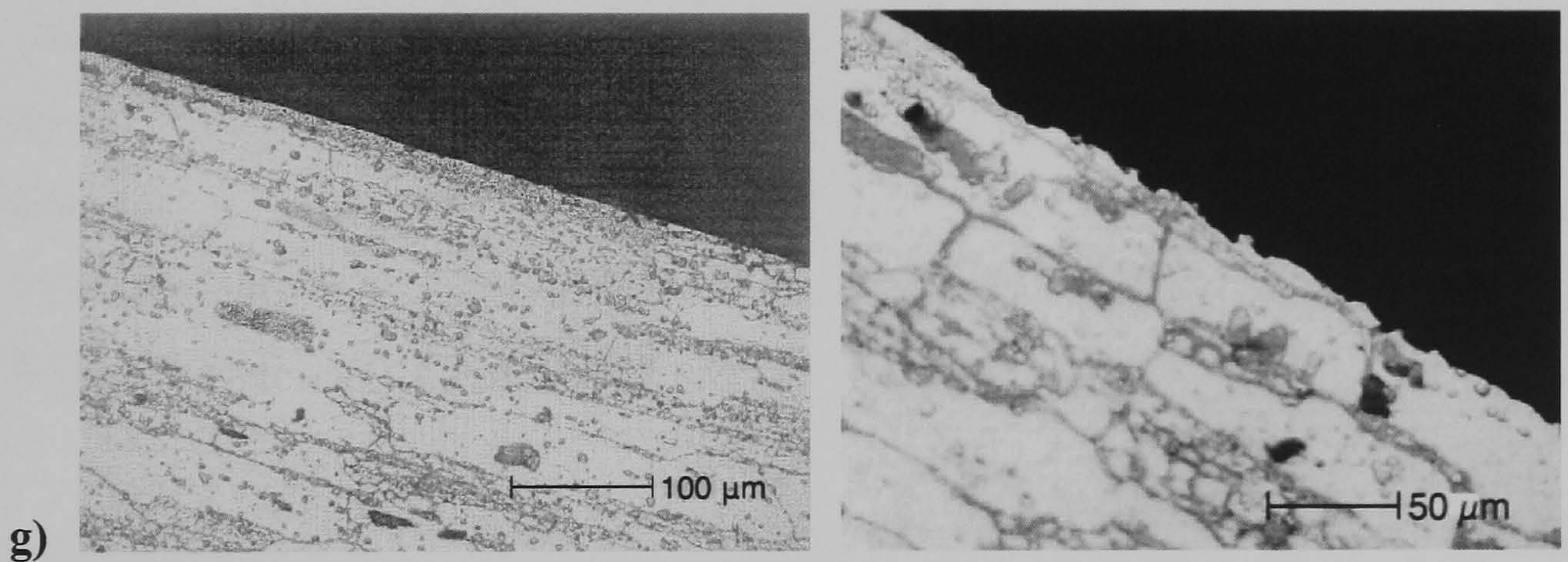

UIT-6-36 Condition

Figure 5.40 Micro grain size of bare material and after different UIT treatments conditions at 500X (Left) and 1000X (Right) magnifications for aluminium 7150-T651 alloy.

UIT-4-36 condition creates small grains but not uniformly, the grains obtained are small and medium grain sizes shown in fig. 5.40e. Close to the surface small and medium grains are found and the presence of pits can be seen on the surface. UIT-5-36 condition does not affect much the microstucture. Some small grains are obtained between bigger grains but in small proportions. UIT-6-36 condition as well as UIT-5-36 creates small grain refinement on the surface and between grains, as well as some pits on the surface.

CRACK GROWTH RATE - Al 2024-T3

Crack growth rate was necessary in order to know the magnitude of the influence of UIT treatment in Al 2024-T3 alloy and the relative roles of initiation and propagation on fatigue endurance. There were different techniques used in this work to try to get information about it.

Replication technique

In order to get information about crack growth rate effects due to UIT treatments replicas were taken from specimens used in fatigue tension tests (dog bone shape). Specimens made of virgin material under 225 MPa and 243 MPa stress ranges, as well as specimens treated with UIT-1-27 condition within a length of 35 mm in the gauge zone at the same stress range were monitored using the replication technique. It was expected an alteration in fatigue life of the specimen due to the repetitive halting of the test and the use of acetone in the cracks, but comparing the results obtained here with those obtained for S-N curves, they fall close to the curve (Fig. 5.4).

The replication technique was used for four sides of the specimen the edge being the most difficult to get replicas because of the curved shape, for the case of bare material. In treated specimens it was possible to take replicas just from the flat faces, and good replicas could not be obtained from the edges due to the severe deformation.

Table 5.3 shows the data obtained from the replication technique taken from bare material for both amplitudes of load. Crack lengths observed on the four sides were registered in this table and the presence of a secondary crack was observed which later joins the main crack accelerating its propagation. A column of da/dN (m/cycle) is in this table and a different formula to the secant formula was used to calculate da/dN when two cracks join to form one, this formula is:

$$da/dN = (a_{i+1} - (a_i + a_j))/(N_{i+1} - N_i)$$

Where a_j is the crack length of the small crack considered that joins up with the bigger one and a_i is the crack length of the bigger crack [176].

Table 5.3 Data of crack length "a" and crack growth ratio "da/dN" from Al2024-T3 bare material tested at two different stress ranges.

Cycles	Crack length 2a μm	2^{nd} Crack length 2a μm	â (*m*)	â (*m*) 2^{nd} crack	da/dN (m/cycle)	da/dN (m/cycle)
Specimen at stress range of 225 MPa (Untreated)						
Side A (Front Face)						
280500	45.35					
306000	108.88		38.557 E-6		1.245 E-9	
331500	253.94		90.705 E-6		2.844 E-9	
357000	483.77		184.428 E-6		4.506 E-9	
382500	893.95		344.43 E-6		8.042 E-9	
Side B (Back Face)						
306000	39.62					
331500	93.39		33.252 E-6		1.054 E-9	
357000	295.73		97.28 E-6		3.967 E-9	
382500	519.37		203.775 E-6		4.385 E-9	
Specimen at stress range of 243 MPa (Untreated)						
Side A (Front Face)						
208000	106.01					
216000	276.65		95.665 E-6		10.665 E-9	
224000	655.2		232.963 E-6		23.659 E-9	
Side B (Back Face)						
168000	14.31					
176000	141.41		38.93 E-6		7.943 E-9	
184000	193.59		83.75 E-6		3.261 E-9	
192000	224		104.398 E-6		1.9 E-9	
200000	268.32	231.15	123.08 E-6		2.77 E-9	
208000	301.69	270.27	142.503 E-6	125.355 E-6	2.085 E-9	2.445 E-9
216000	415.2	454.96	179.223 E-6	181.3 E-6	7.094 E-9	11.54 E-9
224000	1983.32		599.63 E-6		69.57 E-9	
Side C (Right Edge)						
208000	55.24					
216000	454.34		127.395 E-6		24.943 E-9	
224000	1656.77		527.778 E-6		75.151 E-9	
Side D (Left Edge)						
224000	850		425 E-6			

Data obtained in table 5.3 were plotted and compared as seen in fig. 5.41 where basically three flat faces were important, two from the specimen under 225 MPa stress range and one from specimen under 243 MPa stress range where a coalescence of two cracks was observed. It is observed that crack propagation for specimen under 243 MPa stress range is faster than that under 225 MPa stress range. As it can be seen in table 5.3 the quantity of cracks observed in specimen under 243 MPa stress range is bigger than that under 225 MPa stress range, finding on each side at least one crack.

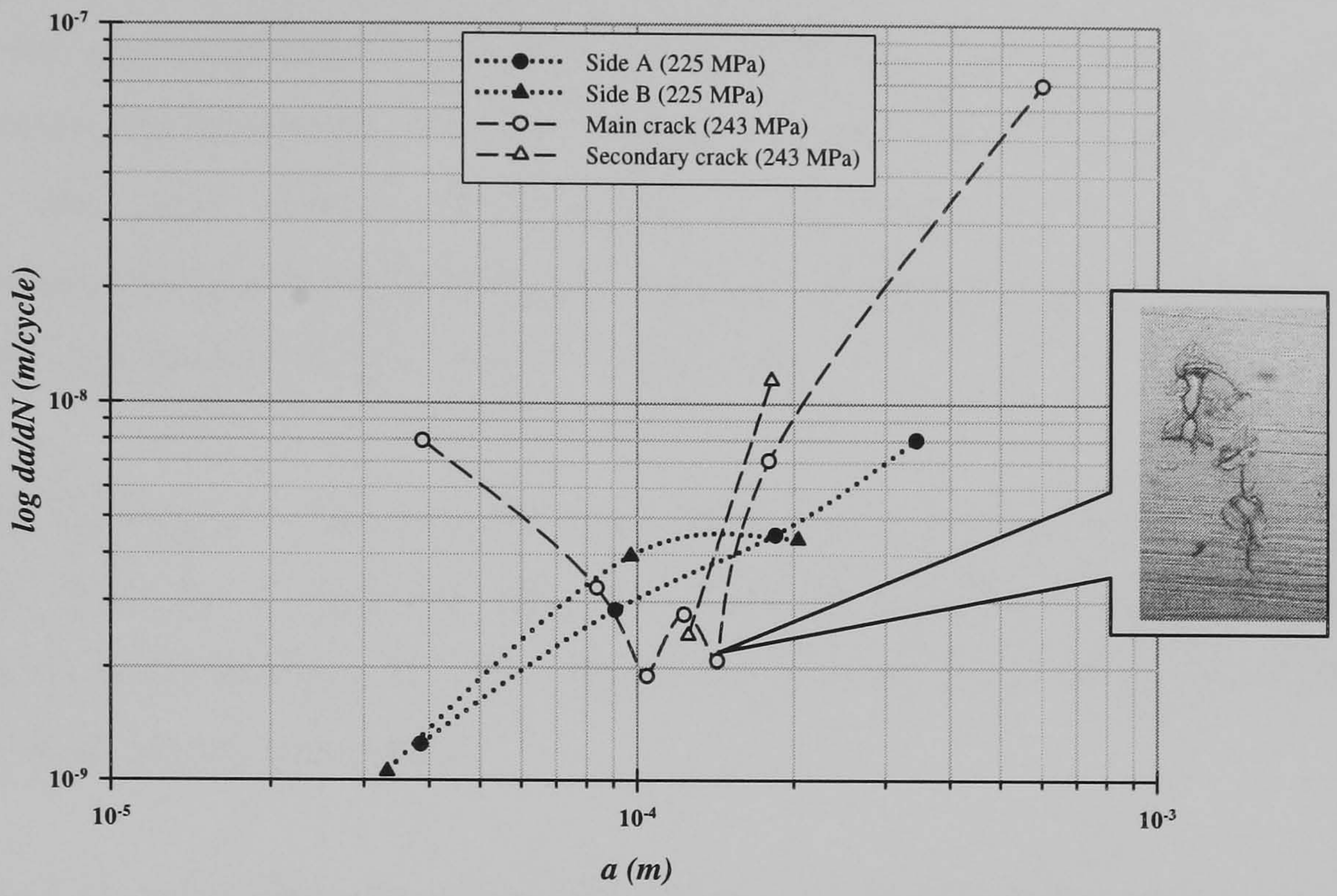

Figure 5.41 Plot of crack growth data obtained from dog bone shape specimens made of Al 2024-T3 virgin material using the replication technique under 225 MPa and 243 MPa stress ranges. Picture on the right shows the secondary crack (top) and the main crack (bottom).

Table 5.4 Data of crack length "a" and "da/dN" from Al 2024-T3 material treated under UIT-1-27 condition at two different stress ranges.

Cycles	Crack length 2a (μm)	Crack length a (m)	â (*m*)	da/dN (m/cycle)
Specimen at stress range of 225 MPa (UIT-1-27 35 mm)				
Side A (From face)				
72900	147.109	7.3554E-05		
75600	1071.668	53.58E-05	30.47E-05	1.7121E-07
81000	2104.253	105.21E-05	79.39E-05	9.56E-08
Specimen at stress range of 243 MPa (UIT-1-27 35 mm)				
Side A (Front face)				
86048	476.829	23.84E-05		
88300	484.7	24.23E-05	24.03E-05	1.747E-09
90350	515.58	25.77E-05	25.007E-05	7.5317E-09
92400	564.02	28.201E-05	26.99E-05	11.814E-09
94500	579.98	28.99E-05	28.6E-05	3.8E-09
98780	630.924	31.54E-05	30.27E-05	5.9514E-09
102200	1385.22	69.26E-05	50.4E-05	110.277E-09
105200	1399.53	69.97E-05	69.61E-05	2.385E-09
109200	1435.48	71.77E-05	70.87E-05	4.493E-09
114000	1606.71	80.33E-05	76.05E-05	17.83E-09

Table 5.4 shows the data obtained from specimens treated under UIT-1-27 condition at two different stress ranges which are the same as those used for bare material, and a difference from specimens made of bare material that it was not possible to get information from the edges. Using data from table 5.4 a graph of "a" Vs da/dN was obtained and is showed in fig. 5.42. Here it is not possible to see a pattern that the crack follows in the specimen under stress range of 225 MPa because of the small number of scattered points. Points obtained from specimen under stress range of 243 MPa were more numerous. The graph obtained from replicas of the specimen treated at UIT-1-27 condition along 35 mm and loaded at stress maximum of 270 MPa looks like acceleration and after that deceleration, twice before the final crack.

This behaviour is observed in the specimen made of bare material and under the same stress range but it happened only one time meanwhile in treated specimens it happens twice and it seems as if crack growth rate decrease is always at around $2X10^{-9}$ m/cycle to increase again drastically.

Fig. 5.43 shows the mix of the data plotted for bare material and for material treated under UIT-1-27 condition comparing the behaviour of two stress ranges used. Open symbols represents data obtained from specimens subjected to a stress range of 225 MPa and closed symbols represent the data obtained from specimens loaded under stress range of 243 MPa. In this plot it is observed that only in specimens made of bare material were smaller cracks found compared to those from treated specimens.

Specimens loaded under the same stress range of 225 MPa bare and treated are compared in this plot, and it is observed that in untreated specimens a steady increment in crack growth rate in two cracks, one each side, is achieved with longer crack increments. In treated specimens a dramatic decrement from a very high crack growth rate is obtained but for shorter crack increments.

Specimens loaded with higher stress range show that for untreated material a decrement and an increment before failure are observed with shorter crack increments, meanwhile in treated specimens an increment, decrement, massive increment, massive decrement and increment before failed are achieved in longer crack increments.

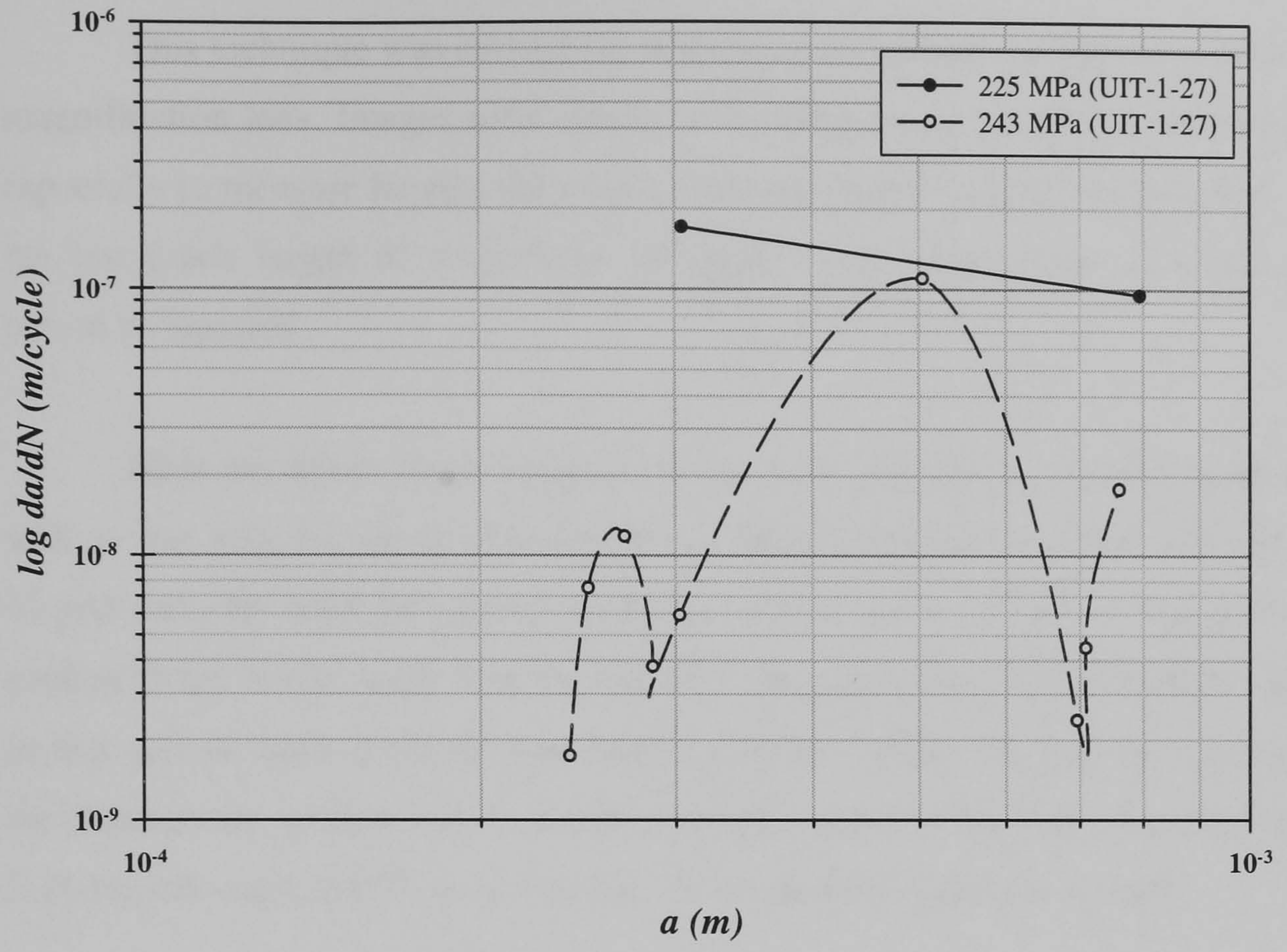

Figure 5.42 Crack growth ratio graph from data obtained from dog bone specimens made of Al 2024-T3 alloy treated in four sides at UIT-1-27 condition along 35 mm in the gauge zone.

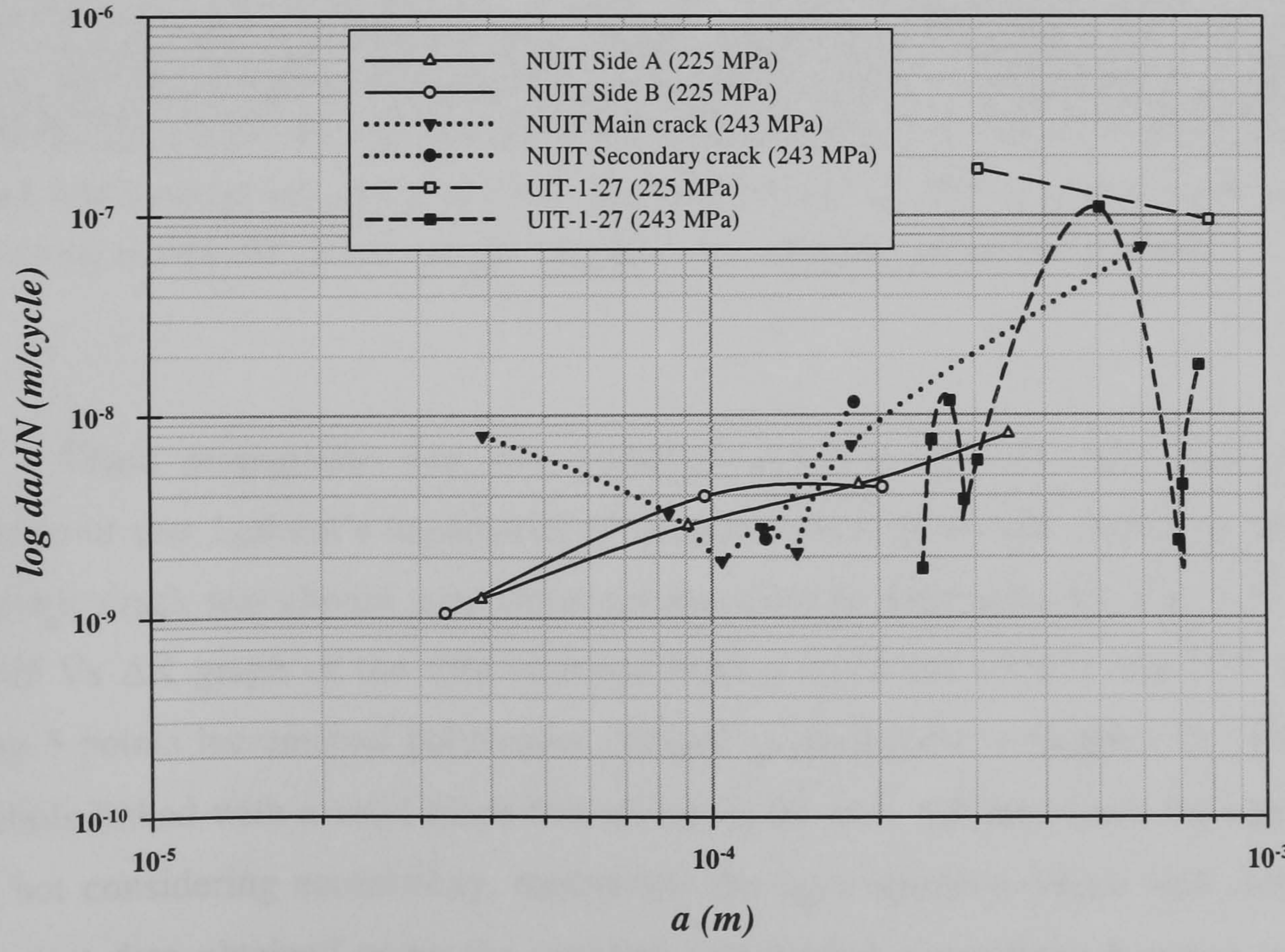

Figure 5.43 Comparison among the data obtained in specimens made of Al 2024-T3 without treatment and treated at UIT-1-27 condition along 35 mm in the gauge zone and under the same stress range.

Optical technique

This technique was carried out with the aid of a high resolution camera and a high magnification lens. Images were stored on a computer and with the aid of a programme especially to measure lengths the cracks were monitored through the test. Fig. 5.44 shows the last crack length of a specimen designed to get information of crack growth rate before it fractured.

Here the notch shape (centre) can be seen and the pattern the crack followed as well as the way the crack was monitored. Highlighted are the start and the end of the treated zone for each side of the notch tip, and it can be observed the right side treated zone is closer to the notch than the left one. The specimens with treatment were designed in that way so each crack tip was named with the suffix "10 mm" or "15 mm" meaning the distance the treated zone is placed from the centre of the plate. Because of that in fig. 5.44 the left crack will have as a suffix 15 mm and the right one 10 mm.

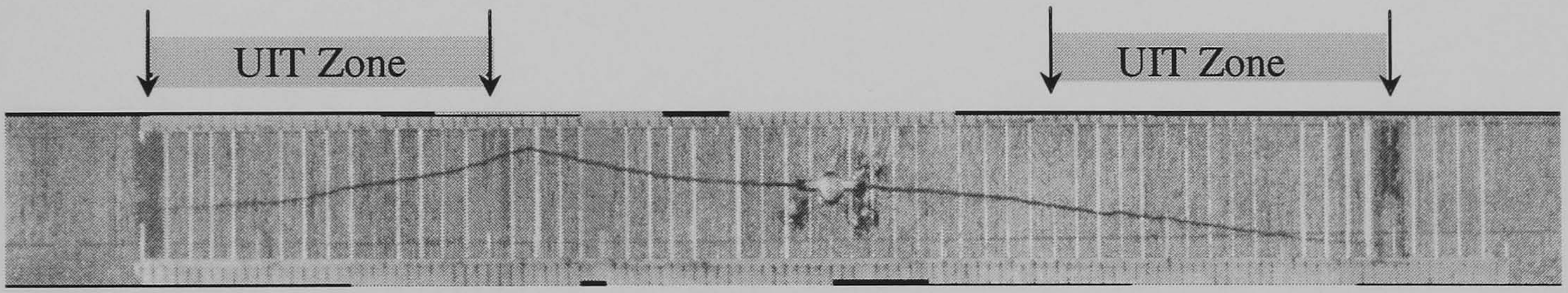

Figure 5.44 Crack growth pattern in a M(T) specimen made of Al 2024-T3 pointed out the position of treated zone in every side of the notch tip. Last photo obtained before the specimen fractured.

Crack propagation was unsymmetrical between left and right crack tips, and because of that Laurent's expansions of complex stress potentials method to analyse an eccentric crack was chosen [177]. These are described in **Appendix A9**. Fig. 5.45 shows a da/dN Vs ΔK graph of the data obtained from a specimen without any UIT treatment using 5 points incremental polynomial method as mentioned in **chapter IV**. The closed symbols linked with a solid black line represent the data obtained from the equation for ΔK not considering eccentricity, meanwhile the open symbols linked with dotted lines represent data obtained using the equation considering eccentricity between two crack tips, left and right.

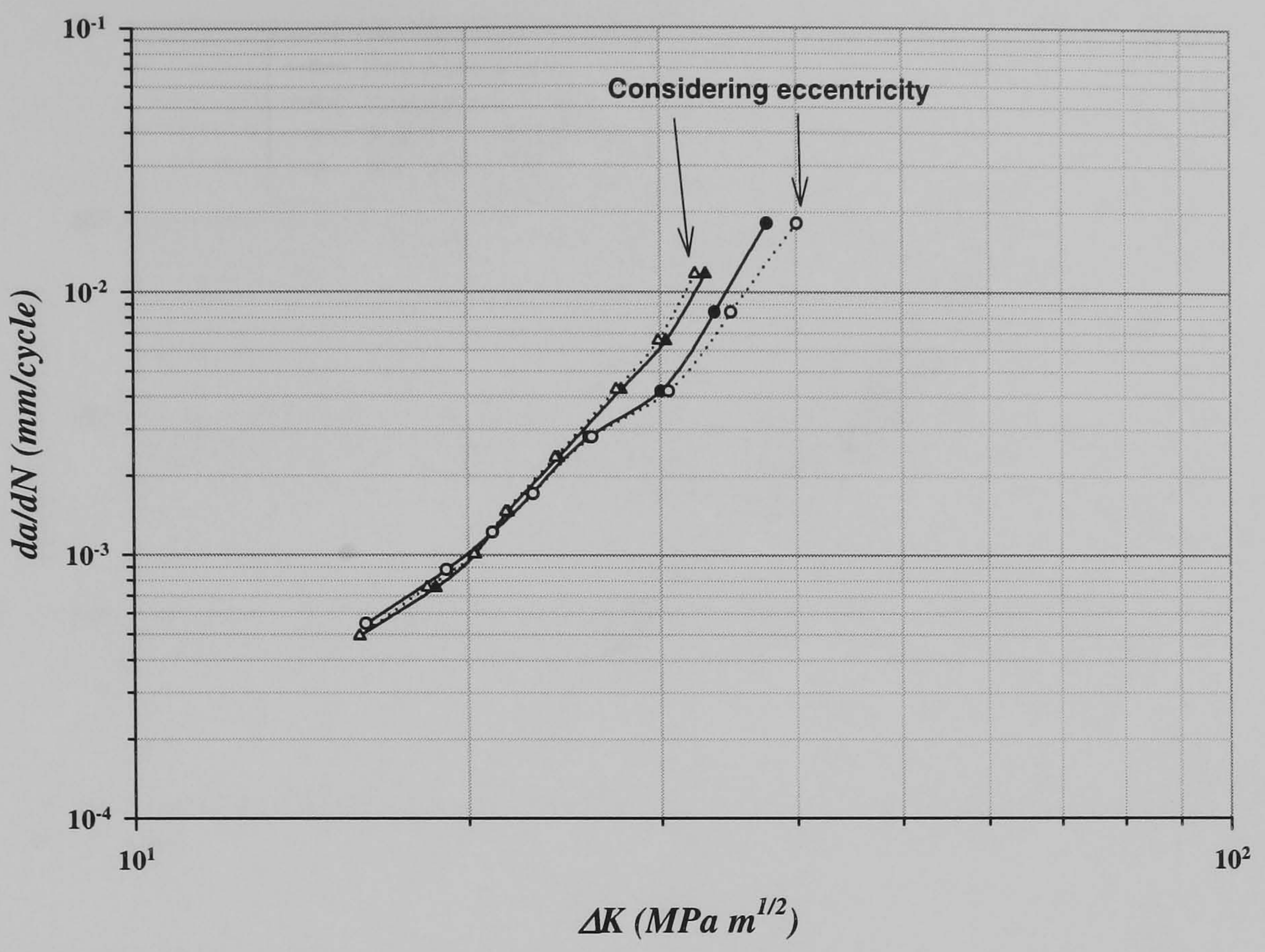

Figure 5.45 Crack growth ratio plot from M(T) specimen Al 2024-T3 bare material using 5 points method together with and without eccentricity considerations.

It is seen that the data are quite similar and they do not differ much in most of the process, but in the last readings (higher ΔK's) they do. The data plotted were obtained using Laurent's expansions of complex stress potentials method together with a incremental polynomial 5 points method, for each crack tip independently.

Fig. 5.46 shows data comparison between a specimen made fully of virgin material and a specimen in the same conditions but with two strips of UIT-1-36 treatment placed one on each notch tip side at different distances from the plate centre. Closed symbols linked with the wider solid black lines are from specimens without any treatment, the rest represent the crack growth rate pattern obtained from material with treatment. It is observed that at lower stress intensity values a constant slope is followed by both specimens with their respective crack tips growth. This slope is altered before 20 MPa $m^{1/2}$ ΔK value in specimens with treated zones suggesting that retardation in crack growth exists.

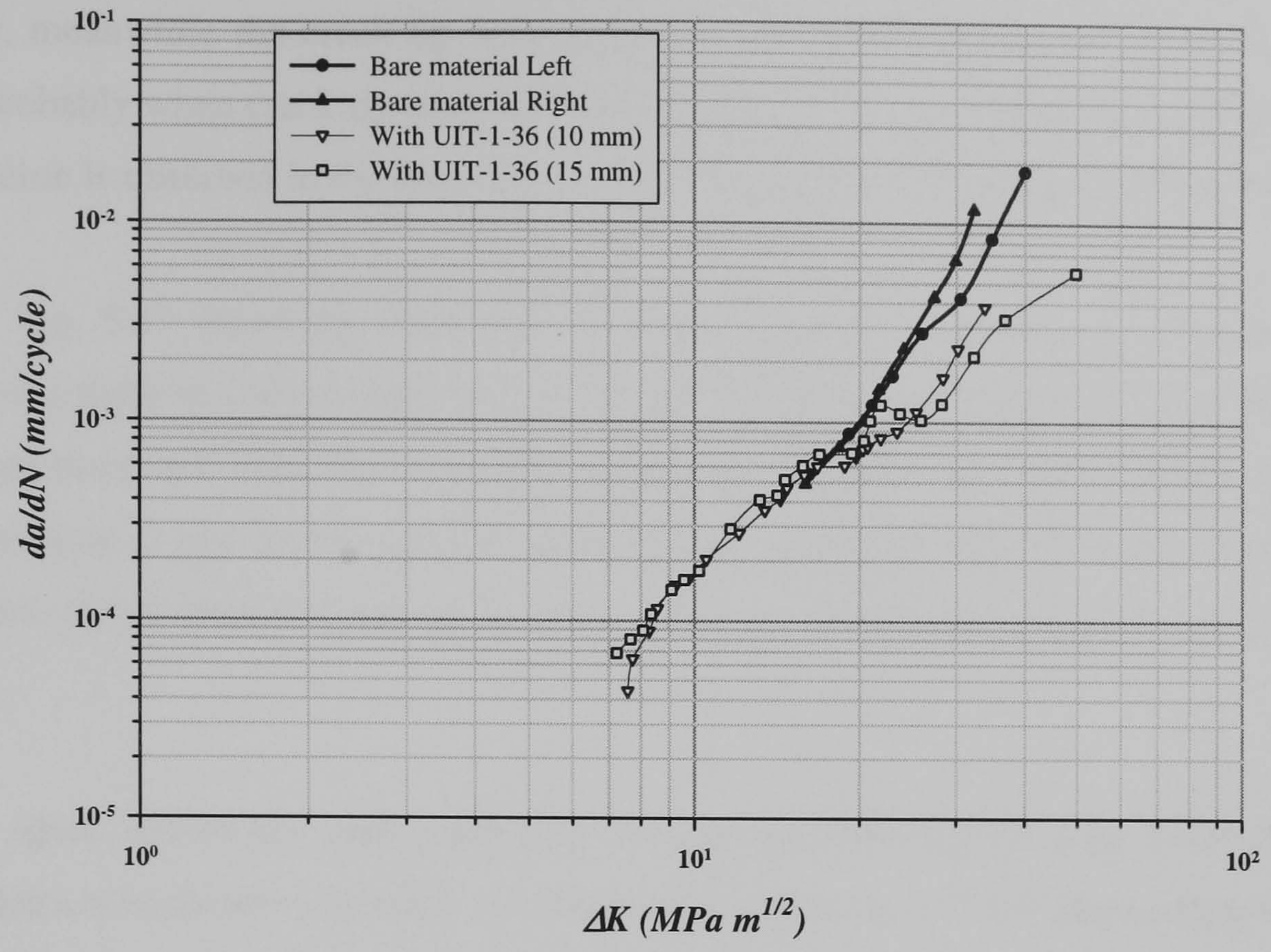

Figure 5.46 Data from Al 2024-T3 bare material and bare material with two strips of UIT-1-36 condition treatment placed one in every side of the tips are compared considering eccentricity.

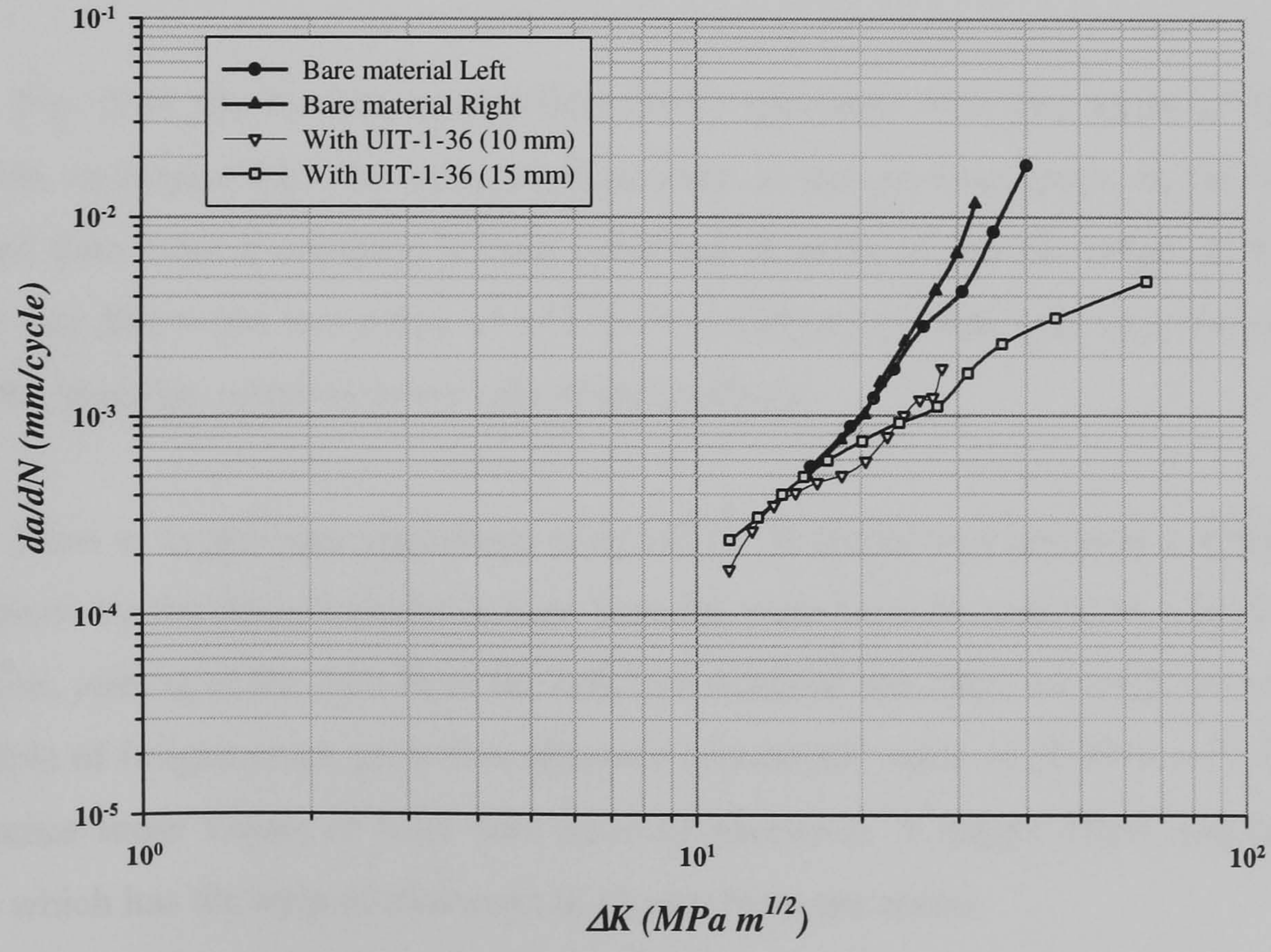

Figure 5.47 Comparison data from specimen of Al 2024-T3 bare material and from a second specimen with two strip of UIT-1-36 condition treatment.

Retardation of the crack tip with a strip at 10 mm is smaller but it can be observed clearly, meanwhile the crack tip with strip at 15 mm suffered retardation after 20 MPa $m^{1/2}$, probably when crack tip entered to the treated zone, a big difference in crack growth retardation is observed in the last value of crack tip with a strip at 15 mm from the centre.

Fig. 5.47 shows the same pair of curves from the bare material specimen and a different couple of curves taken from a second specimen with the same configuration of strip positions and with the same UIT treatment condition and load. Those curves are referenced in a key in the top left region of the graph, and can be used to assess the expected curves from full treated material, where crack retardation will occur for all ΔK values.

Here almost the same pattern as the last specimen can be seen under the same conditions of treatment and loads. An alteration in the pattern of the slope happens around the same ΔK value as in the first specimen (probably at the beginning of the treatment zone at 10 mm), then a second crack growth retardation is followed after 20 MPa $m^{1/2}$, not as clearly marked as in the above but it is of considerable magnitude at the last point obtained.

Fig. 5.48 shows data results from M(T) specimen with two strips of UIT-2-36 condition treatment with the same configuration as the previous ones. In this figure is included data from a completely bare specimen in order to see the effect of the crack growth rate due to the two strips of UIT-2-36 condition treatment placed at two different distances from the centre in every side of the crack tip.

Here as in previous specimens with UIT-1-36 condition treatment; a similar slope is followed by the data obtained in bare material zone from the specimen with UIT-2-36 condition, joining to the data from the full bare material specimen. A small effect, almost negligible of fatigue crack growth is observed around ΔK value of 20 MPa $m^{1/2}$, taking as a reference those values of fully bare material specimen. A bigger effect was found for the tip which has the strip of treatment at 15 mm from the centre.

Fig. 5.49 shows data obtained from a second specimen with strips of UIT-2-36 condition treatment and is compared to that obtained from a fully bare material specimen.

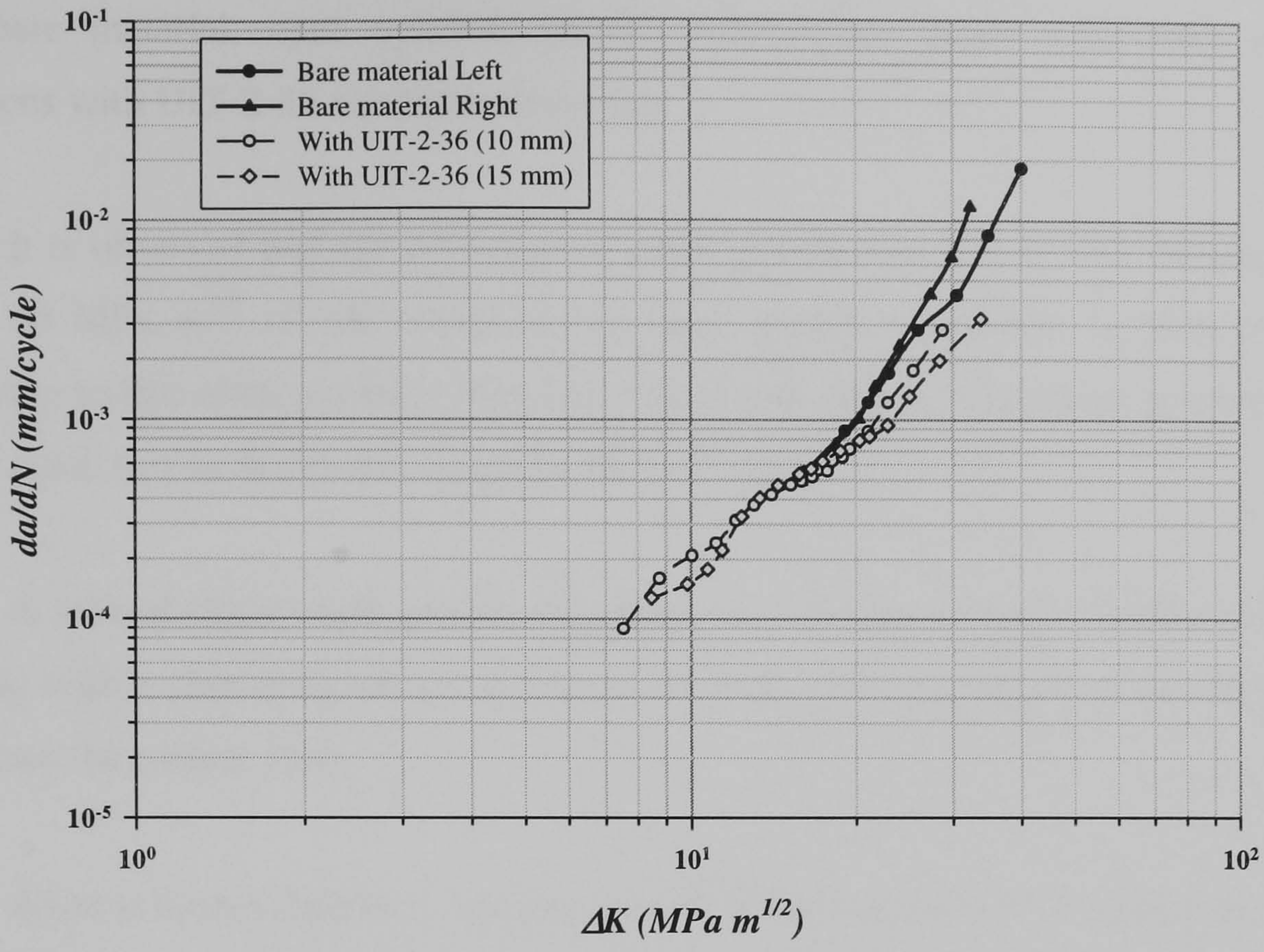

Figure 5.48 Curves obtained from the first Al 2024-T3 M(T) specimens with two strips of UIT-2-36 condition treatment comparing with curves already obtained from full bare material.

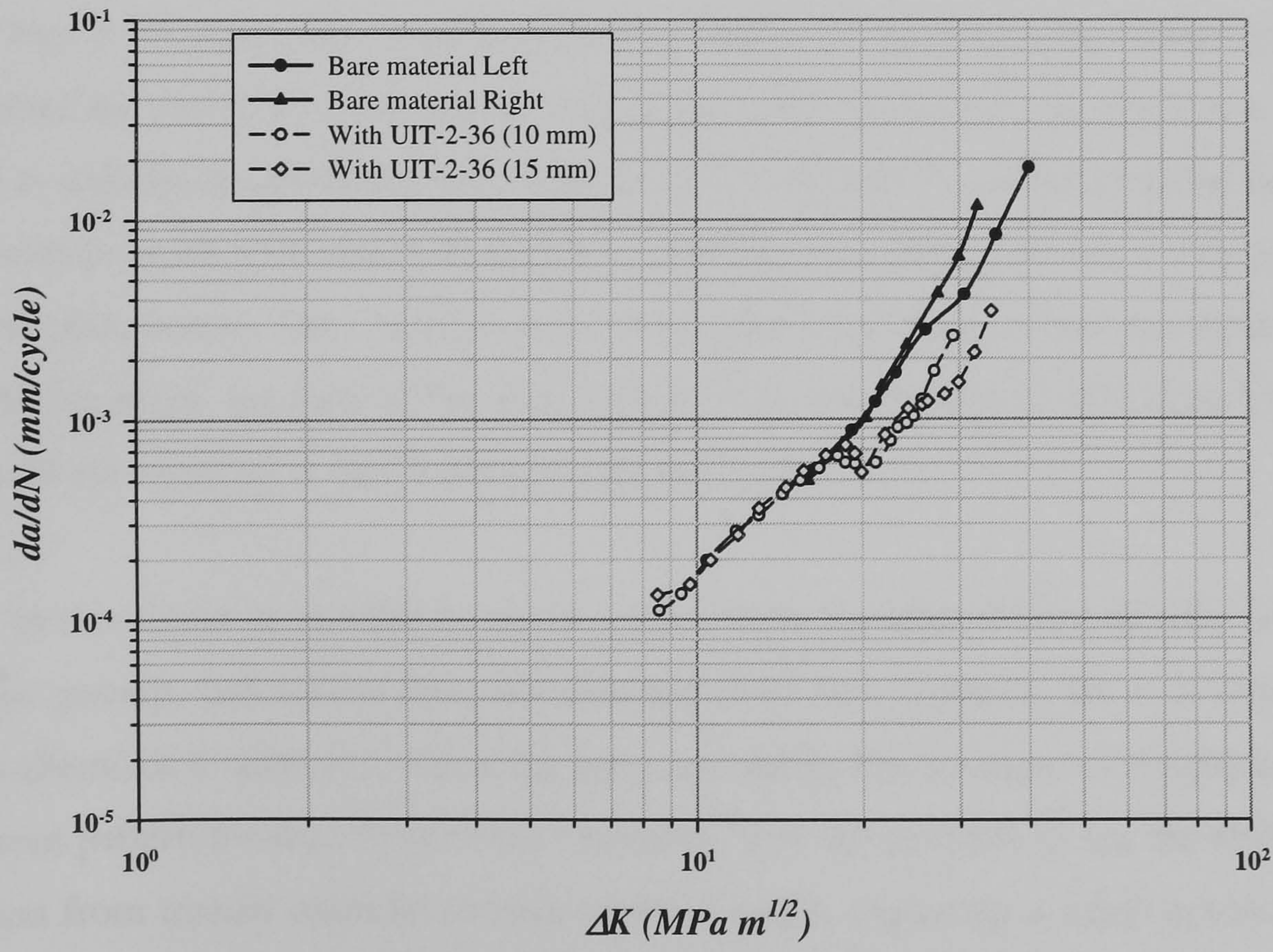

Figure 5.49 Curves from a second Al 2024-T3 M(T) specimen with two strips of UIT-2-36 condition treatment comparing with full bare material results.

Closed symbols linked with wider black solid lines represent the data obtained from bare material, open symbols linked with thinner black solid lines represent specimens with UIT-2-36 condition treatment.

It is observed that the influence of crack growth rate due to UIT treatment starts before 20 MPa $m^{1/2}$ of ΔK experiencing crack growth retardation in both crack tips comparing to that obtained from bare material. Crack growth retardation is more marked in both crack tips in this graph, specially the first one.

A second slight crack growth retardation is experienced after 20 MPa $m^{1/2}$ by the crack tip with a strip of treatment at 15 mm from the centre, probably when the crack tip enters into the treated zone.

As in previous figures it was not easy to differentiate data obtained from the bare zone and data obtained from the treated zone in specimens with strips of UIT treatment at different distances from plate centre. In the next figures a line is added to point out where each treated zones starts and where it ends.

Fig. 5.50 shows data from both sides of the crack in specimens without treatment represented by closed symbols linked with wider solid black lines. In this figure data are plotted as well from specimens with strips of UIT-1-36 and UIT-2-36 condition treatment. For specimens with UIT treatment data are only from one crack tip with a strip at 10 mm from the plate centre. Two vertical wider dark grey lines settle in the plot represent the limits of the strips. Because of the zone delimited it can be inferred what data belongs to the treated zone and what data belongs to the bare zone.

In this figure is possible to observe that before the treated zone all data fall within the same pattern, and follow the path obtained from bare material, but it is clearly seen that an alteration is achieved where the grey line marks the initiation of treatment getting a different pattern for data from treated material. It is not possible to see the effect of the transition from treated material to bare material again, expecting a small acceleration in crack growth, because the total fracture occurred before the crack tip left the treated zone at 25 mm from the centre of the plate.

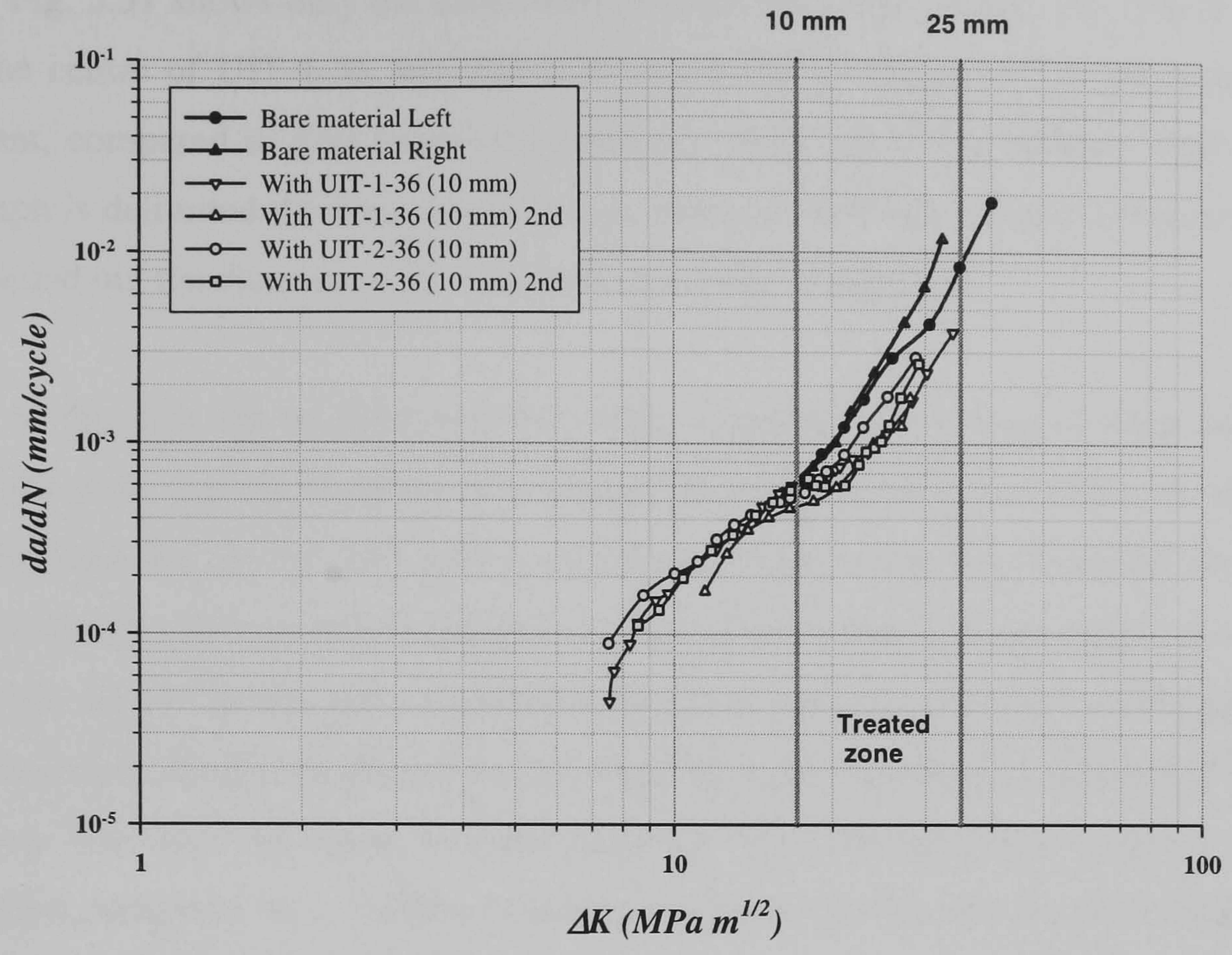

Figure 5.50 Plotted data from Al 2024-T3 bare material (both sides) and data from specimens with strips of UIT-1-36 and UIT-2-36 condition treatment at 10 mm from the centre pointed out treated zone in the graph.

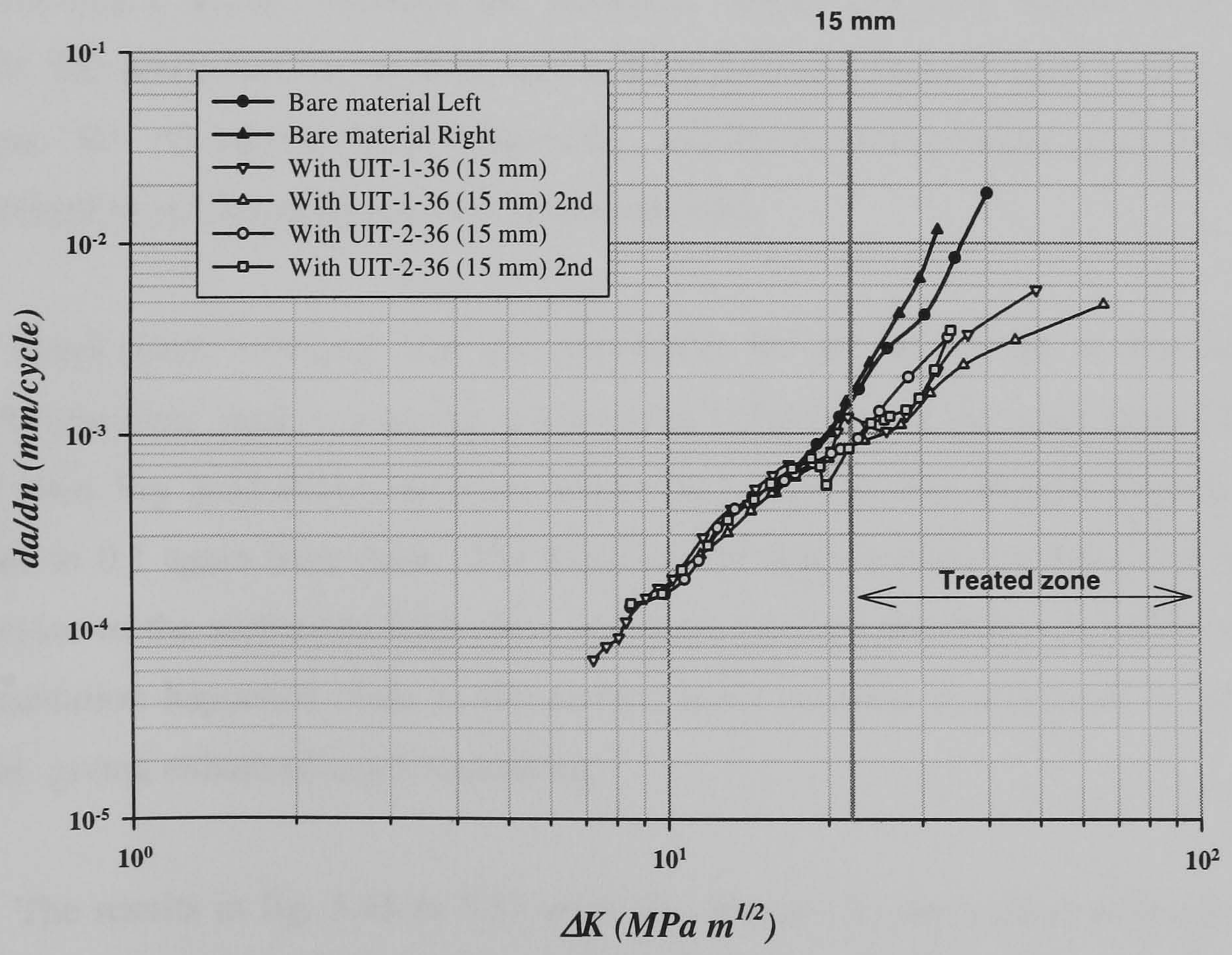

Figure 5.51 Plotted data from Al 2024-T3 bare material (both sides) and data from specimens with strips of UIT-1-36 and UIT-2-36 condition treatment at 15 mm from the centre pointed out treated zone in the graph.

Fig. 5.51 shows only the data obtained from the crack tip with the strip at 15 mm from the centre of UIT-1-36 and UIT-2-36 treatments conditions of all the plates with treatment, compared to data from both crack tips from specimens without treatment. In this graph is delimited the zone where the treated zone were placed by a wider solid grey line pointed out the distance of 15 mm from the centre of the plate.

In this plot can be observed that before reaching treated zone for that particular side of the plate, a small deviation of crack growth rate happened. For UIT-1-36 condition it can be seen that for the first plate a small retardation before the treatment took place and then abrupt crack growth retardation happened at the point where treated zone starts meanwhile for the second plate a gentler retardation was accomplished a little bit before the treated zone. Both tests gave a greater retardation effect compared to that of UIT-2-36 condition. The same behaviour is observed in the UIT-2-36 line pattern where a gradual retardation compared to a sudden retardation obtained in the second plate happened a little bit before reaching the treated zone.

Marking of the crack front shape was achieved in order to get more information about the crack growth through the thickness before and after entering the treated material. The procedure for marking was making some decades of cycles with a different load ratio "R". As normal the R value is 0.1, and the R value to mark crack front shape was changed to 0.5, keeping constant maximum load.

Crack front marking was not successful for all the places it was intended. However one clear mark was stored in one of the samples when the crack front was in the treated zone. Fig. 5.52 shows the crack shape front when R ratio changes from 0.1 to 0.5 and then to 0.1 again were done. The mark can be appreciated as a black line with flat shape close to the surface in both sides and then a curved shape in the matrix inferring that retardation happened close to the surface and a possible acceleration in the matrix material, giving enhanced crack tunnelling.

The results in fig. 5.45 to 5.51 were all collected by the optical technique with a high resolution camera. Crack length in these test were monitored by electric potential drop simultaneously. The potential drop readings were in agreement with the results presented in these figures.

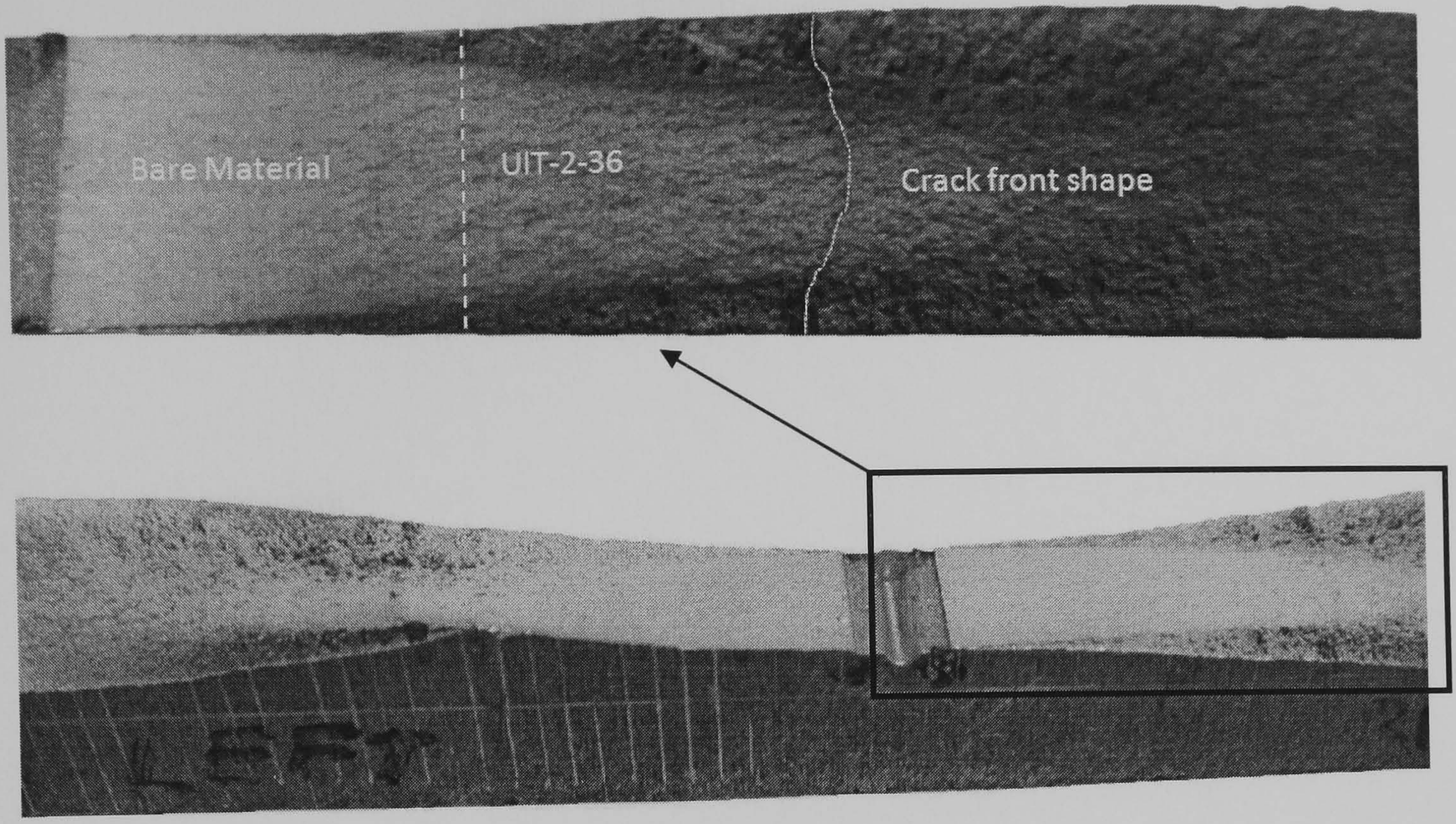

Figure 5.52 Crack front shape marked in the side of the treated zone under UIT-2-36 condition on Al 2024-T3. Flat lines close to the surfaces showing retardation compared to that in the matrix with a curved shape.

CHAPTER VI

DISCUSSION

Discussions of experimental results are presented in this chapter in order to clarify the effects of different UIT conditions on aluminium alloys.

As seen in early chapters there were two different aluminium alloys which have been worked with. Because of the facilities more experiments were done in Al 2024-T3 than in Al 7150-T651. Distinct advantages of UIT treatment have been highlighted from various materials, previously affected by welding which left tensile residual stresses, thereby reducing fatigue life and other mechanical properties. The main effect on these materials was the increase in fatigue life which is reduced considerably by the weld.

Al 2024-T3

First batch of UIT at 36 KHz and 27 KHz

As a general observation, fatigue life data can give the first indication of the effects this treatment produces in Al alloys. Different UIT conditions were tested on all surfaces of Al 2024-T3 samples. Comparison among specimens treated on four sides of the gauge section and bare material shows a great fatigue life reduction, as the effect UIT treatment causes in the first batch of UIT-1-36 and UIT-1-27 is almost the same loss of fatigue strength in HCF as in LCF, considering [13] and [14] definitions.

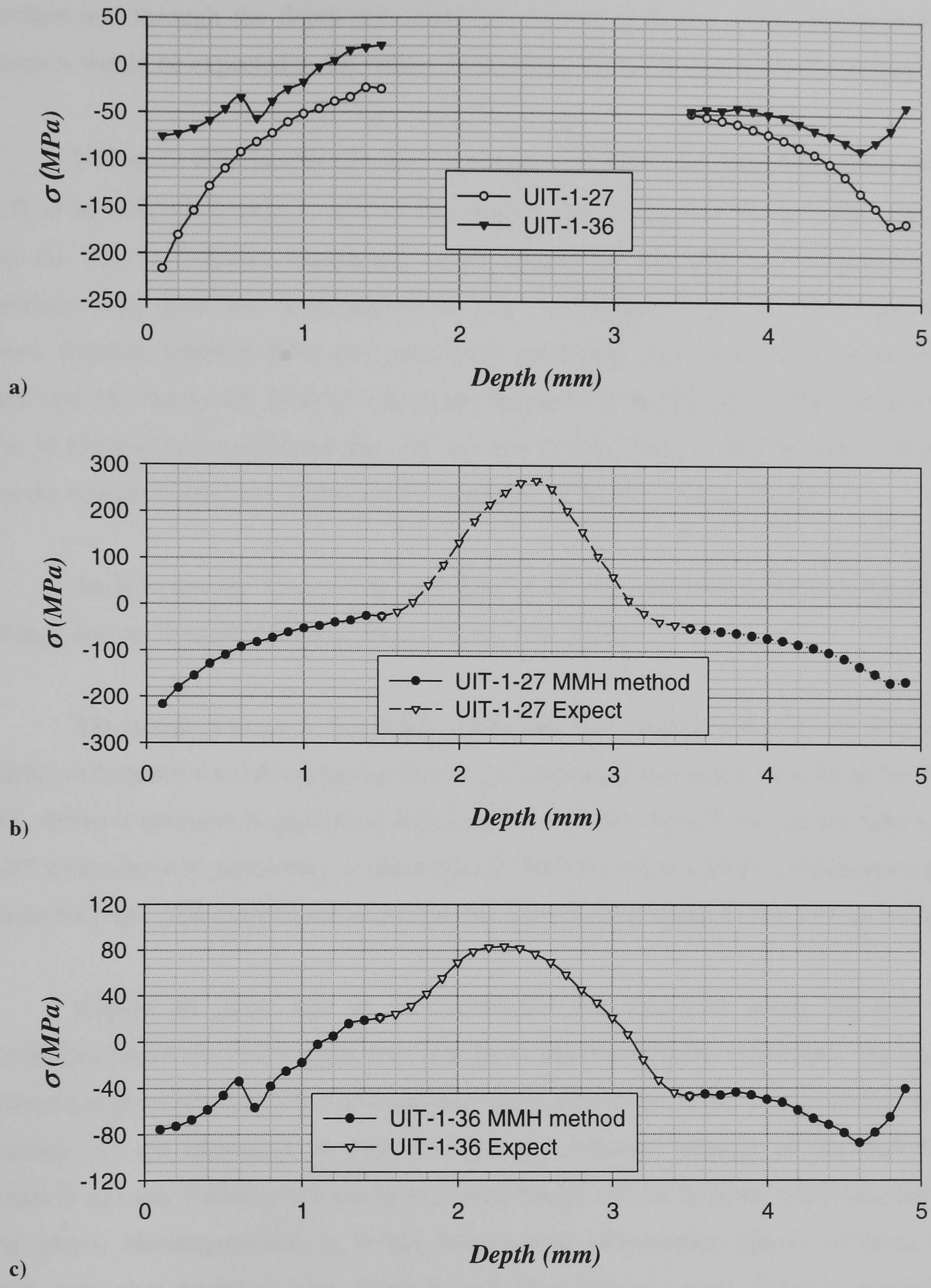

Figure 6.1 a) Data obtained directly from hole drilling technique after being computed with the aid of re-stress programme and use the MMH method from Al 2024-T3 for UIT-1-27 and UIT-1-36 conditions. b) Tensile residual stresses expected in the middle of the plate in order to have balance through the depth for UIT-1-27 condition. c) Data expected in the middle of the plate to have balance of residual stress for UIT-1-36 condition.

Because of the data obtained in fatigue tests, a residual stress analysis on the surface and through the depth was done and according to the results tensile residual stresses would be expected in the middle of samples, and compressive on the surface.

UIT at 27 KHz has the pin diameter bigger (Ø 6.35 mm) than that carried out for UIT at 36 KHZ (Ø 5 mm), as well as the pressure force (7 kg for UIT at 27 kHz and 3 kg for the UIT at 36 kHz). Parameters varied, mainly in both materials, throughout this research were feed rate, amplitude under load and impact frequency. Two parameters were different between these two conditions, amplitude under load (22 microns for 27 kHz and 18 microns for 36 kHz) and impact frequency (236 kHz for 27 kHz and 260 kHz for 36 kHz), in both conditions the feed rate was of 400 mm/min. The amount of impacts on the surface treated was higher for the condition at 36 kHz than at 27 kHz.

As it is known, fatigue life will depend on the competition between beneficial effects and detrimental effects produced by the UIT process.

The research done in this work shows that UIT creates different reactions with different intensities on aluminium alloys in its mechanical properties. Results in Al 2024-T3, shows a variation in precipitation population and size close to the surface after using UIT treatment over the surface of this material. With the aid of GDOES, the percentage of mass for every alloying element was observed that varied throughout the first 2μm depth.

Change in grain size in Al 7150-T651 was observed using different UIT conditions, from no much grain size change to significant grain refinement. Its biggest effect was observed for UIT-1-36 condition where grain refinement was developed on the surface. So the increment in yield strength was expected because of the Hall Petch relation [107, 108]. Nanocrystallization improves fatigue life of different materials, such as Al alloys. Nanocrystallization results from plastic deformation due to methods like, ultrasonic shot peening, laser peening, and shot peening, with different penetration through the depth depending in strain distribution [74, 77-80, 88, 89].

Beneficial effects observed by UIT treatment were high compressive residual stresses below the surface. The highest compressive residual stress observed (310 MPa) was obtained for the UIT-1-36 condition, but for the UIT-1-27 condition the average was between 160 and 220 MPa in Al 2024-T3. In aluminium 7150-T651 the highest compressive residual stress in the surface was registered for the UIT-3-36 condition, but the less depth penetration. Residual stresses are important because they can fracture the material, if they are tensile on the surface [52], or can increment their fatigue life, if they are compressive [53]. Compressive residual stresses originated by UIT are due to the plastic deformation due to the impact of the indenters together with ultrasonic pulses, which introduce a layer with permanent stretch in the surface. The material in the bulk tries to recover its initial state, forcing the layer at the surface to compress. The increment of compressive residual stresses agrees with results on welding joints of aluminium alloys [10], where tensile residual stresses were removed with this treatment.

Grain refinement improves micro-hardness as seen in [118-121]. So micro-hardness is affected by the UIT treatment, as can be deducted from the change of size in crystals after UIT treatment. Measurements of micro-hardness after UIT-1-36, UIT-2-36, and UIT-3-36 conditions in Al 2024-T3 and Al 7150-T651, showed that UIT treatment affects in different ways each material. The highest micro-hardness obtained in Al 2024-T3 was due to UIT-1-36 condition, meanwhile for Al 7150-T651 was due to UIT-2-36 condition. Basically, an increment of micro-hardness in Al 7150-T651 was observed with the three conditions considered; meanwhile in Al 2024-T3 only one condition could increase the micro-hardness. Much more increment of micro-hardness was obtained in Al 7150-T651.

Results for Al 2024-T3 show that roughness can be decreased or increased by different UIT treatments depending of the amount of impacts and how severe these are. Observations in Al 2024-T3 between UIT-1-36 and UIT-3-36 conditions showed that if the number of impacts and amplitude under load increase, roughness will increase too (UIT-1-36); on the other hand, if the number of impacts and amplitude under load decrease, roughness will decrease (UIT-3-36).

The presence of porosity in material treated was observed, although no evidence of implication in the increment of crack growth rate was observed. Even so, this is considered as an intrinsic mechanism which acts ahead of the crack tip when porosity coalescences with the crack, increasing the crack length [21, 34, 35].

Even though UIT treatments can potentially cause great beneficial effects to the fatigue life, results from this study showed a reduction of the fatigue life due to detrimental effects, which were stronger than beneficial effects. Fatigue life of both materials, Al 2024-T3 and Al 7150-T651 were affected by UIT treatments.

Nevertheless, an improvement in crack growth rate was observed in Al 2420-T3 for UIT-1-36 and UIT-2-36 conditions, retarding the crack growth rate of the material when approaching a treated zone, where compressive residual stress exist, having the same effect as in shot peening [74]. Once the crack is totally into the treated zone, accelerates to reach the growth rate as in untreated material.

It was observed that variation of amplitude under load produced changes in mechanical properties of both Al alloys, affecting their fatigue life in different ways. A comparison between the effects produced by UIT-2-36 and UIT-3-36 conditions in Al 2024-T3 where amplitude under load was the only parameter varied, showed that increasing amplitude under load reduce its fatigue endurance. It was observed within this comparison that residual stress and precipitation close to the surface varied proportional to amplitude under load.

In Al 7150-T651 alloy, amplitude under load affected the penetration of residual stress, considering XRD results. It means that the less amplitude under load the less penetration compressive residual stress. Micro-hardness and grain size were affected proportionally to amplitude under load.

Considering feed rate and impact frequency as a single parameter, which gives the amount of treatment per area, its effects can be seen comparing UIT-1-36 and UIT-2-36 conditions. It was observed that compressive residual stress and micro-hardness increase with the increasing of the amount of treatment in Al 2024-T3, but a reduction of precipitation close to the surface as well as increase in roughness was achieved.

On the other hand, in Al 7150-T651 comparison between UIT-1-36 and UIT-2-36, the increment of amount of treatment per area reduced compressive residual stress on the surface. Micro-hardness does not seem to have much effect due to the increment of amount of treatment per area. Grain refinement is also affected by this parameter, showing an increase of the grain refinement proportional to the amount of treatment.

Effects observed exclusively for Al 7150-T651 were achieved comparing UIT-1-36 with UIT-4-36 conditions where the impacts were the most severe of all the UIT conditions. Considering feed rate and impact frequency as a single parameter, it was observed that micro-hardness, compressive residual stress (considering XRD) and grain refinement increase by reducing feed rate and impact frequency. Fatigue life was also reduced.

A fourth parameter varied for UIT conditions used exclusively in Al 7150-T651 was pressure force by increment of 1 kg. The effects of this were observed comparing UIT-5-36 and UIT-6-36 conditions. Increasing the pressure force, caused some grain refinement, a reduction in the amount of compressive residual stress and micro-hardness. Fatigue life did not vary much.

UIT did not increase fatigue strength in Aluminium alloys unlike in previous research done in aluminium alloys where an increment of 80% was obtained after treating welded joints [140-142], but crack growth retardation was observed as in previous work [143].

CHAPTER VII

CONCLUSION AND FURTHER WORK

Results obtained in this work are valid just for R = 0.1 under ambient conditions. Two UIT frequencies were used 27 KHz and 36 KHz being the last one used meanly in both materials Al 2024-T3 and 7150-T651, for this work. The implementation of UIT in aluminium alloys, generally used in aerospace industry, without prior welding was investigated in order to get a new possible treatment to extend the fatigue life. Data collected throughout this research gave the next conclusions.

- Fatigue crack retardation in plates of Al 2024-T3 was noticed in mode I when passes from virgin material to treated material in M(T) specimens. Crack retardation was greater on the surface than in the bulk as observed over the fracture surface after fail marks were done with increments of load ratio during few thousands cycles keeping maximum load constant then returning to R = 0.1.

- Fatigue life in dog bone specimens was affected due to the UIT process accelerating crack initiation. The process creates subsurface voids which can coalescence and accelerates crack growth. UIT process can be severe increasing surface roughness that together with surface defects, as pits, accelerates crack initiation.

- Increment of micro-hardness, variation of amount and size of precipitation hardening dispersion and in change in grain size was observed close to the surface of the two different aluminium alloys after the UIT treatment.

- Variations in parameters in UIT process can bring variations in the magnitude of materials properties. The highest effect in both materials was done by UIT-1-36 condition which the time of treatment per area was the highest.

- Different magnitudes of compressive residual stress were achieved by different UIT treatment conditions.

- Improvement over the bare material was observed in dog bone specimens after milled them 50 μm, removing superficial defects and voids as well as, micro-hardness and residual stresses. Surface milled is limited by the depth of compressive residual stresses and micro-hardness.

FURTHER WORK

The work done in this thesis showed that material can get improvement in fatigue crack growth rather than in fatigue crack initiation where no improvement at all was obtained. Further work is suggested in order to get just improvement effects.

- Selection of the best combination of amplitude under load, impact frequency, feed rate and press force in order to get the best fatigue crack growth retardation in 2024-T3 aluminium alloy.

- Research on 7150-T651 Aluminium alloy using the same UIT conditions as in 2024-T3 Aluminium alloy would need to be done, compare results between them and look for the best combination of parameters in UIT effective for this aluminium alloy.

- Research on constant amplitude should be concluded and then start with variable amplitude which can give information closer to the reality.

REFERENCES

1. Suresh, S. (1998), *Fatigue of Materials*, Second edition, Cambridge, Cambridge University Press
2. http://www.industrialheating.com/CDA/ArticleInformation/features/BNP__Features__Item/0,2832,20491,00.html
3. Huang, J. Y.,Zhu, Y. T., Jiang, H. and Lowe, T. C. (2001), Microstructures and Dislocation Configurations in Nanostructured Cu Processed by Repetitive Corrugation and Straightening, *Acta Materialia*, Vol. **49**, No. 9, pp. 1497-1505
4. Saito, Y., Utsunomiya, H., Tsuji, N. and Sakai, T. (1999), Novel Ultra-high Straining Process for Bulk Materials-development of the Accumulative Roll-bonding (ARB) Process, *Acta materialia*, Vol. **47**, No. 2, pp. 579-583
5. Zhu, Y. T. and Lowe, T. C. (2000),Observations and Issues on Mechanism of Grain Refinement During ECAP Process, *Materials Science and Engineering A*, Vol. **291**, No. 1-2, , pp. 46-53.
6. Horita, Z., Smith, D. J., Furukawa, M., Nemoto, M., Valiev, R. Z., Langdon, T. G. (1997), *Characterisation of Ultra-fine Grained Materials Produced by Torsion Straining,* Chandra, T. and Sakai, T. Ed., Proc. Thermec '97 TMS, pp. 1937-1943.
7. Ghosh, A. K., Huang, W. (2000), *Investigation and Application of Severe Plastic Deformation Series*, Lowe, T. C. and Valiev, Z. Ed., **80:29**, Boston: Kuwer Academic.
8. Statnikov, E. (2004), Physics and Mechanism of Ultrasonic Impact Treatment, *International Institute of Welding*, IIW Document XIII-2004-04
9. Lihavainen, V-M. and Marquis, G. (2003), Fatigue Strength of a Longitudinal Attachment Improved by Ultrasonic Impact Treatment, *International Institute of Welding*, IIW Document XIII-1990-03, Birmingham
10. Statnikov, E. S. (1997), Applications of Operational Ultrasonic Impact Treatment (UIT) Technologies in Production of Welded Joints, *International Institute of Welding*, IIW Document XIII-1667-97
11. Ultrasonic Impact Treatment, *Esonix*, Applied Ultrasonics, Birmingham
12. McEvily Arthur J. (2002), *Metal Failures: Mechanisms, Analysis, Prevention*, New York John Wiley & Sons.
13. Hosford William, F. (2005), *Mechanical Behaviour of Materials*, Cambridge, Cambridge University Press.
14. Dowling, N.E. (1998), *Mechanical Behaviour of Materials*, Second edition, New Jersey, Prentice-Hall International
15. Forsyth, P.J.E. (1969), *The Physical Basis of Metal Fatigue*, New York, American Elsevier Publishing Co.
16. Fuchs, H. O. (1980), *Metal Fatigue in engineering*, John Wiley & Sons, 1980
17. Murakami, Y. (2002), *Metal Fatigue: Effects of Small Defects and Nonmetallic Inclusions, Oxford:* Elsevier.
18. Verpoest, I., Aernoudt, E., Deruyttere, A. and De Bondt, M. (1985), The Fatigue Threshold, Surface Condition and Fatigue Limit of Steel Wire, *Int. J. Fatigue*, Vol.**7**, No 4, pp. 199-214
19. Cui, W. (2002), A state-of-the-art Review on Fatigue Life Prediction Methods for Metal Structures, *Journal of Marine Science and Technology*, Vol. **7**, pp. 43-56
20. Ritchie, R. O. (1977), Influence of Microstructure on Near Threshold Fatigue Crack Propagation in Ultra-high Strength Steel, *Metal Science*, Vol. **11**, pp. 368-381.
21. Ritchie, R. O. (1999), Mechanisms of Fatigue Crack Propagation in Ductile and Brittle Solids, *International Journal of Fracture*, Vol. **100**, pp. 55-83.

22. Forsyth, P. J. E. (1962), A Two Stage Process of Fatigue Crack Growth, *In Crack Propagation: Proceedings of Cranfield Symposium*, pp. 76-94. London: Her Majesty's Stationery Office.
23. Baudoux, C. S., Chabanne, Y. and Petit, J. (1999), Influence of Environment and of Mean Stress on Fatigue Crack Growth on A Ti6246 Alloy, *Fatigue 99 Proceedings of the Seventh International Fatigue Congress*, Beijing, P. R. China, Vol. **1/4**, pp. 421-426
24. Choi, S. D., Mayama, H., Misawa, H. Akita, K. and Lee, J. H. (1999), Characteristic of Fatigue Crack Initiation and Propagation on Ti-6AL-4V Alloy Heat Treated in Beta-field, *Fatigue 99 Proceedings of the Seventh International Fatigue Congress*, Beijing, P. R. China, Vol. **1/4**, pp. 427-432
25. Pook, L. P. and Frost, N. E. (1973), Fatigue Crack Growth Theory, *International Journal of Fracture*, Vol. **9**, No 1, pp 53-61
26. Erdogan, F. J. (1983), Stress Intensity Factor, *Journal of Applied Mechanism*, Vol. **50**, pp. 992-1002.
27. Forsyth, P. J. E. (1969), *The Physical Basis of Metal Fatigue.*, New York, American Elsevier.
28. Pook, L. P. (1999), Fatigue Crack Paths, *Fatigue 99 Proceedings of the Seventh International Fatigue Congress*, Beijing, P. R. China, Vol. **1/4**, pp 407-414
29. Cotterell, B. (1965), *International Journal of Fracture Mechanics*, Vol. **1**, pp. 96-103
30. Paris, P. C., Gomez, M. P. & Anderson, W. P. (1961), A Rational Analytic Theory of Fatigue, *The Trend in Engineering*, Vol. **13**, pp. 9-14.
31. Paris, P. C. & Erdogan, F. (1963), A Critical Analysis of Crack Propagation Laws, *Journal of Basic Engineering*, Vol.**85**, pp.528-534.
32. Sun, X. W, Sun, J. G., Jin, H. M., Xue, S. and Hua, X. (1999), Experimental Study on Fatigue Crack Growth Behavior of 304 Steel Suface Crack Plates Under Tension, *Fatigue 99 Proceedings of the Seventh International Fatigue Congress*, Beijing, P. R. China, Vol. **1/4**, pp. 439-444.
33. Anderson, N. E. and Johansson, S. (1999), Fatigue Crack Growth Rate in Thick Plates of 7010, Fatigue 99 Proceedings of the Seventh International Fatigue Congress, Beijing, P. R. China, Vol. **1/4**, pp 445-450.
34. Kåre, H. (1984), *Introduction to Fracture Mechanics*, McGraw-Hill.
35. Vaidya, W. V.(1985), Fatigue Crack Propagation Under a Micro-structural Gradient in a Plain Carbon Steel, *Scripta metallurgica*, Vol. **19**, No. 5, pp. 597-602.
36. McEvily, A.J. and Minakawa, K. (1984),Crack Closure and the Growth of Short and Long Fatigue Cracks, *Scripta Metallurgica* , Vol. **18**, pp. 71-76.
37. Hu, Y.M., Floer, W., Krupp, U. and Christ H.J. (1999), Fatigue Crack Initiation and Microcrack Growth in a Beta Titanium Alloy, *Fatigue 99 Proceedings of the Seventh International Fatigue Congress*, Beijing, P.R. China, Vol. **1/4**, pp. 277-282.
38. Niinomi, M.,Fukunaga, K., Akahori, T., Ozeki, A. and Wang L. (1999), Small Fatigue Crack Initiation and Propagation Characteristics of Ti-6Al-7Nb, *Fatigue 99 Proceedings of the Seventh International Fatigue Congress*, Beijing, P.R. China, Vol. **1/4**, pp 353-358.
39. Vinogradov, A., Hashimoto, S. and Miura, S. (1996), Fatigue Crack Initiation and Propagation in [210] Oriented Copper Single Crystals in Vacuum and in Air, *Scripta Materialia*, Vol **34**, No 5, pp 775-779.
40. Turnbull, A. and De Los Rios, E. R. (1995), The Effect of Grain Size on Fatigue Crack Growth in an Aluminium Magnesium Alloy, *Fatigue and Fracture of Engineering Materials and Structures*, Vol. **18**, No. 11, pp. 1355-1366.
41. Hong, Y., Qiao, Y., Liu, N. and Zheng, X. (1999), Collective Damage of Short Cracks and Fatigue Life Estimation for Metallic Materials, *Fatigue 99 Proceedings of the Seventh International Fatigue Congress*, Beijing, P.R. China, Vol. **1/4**, pp.337-344.
42. Wang, J. N. and Xie, L.Y. (1999), Experimental Investigation of Micro-Crack Behavior of St37 Steel, *Fatigue 99 Proceedings of the Seventh International Fatigue Congress*, Beijing, P.R. China, Vol. **1/4**, pp 377-382.
43. Newman, J. C. Jr. (1994), A Review of Modelling Small-crack Behavior and Fatigue-life Prediction for Aluminium Alloys, *Fatigue and Fracture Engineering of Materials and Structures*, Vol. **17**, No 4, pp. 429-439.

44. Liu, J.Z., Wu, X. R., Ding, C. F., Romanowski, A.L., Annigeri, B. S., Favrow, L.H., Schneider, G.J., Wang, J. and Smith, S.L. (1999), Small Crack Growth Behavior and Life Prediction of 7075-T73 Forged Aluminium Alloy, *Fatigue 99 Proceedings of the Seventh International Fatigue Congress*, Beijing, P.R. China, Vol. **1/4**, pp. 345-351.
45. Huang, H. and Liu, S. (1999), Small Crack Growth and Growth Rate Predictions for Titanium Alloy TC11, *Fatigue 99 Proceedings of the Seventh International Fatigue Congress*, Beijing, P.R. China, Vol. **1/4**, pp 371-376.
46. Lee, J. J., Sharpe Jr., W. N. (1986), *Small Fatigue Cracks*, Edited by Rietchie, R. O. and Lankford, J., pp. 323-343
47. Forte, T. P., Leis, B. N. (1981), ASTM STP 743, *American Society for Testing and Materials*, Philadelphia, pp. 100-124.
48. Newman, Jr., J.C., Wu, X.R., Swain, M.H., Zhao, W. et al (1994), Small Crack Growth Behavior in High Strength Aluminium Alloys, *A NASA/CAE Cooperative Program*, NASA RP1309
49. Newman Jr., J. C. (1994), *Fatigue and Fracture of Engineering Materials and Structures*, Vol. **17**, No. 4, pp. 429-439.
50. Kaneko, Y., Kitagawa, K. and Hashimoto, S. (1999), Fatigue Crack Propagation in Single- and Bicrystals of a Ferritic Stainless Steel, *Fatigue 99 Proceedings of the Seventh International Fatigue Congress*, Beijing, P. R. China, Vol. **1/4**, pp. 469-474.
51. Suresh, S. and Ritchie, R. O. (1984), Propagation of Short Fatigue Cracks, *International Metals Review*, V **29**, No. 6, pp 445-476.
52. Osgood, W. R. (1954), *Residual Stress in Metals and Metals Construction*, New York, Reinhold Publishing Corporation.
53. Guechichi, H., Castex, L. (2006), Fatigue Limits Prediction of Surface Treated Materials, *Journal of Materials Processing Technology*, Vol. **172**, pp. 381-387.
54. Altenberger, I., Alternative Mechanical Surface Treatments: Microstructures, Residual Stress & Fatigue Behavior, *Shot Peening*, Wagner Ed., Wiley-VCH, pp.421-434.
55. Rassweiler, G. M. and Grube, W. L. (1959), *Internal Stress and Fatigue in Metals*, Elsevier Publishing Company.
56. Bruno, G., Ceretti, M., Girardin, E., Giuliani, A. and Manescu, A. (2004), Relaxation of Residual Stress in MMC After Combined Plastic Deformation and Heat Treatment, *Scripta Materialia*, Vol. **51**, pp. 999-1004.
57. Trojanová, Z., Lukáč, P. Riehemann, W. and Mordike, B. L. (2002), Study of Relaxation of Residual Internal Stress in Mg Composites by Internal Friction, *Materials Science and Engineering A*, Vol. **324**, pp. 122-126.
58. Treuting, R. G., Wishart, H. B., Lynch, J. J. and Richards, D. G. (1952), Residual Stress Measurements, *American Society for Metals*, Cleveland, Ohio.
59. Hill, M. R., DeWald, A. T., Rankin, J. E. and Lee, M. J. (2005), Measurement of Laser Peening Residual Stresses, *Materials Science Technology*, Vol. **21**, No. 1, pp. 3-9.
60. Rohde, R. W. and Jones, W. B. (1981), Comparison of Tensile Loading and Stress Relaxation as Probes of Mechanical State, *Scripta Metallurgica*, Vol. **15**, pp. 625-628.
61. Juijerm, P., Altenberg, I. and Scholtes, B. (2006), Fatigue and Residual Stress Relaxation of Deep Rolled Differently Aged Aluminium Alloy AA6110, *Materials Science and Egineering A*, Vol. **426**, pp. 4-10.
62. Evans, A., Kim, S-B., Shackleton, J., Bruno, G., Preuss, M. and Withers, P. J. (2005), Relaxation of Residual Stress in Shot Peened Udimet 720Li Under High Temperature Isothermal Fatigue, *International Journal of Fatigue*, Vol. **27**, pp. 1530-1534.
63. Holzapfel, H., Schulze, V., Vöhringer, O. and Macherauch, E. (1998), Residual Stress Relaxation in an AISI 4140 Steel Due to Quasistatic and Cyclic Loading at Higher Temperatures, *Materials Science and Engineering A*, Vol. **248**, pp. 9-18.
64. Zhuang, W. Z. and Halford, G. R. (2001), Investigation of Residual Stress Relaxation Under Cyclic Load, *International Journal of Fatigue*, Vol. **23**, pp. S31-S37.
65. Torres, M. A. S. and Voorwald, H. J. C. (2002), An Evaluation of Shot Peening, Residual Stress and Stress Relaxation on the Fatigue Life of AISI 4340 Steel, *International Journal of Fatigue*, Vol. **24**, pp. 877-886.
66. Juijerm, P. and Altenberger, I. (2006), Residual Stress Relaxation of Deep-rolled Al-Mg-Si-Cu Alloy During Cyclic Loading at Elevated Temperatures, *Scripta Materialia*, Vol. **55**, pp. 1111-1114.

67. Mordyuk, B. N. and Prokopenko, G. I. (2006), Fatigue Life Improvement of α-titanium by Novel Ultrasonically Assisted Technique, *Materials Science and Engineering A*, Vol. **437**, pp.396-405.
68. Al-Obaid, Y. F. (1995), Shot Peening Mechanics: Experimental and Theoretical Analysis, *Mechanics of Materials*, Vol. **19**, pp. 251-260.
69. Xiao, Z., Fok, W. C. and Lwin, T. (1993), Parametric Study of Residual Stress Due to Shot Peening, *Journal of Materials Processing Technology*, Vol. **39**, pp. 469-483.
70. Saritas, S., Dogan, C. and Varol, R. (1999), Improvement of Fatigue Properties of PM Steels by Shot Peening, *Powder Metallurgy*, Vol. **42**, No. 2, pp 126-130.
71. Sharp, P. K., Lius, Q., Bater, S. A., Baburamani, P. and Clark, G. (2002), Fatigue Life Recovery in Aluminium Alloy Aircraft Structure, *Fatigue and Fracture of Engineering and Structures*, Vol. **25**, pp.99-110.
72. Honda, T., Ramulu, M. and Kobayashi, A. S. (2006), Fatigue of Shot Peened 7075-T7351 SENB Specimen - A 3-D Analysis, *Fatigue and Fracture Engineering Materials and Structures*, Vol. **29**, No. 6, pp. 416-424.
73. Rodopoulos, C. A., Curtis, S. A., De Los Rios, E. R. and SolisRomero, J. (2004), Optimisation of the Fatigue Resistance of 2024-T351 Aluminium Alloys by Controlled Shot Peening-methodology, Results and Analysis, *International Journal of Fatigue*, Vol. **26**, pp. 849-856
74. Hammond, D. W. and Meguid, S. A. (1990), Crack Propagation in the Presence of Shot-peening Residual Stress, *Engineering Fracture Mechanics*, Vol. **37**, No. 2, pp.373-387.
75. Curtis, S., de los Rios, E. R., Rodopoulos, C. A. and Levers, A. (2003), Analysis of the Effects of Controlled Shot Peening on Fatigue Damage of High Strength Aluminium Alloys, *International Journal of Fatigue*, Vol **25**, pp. 59-66.
76. Metal Improvement Company (2007), World Leaders in Metal Treatment Services, http://www.metalimprovement.com/shot_peening.php#.
77. Liu, G., Wang, S. C., Lou, X. F, Lu, J. and Lu, K. (2001), Low Carbon Steel With Nanostructured Surface Layer Induced by High-energy Shot Peening, *Scripta Materialia*. Vol. **44**, pp.1791-1795.
78. Yan, W., Fang, L., Sun, K. and Xu, Y. (2007), Thermodynamics of Nanocrystalline Formation in Surface Layer of Hadfield Steel by Shot Peening, *Materials Science and Engineering A*, Vol. **445-446**, pp. 392-397.
79. Ni, Z., Wang, X., Wang, J. and Wu, E. (2003), Characterization of the Phase Transformation in a Nanostructured Surface Layer of 304 Stainless Steel Induced by High-energy Shot Peening, *Physica B*, Vol. **334**, pp. 221-228.
80. Wang, T., Yu, J. and Dong, B. (2006), Surface Nanocrystallization Induced by Shot Peening and its Effect on Corrosion Resistance of 1Cr18Ni9Ti Stainless Steel, *Surface & Coatings Technology*, Vol. **200**, pp. 4777-4781.
81. Papakyriacou, M., Mayer, H., Pypen, C., Plenk Jr, H. and Stanzl-Tschegg, S. (2000), Effects of Surface Treatments on High Cycle Corrosion Fatigue of Metallic Implant Materials, *International Journal of Fatigue*, Vol. **22**, 873-886.
82. Sabelkin, V., Martinez, S. A., Mall, S., Sathish, S. and Blodgett, M. P. (2005), Effects of Shot-peening Intensity on Fretting Fatigue Crack-initiation Behaviour of Ti-6Al-4V, *Fatigue and Fracture of Engineering Materials and Structures*, Vol. **28**, No. 3, pp. 321-332.
83. Metal Finishing News (2007), Presentation of LASMIS, a French Research Laboratory Working on Shot Peening, http://www.mfn.li/article/?id=194
84. Toyo Seiko (2007), www.toyoseiko.co.jp/eng/Products/e-usp.html
85. Xing, Y. M. and Lu, J. (2004), An Experimental Study of Residual Stress Induced by Ultrasonic Shot Peening, *Journal of Materials Processing Technology*, Vol. **152**, pp. 56-61
86. Guo, F. A., Trannoy, N. and Lu, J. (2004), Analysis of Thermal Properties by Scanning Thermal Microscopy in Nanocrystallized Iron Surface Induced by Ultrasonic Shot Peening, *Materials Sciance and Engineering A*, Vol **369**, pp. 36-42
87. Guo, F. A., Trannoy, N. and Lu, J. (2006), Characterization of the Thermal Properties by Scanning Thermal Microscopy in Ultrafine-grained Iron Surface Layer Produced by Ultrasonic Shot Peening, *Materials Chemistry and Physics*, Vol. **96**, pp. 59-65
88. Tao, N. R., Sui, M. L., Lu, J. and Lu, K. (1999), Surface Nanocrystallization of Iron Induced by Ultrasonic Shot Peening, *Nano Structured Materials*, Vol. **11**, No. 4, pp. 433-440

89. Wang, X., Wang, J., Wu, P. and Zhang, H. (2004), The Investigation of Internal Friction and Elastic Modulus in Surface Nanostructured Materials, *Materials Science and Engineering A*, Vol. **370**, pp. 158-162
90. Wu, X., Tao, N., Hong, Y., Xu, B.,Lu, J. and Lu, K. (2002), Microstructure and Evolution of Mechanically-induced Ultrafine Grain in Surface Layer of Al-alloy Subjected to USSP, *Acta Materialia*, Vol. **50**, pp. 2075-2084.
91. Liu, G., Lu, J. and Lu, K. (2000), Surface Nanocrystallization of 316L Stainless Steel Induced by Ultrasonic Shot Peening, *Materials Science and Engineering A*, Vol. **286**, pp. 91-95.
92. Benrabah, A., Langlade, C. and Vannes, A. B. (1999), Residual Stress and Fretting Fatigue, *Wear*, Vol. **224**, pp. 267-273.
93. Watanabe, Y., Hattori, K., Handa, M., Hasegawa, N., Tokaji, K., Ikeda, M. and Duchazeaubeneix, J. M., Effect of Ultrasonic Shot Peening on Fatigue Strenght of High Strength Steel, Date of access April 2007 , http://www.shotpeener.com/library/pdf/2002039.pdf
94. Huo, L., Wang, D. and Zhang, Y. (2005), Investigation of the Fatigue Behaviour of the Welded Joints Treated by TIG Dressing and Ultrasonic Peening Under Variable-amplitude Load, *International Journal of Fatigue*, Vol. **27**, pp. 95-101.
95. Chen, H., Kysar, J. W. and Yao, Y. L. (2004), Characterization of Plastic Deformation Induced by Microscale Laser Shock Peening, *Journal of Applied Mechanics*, Vol. **71**, pp. 713-723.
96. Aldajah, S. H., Ajayi, O. O., Fenske, G. R. and Xu, Z. (2005), Effect of Laser Surface Modifications Tribological Performance of 1080 Carbon Steel, *Transactions of the ASME*, Vol. **127**, pp. 596-604.
97. Gregory, J. K., Rack, H. J., and Eylon, D. (1996), Laser Shock Peening for Fatigue Resistance, Surface performance of Titanium, *The metal Society of ASME (TMS)*, Warendale, PA, pp. 217-230.
98. Gomez-Rosas, G., Rubio-Gonzalez, C., L Ocaña, J., Molpeceres, C., Porro, J. A., Chi-Moreno, W. and Morales, M. (2005), High Level Compressive Residual Stresses Produced in Aluminium Alloys by Laser Shock Processing, *Applied Surface Science*, Vol. **252**, pp. 883-887.
99. Peyre, P., Fabbro, R., Merrien, P. and Lieurade, H. P. (1996), Laser Shock Processing of Aluminium Alloys. Application to High Cycle Fatigue Behaviour, *Materials Science and Engineering A*, Vol. **210**, pp. 102-113.
100. Rankin, J. E., Hill, M. R. and Hackel, L. A. (2003), The Effects of Process Variations on Residual Stress in Laser Peened 7049 T73 Aluminium Alloy, *Materials Science and Engineering A*, Vol. **349**, pp. 279-291.
101. Hatamleh, O., Lyons, J. and Forman, R. (2007), Laser and Shot Peening Effects on Fatigue Crack Growth in Friction Stir Welded 7075-T7351 Aluminium Alloy Joints, *International Journal of Fatigue* , Vol. **29**, pp. 421-434.
102. Hatamleh, O., Lyons, J. and Forman, R. (2007), Laser Peening and Shot Peening Effects on Fatigue Life and Surface Roughness of Friction Stir Welded 7075-T7351 Aluminium, *Fatigue and Fracture Engineering of Materials and Structures*, Vol. **30**, pp. 115-130.
103. Effects of Fatigue and Fretting on Residual Stress Introduced by Laser Shot Peening, King, A., Steuwer, A., Woodward, C., and Withers, P. J., Materials Science and Engineering A, Vol. 435-436. 2006, pp. 12-18
104. Nalla, R. K., Altenberger, I., Noster, U., Liu, G. Y., Scholtes, B. and Ritchie, R. O. (2003), On the Influence of Mechanical Surface Treatments-deep Rolling and Laser Shock Peening-on the Fatigue Behavior of Ti-6Al-4V at Ambient and Elevated Temperatures, *Materials Science and Engineering A*, Vol. **355**, pp. 216-230.
105. Sano, Y., Obata, M., Kubo, T., Mukai, N., Yoda, M., Masaki, K. and Ochi, Y. (2006), Retardation of Crack Initiation and Growth in Austenitic Stainless Steel by Laser Peening Without Protective Coating, *Materials Science and Engineering A*, Vol. **417**, pp. 334-340.
106. Peyre, P., Scherpereel, X., Berthe, L., Carboni, C., Fabbro, R., Béranger, G. and Lemaitre, C. (2000), Surface Modifications Induced in 316L Steel by Laser Peening and Shot-peening. Influence on Pitting Corrosion Resistance, *Materials Science and Engineering A*, Vol. **280**, 294-302.

107. Hall, E. O. (1951), The Deformation and Ageing of Mild Steel: III Discussion of Results, *Proceedings of the Physical Society, Section B*, Vol. **64**, No. 9, pp. 747-753.
108. Petch, N. J. (1953), The Cleavage Strength of Polycrystals, *Journal of Iron Steel Institute*, Vol. **174**, pp. 25-28.
109. Hansen, N. (2004), Hall-Petch Relation and Boundary Strengthening, *Scripta Materialia*, Vol. **51**, pp. 801-806.
110. Tao, N. R., Wang, Z. B., Tong, W. P., Sui, M. L., Lu, J. and Lu, K. (2002), An Investigation of Surface Nanocrystallization Mechanism in Fe Induced by Surface Mechanical Attrition Treatment, *Acta Materialia* , Vol. **50**, pp. 4603-4616.
111. Todaka, Y., Umemoto, M. and Tsuchiya, K. (2004),, Comparison of Nanocrystalline Surface Layer in Steels Formed by Air Blast and Ultrasonic Shot Peening, *Materials Transactions*, (The Japan Institute of Metals), Vol. **45**, No. 2, pp. 376-379,
112. Wang, Z. B., Tao, N. R., Li, S., Wang, W., Liu, G., Lu, J. and Lu, K. (2003), Effect of Surface Nanocrystallization on Friction and Wear Properties in Low Carbon Steel, *Materials Science and Engineering A*, Vol. **352**, pp. 144-149.
113. Zhu, K. Y., Vassel, A., Brisset, F., Lu, K. and Lu, J. (2004), Nanostructure Formation Mechanism of α-titanium Using SMAT, *Acta Materialia*, Vol. **52**, pp. 4101-4110.
114. Park, J. W., Kim, J. W. and Chung, Y. H. (2004), Grain Refinement of Steel Plate by Continuous Equal-channel Angular Process, *Scripta Materialia*, Vol. **51**, pp. 181-184.
115. Villegas, J. C., Shaw, L. L., Dai, K., Yuan, W., Tian, J., Liaw, P. K. and Klarstrom, D. L. (2005), Enhanced Fatigue Resistance of a Nickel-based Hastelloy Induced by a Surface Nanocrystallization and Hardening Process, *Philosophical Magazine Letters*, Vol. **85**, No. 8, pp. 427-438.
116. Hanlon, T., Kwon, Y. N. and Suresh, S. (2003), Grain Size Effects on the Fatigue Response of Nanocrystalline Metals, *Scripta Materialia*, Vol. **49**, pp.675-680.
117. Valiev, R. Z., Islamgaliev, R. K. and Alexandrov, I. V. (2000), Bulk Nanostructured Materials from Severe Plastic Deformation, *Progress in Materials Science*, Vol **45**, pp. 103-189.
118. Lu, K. (1996), Nanocrystalline Metals Crystallized from Amorphous Solids: Nanocrystallization, Structure, and Properties, *Materials Science and Engineering*, Vol. **R16**, pp. 161-221.
119. Yin, J., Umemoto, M., Liu, Z. G. and Tsuchiya, K. (2001), Formation Mechanism and Annealing Behavior of Nanocrystalline Ferrite in Pure Fe Fabricated by Ball Milling, *ISIJ International*, Vol. **41**, No. 11, pp. 1389-1396.
120. Umemoto, M., Huang, B., Tsuchiya, K. and Suzuki, N. (2002), Formation of Nanocrystalline Structure in Steels by Ball Drop Test, *Scripta Materialia*, Vol. **46**, pp. 383-388.
121. Todaka, Y., Umemoto, M. and Tsuchiya, K. (2002), Nanocrystallization in Fe-C Alloys by Ball Milling and Ball Drop Test, *ISIJ International*, Vol. **42**, No. 12, pp. 1430-1437.
122. Hutchings, I. M. (1992), *Tribology: Friction and Wear of Engineering Materials*, Butterworth Heinemann
123. Thomas, T. R. (1999), *Rough Surfaces*, Second edition, Imperial College Press
124. Thomas, T. R. (1982), *Rough Surfaces*, Longman
125. Folprecht, J. W. (1984), Morphometrical Evaluation of Surface Roughness During the Initial Fatigue Stage in an Austenitic Steel, *International Journal of Fatigue*, Vol. **6**, No. 3, pp. 157-167
126. Laue, S., Bomas, H. and Hoffmann, F. (2006), Influence of Surface Condition on the Fatigue Behaviour of Specimens Made of a SAE 5115 Case-hardened Steel, *Fatigue and Fracture of Engineering Materials and Structures*, Vol. **29**, pp. 229-241.
127. Huang, Q. and Ren, J. X. (1991), Surface Integrity and its Effects on the Fatigue Life of the Nickel-based Superalloy GH33A, *International Journal of Fatigue*, Vol. **13**, No. 4, , pp. 322-326
128. Yuri, T., Ono, Y. and Ogata, T. (2003), Effects of Surface Roughness and Notch on Fatigue Properties for Ti-5Al-2.5Sn ELI Alloy at Cryogenic Temperatures, *Science and Technology of Advanced Materials*, Vol. **4**, pp. 291-299.
129. Itoga, H., Tokaji, K., Nakajima, M. and Ko, H.-N. (2003), Effect of Surface Roughness on Step-wise S-N Characteristics in High Strength Steel, *International Journal of Fatigue*, Vol. **25**, pp. 379-385.

130. Merati, A. and Eastaugh, G. (2007), Determination of Fatigue Related Discontinuity State of 7000 Series of Aerospace Aluminium Alloys, *Engineering Failure Analysis*, Vol. **14**, pp. 673-685.
131. Jiang, H., Bowen, P. and Knott, J. F. (1999), Fatigue Performance of a Cast Aluminium Alloy Al-7Si-Mg with Surface Defects, *Journal of Materials Science*, Vol. **34**, pp. 719-725.
132. Ghanem, F., Braham, C., Fitzpatrick, M. E. and Sidhom, H. (2002), Effect of Near-Surface Residual Stress and Microstructure Modification from Machining on the Fatigue Endurance of a Tool Steel, *Journal of Materials Engineering and Performance*, Vol. **11**, No. 6, pp. 631-639.
133. Haagensen, P. J., Statnikov, E. S. and Lopez-Martinez, L. (1998), Introductory Fatigue Tests on Welded Joints in High Strength Steel and Aluminium Improved by Various Methods Including Ultrasonic Impact Treatment (UIT), *International Institute of Welding*, IIW Doc.XIII-1748-98
134. Statnikov, E. S. (1977), Ultrasonic Impact Tool for Strengthening Weld and Reducing Residual Stresses, *New Physical Methods of Intensification of Technological Processes.*
135. Trufiakov, V. I., Statnikov, E. S., Mikheev, P. P. and Kuzmenko, A. Z. (1998), The Efficiency of Ultrasonic Impact Treatment for Improving the Fatigue Strength of Welded Joints, *International Institute of Welding*, IIW Document XIII-1745-98
136. Statnikov, E. S., Muktepavel, V. O., Trufiakov, V. I., and Kuzmenko, A. Z. (1997), Comparison of Efficiency and Processibility of Post-weld Deformation Methods for Increase in Fatigue Strength of Welded Joints, *International Institute of Welding*, IIW-Document XIII-1668-97
137. Statnikov S. E. (1999),Guide for Application of Ultrasonic Impact Treatment Improving Fatigue Life of Welded Structures, *International Institute of Welding*, IIW/IIS -Document XIII-1757-99.
138. Statnikov, E. S., Korolkov, O. V. and Vityazev, V. N. (2006), Physics and Mechanism of Ultrasonic Impact, *Ultrasonics*, Vol. **44**, pp. e533-e538.
139. Uppal, S., Yoshino, D. and Tehini, L. (2002), Ultrasonic Impact Treatment of Vertical Stiffener Weld at FAST Bridge, *Transportation Technology* Center, Inc.
140. Statnikov, E. S., Muktepavel, V. O., Trufyakov, V. I., Mikheev, P. P., Kuzmenko, A. Z. and Blomqvist, A. (2000), Efficiency Evaluation of Ultrasonic Impact Treatment (UIT) of Welded Joints in Weldox 420 Steel in Accordance With the IIWW Program, Applied Ultrasonics, *Technical Report*, IIW/IIS-DOCUMENT XIII-1817-00.
141. Roy, S. and Fisher, J. W., Enhancing Fatigue Strength by Ultrasonic Impact Treatment, *ATLSS Engineering Research Centre*, USA, pp.1-35
142. Fisher, J. W., Statnikov, E. and Tehini, L. (2001), Fatigue Strength Enhancement by Means of Weld Design Change and the Application of Ultrasonic Impact Treatment, *Proc. Of Intl. Symp. On Steel Bridges*, Chicago.
143. Application Guide "Repair of Welded Members" (2000), *ESONIX*, Birmingham USA.
144. Galtier, A. and Statnikov, E. (2003), The Influence of Ultrasonic Impact treatment on Fatigue Behaviour of Welded Joints in High-strength Steel, *International Institute of Welding*, IIW/IIS Document XIII-1976-03
145. Statnikov, E. S., Rodopoulos, C. A., Vityazev, V. N., Korolkov, O. V. and Davidovich M. V. (2004), Scientific and Technical Report Improvement of Strength and Corrosion Fatigue Resistance of Samples of Aluminium Alloy, *Applied Ultrasonics*,
146. Statnikov, E. S., Muktepavel, V. O., Vityazev, V. N., Trufyakov, V. I., Kovalchuk, V. S. and Haagensen, P. J. (2003, Comparison of the Improvement in Corrosion Fatigue Strength of Weld Repaired Marine Cu 3-grade Bronze Propellers by Ultrasonic Impact Treatment (UIT) or Heat Treatment, *International Institute of Welding*, IIW/IIS-DOCUMENT XIII-1964-03
147. Vityazev V. N. and Davidovich M. V. (2004), Improvement of Strength and Resistance to Corrosion Fatigue, Pitting Damage and Corrosion Exfoliation of Aluminium Samples (Methodical plan), *Applied Ultrasonics*, Birmingham.
148. Verma, K. K. and Tehini, L., Improving Service Life of Highway and Traffic Structures Through the Use of Ultrasonic Impact Treatment, *Esonix, Ultrasonic Impact Treatment.*
149. Wright, W. (1996), Post-weld Treatment of a Welded Bridge Girder by Ultrasonic Impact Treatment, *Federal Highway Administration.*
150. Günther, H.-P., Kuhlmann, U. and Dürr, A. (2005), Rehabilitation of Welded Joints by Ultrasonic Impact Treatment (UIT), *IABSE Symposium Lisbon 2005.*

151. ALCOA, Alcoa North America Rolled Products, Date accessed April 2007, http://www.alcoa.com/mill_products/north_america/en/product.asp?cat_id=1478&prod_id=595
152. Rice, R. C., Jackson, J. L., Bakuckas, J. and Thompson, S. (2003), Metallic Materials Properties Development and Standardization (MMPDS), *Scientific Report, DOT/FAA/AR-MMPDS-01.*
153. Riddell, W. T. and Piascik, R. S. (1998), Stress Ratio Effects on Crack Opening Loads and Crack Growth Rates in Aluminium Alloy 2024, *NASA/TM-1998-206929*,
154. ASM Aerospace Specification Metals INC., Aluminium 2024-T3, Date accessed April 2007, http://asm.matweb.com/search/SpecificMaterial.asp?bassnum=MA2024T3
155. Comair Rotron ThermaFlo, Engineering Reference Typical Mechanical Properties of Aluminium Alloys, Date accessed April 2007, http://www.thermaflo.com/engref_mech.shtml
156. Hatch, J. E. (1984), *Aluminium: Properties and Physical Metallurgy*, ASM, 2nd edition,
157. Van Horn, K. R. (1967), *Aluminium Vol. 1. Properties, Physical Metallurgy and Phase Diagrams*, ASM
158. TENNALUM, Aluminium Alloys, Tempers and Terminology, Date accessed April 2007, http://www.tennalum.com/AATT.htm
159. Annual Book of ASTM Standards - Section 3 - Metals Test Methods and Analytical Procedures (1999), Standard Practice for Conducting Constant Amplitude Axial Fatigue Test of Metallic Materials, *ASTM*, Volume **03.01**, Designation E 466
160. Annual Book of ASTM Standards - Section 3 - Metals Test Methods and Analytical Procedures (1999), Standard Test Method for Measurement of Fatigue Crack Growth Rates, *ASTM*, Volume **03.01**, Designation E 647
161. Schajer, G. S. (1988), Measurements of Non-uniform Residual Stresses Using the Hole Drilling Method. Part I-stress Calculation Procedures, *Journal of Engineering Materials and Technology*, Vol. **110**, Number 4, pp. 338-343
162. Schajer, G. S. (1988), Measurements of Non-uniform Residual Stresses Using the Hole Drilling Method. Part II-Practical Application of the Integral Method, *Journal of Engineering Materials and Technology*, Vol. **110**, Number 4, pp. 344-349
163. Annual Book of ASTM Standards - Section 3 - Metal Test Methods and Analytical Procedures (1999), Standard Test Method for Determining Residual Stresses by the Hole-drilling Strain-gage Method, *ASTM*, Volume **03.01**, Designation E 837
164. National Physical Laboratory, The Measurement of Residual Stress in Plastics: A Technique Review A S Maxwell, Date Accessed: April 2007, http://www.npl.co.uk/materials/residualstress/plastics.html
165. Scintag, Inc. Providing solutions to your diffraction needs, Chapter 7: Basics of X-ray diffraction, Date accessed September 2008, http://epswww.unm.edu/xrd/xrdbasics.pdf
166. Anderoglu, O. (2004), Residual stress measurement using X-ray diffraction, Texas A&M University, Date accessed September 2008, http://repository.tamu.edu/handle/1969.1/1507
167. Prevéy, P. S., Lambda Research, Inc., X-ray diffraction residual stress technique, Date accessed September 2008, http://www.lambdatechs.com/html/resources/200.pdf
168. Prevéy. P. S., Lambda reseach, Current applications of the X-ray diffraction residual stress measurement, Date accessed September 2008, http://www.lambdatechs.com/html/resources/214.pdf
169. Proto manufacturing, X-ray diffraction (XRD) information, Date accessed September 2008, http://www.protoxrd.com/xrdinfo.html
170. Mott, B. W. (1956), *Micro-identation Hardness Testing*, Butter Worths Scientific Publications.
171. Westbrook, J. H. and Conrad, H. (1971), *The Science of Hardness Testing and its Research Applications*, American Society for Metals,
172. Boyer, H. E. (1987), *Hardness Testing*, ASM International,
173. Weibull, W. (1961), *Fatigue Testing and Analysis of Results*, Pergamon Press,
174. Taylor, D. (1989), *Fatigue Thresholds*, Butterworths
175. Saxena, A., Muhlstein, C. L., Fatigue Crack Growth Testing, pp. 740-757
176. Gao, N., Brown, M. W., Miller, K. J. (1995), Short Crack Coalescence and Growth in 316 Stainless Steel Subjected to Cyclic and Time Dependent Deformation, *Fracture Engineering Materials Structural*, Vol. **18**, No 12, pp. 1423-1441.
177. Murakami Y. (1987), *Stress Intensity Factors Handbook Vol. 1*, Pergamon Press.

APPENDIX

A 1: Table and graphs for different rosettes used in hole-drilling method [163].

Table A1: Numerical values of coefficients ā and $\bar{b}$.

Rosette A	ā					$\bar{b}$				
Blind Hole	Hole diameter, D_0/D					Hole Diameter, D_0/D				
Depth/D	0.3	0.035	0.40	0.45	0.50	0.30	0.35	0.40	0.45	0.50
0.00	.000	.000	.000	.000	.000	.000	.000	.000	.000	.000
0.05	.027	.037	.049	.063	.080	.051	.069	.090	.113	.140
0.10	.059	.081	.108	.138	.176	.118	.159	.206	.255	.317
0.15	.085	.115	.151	.192	.238	.180	.239	.305	.375	.453
0.20	.101	.137	.177	.223	.273	.227	.299	.377	.459	.545
0.25	.110	.147	.190	.238	.288	.259	.339	.425	.513	.603
0.30	.113	.151	.195	.243	.293	.279	.364	.454	.546	.638
0.35	.113	.151	.195	.242	.292	.292	.379	.472	.566	.657
0.40	.111	.149	.192	.239	.289	.297	.387	.482	.576	.668
Through Hole	.090	.122	.160	.203	.249	.288	.377	.470	.562	.615
Rosette B	ā					$\bar{b}$				
Blind Hole	Hole Diameter, D_0/D					Hole diameter, D_0/D				
Depth/D	0.30	0.35	0.40	0.45	0.50	0.30	0.35	0.40	0.45	0.50
0.00	.000	.000	.000	.000	.000	.000	.000	.000	.000	.000
0.05	.029	.039	.053	.068	.086	.058	.078	.102	.127	.157
0.10	.063	.087	.116	.148	.189	.134	.179	.231	.286	.355
0.15	.090	.123	.162	.205	.254	.203	.269	.343	.419	.504
0.20	.107	.145	.189	.236	.289	.256	.336	.423	.511	.605
0.25	.116	.156	.202	.251	.305	.292	.381	.476	.571	.668
0.30	.120	.160	.206	.256	.309	.315	.410	.509	.609	.707
0.35	.120	.160	.206	.256	.308	.330	.427	.529	.631	.730
0.40	.118	.158	.203	.253	.305	.337	.437	.541	.644	.743
Through Hole	.096	.131	.171	.216	.265	.329	.428	.531	.630	.725
Rosette C	ā					$\bar{b}$				
Blind Hole	Hole diameter, D_0/D					Hole diameter, D_0/D				
Depth/D	0.40	0.45	0.50	0.55	0.60	0.40	0.45	0.50	0.55	0.60
0.00	.000	.000	.000	.000	.000	.000	.000	.000	.000	.000
0.05	.065	.084	.106	.130	.157	.105	.132	.158	.185	.217
0.10	.147	.191	.238	.293	.361	.250	.314	.373	.440	.519
0.15	.218	.281	.347	.420	.506	.391	.484	.570	.658	.754
0.20	.270	.343	.421	.504	.595	.506	.617	.719	.816	.912
0.25	.302	.381	.465	.554	.648	.591	.712	.823	.923	1.015
0.30	.321	.403	.491	.583	.679	.650	.778	.893	.994	1.081
0.35	.331	.415	.505	.599	.698	.690	.822	.939	1.041	1.125
0.40	.336	.421	.512	.608	.709	.719	.851	.970	1.073	1.154
Through Hole	.316	.399	.494	.597	.707	.623	.723	.799	.847	.859

Figure A1: Plots of percent of strain Vs Hole Depth / D for three different rosettes for case of D_0/D.

Type A Rosette

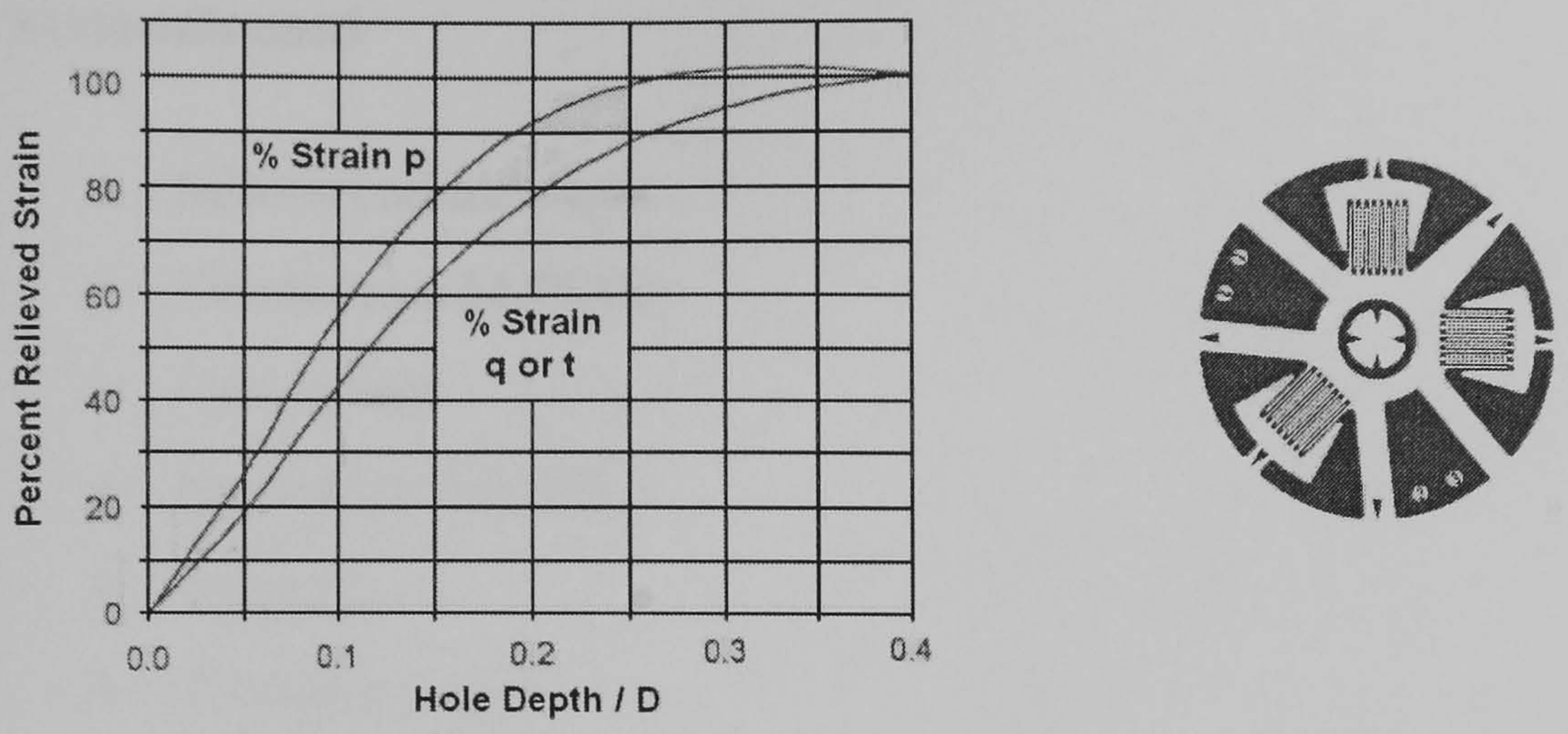

Type B Rosette

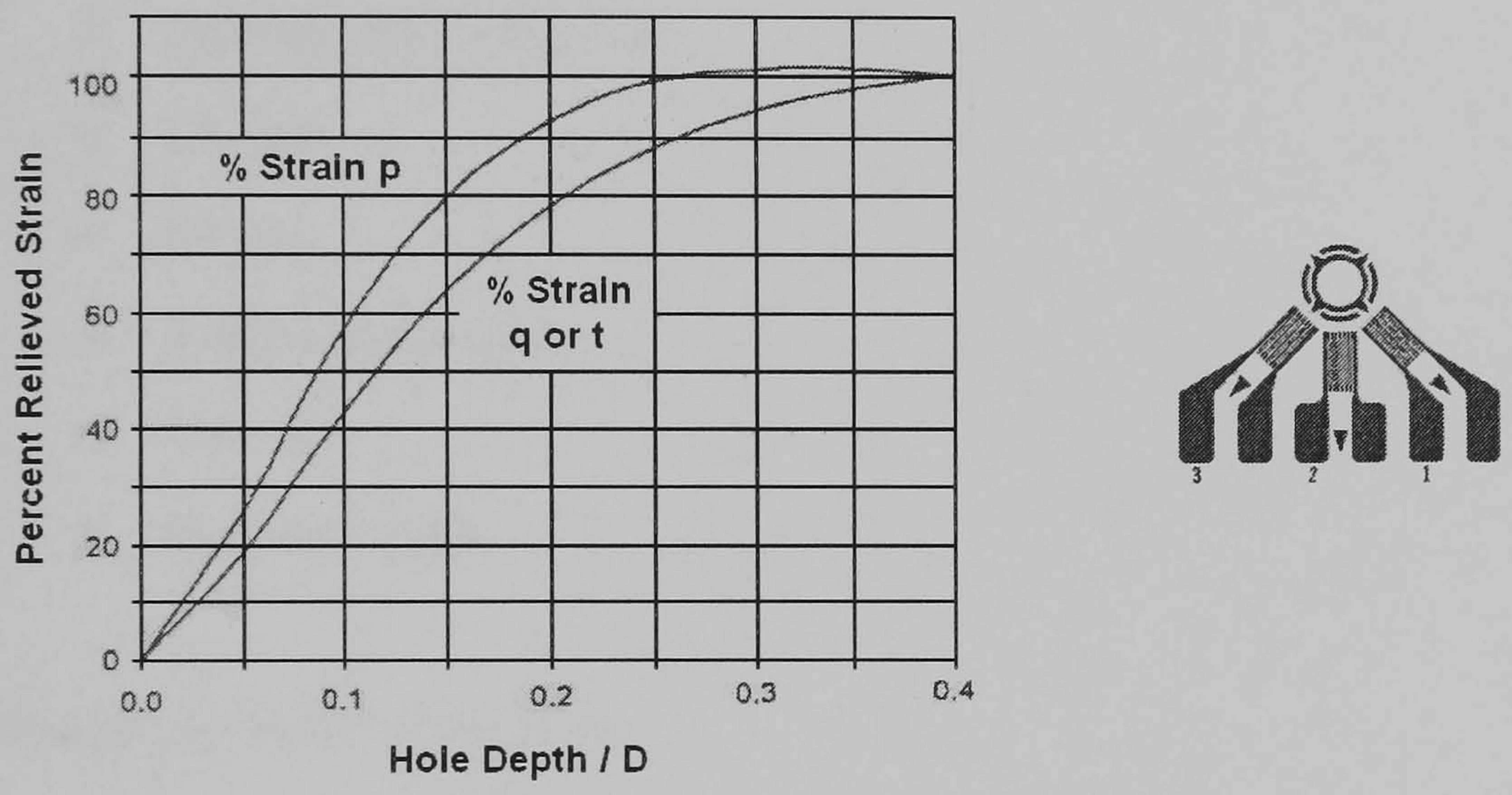

Type C Rosette

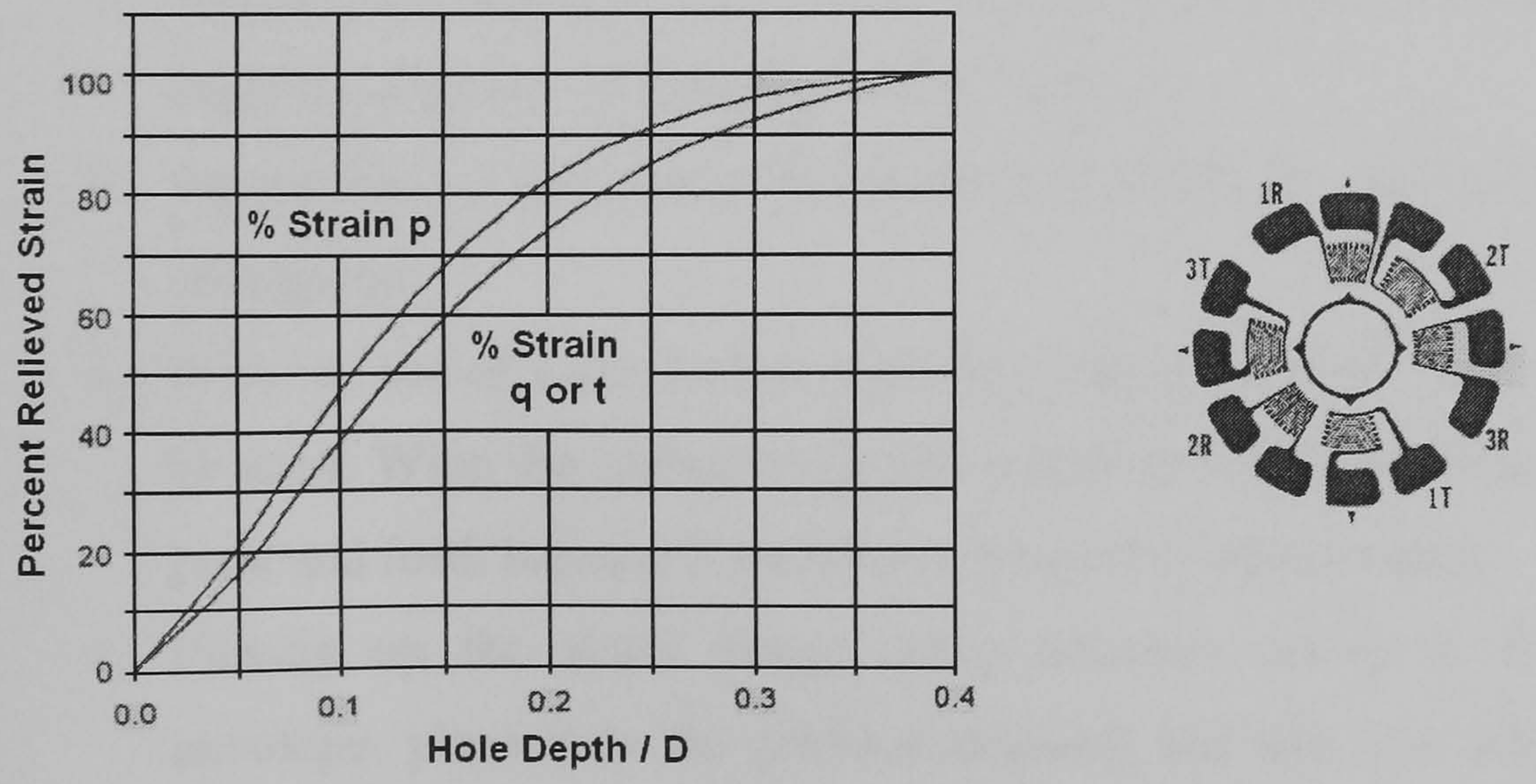

Where $p = (\varepsilon_3 + \varepsilon_1)/2$

$q = (\varepsilon_3 + \varepsilon_1)/2$

$t = (\varepsilon_3 + \varepsilon_1 - 2\varepsilon_2)/2$

A 2: Strain gauge installation

Materials used

- Silicon carbide paper
- Conditioner M-PREP
- Cotton bud
- Neutralizer M-PREP
- Tweezers
- Cellophane tape
- M-Bond 200 Catalyst
- M-bond 200 Adhesive
- M-flux
- Wires
- Solder equipment
- Cement
- Cement liquid

Gauge application technique

1. Abrade the surface if it is too smooth with the silicon carbide paper in order to facilitate adhesion of the gauge to the surface.
2. Throw two or three drops of conditioner M-PREP over the surface then wipe it with gauze.
3. With the aid of a cotton bud apply neutralizer M-PREP throughout the surface to be used. Wipe the surface with new gauze in a specific direction without wiping back and forth because it introduces deposited contaminants.
4. Picking up the strain gauge using tweezers, taking it from the transparent envelope, place it in the position required and then put cellophane tape on the gauge.
5. Lift the tape with gauge at around 45° until the whole gauge releases from the surface, holding the loose end and sticking down the other side leaving the gauge exposed.

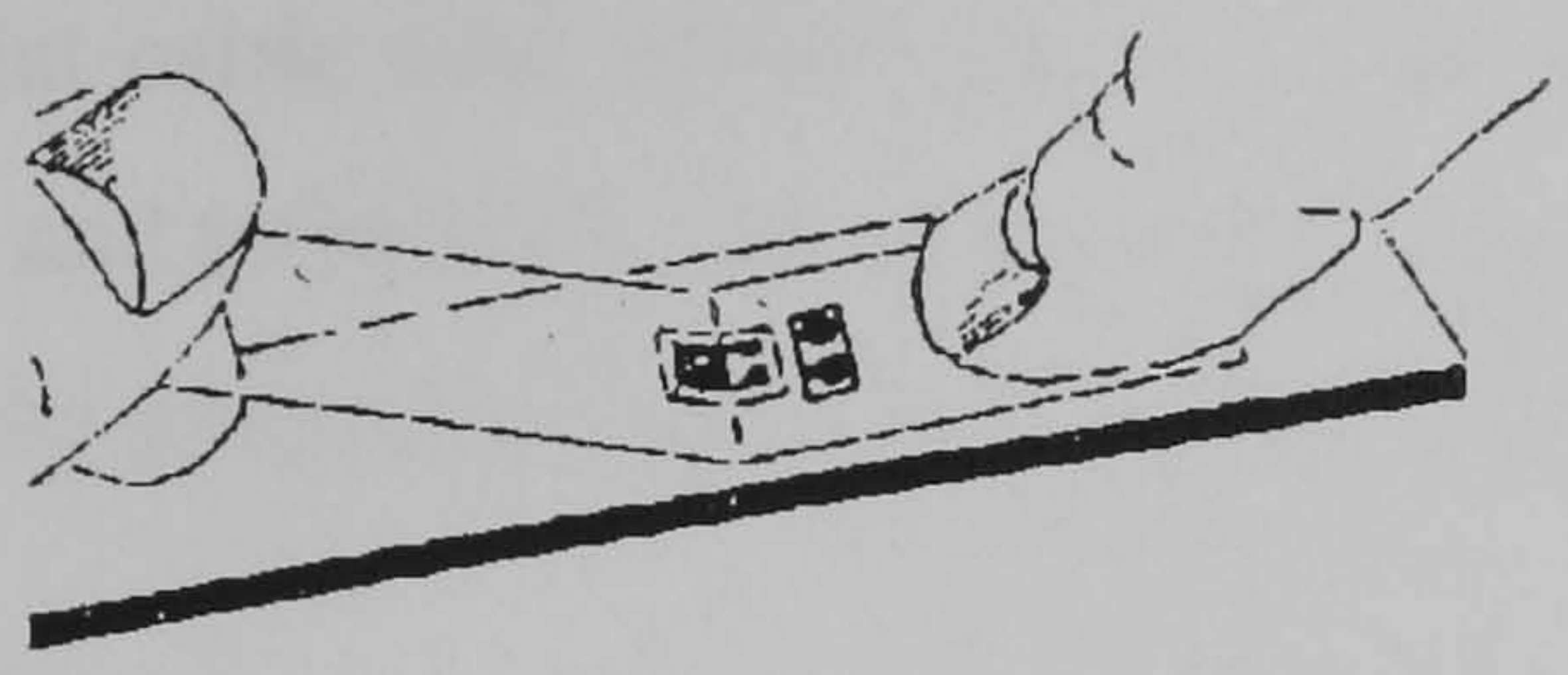

6. M-Bond 200 catalyst is applied on the surface exposed from gauge in small quantity leaving dry for a moment.

7. Add one or two drops of adhesive M-Bond 200 on the base where tape is stuck to the surface and then return the gauge in the original position slipping gauze over the tape in order to eliminate great amounts of M-Bond 200 between the gauge and the surface, the thinner the layer of adhesive the more optimum performance is.

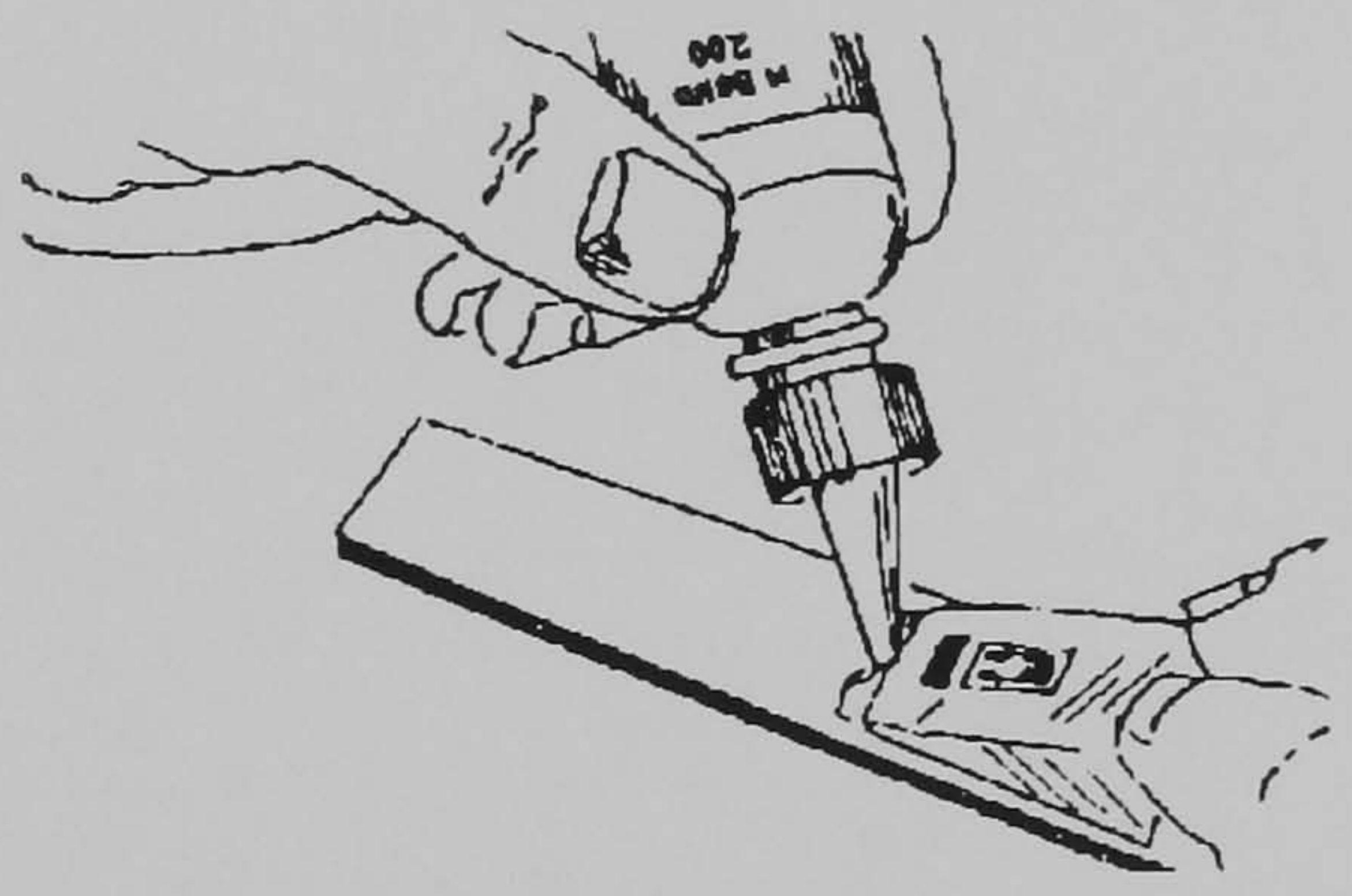

8. Apply pressure with the aid of the fingers for about 5 mins. Remove the tape with an angle of around 150° or 160°.

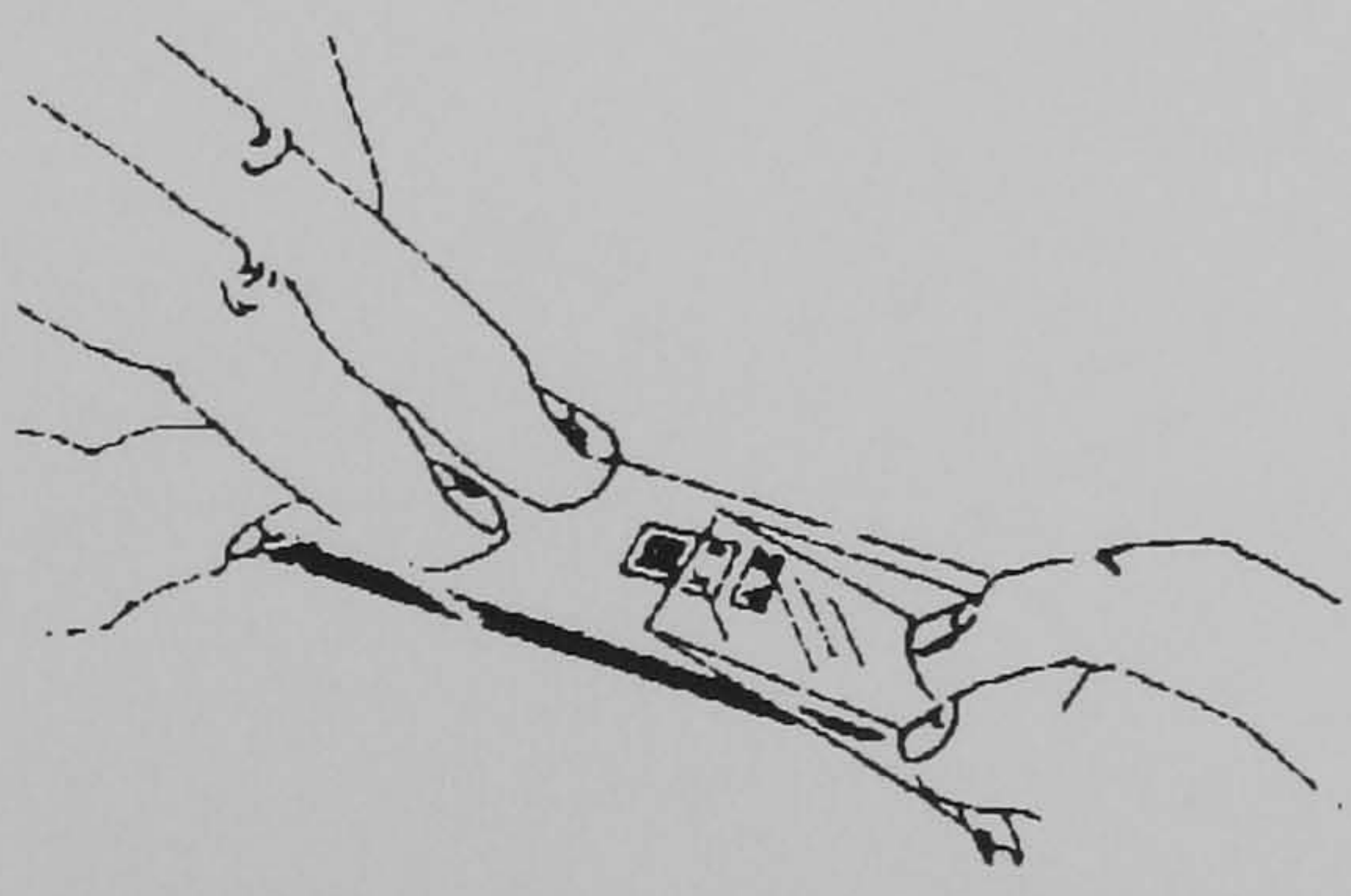

9. Protect part of the gauge with masking tape leaving solder terminals free.
10. Use 3-conductor flat cable with colours black, white and red. Strip the wire tips about 2 mm length and twist black and white wires together.
11. Apply M-Flux on the gauges terminals and weld the wires on every terminal.

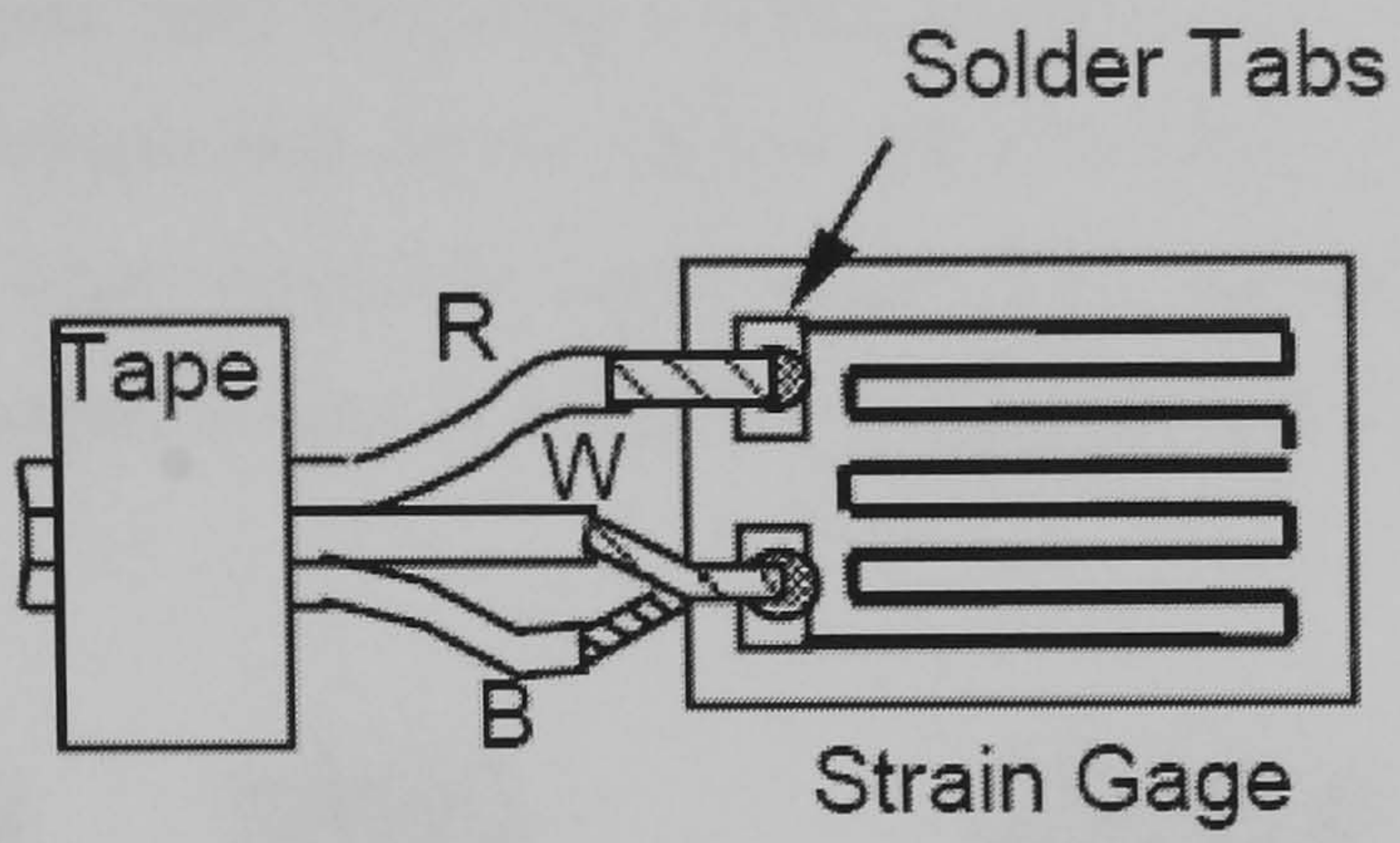

12. Wires are connected to the Vishay measuring unit in the next order:

P+ …………Red

D………… White

S-………… Black

A 3: Procedure of the MMH method.

A method developed in collaboration with Professor Brown was used in order to get results of residual stress showing the balance of stress into the material depth. For the case of a residual stress field including a stress gradient, this method was developed considering that the deformation on the surface due to drilling a small distance "t" at a depth "z" in a thick plate should be equal to that in a hypothetical plate of uniform residual stresses equal to σ_i as seen in fig. A.3.1, drilling through the same distance "t".

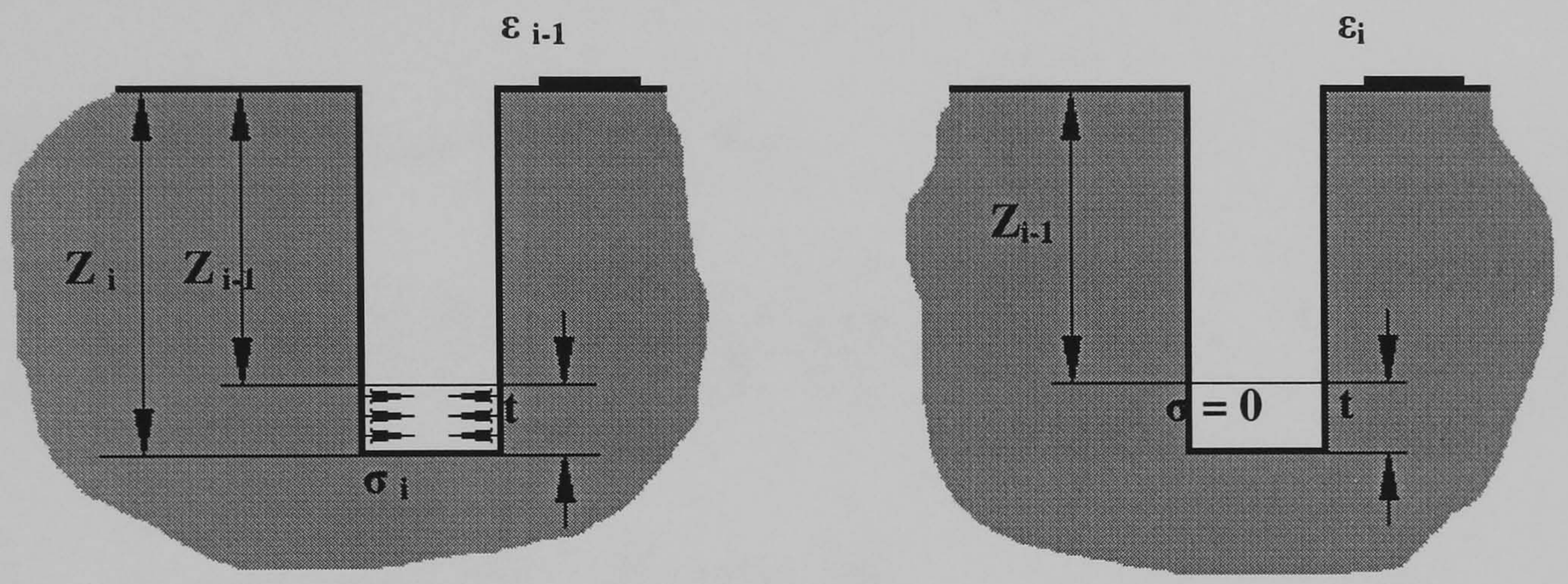

Hole drilled to depth Z_{i-1}

$\Delta\varepsilon = \varepsilon_i - \varepsilon_{i-1}$
Strain change due to relief of σ_i
over Z_{i-1} to Z_i.

Figure A3.1 Comparison of residual stresses relieved due to a small drilled distance "t" between two thick plates being one of them an hypothetical plate of uniform residual stress.

From equation 1 in chapter 4 to get σ_{max} and σ_{min} previously mentioned, the two main terms can be written as:

$$M = \frac{\varepsilon_3 + \varepsilon_1}{4\bar{A}} = \frac{\varepsilon_m}{\bar{\bar{A}}} G \qquad \text{A3-1}$$

$$N = \frac{\sqrt{(\varepsilon_3 - \varepsilon_1)^2 + (\varepsilon_3 + \varepsilon_1 - \varepsilon_2)^2}}{4\bar{B}} = \frac{\varepsilon_n}{\bar{\bar{B}}} H \qquad \text{A3-2}$$

Where G and H are constants.

Consider a uniform residual stress field where:

$$\sigma_u = \frac{\varepsilon_m G}{\overline{A}} + \frac{\varepsilon_n H}{\overline{B}} \qquad \text{A3-3}$$

$$\frac{dM}{M} = \left(\frac{\overline{A}}{\varepsilon_m G}\right)\left(\frac{G}{\overline{A}} d\varepsilon_m - \frac{\varepsilon_m G}{\overline{A}^2} d\overline{A}\right) = \frac{1}{\varepsilon_m} d\varepsilon_m - \frac{1}{\overline{A}} d\overline{A} \qquad \text{A3-4}$$

$$\frac{dN}{N} = \left(\frac{\overline{B}}{\varepsilon_n H}\right)\left(\frac{H}{\overline{B}} d\varepsilon_n - \frac{\varepsilon_n H}{\overline{B}^2} d\overline{B}\right) = \frac{1}{\varepsilon_n} d\varepsilon_n - \frac{1}{\overline{B}} d\overline{B} \qquad \text{A3-5}$$

Grouping the terms into the brackets we have:

$$d\sigma_u = \left(\frac{\varepsilon_m G}{\overline{A}}\right)\left(\frac{d\varepsilon_m}{\varepsilon_m} - \frac{d\overline{A}}{\overline{A}}\right) + \left(\frac{\varepsilon_n H}{\overline{B}}\right)\left(\frac{d\varepsilon_n}{\varepsilon_n} - \frac{d\overline{B}}{\overline{B}}\right) \qquad \text{A3-6}$$

If we assume that $\frac{d\varepsilon_m}{\varepsilon_m} - \frac{d\overline{A}}{\overline{A}} \cong \frac{d\varepsilon_n}{\varepsilon_n} - \frac{d\overline{B}}{\overline{B}}$ A3-7

Putting A3-3, A3-4, A3-5 and A3-7 into A3-6

$$d\sigma_u = \sigma_u \left(\frac{dM}{M} + \frac{dN}{N}\right)\frac{1}{2} \qquad \text{A3-8}$$

From fig. A3.1, for the real case of a stress gradient, the stress increment dσ is equivalent to $d\sigma_u$ in equation A3-8. Thus the stress at the depth for increment "i" is (σ + dσ) where:

$$\sigma + d\sigma = \sigma_{i-1} + \sigma_u \left[\frac{1}{M} dM + \frac{1}{N} dN\right]\frac{1}{2} \qquad \text{A3-9}$$

Even though the stress is not uniform at the surface, considering the shallowest hole due to the first hole drilling stage equation A3-3 gives the stress, assuming that the first depth is small enough that the stress does not change significantly over that depth. Therefore equation A3-9 uses the initial values of σ_{max} obtained from equation A3-3, and a second value of stress is obtained for second increment of hole drilling. This value includes the amount of stress due to the strains in the surface and the amount of additional stress introduced over the increment in depth. This will be repeated for every stage drilled, increasing iteratively the considering those stresses computed by equation A3-9.

Making an arrangement to equation A3-9 in order to use it directly gives:

$$\sigma_i = \sigma_{i-1} + \sigma_u \left[\frac{M_i - M_{i-1}}{M_{i-1}} + \frac{N_i - N_{i-1}}{N_{i-1}} \right] \frac{1}{2} \qquad \text{A3-10}$$

Where:

σ_i. Maximum residual stresses at a specific depth.

σ_{i-1}. Stress from the last depth worked out with equation A3-10.

σ_u. Maximum stress at that depth worked out with equation A3-3.

This method was chosen for use in this work because it is cheap and used widely by industry compared to others like the non-destructive method "neutron-beam stress measurement". The latter method is advantageous, as the material can be used subsequently in other kinds of test like fatigue test, however it is expensive and inaccessible.

A 4: Procedure of the MMX Method.

A method of analysis is required to allow for bending of plates after removal of a thin layer in order to measure residual stresses through the depth with the X-ray diffraction technique. This is needed to avoid getting unreal values, because every time a layer is removed, the plate will "spring", or bend as residual stress is released by layer removal.

Initially when no layering action has been taken on the material we have two equations which give us the equilibrium for axial tension and bending moment of the plate of thickness W, and are represented by:

$$\int_0^W \sigma_R \cdot dy = 0 \qquad \text{A4-1}$$

$$\int_0^W \sigma_R \cdot y dy = 0 \qquad \text{A4-2}$$

where σ_R is the residual stress distributed through the plate.

But as material tends to relax after layer removal, modifying residual stresses throughout the depth due to internal moments, equations A4-1 and A4-2 will change to equations A4-3 and A4-4 respectively after the first layer removal:

$$\int_0^{W-t_1} (\sigma_R + A_1 + B_1 y) \cdot dy = 0$$

and using equation A4-1, this becomes

$$\int_0^{W-t_1} (A_1 + B_1 y) \cdot dy = \int_{W-t_1}^{W} \sigma_R \cdot dy$$

$$\approx (\sigma_{R1} + \sigma_{R0})\, t_1/2 \qquad \text{A4-3}$$

assuming σ_R can be taken as $(\sigma_{R_1} + \sigma_{R_0})/2$ across the thin layer t_1.

$$\int_0^{W-t_1} (\sigma_R + A_1 + B_1 y) \cdot y dy = 0$$

using equation A4-2, this becomes:

$$\int_0^{W-t_1} (A_1 + B_1 y) \cdot y dy = \int_{W-t_1}^{W} \sigma_R \cdot y dy$$

$$\approx (\sigma_{R1} + \sigma_{R0})(2Wt_1 - t_1^2)/4 \qquad \text{A4-4}$$

where (A_1+B_1y) represents the change of stress as the plate springs assuming unloading is linear elastic. σ_{R0} and σ_{R1} are the original values of σ_R at $y = W$ and $y = W\text{-}t_1$ respectively.

As layer removal continues, equations for residual stresses after the second layer removal are as follows:

$$\int_0^{W-t_2} (\sigma_R + A_2 + B_2 y) \cdot dy = 0$$

$$\int_0^{W-t_2} (A_2 + B_2 y) \cdot dy = \int_{W-t_2}^{W-t_1} \sigma_R \cdot dy + \int_{W-t_1}^{W} \sigma_R \cdot dy$$

$$\approx (\sigma_{R2} + \sigma_{R1})(t_2 - t_1)/2 + (\sigma_{R1} + \sigma_{R0})\, t_1/2 \qquad \text{A4-5}$$

$$\int_0^{W-t_2} (\sigma_R + A_2 + B_2 y) \cdot y dy = 0$$

$$\int_0^{W-t_2} (A_2 + B_2 y) \cdot y dy = \int_{W-t_2}^{W-t_1} \sigma_R \cdot y dy + \int_{W-t_1}^{W} \sigma_R \cdot y dy$$

$$\approx (\sigma_{R2} + \sigma_{R1})(2W(t_2 - t_1) + t_1^2 - t_2^2)/4 + (\sigma_{R1} + \sigma_{R0})(2Wt_1 - t_1^2)/4 \qquad \text{A4-6}$$

Similar equations follow for the third and subsequent layers.

As the second terms on the right hand side in both equations A4-5 and A4-6 are similar to those in A4-3 and A4-4 respectively, it is enough to solve the residual stresses of the first equations once only, and then just add the values obtained into the equations derived for subsequent layers, e.g. equations A4-5 and A4-6. In order to solve for A_n and B_n, in the general case, equations such as A4-5 and A4-6 will be represented as follows:

$$\int_0^{W-t_n}(A_n + B_n y)\cdot dy = \left(\sigma_{R_n} + \sigma_{R_{n-1}}\right)\cdot R + S \qquad \text{A4-7}$$

$$\int_0^{W-t_n}(A_n + B_n y)\cdot ydy = (\sigma_{R_n} + \sigma_{R_{n-1}})\cdot T + U \qquad \text{A4-8}$$

Where:

$$R = (t_n - t_{n-1})/2 \qquad \text{A4-9}$$

$$S = \sum_{i=1}^{n-1}\left[\frac{\left(\sigma_{R_i} + \sigma_{R_{i-1}}\right)\left(t_i - t_{i-1}\right)}{2}\right] \qquad \text{A4-10}$$

$$T = (2W\,(t_n - t_{n-1}) + t_{n-1}^2 - t_n^2)/4 \qquad \text{A4-11}$$

$$U = \sum_{i=1}^{n-1}\left[\frac{\left(\sigma_{R_i} + \sigma_{R_{i-1}}\right)\left(2W\left(t_i - t_{i-1}\right) + t_{i-1}^2 - t_i^2\right)}{4}\right] \qquad \text{A4-12}$$

where $t_0 = 0$

Integrating left hand of equation A4-7 and multiplying the equation by $(W-t_n)$:

$$A_n\,(W - t_n)^2 + B_n\,(W - t_n)^3/2 = \left(\sigma_{R_n} + \sigma_{R_{n-1}}\right)R(W - t_n) + S(W - t_n) \qquad \text{A4-13}$$

In the same way integrating the left hand of equation A4-8 and multiplying by 2, then subtracting equation A4-13, we have an equation with one unknown $\mathbf{B_n}$ as follows:

$$B_n\,(W - t_n)^3/6 = \left(\sigma_{R_n} + \sigma_{R_{n-1}}\right)(2T - R(W - t_n)) + 2U - S(W - t_n) \qquad \text{A4-14}$$

Having found B_n, equation A4-13 provides A_n.

Considering each residual stress value read (with the aid of XRD technique) in every layer as "$\sigma_{measured_n}$", we have:

$$\sigma_{measured_n} = \sigma_{R_n} + A_n + B_n\,(W - t_n) \qquad \text{A4-15}$$

Where σ_{R_n} is the original residual stress. Equation A4-15 takes into account the redistribution of residual stresses after layering every time. Substituting equations A4-14 and A4-13 into equation A4-15 to eliminate A_n and B_n finally we have:

$$\sigma_{measured_n} =$$

$$\frac{1}{(W-t_n)^2}\left[\sigma_{R_n}(W-t_n)^2+\sigma_{R_n}(6T-2R(W-t_n))+\sigma_{R_{n-1}}(6T-2R(W-t_n))+6U-2S(W-t_n)\right]$$

A4-16

A 5: Raw data for Hole-drilling.

UIT-1-27

Depth (mm)	Gauge readings			σ (MPa)
	1	2	3	
0.1	61	37	19	-216.54
0.2	107	75	45	-195.91
0.3	150	115	74	-189.47
0.4	188	153	106	-176.84
0.5	220	187	134	-168.1
0.6	247	216	161	-162.4
0.7	228	177	115	-119.02
0.8	247	202	141	-120.71
0.9	260	222	167	-122.3
1	254	202	161	-113.46
1.1	257	206	163	-108.78
1.2	254	210	166	-105.26
1.3	255	218	171	-104.82
1.4	234	206	160	-96.07
1.5	228	208	152	-91.83

Depth (mm)	Gauge readings			σ (MPa)
	1	2	3	
0.1	68	31	-7	-165.11
0.2	140	69	-1	-179.16
0.3	196	105	12	-175.93
0.4	250	142	26	-166.01
0.5	285	172	40	-154.33
0.6	315	201	57	-148.07
0.7	342	225	74	-144.36
0.8	369	238	92	-143.42
0.9	386	251	106	-140.92
1	396	263	118	-140.53
1.1	405	271	125	-137.28
1.2	408	276	131	-135.08
1.3	412	279	136	-134.84
1.4	411	283	141	-134.6
1.5	409	285	145	-133.88

UIT-1-36

Depth (mm)	Gauge readings			σ (MPa)
	1	2	3	
0.1	29	15	38	-190
0.2	55	29	58	-141.5
0.3	78	44	54	-102.5
0.4	99	57	82	-101
0.5	120	69	82	-89
0.6	132	78	97	-84
0.7	141	84	99	-76.5
0.8	146	94	96	-69.5
0.9	151	92	84	-63
1	152	88	98	-63
1.1	154	95	95	-60
1.2	155	103	98	-60
1.3	153	100	99	-58
1.4	152	100	101	-58
1.5	155	103	99	-57

Depth (mm)	Gauge readings			σ (MPa)
	1	2	3	
0.1	2	2	35	-114
0.2	12	50	64	-104
0.3	25	32	90	-97.5
0.4	40	51	119	-97
0.5	53	67	144	-94.5
0.6	65	79	163	-91.5
0.7	75	89	180	-89
0.8	81	95	194	-86.5
0.9	85	100	203	-83.5
1	88	101	209	-81.5
1.1	90	104	215	-80.5
1.2	92	107	219	-80
1.3	92	107	222	-76.5

Depth (mm)	Gauge readings			σ (MPa)
	1	2	3	
0.1	28	60	88	-313.98
0.2	59	115	158	-279.69
0.3	90	167	231	-271.52
0.4	122	218	299	-253.23
0.5	147	256	351	-236.48
0.6	168	287	394	-223.7
0.7	191	318	434	-216.88
0.8	207	340	466	-209.38
0.9	220	356	487	-202.5
1	231	370	502	-200.41
1.1	236	377	511	-193.48
1.2	239	382	519	-189.97
1.3	242	387	524	-188.48
1.4	244	390	528	-188.25
1.5	249	393	532	-188.74

Depth (mm)	Gauge readings			σ (MPa)
	1	2	3	
0.1	2	8	26	-75.78
0.2	19	25	52	-91.51
0.3	45	58	86	-110.8
0.4	72	85	118	-114.28
0.5	95	115	145	-113.96
0.6	118	138	167	-113.44
0.7	205	162	182	-134.29
0.8	220	181	193	-128.49
0.9	227	190	199	-122.01
1	234	198	205	-120.02
1.1	236	206	208	-115
1.2	236	208	213	-112.53
1.3	236	212	216	-111.22
1.4	236	213	219	-110.95
1.5	236	214	222	-110.68

Depth (mm)	Gauge readings			σ (MPa)
	1	2	3	
0.1	3	7	12	-40.6
0.2	14	21	35	-65.16
0.3	32	43	66	-78.34
0.4	58	72	105	-87.33
0.5	79	92	128	-78.84
0.6	97	111	149	-71.73
0.7	115	122	164	-66.32
0.8	128	133	175	-59.17
0.9	137	138	180	-52.6
1	144	141	184	-49.86
1.1	149	140	183	-46.12
1.2	153	141	184	-43.72
1.3	155	138	185	-46.26
1.4	159	139	185	-45.26
1.5	162	138	186	-47.25

UIT-2-36

Depth (mm)	Gauge readings			σ (MPa)
	1	2	3	
0.1	2	4	6	-21.65
0.2	6	7	9	-19.33
0.3	7	10	6	-10.99
0.4	10	6	14	-14.43
0.5	15	4	18	-15.67
0.6	14	7	7	-8.35
0.7	19	4	18	-12.83
0.8	19	3	5	-7.466
0.9	20	2	18	-10.88
1	23	5	10	-9.02
1.1	23	8	11	-8.8
1.2	22	5	7	-7.26
1.3	21	5	15	-8.85
1.4	21	2	7	-6.82
1.5	21	-3	8	-7

Depth (mm)	Gauge readings			σ (MPa)
	1	2	3	
0.1	3	2	3	-16.24
0.2	7	3	5	-15.46
0.3	12	6	5	-14.37
0.4	14	8	6	-12.03
0.5	18	10	8	-12.34
0.6	20	12	7	-10.74
0.7	22	12	7	-10.06
0.8	24	14	8	-9.95
0.9	25	14	6	-8.87
1	26	16	6	-8.74
1.1	26	16	6	-8.28
1.2	28	15	6	-8.52
1.3	27	15	5	-7.87
1.4	27	14	4	-7.55
1.5	26	15	4	-7.25

Depth (mm)	Gauge readings			σ (MPa)
	1	2	3	
0.1	6	5	5	-29.77
0.2	9	8	8	-21.91
0.3	14	12	12	-21.99
0.4	18	15	14	-19.24
0.5	20	17	14	-16.14
0.6	22	18	15	-14.72
0.7	22	18	15	-12.83
0.8	19	-1	7	-8.08
0.9	21	7	5	-7.44
1	22	11	8	-8.2
1.1	22	12	9	-8.02
1.2	22	11	8	-7.51
1.3	22	11	8	-7.38
1.4	22	10	8	-7.31
1.5	21	9	8	-7

UIT-3-36

Depth (mm)	Gauge readings			σ (MPa)
	1	2	3	
0.1	2	5	-6	-23
0.2	6	6	3	-6
0.3	9	10	3	-6.5
0.4	15	10	3	-8
0.5	13	14	7	-7.5
0.6	12	13	10	-6.5
0.7	15	14	8	-6.5
0.8	17	17	6	-5.5
0.9	15	11	6	-4.5
1	12	14	9	-4
1.1	14	10	10	-5
1.2	13	11	8	-4
1.3	15	7	9	-4
1.4	12	8	10	-3
1.5	13	6	8	-2.5

Depth (mm)	Gauge readings			σ (MPa)
	1	2	3	
0.1	-3	-3	2	2.7
0.2	-3	1	8	-6.44
0.3	-10	3	7	2.53
0.4	-13	-5	8	3
0.5	-16	-5	13	1.42
0.6	-20	-4	16	1.59
0.7	-25	-6	18	2.42
0.8	-27	-7	20	2.17
0.9	-26	-7	21	1.43
1	-27	-4	24	0.82
1.1	-29	-8	25	1.03
1.2	-29	-19	25	1
1.3	-31	-18	25	1.47
1.4	-30	-17	26	0.97
1.5	-32	18	26	1.45

A 6: Fortran Programme used to analyse crack growth rate.

```
! THIS PROGRAM USE THE FIVE POINT INCREMENTAL POLYNOMIAL METHOD FOR
! DETERMINING DA/DN AND NUMBER OF CYCLES AND CAN BE MODIFIED TO USE
! 5& 7 POINT INCREMENTAL POLYNOMIAL METHOD
```

```
INTEGER NPTS,N,I,J,QQ,L,K,K1,RESP,KIND,M,IFAIL
DIMENSION A(100),N(100),DADN(100),DELK(100)
DIMENSION AA(10),NN(10),BB(3)
REAL PMIN,PMAX,F,A,B,B1,W,W1,AM,AM1,TEMP,R,C1,C2,YS
CHARACTER ID *20,DATE*11,NAME*12,SPE*4,ENVIRO*15,CRACKL*12,CYCLI*12
130 FORMAT(/1X,'FIVE POINT INCREMENTAL POLYNOMIAL METHOD FOR DETERMINING DA/DN')
200 FORMAT(//1X,'DATE: ',A11,2X,'SPECIMEN ID:',3X,A20,7X,'NO. POINTS =',I3)
300 FORMAT(/1X,'Pmin=',1X,F7.2,1X,'KNw',5X,'Pmax=',1X,F6.2,1X,'KNw',5X,'R=',F6.3,5X,'TEST FREQ=',F6.3,1X,'HZ.')
400 FORMAT(/1X,'M(T)SPECIMEN',5X,'B=',1X,F6.3,1X,'m.',6X,'W=',1X,F6.3,1X,'m.',6X,'AN=',1X,F6.3,1X,'m.')
401 FORMAT(/1X,'C(T) SPECIMEN',5X,'B=',1X,F6.3,1X,'m.',6X,'W=',1X,F6.3,1X,'m.',6X,'AN=',1X,F6.3,1X,'m.')
500 FORMAT(/1X,'TEM.=',F4.0,1X,'C',2X,'ENVIRONMENT=',A15,2X,'0.2% YIELD STRESS =',1x,F6.2,1x,'MPa')
600    FORMAT(/'OBS.NO.',2X,'CYCLES',1X,'A(MEAS.)mm',1X,'A(REG.)mm',1X,'M.C.C.',1X,'DELK(MPa    m^1/2)',1X,'DA/DN
(mm/Cy)'//)
700 FORMAT(/80('-')/)
800 FORMAT(1X,'*-DATA VIOLATE SPECIMEN SIZE REQUIREMENTS')
900 FORMAT(I3,4X,I8,1X,F6.3)
150 FORMAT(I3,4X,I8,1X,F6.3,5X,F6.3,4X,F7.5,3X,F5.2,7X,E8.3)
250 FORMAT(I3,4X,I8,1X,F6.3,5X,F6.3,4X,F7.5,3X,F5.2,7X,E8.3,'*')
    WRITE(5,*)'DATE?'
    READ(5,*)DATE
    WRITE(6,*)'ID OF THE SPECIMEN?'
    READ(5,*)ID
    WRITE(6,*)'NUMBER OF DATA POINTS (a,N)?'
    READ(5,*)NPTS
    WRITE(6,*)'Pmin (KN)?'
    READ(5,*)PMIN
    WRITE(6,*)'Pmax (KN)?'
    READ(5,*)PMAX
    WRITE(6,*)'TEST FREQUENCY(Hz)'
    READ(5,*)F
    WRITE(6,*)'SPECIMEN THICKNESS (B)(mm)? '
    READ(5,*)B
    WRITE(6,*)'SPECIMEN WIDTH (W)(mm)?'
    READ(5,*)W
    WRITE(6,*)'MACHINE NOTCH LENGTH (AM)(mm)?'
    READ(5,*)AM
10  WRITE(6,*)'WHAT KIND OF SPECIMEN ARE YOU WORKING WITH?'
    WRITE(6,*)'TYPE 1 FOR C(T), TIPE 2 FOR M(T)'
    READ(5,*)KIND
```

```
      IF (KIND.GE.3)GO TO 10
      WRITE(6,*)'WHAT IS THE NAME OF THE FILE WHERE CRACK LENGHTS ARE (in mm)?'
      READ(5,*)CRACKL
       OPEN(20,FILE=CRACKL)
        READ(20,*)(A(I),I=1,NPTS)
       CLOSE (20)
      WRITE(6,*)'WHAT IS THE NAME OF THE FILE WHERE CYCLES READINGS ARE?'
      READ(5,*)CYCLI
       OPEN(40,FILE=CYCLI)
        READ(40,*)(N(I),I=1,NPTS)
       CLOSE (40)
      WRITE(6,*)'TEMPERATURE DREGREES C'
      READ(5,*)TEMP
      WRITE(6,*)'ENVIRONMENT (Air,Vacuum,salted water,etc.)'
      READ(5,*)ENVIRO
      WRITE(6,*)'MATERIAL 0.2% YIELD STRESS (MPa)'
      READ(5,*)YS
      WRITE(5,*)'WOULD YOU LIKE TO SAVE THE DATA IN A FILE?'
  160 WRITE(5,*)'PRESS 1 IF YES, PRESS 2 IF NOT'
      READ(6,*)RESP
      IF(RESP.GE.3)GO TO 160
       IF(RESP.EQ.2)GO TO 140
        IF(RESP.EQ.1) THEN
        WRITE(5,*)'ENTER THE NAME OF THE FILE, NO MORE THAN 10 CHARACTERS'
        READ(6,*)NAME
        OPEN(5,FILE = NAME)
        PRINT *,'YOUR DATA HAVE BEEN SAVED IN ',NAME,' FILE'
        END IF
  140 WRITE(5,700)
      R=PMIN/PMAX
      WRITE (5,130)
      WRITE(5,200)DATE,ID,NPTS
      B1=B/1000
      W1=W/1000
      AM1=AM/1000
       IF (KIND.EQ.1)THEN
        WRITE(5,401)B1,W1,AM1
       END IF
      WRITE(5,400)B1,W1,AM1
      WRITE(5,300)PMIN,PMAX,R,F
      WRITE(5,500)TEMP,ENVIRO,YS
      WRITE(5,700)
      WRITE(5,600)
      DO 31 I=1,NPTS
      A(I)=A(I)+AM
   31 CONTINUE
      K=0
      PI=3.1416
      PP=PMAX-PMIN
       DO 110 I=1,2
```

```
      WRITE(5,900)I,N(I),A(I)
110 CONTINUE
     NPTS=NPTS-4
      DO 100 I=1,NPTS
      L=0
      K=K+1
      K1=K+4
       DO 60 J=K,K1
       L=L+1
       AA(L)=A(J)
       NN(L)=N(J)
60  CONTINUE
      C1 = 0.5*(NN(1)+NN(5))
      C2 = 0.5*(NN(5)-NN(1))
      SX=0
      SX2=0
      SX3=0
      SX4=0
      SY=0
      SYX=0
      SYX2=0
       DO 70 J=1,5
       X=(NN(J)-C1)/C2
       YY=AA(J)
       SX=SX+X
       SX2=SX2+X**2
       SX3=SX3+X**3
       SX4=SX4+X**4
       SY=SY+YY
       SYX=SYX+X*YY
       SYX2=SYX2+YY*X**2
70  CONTINUE
      DEN=5.0*(SX2*SX4-SX3**2)-SX*(SX*SX4-SX2*SX3)+SX2*(SX*SX3-SX2**2)
      T2=SY*(SX2*SX4-SX3**2)-SYX*(SX*SX4-SX2*SX3)+SYX2*(SX*SX3-SX2**2)
      BB(1)=T2/DEN
      T3=5.0*(SYX*SX4-SYX2*SX3)-SX*(SY*SX4-SYX2*SX2)+SX2*(SY*SX3-SYX*SX2)
      BB(2)=T3/DEN
      T4=5.0*(SX2*SYX2-SX3*SYX)-SX*(SX*SYX2-SX3*SY)+SX2*(SX*SYX-SX2*SY)
      BB(3)=T4/DEN
      YB=SY/5.0
      RSS=0
      TSS=0
       DO 75 J=1,5
       X=(NN(J)-C1)/C2
       YHAT=BB(1)+BB(2)*X+BB(3)*X**2
       RSS=RSS+(AA(J)-YHAT)**2
       TSS=TSS+(AA(J)-YB)**2
75 CONTINUE
      R2=1.0-RSS/TSS
      DADN(I)=BB(2)/C2+2.0*BB(3)*(NN(3)-C1)/C2**2
```

```
      X=(NN(3)-C1)/C2
      AR=BB(1)+BB(2)*X+BB(3)*X**2
      S=1E+10
      SNET=0
      QQ=I+2
      IF (KIND.EQ.1) GO TO 1
      IF (KIND.EQ.2) GO TO 2
1    CONTINUE
      T=AR/W
      FT=((2+T)*(0.886+4.64*T-13.32*T**2+14.72*T**3-5.6*T**4))/(1-T)**1.5
      S=YS*SQRT(PI*W1*(1-T))/2
      GO TO 190
2    CONTINUE
      T=2*AR/W
      SEC=1.0/(COS(PI*T/2))
      FT=SQRT((PI*T*SEC)/2.0)
      SNET=(PMAX*1000)/(B*W*(1-T))
190  DELK(I)=(FT*PP)/(B*SQRT(W1))
      AX=DELK(I)/(1-R)
      IF(AX.GE.S) GO TO 97
      IF(SNET.GE.YS) GO TO 97

      WRITE(5,150)QQ,N(QQ),A(QQ),AR,R2,DELK(I),DADN(I)
      GO TO 100
97   WRITE(5,250)QQ,N(QQ),A(QQ),AR,R2,DELK(I),DADN(I)
100  CONTINUE
      J=NPTS+3
      K=NPTS+4
       DO 120 I=J,K
       WRITE (5,900)I,N(I),A(I)
120  CONTINUE
      WRITE(5,700)
      WRITE(5,800)
      CLOSE(20)
      CLOSE(40)
      STOP
      END
```

A 6.1: Example output from crack growth programme using five incremental polynomial method.

```
--------------------------------------------------------------------------------

 FIVE POINT INCREMENTAL POLYNOMIAL METHOD FOR DETERMINING DA/DN

 DATE: 26-Oct-2006  SPECIMEN ID:   NUITL                          NO. POINTS = 12

 M(T) SPECIMEN     B=  0.005 m.       W=  0.080 m.       AN=  0.002 m.

 Pmin=     4.13 KNw      Pmax=  41.33 KNw      R= 0.100     TEST FREQ= 7.000 HZ.

 TEM.= 20. C  ENVIRONMENT=Air                0.2% YIELD STRESS = 450.00 MPa

--------------------------------------------------------------------------------

OBS.NO.  CYCLES A(MEAS.)mm A(REG.)mm M.C.C. DELK(MPa m^1/2) DA/DN (mm/Cy)

  1       55227  5.130
  2       62443  7.960
  3       65003  8.830      9.022    0.99739   16.17       .549E-03
  4       70002 12.050     12.001    0.99865   19.13       .879E-03
  5       71998 13.750     13.950    0.99663   21.07       .122E-02
  6       73502 15.760     15.744    0.99812   22.91       .171E-02
  7       74901 18.270     18.416    0.98659   25.83       .281E-02
  8       75989 21.320     21.793    0.99190   30.05       .421E-02
  9       76454 24.370     24.235    0.95276   33.68       .839E-02
 10       76685 24.930     26.440    0.91486   37.61       .182E-01
 11       76848 28.980
 12       76900 32.380

--------------------------------------------------------------------------------

 *-DATA VIOLATE SPECIMEN SIZE REQUIREMENTS
```

A 7: Procedure to work out constants and crack length values from EPD readings.

From equations obtained in **chapter 4** showed below, values for Ka, Kb, e, a_a and a_b will be worked out.

$$\mathrm{Cosh}\,(K_aV_a) = \frac{Cos\left(\dfrac{\pi(x_a+e)}{2(W+e)}\right)}{Cos\left(\dfrac{\pi(a_a+e)}{2(W+e)}\right)} \qquad \text{A7-1}$$

$$\mathrm{Cosh}\,(K_bV_b) = \frac{Cos\left(\dfrac{\pi(x_b-e)}{2(W-e)}\right)}{Cos\left(\dfrac{\pi(a_b-e)}{2(W-e)}\right)} \qquad \text{A7-2}$$

$$\mathrm{Cosh}\,(K_aV_c) = \sqrt{1+\frac{Cosh^2\left(\dfrac{\pi y_c}{2(W+e)}\right)-1}{Cos^2\left(\dfrac{\pi(a_a+e)}{2(W+e)}\right)}} \qquad \text{A7-3}$$

$$\mathrm{Cosh}\,(K_bV_d) = \sqrt{1+\frac{Cosh^2\left(\dfrac{\pi y_c}{2(W-e)}\right)-1}{Cos^2\left(\dfrac{\pi(a_b-e)}{2(W-e)}\right)}} \qquad \text{A7-4}$$

1st. Solving equations A7-1 and A7-3 eliminating the term where crack length appears and doing the same for equation A7-2 and A7-4 we have two equations and three unknowns. The equations are shown below.

$$\frac{Cosh^2(K_aV_c)-1}{Cosh^2(K_aV_a)} = \frac{Cosh^2\left(\dfrac{\pi y_c}{2(W+e)}\right)-1}{Cos^2\left(\dfrac{\pi(x_a+e)}{2(W+e)}\right)} \qquad \text{A7-5}$$

$$\frac{Cosh^2(K_bV_d)-1}{Cosh^2(K_bV_b)} = \frac{Cosh^2\left(\frac{\pi y_c}{2(W-e)}\right)-1}{Cos^2\left(\frac{\pi(x_b-e)}{2(W-e)}\right)} \qquad \text{A7-6}$$

2nd. Giving an initial estimated value for "e" solve equation A7-5 for Ka and A7-6 for Kb using bisection method.

3rd. Using a fifth relationship assuming the "e" line is straight and considering local coordinates (x*, y*) for the moment, with origin on the "e" line, where for one half of the specimen divided along the "e" line:

$$\text{Cos}\left(\frac{\pi x^*}{2W^*}\right) = 1 \qquad \text{for } x^* = 0$$

So for equation 22 in chapter 4,

$$\text{Cosh (KV)} = \frac{Cosh\left(\frac{\pi y^*}{2W^*}\right)}{Cos\left(\frac{\pi a^*}{2W^*}\right)} \qquad \text{A7-7}$$

Solving equation A7-7 for KV we have that:

$$\text{KV} = \frac{\pi y^*}{2W^*} - \ln\left(\text{Cos}\left(\frac{\pi a^*}{2W^*}\right)\right) \qquad \text{A7-8}$$

Remote from crack, potential gradient $\delta V / \delta y^*$ is the same for sides A and B of the specimen:

$$\delta V / \delta y^* = \frac{\pi}{(2WK^*)} \qquad \text{A7-9}$$

So **Ka (w + e) = Kb (w – e)** (fifth relationship)

Solving for "e":

$$e = w\,(Kb - Ka)/(Kb + Ka) \qquad \text{A7-10}$$

Equation A7-10 gives a new estimated value for "e", this value must be reused in the second step above mentioned and iterate until "e" value converges.

4th. Finally solving equation A7-1 for crack tip A and equation A7-2 for crack tip B we have:

$$a_A = \frac{2(W+e)}{\pi} \text{ Arc Cos} \left[\frac{Cos\left(\frac{\pi(x_a+e}{2(W+e)}\right)}{Cosh(K_a V_a)} \right] \text{-e} \qquad \text{A7-11}$$

$$a_B = \frac{2(W-e)}{\pi} \text{ Arc Cos} \left[\frac{Cos\left(\frac{\pi(x_b-e)}{2(W-e)}\right)}{Cosh(K_b V_b)} \right] +e \qquad \text{A7-12}$$

A 8: Fortran Programme used to get crack length from AC-EPD readings from M(T) specimen, for an eccentric crack.

```
! Program to calculate the crack length using Electrical Potential Drop Technique
! Gilbey and Pearson Equation (For unequal cracks, a1 and a2)
!
! ((Cos^2((pi*x)/(2*w))*Cosh^2((pi*y)/(2*w)))/Cosh^2(K*V))+
! ((1-(Cos^2((pi*x)/(2*w))))*(Cosh^2((pi*y)/(2*w))-1))/(Cosh^2(K*V)-1) =
! Cos^2((pi*a)/(2*w))
!
! Known Variables Va, Vb, Vc, Vd, Xa, Xb, Yc, Yd & W
!
! Unknow variables Ka, Kb, Aa, Ab & e
!
     CHARACTER VOLTFI*12,NAME*10
     Real Aa,Ab,e,e1,Ka,Kb,W,Xa,Xb,Yc,Yd                    !Unknown
     Real A,B0,B1,B4,C,D0,D1,D4,eccen,F,G0,G1,G4,H,I0,I1,I4,J0,J1,J4,K0,K1,K2,K3,K4
     Real L0,L1,L4,M,Pi,Va,Vb,Vc,Vd
     Integer I,N,LIMIT,NVOLT,Q,RESP
     PARAMETER (LIMIT = 500)                                !How many values are the maximum to input
     REAL Vola(LIMIT),Volb(LIMIT),Volc(LIMIT),Vold(LIMIT)
     WRITE(5,*)'PROGRAM TO CALCULATE THE VALUES OF A CRACK GROWTH IN A PLATE WITH'
      WRITE(5,*)'A CRACK IN THE CENTER USING ELECTRICAL POTENTIAL DROP TECHNIQUE'
      WRITE(5,400)
      WRITE(5,*)'Input the next values'
      WRITE(5,*)'Xa (Distance from the crack centre to the point "a")'
      READ(6,*)Xa
      WRITE(5,*)'Xb (Distance from the crack centre to the point "b")'
      READ(6,*)Xb
      WRITE(5,*)'Yc (Distance from the crack centre to the point "c" in "Y" direction)'
      READ(6,*)Yc
      WRITE(5,*)'Yd (Distance from the crack centre to the point "d" in "Y" direction)'
      READ(6,*)Yd
      WRITE(5,*)'W (The width of the specimen)'
      READ(6,*)W
      WRITE(5,*)'Propose an intial value for "e" (Eccentricity)'
      READ(6,*)eccen
      WRITE(5,*)'How many values of volts will be calculated'
      READ(6,*)NVOLT
      WRITE(6,*)
      WRITE(5,*)'Enter the values in the next sequence'
      WRITE(6,50)
      WRITE(5,*)' Va     Vb     Vc     Vd'
      WRITE(5,50)
      WRITE(5,*)'WHAT IS THE NAME OF THE FILE WHERE DATA IS ALOCATED?'
      READ(6,*)VOLTFI
       OPEN(20,FILE=VOLTFI)
```

```
      READ(20,*)(Vola(I),Volb(I),Volc(I),Vold(I),I=1,NVOLT)
      CLOSE (20)
      WRITE(5,50)
      WRITE(5,*)'Give the two initial points for "Ka" and "Kb" as this program is going'
      WRITE(5,*)'to use the bisection method'
45    WRITE(5,*)
      WRITE(5,*)'K0'
      READ(6,*)K2
      WRITE(5,*)'K1'
      READ(6,*)K3
      WRITE(5,400)
50    Format(/80('-'))
100   FORMAT(/80('-')/'Values from Ka ',F10.6,',',F10.6,/'Values from Kb ',F10.6,',',F10.6/)
200   Format(/'Xa = ',F6.3,2x,'Xb = ',F6.3,2x,'Yc = ',F6.3,2x,'Yd = ',F6.3/)
400   Format (//)
600   Format(F7.4,1x,F10.4,1x,F10.4,1x,F7.4,1x,F7.4,1x,F8.6,1x,F8.6,1x,F8.6,1x,F8.6)
      WRITE(5,*)'WOULD YOU LIKE TO SAVE THE DATA IN A FILE?'
160   WRITE(5,*)'PRESS 1 IF YES, PRESS 2 IF NOT'
      READ(6,*)RESP
      IF(RESP.GE.3)GO TO 160
      IF(RESP.EQ.2)GO TO 140
      IF(RESP.EQ.1) THEN
      WRITE(5,*)'ENTER THE NAME OF THE FILE, NO MORE THAN 10 CHARACTERS'
      READ(6,*)NAME
      OPEN(5,FILE = NAME)
      PRINT *,'YOUR DATA HAVE BEEN SAVED IN ',NAME,' FILE'
      END IF
140   DO 35 I=1,NVOLT
      Va=Vola(I)
      Vb=Volb(I)
      Vc=Volc(I)
      Vd=Vold(I)
      e=eccen
      N=0
      Do 15 N=1,10
      M=0
      K0=K2
      K1=K3
      Pi=3.141592654
20    A=((COSH((Pi*Yc)/(2*(w+e))))**2)-1
      B0=((COSH(K0*Va))**2)                  !For points A and C in the plate
      B1=((COSH(K1*Va))**2)
      C=(COS((Pi*(Xa+e))/(2*(w+e))))**2           !A (Xa,0) and C (W,Yc)
      D0=((COSH(K0*Vc))**2)
      D1=((COSH(K1*Vc))**2)
! Solving equation 1 and 3 for Ka eliminating Aa
      J0=1-D0+((A*B0)/C)                 !Equation to solve Ka
      J1=1-D1+((A*B1)/C)
! Checking there are a positive and a negative value in the initial two points
      IF (J0.GT.0.AND.0.LT.J1) THEN
```

```
      WRITE(5,50)
      WRITE(5,*)'Between those two initial points (K) is no one value for Ka'
      WRITE(5,*)'and both of them are positives'
      M=1.5
      GOTO 10
      END IF
      IF (J0.LT.0.AND.J1.LT.0) THEN
      WRITE(5,50)
      WRITE(5,*)'Between those two initial points (K) are no one value for Ka'
      WRITE(5,*)'and both of them are negatives'
      M=1.5
      GOTO 10
      END IF
! Dividing the two initial points and obtaining the middle one
      K4=(K0+K1)/2
      B4=((COSH(K4*Va))**2)
      D4=((COSH(K4*Vc))**2)
      J4=1-D4+((A*B4)/C)
! Checking if that point is close to cero in order to get the approach to the real value of Ka
      IF (J4.LT.0.01.AND.J4.GT.-0.01) THEN
      Ka=K4
      M=1
      GOTO 10
      END IF
! Getting the new point on the method
      IF (J0.LT.0.AND.J4.LT.0) THEN
      K0=K4
      GOTO 20
      END IF
      IF (J0.GT.0.AND.J4.GT.0) THEN
      K0=K4
      GOTO 20
      END IF
      IF (J1.LT.0.AND.J4.LT.0) THEN
      K1=K4
      GOTO 20
      END IF
      IF (J1.GT.0.AND.J4.GT.0) THEN
      K1=K4
      GOTO 20
      END IF
! Start with the value of Kb
10    K0=K2
      K1=K3
25    F=((COSH((Pi*Yd)/(2*(w+e))))**2)-1
      G0=(COSH(K0*Vb))**2                    !For points B and D in the plate
      G1=(COSH(K1*Vb))**2
      H=(COS((Pi*(Xb-e))/(2*(w+e))))**2      !B (Xb,0) and D (W,Yd)
      I0=(COSH(K0*Vd))**2
      I1=(COSH(K1*Vd))**2
```

```
!Solving the equation 2 and 4
      L0=1+((F*G0)/H)-I0
      L1=1+((F*G1)/H)-I1                                    !Equation to solve Kb
! Checking the initial point for Kb
      IF (L0.GT.0.AND.0.LT.L1) THEN
      WRITE(5,50)
      WRITE(5,*)'Between those two initial points (K) is no one value for Kb'
      WRITE(5,*)'and both of them are positives'
      GOTO 30
      END IF
      IF (L0.LT.0.AND.L1.LT.0) THEN
      WRITE(5,50)
      WRITE(5,*)'Between those two initial points (K) are no one value for Kb'
      WRITE(5,*)'and both of them are negatives'
      GOTO 30
      END IF
! Dividing the two initial points and obtaining the middle one
      K4=(K0+K1)/2
      G4=(COSH(K4*Vb))**2
      I4=(COSH(K4*Vd))**2
      L4=1+((F*G4)/H)-I4
! Checking if that point is close to cero in order to get the aproch to the real value of Kb
      IF (L4.LT.0.001.AND.L4.GT.-0.001) THEN
      Kb=K4
      GOTO 60
      END IF
! Getting the new point on the method
      IF (L0.LT.0.AND.L4.LT.0) THEN
      K0=K4
      GOTO 25
      END IF
      IF (L0.GT.0.AND.L4.GT.0) THEN
      K0=K4
      GOTO 25
      END IF
      IF (L1.LT.0.AND.L4.LT.0) THEN
      K1=K4
      GOTO 25
      END IF
      IF (L1.GT.0.AND.L4.GT.0) THEN
      K1=K4
      GOTO 25
      END IF
 30   WRITE(5,100)J0,J1,L0,L1
      GOTO 55
 60   IF (M.EQ.1.5) THEN
      WRITE(5,100)J0,J1,L0,L1
      GOTO 55
      END IF
      e1=(W*(Kb-Ka)/(Kb+Ka))
```

```
      e=e1
15    Continue
      Aa=((2*(W+e)/Pi)*ACOS(COS((Pi*(Xa+e))/(2*(w+e)))/COSH(Ka*Va)))-e  !From eq 1
      Ab=((2*(W-e)/Pi)*ACOS(COS((Pi*(Xb-e))/(2*(w-e)))/COSH(Kb*Vb)))+e  !From eq 2
      IF (I.EQ.1) THEN
      Write(5,50)
      Write(5,200)Xa,Xb,Yc,Yd
      Write(5,*)'W = ',w
      WRITE(5,50)
      WRITE(5,*)'  e     Ka     Kb     Aa     Ab     Va     Vb     Vc     Vd'
      Write(5,*)
      WRITE(5,50)
      END IF
      Write(5,600)e,Ka,Kb,Aa,Ab,Va,Vb,Vc,Vd
35    CONTINUE
      Write(5,50)
      GOTO 40
55    Write(5,*)'Would you like to try new values for K0 and K1?'
      Write(5,*)'Type 1 if yes'
      Read(6,*)Q
      IF (Q.EQ.1) THEN
      GOTO 45
      END IF
      Write(5,50)
40    Stop
      End
```

A 8.1 : Example output from programme obtaining crack length from voltage difference.

```
--------------------------------------------------------------------------------

Xa =   1.600  Xb =   1.600  Yc = 20.000  Yd = 20.000

 W =       40.0000

--------------------------------------------------------------------------------
    e        Ka          Kb        Aa        Ab        Va        Vb        Vc        Vd


--------------------------------------------------------------------------------
 0.0217   561.5234   562.1338  1.8128  1.8045 0.000060 0.000058 0.001400 0.001400
-0.4066   576.1719   564.5752  1.8587  1.7528 0.000057 0.000055 0.001380 0.001410
-0.1949   566.4063   560.9131  1.8278  1.7833 0.000058 0.000058 0.001390 0.001410
-0.1080   566.4063   563.3545  1.7965  1.7740 0.000055 0.000055 0.001390 0.001400
-0.1080   566.4063   563.3545  1.8171  1.7989 0.000058 0.000059 0.001390 0.001400
-0.1080   566.4063   563.3545  1.7965  1.7989 0.000055 0.000059 0.001390 0.001400
-0.1949   566.4063   560.9131  1.8351  1.7833 0.000059 0.000058 0.001400 0.001410
-0.3203   576.1719   567.0166  1.8611  1.8010 0.000059 0.000062 0.001380 0.001400
-0.4066   576.1719   564.5752  1.8671  1.7749 0.000058 0.000059 0.001380 0.001410
-0.1732   566.4063   561.5234  1.8547  1.8303 0.000062 0.000065 0.001390 0.001410
 0.0217   561.5234   562.1338  1.8062  1.8460 0.000059 0.000064 0.001400 0.001400
-0.1949   566.4063   560.9131  1.8811  1.8018 0.000065 0.000061 0.001390 0.001410
-0.1080   566.4063   563.3545  1.8608  1.7989 0.000064 0.000059 0.001390 0.001400
-0.1080   566.4063   563.3545  1.8386  1.7989 0.000061 0.000059 0.001390 0.001400
 0.0000   566.4063   566.4063  1.8119  1.7856 0.000059 0.000055 0.001390 0.001390
 0.0000   561.5234   561.5234  1.8085  1.7889 0.000059 0.000056 0.001400 0.001400
 0.0217   561.5234   562.1338  1.7805  1.8180 0.000055 0.000060 0.001400 0.001400
 0.0000   561.5234   561.5234  1.7889  1.7763 0.000056 0.000054 0.001400 0.001400
-0.1949   566.4063   560.9131  1.8426  1.7894 0.000060 0.000059 0.001400 0.001410
-0.3203   576.1719   567.0166  1.8218  1.7888 0.000054 0.000060 0.001380 0.001400
-0.4066   576.1719   564.5752  1.8755  1.7749 0.000059 0.000059 0.001380 0.001410
-0.1080   566.4063   563.3545  1.8313  1.7801 0.000060 0.000056 0.001390 0.001400
-0.3203   576.1719   567.0166  1.8611  1.7655 0.000059 0.000056 0.001380 0.001400
-0.1286   571.2891   567.6270  1.8089  1.7748 0.000056 0.000055 0.001380 0.001390
 0.2181   556.6406   562.7441  1.7671  1.8208 0.000056 0.000057 0.001400 0.001390
-0.3203   576.1719   567.0166  1.8295  1.7655 0.000055 0.000056 0.001380 0.001400
-0.1949   566.4063   560.9131  1.8205  1.7833 0.000057 0.000058 0.001390 0.001410
 0.0000   566.4063   566.4063  1.7920  1.8256 0.000056 0.000061 0.001390 0.001390
 0.2181   556.6406   562.7441  1.7787  1.8580 0.000058 0.000062 0.001400 0.001390
-0.3203   576.1719   567.0166  1.8775  1.7770 0.000061 0.000058 0.001380 0.001400
 0.0000   566.4063   566.4063  1.8326  1.7730 0.000062 0.000053 0.001390 0.001390
-0.3203   576.1719   567.0166  1.8531  1.7598 0.000058 0.000055 0.001380 0.001400
 0.0000   566.4063   566.4063  1.8119  1.7856 0.000059 0.000055 0.001390 0.001390
-0.1286   571.2891   567.6270  1.8160  1.7871 0.000057 0.000057 0.001380 0.001390
-0.3203   576.1719   567.0166  1.8611  1.7435 0.000059 0.000052 0.001380 0.001400

--------------------------------------------------------------------------------
```

A 9: Methods to get K values for eccentric cracked plate under uniform tension [177].

Two solutions have been used in this work.

A 8.1 : Empirical formulation.

Having an eccentric crack in a plate under uniform tension as the next figure, K solutions are given by the following table [177].

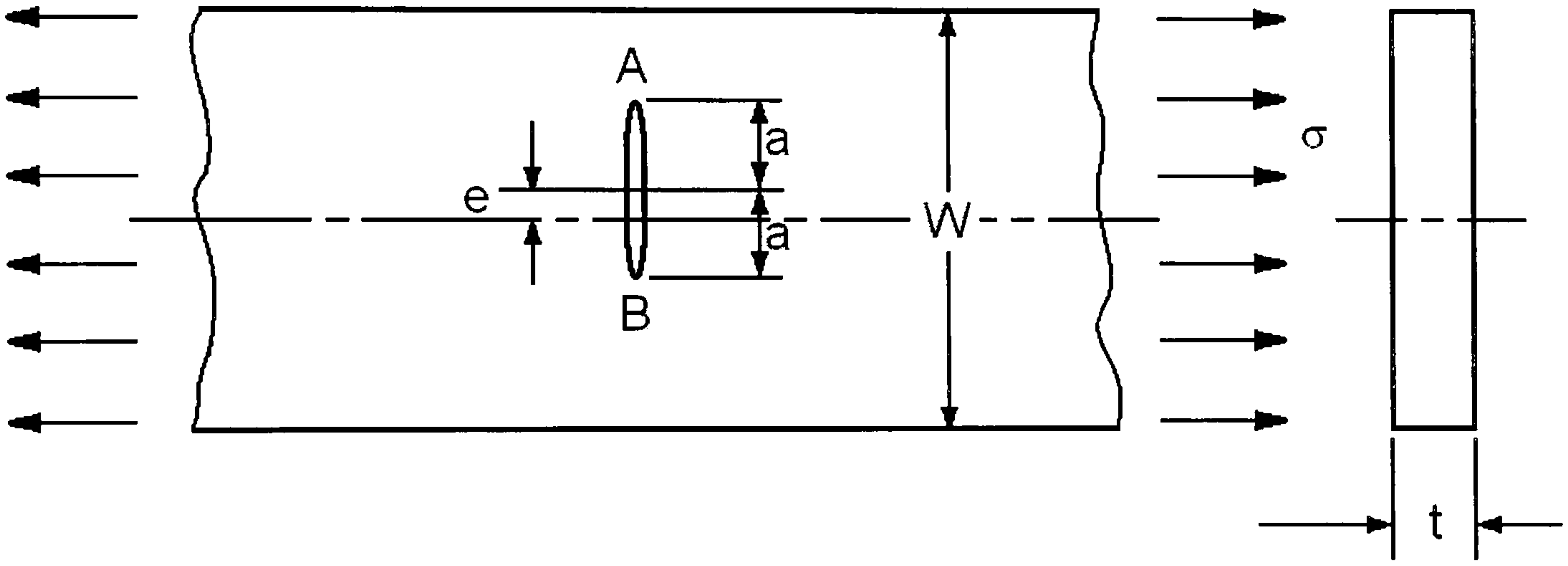

$$[K_I]_A = \sigma\sqrt{\pi a} \cdot [F_I(\alpha, \beta)]_A,$$

$$\alpha = \frac{2a}{W - 2e} \qquad \beta = \frac{2e}{W}$$

$$[F_I]_A = (\sec \frac{\pi\alpha}{2} \cdot \frac{Sin2\alpha\beta}{2\alpha\beta})^{1/2}$$

for ±3% accuracy, $0.1 \le \alpha \le 0.9, 0 \le \beta \le 0.4$ and / or $0.1 \le \alpha \le 0.7, 0 \le \beta \le 1.0$

A 9.2 : Laurent's expansion of complex stress potentials.

Taking the figure sown above as a reference, nomenclature can be used in this method.

$[K_I]_{A,B} = \sigma\sqrt{\pi a} \cdot [F_I(\alpha, \beta)]_{A,B}$, $\alpha = \frac{2a}{W-2e}$, $\beta = \frac{2e}{W}$

Table boundary correction factors, $[F_I(\alpha, \beta)]_A$, for upper crack tip A

$[\{F_I(\alpha, \beta)\}_A = \{K_I\}_A / \sigma\sqrt{\pi a}]$

β \ α	0.1	0.2	0.3	0.4	0.5	0.6	0.7	0.8	0.9
0	1.0060	1.0246	1.0577	1.1094	1.1867	1.3033	1.4881	1.811	2.47
0.02	1.0058	1.0239	1.0564	1.1073	1.1837	1.2994	1.4832	1.806	2.47
0.04	1.0056	1.0234	1.0553	1.1056	1.1814	1.2965	1.4799	1.804	2.48
0.06	1.0055	1.0229	1.0544	1.1042	1.1795	1.2943	1.4777	1.803	2.49
0.08	1.0054	1.0225	1.0537	1.1031	1.1781	1.2927	1.4764	1.804	2.50
0.1	1.0053	1.0222	1.0530	1.1022	1.1770	1.2916	1.4758	1.805	2.51
0.2	1.0050	1.0212	1.0513	1.0999	1.1745	1.2898	1.4765	1.814	2.54
0.3	1.0049	1.0208	1.0507	1.0989	1.1732	1.2881	1.4743	1.810	2.54
0.4	1.0048	1.0205	1.0497	1.0969	1.1695	1.2812	1.4614	1.784	2.47
0.5	1.0046	1.0197	1.0476	1.0926	1.1613	1.2664	1.4344	1.732	2.36
0.6	1.0043	1.0183	1.0442	1.0855	1.1483	1.2436	1.3943	1.657	2.20
0.7	1.0039	1.0164	1.0395	1.0762	1.1316	1.2152	1.3460	1.572	2.03
0.8	1.0034	1.0142	1.0341	1.0659	1.1136	1.1854	1.2972	1.489	1.88
0.9	1.0029	1.0122	1.0295	1.0569	1.0985	1.1608	1.2583	1.426	1.77
1.0	1.0026	1.0112	1.0272	1.0528	1.0915	1.1497	1.2407	1.397	1.72

Table boundary correction factors, $[F_I(\alpha, \beta)]_B$, for lower crack tip B

$[\{F_I(\alpha, \beta)\}_B = \{K_I\}_B / \sigma\sqrt{\pi a}]$

β \ α	0.1	0.2	0.3	0.4	0.5	0.6	0.7	0.8	0.9
0	1.0060	1.0246	1.0577	1.01094	1.1867	1.3033	1.4881	1.811	2.47
0.02	1.0057	1.0234	1.0544	1.1021	1.1724	1.2759	1.4342	1.695	2.18
0.04	1.0055	1.0223	1.0516	1.0959	1.1602	1.2531	1.3910	1.608	1.98
0.06	1.0053	1.0214	1.0491	1.0906	1.1500	1.2341	1.3562	1.542	1.85
0.08	1.0052	1.0206	1.0470	1.0861	1.1413	1.2184	1.3280	1.490	1.75
0.1	1.0050	1.0199	1.0452	1.0823	1.1340	1.2053	1.3051	1.450	1.67
0.2	1.0046	1.0179	1.0399	1.0709	1.1127	1.1680	1.2426	1.348	1.51
0.3	1.0045	1.0172	1.0380	1.0672	1.1058	1.1565	1.2249	1.324	1.48
0.4	1.0044	1.0170	1.0374	1.0660	1.1040	1.1540	1.2218	1.321	1.48
0.5	1.0042	1.0165	1.0364	1.0645	1.1018	1.1510	1.2177	1.315	1.47
0.6	1.0040	1.0155	1.0343	1.0608	1.0960	1.1424	1.2047	1.294	1.44
0.7	1.0036	1.0139	1.0309	1.0546	1.0860	1.1269	1.1813	1.258	1.38
0.8	1.0031	1.0120	1.0264	1.0465	1.0729	1.1068	1.1511	1.212	1.31
0.9	1.0026	1.0101	1.0222	1.0388	1.0603	1.0876	1.1227	1.170	1.24
1.0	1.0024	1.0092	1.0201	1.0349	1.0540	1.0779	1.1084	1.149	1.21